Individual particle motion in colloids: Microviscosity, microdiffusivity, and normal stresses

Thesis by

Roseanna N. Zia

In Partial Fulfillment of the Requirements

for the Degree of

Doctor of Philosophy

California Institute of Technology

Pasadena, California

2011

(Defended May 6, 2011)

Dedicated to my husband, Jeffry Zolkower,

to the memory of my mother, Rosalie Emma Staub,

and of my stepfather, Jack Edward Brown;

to Laurie

and to the C.T.W.

Acknowledgements

Several remarkable people have provided the foundation upon which my development as a scientist at Caltech has been built. The first and most important intellectual and scientific influence is my thesis advisor, Professor John Brady. When I was in the process of selecting a graduate school, my undergraduate advisor gave me the following advice: The three most important decisions you can make about graduate school are: (1) choose your advisor well, (2) choose your advisor well, and (3) choose your advisor well. I am happy to say that I followed that advice from my other primary academic influence, Professor David Wollersheim, and chose the very best advisor at the California Institute of Technology. I was influenced by Professor Brady's talent for combining physical insight with extraction of the fundamental physics in complex problems, and his vision for where the important problems in soft matter science lie. I have learned from him how to explore problems both inside and outside my field, how to see the fundamental questions that should be asked, how to know the answer to a problem before solving it, and how to deliver a presentation with poise and authority immediately after taking three flights of stairs and running a half mile at top speed. As I move forward to a faculty position of my own, my intellectual foundation is equal parts John Brady and Caltech, with a sense of professional responsibility instilled by David Wollersheim. I could not be more proud of that foundation.

I chose to come to Caltech because I wanted to learn. Not just to gain knowledge, but to learn how to see the physical world differently, more fundamentally. No one does this more elegantly and powerfully than Professor Zhen-Gang Wang. His lectures in statistical mechanics and polymer physics are a study in illustrating the beauty of science, and how much one can understand about states of matter by identifying fundamental driving forces, examining limiting behavior, and making

simple scaling arguments. I am grateful to have taken several classes under his instruction.

To Dr. James Swan I owe an unpayable debt for many, many hours of discussions and teaching about colloid science, probability and statistics, hydrodynamics, and the angst of intellectual development. He is hands-down the best teacher I have ever met. I also thank him for superb Brownian dynamics simulation code.

I thank Dr. Olawale Oladiran, under whose guidance at the University of Missouri Research Reactor I worked as an engineering intern—my first job as an engineer—and whose rigorously high standards and confidence in me set my foundation as an engineer. In addition, the professional guidance of Professors Ravi Ravichandran, Tim Colonius, David Tirrell, Bradley Olsen, Aditya Khair, and Eric Lauga were invaluable in the process of seeking and acquiring a faculty position in which I can continue to thrive intellectually. I thank Professor David Goodwin for being willing to offer Thermodynamics to a class of one, Professor Dan Meiron for my ability to solve PDE's, and Professor Niles Pierce, who gave me a fantastic introduction to complex variables, and after whose midterms nothing can ever scare me again.

I found wonderful friends at Caltech: Jim Swan, Manuj Swaroop, Shelby Hutchens, Gabriela Venturini, Ashley Moore, Daniel Hurtado, Vaughan Thomas, and Nick Hoh. I also thank one particularly outstanding SURF student, Kevin Gu, for tireless, high-quality work; Natalie Gilmore and the Grad Office; Shane Clarke and CLS; Kathy Bubash and Cheryl Geer, and Cristina DeZan.

I am grateful for the deep commitment to education instilled in me by my parents, Rosalie Emma Staub and Ashoor Zia; to my stepfather, Jack Edward Brown, who taught me self-respect and moral responsibility; for the support of Ninev and Laura; and for everything, to Laurie and to Bill Wilson.

Finally, and most importantly, I thank my husband and best friend, Jeffry Zolkower. Words cannot express my gratitude for his presence in my life, his shared happiness in my scientific achievement, and his tireless support. From the time I called you and said, "I got in to Caltech, we're moving to California," through branch cuts and Hilbert spaces and perturbation theory and qualifying exams and conferences and never-ending derivations of normal stress differences, you have been the fundamental source of happiness in my life.

The research in this thesis was supported by the United States Department of Defense, through the National Defense Science and Engineering Graduate Fellowship program and the Air Force Office of Scientific Research. Their support is gratefully acknowledged.

Abstract

Colloidal dispersions play an important role in nearly every aspect of life, from paint to biofuels to nanotherapeutics. In the study of these so-called complex fluids, a connection is sought between macroscopic material properties and the micromechanics of the suspended particles. Such properties include viscosity, diffusivity, and the osmotic pressure, for example. But many such systems are themselves only microns in size overall; recent years have thus seen a dramatic growth in demand for exploring microscale systems at a much smaller length scale than can be probed with conventional macroscopic techniques. Microrheology is one approach to such microscale interrogation, in which a Brownian "probe" particle is driven through a complex fluid, and its motion tracked in order to infer the mechanical properties of the embedding material. With no external forcing the probe and background particles form an equilibrium microstructure that fluctuates thermally with the solvent. Probe motion through the dispersion distorts the microstructure; the character of this deformation, and hence its influence on probe motion, depends on the strength with which the probe is forced, F^{ext}, compared to thermal forces, kT/b, defining a Péclet number, $Pe = F^{ext}/(kT/b)$, where kT is the thermal energy and b the bath-particle size. Both the mean and the fluctuating motion of the probe are of interest. Recent studies showed that the reduction in mean probe speed gives the effective material viscosity. But the velocity of the probe also fluctuates due to collisions with the suspended particles, causing the probe to undergo a random walk process. It is shown that the long-time mean-square fluctuational motion of the probe is diffusive and the effective diffusivity of the forced probe is determined for the full range of Péclet number. At small Pe Brownian motion dominates and the diffusive behavior of the probe characteristic of passive microrheology is recovered, but with an incremental flow-induced "micro-diffusivity" that scales as $D^{micro} \sim D_a Pe^2 \phi_b$, where

ϕ_b is the volume fraction of bath particles and D_a is the self-diffusivity of an isolated probe. At the other extreme of high Péclet number the fluctuational motion is still diffusive, and the diffusivity becomes primarily force-induced , scaling as $(F^{ext}/\eta)\phi_b$, where η is the viscosity of the solvent. The force-induced "microdiffusivity" is anisotropic, with diffusion longitudinal to the direction of forcing larger in both limits compared to transverse diffusion, but more strongly so in the high-Pe limit.

Previous work in microrheology defined a scalar viscosity; however, a tensorial expression for the suspension stress in microrheology was still lacking. The notion that diffusive flux is driven by gradients in particle-phase stress leads to the idea that the microdiffusivity can be related directly to the suspension stress. In consequence, the anisotropy of the diffusion tensor may reflect the presence of normal stress differences in nonlinear microrheology. While the particle-phase stress can be determined as the second moment of the deformed microstructure, in this study a connection is made between diffusion and stress gradients, and an analytical expression for particle-phase stress as a function of the microdiffusivity and microviscosity is obtained. The two approaches agree, suggesting that normal stresses and normal stress differences can be measured in nonlinear microrheological experiments if both the mean and mean-square motion of the probe are monitored. Owing to the axisymmetry of the motion about a spherical probe, the second normal stress difference is zero, while the first normal stress difference is linear in Pe for $Pe \gg 1$ and vanishes as Pe^4 for $Pe \ll 1$. An additional important outcome is that the analytical expression obtained for stress-induced migration can be viewed as a generalized non-equilibrium Stokes-Einstein relation.

Studies of steady-state dispersion behavior reveal the hydrodynamic and microstructural mechanisms that underlie non-Newtonian behaviors (*e.g.* shear-thinning, shear-thickening, and normal stress differences). But an understanding of how the microstructures evolve from the equilibrium state, and how non-equilibrium properties develop in time is much less understood. Transient suspension behavior in the near-equilibrium, linear-response regime has been studied via its connection to low-amplitude oscillatory probe forcing and the complex modulus; at very weak forcing, the microstructural response that drives viscosity is indistinguishable from equilibrium fluctuations. But important information about the basic physical aspects of structural development and relaxation

in a medium are captured by startup and cessation of the imposed deformation in the nonlinear regime, where the structure is driven far from equilibrium. Here we study the evolution of stress and microstructure in a colloidal dispersion by tracking transient probe motion during startup and cessation of a strong flow. For large Pe, steady state is reached when a boundary layer (in which advection balances diffusion) forms at particle contact on the timescale of the flow, a/U, where a is the probe size and U its speed. On the other hand, relaxation following cessation occurs over several timescales corresponding to distinct physical processes. For very short times, the timescale for relaxation is set by the diffusion over the boundary-layer thickness. Nearly all stress relaxation occurs during this process, owing to the dependence of the bath-particle drag on the contact value of the microstructure. At longer times the Brownian motion of the bath particles acts to close the wake. In this long-time limit as structural isotropy is restored, the majority of the microstructural relaxation occurs with very little change in suspension stress. The time to close the wake is independent of the wake length—it is set only by particle size, because Brownian motion is the only diffusive mechanism for closing the wake. Theoretical results are presented and compared with Brownian dynamics simulation. Two regimes of probe motion are studied: an externally applied constant force and an imposed constant velocity. The microstructural evolution is qualitatively different for the two regimes, with a longer transient phase and longer wake at steady state in the latter case. The work is also compared to analogous results for sheared suspensions.

The study moves next to investigations of dual-probe microrheology. Motivated by the phenomenon of equilibrium depletion interactions, we study the interaction between a pair of probe particles translating with equal velocity through a dispersion with their line of centers transverse to the external forcing. The character of the microstructure surrounding the probes is determined both by the distance R by which the two probes are separated and by the strength of the external forcing, $Pe = Ua/D_b$, where U is the constant probe velocity, a is the probe size and D_b the diffusivity of the bath particles. Osmotic pressure gradients develop as the microstructure is deformed, giving rise to an interactive force between the probes. This force is studied for a range of Pe and R. For all separations $R > 2a$, the probes attract when Pe is small. As the strength of the forcing increases,

a qualitative change in the interactive force occurs: the probes repel each other. The probe separation R at which the attraction-to-repulsion transition occurs decreases as Pe increases, because the entropic depletion attraction becomes weak compared to the force-induced osmotic repulsion. The non-equilibrium interactive force is strictly repulsive for two separated probes.

But nonlinear microrheology provides far more than a microscale technique for interrogating complex fluids. It provides a window through which one can view the atomic world. In 1906, Einstein published the famous thought experiment in which he proposed that if matter were indeed composed of atoms, then the motion of a small particle suspended in the fluid would move with the same random trajectories as the solvent atoms. Combining theory from kinetics, diffusion, and thermodynamics, he showed that the diffusive motion of a small particle is indeed evidence of the existence of the atom; Perrin confirmed the theory with measurement in 1909. This is a profound conclusion, drawn by simply by watching the motion of a single particle in a fluid. In our work we follow this example and watch a particle move in a complex fluid—but now for a system that is not at equilibrium. The power of Einstein's result is that it gives the relationship between fluctuation and dissipation at equilibrium—between the atomic description of a atomic energy in the fluid (Boltzmann's constant) and the macroscopic description and temperature of a fluid (the universal gas constant.) By studying fluctuations *away from equilibrium*, we have discovered an analogous non-equilibrium relation between fluctuation and dissipation—and that the balance between the two is stored in the mechanical stress. A final connection can be made between this stress, energy storage and an "effective temperature" of the medium.

Contents

[1]This chapter includes content from our previously published article, Single-particle motion in colloids: force-induced diffusion, by Roseanna N. Zia and John F. Brady, Journal of Fluid Mechanics, Vol. 658 (September 2010), pp. 188-210 Copyright 2010 Cambridge University Press. Reprinted with permission.

List of Tables

List of Figures

Chapter 1

Introduction

Complex fluids encompass such diverse systems as toothpaste, the interior of the cell, and sprayable solar panels, to name just a few. Uniting these diverse materials is their multiphase structure: a collection of microscopic domains or particles embedded in a continuum material. The microstructure formed by the suspended particles can profoundly influence material flow behavior. An understanding of how complex fluids respond to imposed flows or forces is critical to their processing, dispensing, durability, and dynamic performance. Rheology—the study of the flow of complex fluids—is an active area of scientific research; one of its aims is to understand and characterize material properties by connecting them to the mechanics of their internal microstructures. Such transport properties include viscosity, diffusivity, and suspension stress. Traditional rheology experiments are carried out by imposing a bulk shearing motion on a sample of material in a viscometer; the shearing motion may be constant, or an oscillatory shear may be applied in order to explore time-dependent phenomena such as viscoelasticity. Barnes, Hutton, and Walters (1989) provide a thorough review of traditional rheological techniques. Theoretical rheology has the additional goal of deriving the constitutive relation between stress and strain-rate from the statistical mechanics of the particle microstructure; for steady-state systems undergoing shear, the results are well-known for simple hard-sphere, monodisperse systems (Batchelor, 1977; Bossis & Brady, 1989). But recent years have seen a dramatic growth in demand for exploring microscale systems whose dynamic response properties must be measured at a much smaller length scale than is possible to probe with conventional viscometers. Understanding spatial variation in network strength in functionalized hydrogels, interrogating rare

biological fluids, and determination of the diffusive speed of nanotherapeutic devices inside the cell are a just few examples (Heath *et al.*, 2009; Verkman, 2002; Lukacs *et al.*, 1999; Suh *et al.*, 2003). The fundamental process underlying each of these problems is material response to dynamic forcing by a microscale probe—a microscopic version of rheometry. This type of microscale probing, known as "microrheology,"has burst onto the scene of material evaluation in the last decade, and has been accompanied by ground-breaking work (MacKintosh & Schmidt, 1999; Habdas *et al.*, 2004; Meyer *et al.*, 2005; Squires & Brady, 2005; Khair & Brady, 2006; Zia & Brady, 2010).

Microrheology is a collection of techniques in which the motion of a colloidal particle (or set of particles) is tracked in order to determine the properties of the surrounding medium (MacKintosh & Schmidt, 1999). There are two main types of particle-tracking microrheology: *passive*—tracking random motion due to thermal fluctuations—and *active*—applying a constant or oscillatory force to the particles, for example by using optical tweezers or magnetic fields. A detailed comparison can be found in Khair & Brady (2006). Passive microrheology is useful for obtaining linear viscoelastic properties by correlating the random thermally driven displacements of tracers to the complex modulus through a generalized Stokes-Einstein relation—a process which is well understood but which is limited in its scope to equilibrium systems. Yet as noted above, many systems of interest are driven out of equilibrium and display nonlinear behaviors. Recently, a body of work has emerged focusing on this active, nonlinear microrheology regime (Habdas *et al.*, 2004; Squires & Brady, 2005; Meyer *et al.*, 2005; Khair & Brady, 2006; Wilson *et al.*, 2009). In such a system, tracer particles undergo displacements due not only to random thermal fluctuations, but also due to the application of an external force applied directly to the tracer, or "probe". The dispersion is driven out of equilibrium and, as with macrorheology, dynamic responses such as viscosity can be measured. Since the tracer interrogates the material at its own (micro)scale, much smaller samples are required compared to traditional macrorheology, and localized material heterogeneity can be explored. This is a particular benefit for rare biological materials and small systems such as cells. Khair & Brady (2006) and Zia & Brady (2010) recently established the theory that predicts the microviscosity and microdiffusivity of dilute systems of colloids, and defined the relationship between micro- and

macrorheology—a critical step in the development of microrheology as an experimental tool. Recent experiments confirm the theory—and raise important questions and concerns (Meyer *et al.*, 2005; Squires, 2008; Wilson *et al.*, 2009) which are discussed below.

But in both theory and experiment, the focus thus far has been on the *mean* response of the material—the viscosity—and far less work has been devoted to particle fluctuations that occur due to collisions between the probe and bath particles. As the probe moves through the dispersion it must push neighboring particles out of its way; these collisions induce fluctuations in the probe's velocity, scattering it from its mean path. Is this scattering diffusive? Is it isotropic? How important is the scattering compared to the Brownian diffusion the probe simultaneously undergoes? The answers to these questions are fundamental to understanding the motion of an forced or self-propelled microscale particle—important both for scientific and technology considerations. Little work has been published on this topic (Habdas *et al.*, 2004), even though it has implications for a wide range of technologies beyond material interrogation, *e.g.* nanotherapeutics and self-propelled particles such as microscale swimmers and artificial nanomotors.

Previous study of particle fluctuations in colloidal *macro*rheology shows that imposing a shearing flow on a suspension enhances particle diffusivity (Leighton & Acrivos, 1987; Morris & Brady, 1996; Brady & Morris, 1997; Breedveld *et al.*, 1998). The imposed shear flow drives the microstructure from equilibrium, giving rise to mechanisms of diffusion not present in a quiescent suspension: a deformed microstructure and interparticle collisions. A forced *micro*rheological probe also imposes a flow that drives the suspension from equilibrium, again leading to a deformed microstructure and interparticle collisions—and hence to an analogous force-induced diffusion, or "micro-diffusivity." In the first part of this work, we extend the theoretical model of active, nonlinear microrheology to one that is explicit in the fluctuations of the microstructure and thereby develop expressions for predicting the resultant force-induced diffusion.

It is also useful to ask whether the qualitative agreement between micro- and macroviscosity can be extended to the micro- and macrodiffusivity. Both the shear- and force-induced diffusion grow out of fundamentally similar mechanisms: external forcing causes the tracer to scatter off of the

microstructure, rather than wander passively through it. But the directionality and magnitude of the scattering depend on the shape of the deformed microstructure, and this asymmetry is distinct for the two cases, as illustrated in figure 3.1. The idea of whether a direct correlation between macro shear-induced diffusion and micro force-induced diffusion is possible (or even necessary) will be explored in this study, and a comparison between the two sought.

While microviscosity and diffusion can easily be measured by monitoring the mean and fluctuating motion of the driven probe, no such simple technique has yet been put forth to determine suspension stress, or to connect it to viscosity in the constitutive form employed in traditional macrorheology. Suspension stress is strongly influenced by the statistical properties of the dispersed particles—by the degree to which their distribution is driven from equilibrium, and by the Brownian motion which acts to restore a uniform configuration. In this work, we examine the effect of probe forcing on the bulk stress in a Brownian suspension. Previous approaches in nonlinear microrheology were able to produce only a scalar evaluation of the stress due to the axisymmetric geometry surrounding the probe. It is shown that the force-induced diffusion tensor is transversely anisotropic due to the microstructural asymmetry produced by probe motion (Zia & Brady, 2010); together with the premise that diffusion is driven by gradients in the stress, we seek a connection between the microdiffusivity tensor and the stress tensor, and importantly, between the anisotropic microdiffusivity and normal stress differences. A macroscopic approach is taken, in which the momentum balance over the particle phase and suspension are considered, and stress gradients are connected with particle flux. It is found that such gradients drive both advective and diffusive flux—the mean and mean-square motion of the probe particle. The resulting analytical expression gives the stress in terms of the microdiffusivity and microviscosity. Results are compared with Brownian dynamics simulations, as well as the stress computed via a traditional micromechanical (statistical mechanics) approach. Agreement is excellent, suggesting that by simply monitoring the motion of the probe as it is driven through the dispersion, one can obtain its diffusivity, the effective viscosity and the stress tensor for the medium.

Up to this point in the investigation, focus has been placed on the steady-state behavior of

suspensions. But how does a suspension microstructure evolve from the equilibrium state to steady state? How quickly does the stress decay once the flow is "turned off?" An important characteristic of complex fluids is their ability to exhibit time-dependent behaviors such as viscoelasticity and memory effects. Depending on the timescales with which they are forced, they may exhibit the elastic behavior of a solid, the viscous behavior of a liquid, or both. If a sudden strong flow is imposed on a dispersion, the individual particles cannot follow the flow instantaneously; the microstructure is distorted, and the material resists deformation similarly to a solid. If the forcing is continued for longer times, the microstructure begins to relax through the Brownian motion of the dispersed particles, viscously dissipating energy of the imposed flow. At equilibrium, Green-Kubo theory shows that thermal fluctuations give rise to short-term microstructural anisotropies, which in turn produce temporary stresses in the suspension. Brownian motion dissipates these anisotropies in time. In strongly non-equilibrium flows, however, Brownian motion cannot keep up with advection, and some of this energy is stored in the compressed particle configuration, giving rise to much larger suspension stress. Here, we study such behavior by examining stress and microstructural evolution just after the sudden startup of probe forcing, and following the shut-off of probe forcing.

Depletion interactions in suspensions also arise due to entropic forces, and have long been an important area of study. Their influence on particle aggregation has implications for processing, storage, and handling of complex fluids. For example, suspended microparticles in paint that give it tint must remain in suspension long enough for application to a surface; bitter-tasting phenolic compounds in wine are often removed prior to bottling; and the treatment of wastewater and purification of industrial slurries are critical to recovering clean water and safely storing toxic waste. At the microscale, depletion interactions may influence the formation and stability of bacterial colonies and biofilms, or the formation of critical aggregations inside the cell. Asakura & Oosawa (1954) identified the underlying mechanism for one form of aggregation, namely, that due to depletion interactions. When a pair of objects suspended in a dispersion of smaller particles are separated by a gap smaller than the small-particle size, a spatial gradient in osmotic pressure drives the two objects together. From a statistical perspective, the objects want to migrate into the depleted region to

make uniform the statistical distribution of particles in space. While much study has been devoted to equilibrium depletion interactions (see *e.g.* Russel *et al.* (1989)), little work has been devoted to the exploration of such interactions in non-equilibrium systems. In this study, non-equilibrium depletion interactions are investigated by dynamic simulation. The goal is to understand the physical mechanisms underlying such interactions. To this end, a pair of equally sized probes is driven at constant velocity $\boldsymbol{U}$ through an otherwise quiescent suspension of colloidal particles. The character of the microstructure surrounding the probes is determined both by the distance R by which the two probes are separated and by the strength of the external forcing, $Pe = Ua/D_b$, where U is the constant probe velocity and D_b the diffusivity of the bath particles. Osmotic pressure gradients develop as the microstructure is deformed, giving rise to an interactive force between the probes. This force is studied for a range of Pe and R by Brownian dynamics simulation.

As noted above, the use of microrheology as a material interrogation tool has seen enormous growth in recent years, but its use in determining bulk rheological properties must be carefully examined. Several important concerns have been raised in the literature (Meyer *et al.*, 2005; Squires, 2008; Wilson *et al.*, 2009) that we attempt to address here. One of the most important concerns is that a microrheological flow is not viscometric. As in macroscale falling-ball rheometry, the motion of the probe as it interacts with the microstructure is certainly indicative of the local structure around the probe. But how does this local rheology connect with the bulk rheology of the entire suspension? This question is taken up in the concluding chapter.

Finally, and most importantly, we conclude that nonlinear microrheology provides far more than a microscale technique for interrogating complex fluids. It is a lens through which one can view a molecular-scale world. Investigations of the fluctuating motion of microscopic particles has a rich and profound history. The so-called "Brownian movement" is named after the botanist Robert Brown, who wrote about—but never understood—his extensive observations of the vigorous movement of microscopic particles in water (Brown, 1828; Haw, 2007)[1]. The mysterious motion went unexplained for nearly a century. Then in 1906, Einstein published the results of his famous thought-experiment

[1]Random particle motion and its connection to the atomic nature of matter had been observed and written about much earlier; see, *e.g.* Lucretius (ca. 50 B.C.).

in which he proposed that if matter were indeed composed of atoms, then the motion of a small particle suspended in a fluid would move with the same random trajectories as the solvent atoms. Combining the theories of kinetics, diffusion, and thermodynamics, he proved that the diffusive motion of a small particle—Brownian motion—is indeed evidence of the existence of the atom; Perrin confirmed the theory with measurement in 1909, and from this work, Avagadro's number was determined. This is a profound conclusion, drawn by simply watching a particle move in liquid. Here we shall follow this example, and watch a particle move in a complex fluid—but now, for a system that is not at equilibrium. By studying fluctuations *away from equilibrium*, we have discovered an analogous non-equilibrium relation between fluctuation and dissipation—and that the balance between the two is stored in the mechanical stress. What can this tell us more fundamentally about energy and motion? Avogadro's constant is a scaling factor that connects the macroscopic and microscopic views of matter. As such, it provides the relation between other physical constants and properties. For example, it establishes a relationship between the macroscopic gas constant $\mathcal{R}$ and Boltzmann's constant k, which connects energy at the atomic level to temperature at the macroscopic level. Perhaps a similar constant away from equilibrium will reveal a connection between an "effective temperature" and particle energies.

Chapter 2

Background

In this chapter, a brief review is given of some basic aspects of colloidal suspension dynamics. This begins with a discussion of Brownian motion in §2.1, with an emphasis on microscopic versus macroscopic perspectives. In §2.2, an overview of the three diffusive regimes is presented, to set the foundation for a comparison between equilibrium and flow-induced diffusion that will be explored later in chapter 3. Again the microscopic versus macroscopic approaches will be emphasized, as will be done throughout the rest of the work.

Chapter 2 concludes with an introduction to the theoretical framework of microrheology. As discussed in the Introduction, the initial motivation for the study of microrheology was its ability to interrogate much smaller-scale systems than is possible with conventional macroscale rheometry. Thus far, most work in nonlinear microrheology has focused on the *mean* response of the suspension, and on the viscosity. In the remainder of this work, we shall explore the *fluctuations* in probe motion, and what they elucidate about force-induced diffusion and the stress. But before we begin, a brief review of previous work in microrheology will help set the foundation of the current study.

2.1 Brownian motion

In the early 1900's, Einstein was seeking to prove the statistical-atomic nature of matter. He hypothesized that if matter were indeed comprised of atoms or molecules, then in the liquid state their close proximity to one another should render their trajectories and velocities random (Haw, 2007). He reasoned that a small particle placed into a liquid should then move with the same random

trajectories as the solvent molecules themselves (Einstein, 1906). Drawing upon the kinetic theory of Clausius, if one knows the temperature T, one knows the thermal energy kT. The great leap in Einstein's argument was the following: he asserted that the particle must be in thermodynamic equilibrium with the solvent, and hence its kinetic energy must be the same as the thermal energy of the solvent. He then devised an elegant thought experiment to connect thermal motion to mechanical motion for small particles.

One presentation of his thought experiment proceeds as follows: Consider a suspension of particles of size a at number density n in a solvent of viscosity η, acted upon by an external field derivable from a potential $\Phi(\boldsymbol{x})$. The suspension is in a finite container where, for the sake of definiteness, the line of the external force is perpendicular to the plane of the "bottom" surface of the container. Einstein asserted that at equilibrium, the particles are arranged with a Boltzmann distribution

$$n(\boldsymbol{x}) = n_0 e^{-\Phi(\boldsymbol{x})/kT}, \tag{2.1}$$

where n_0 is the constant number density in the absence of the external field. The small-particle size sets the length scale for the Reynolds number $Re = U\,a/\nu \ll 1$ where ν is the kinematic viscosity; thus Stokes' equations govern the fluid mechanics. The velocity of a particle is then the product of the hydrodynamic mobility and the applied force, $\boldsymbol{U} = -\boldsymbol{M} \cdot \nabla\Phi$. The external force $-\nabla\Phi$ drives advective particle flux $\boldsymbol{j}_{adv} = n\boldsymbol{U} = -n\boldsymbol{M} \cdot \nabla\Phi$. This advective flux gives rise to a concentration gradient near the "bottom" of the container, which drives a diffusive, down-gradient flux, $\boldsymbol{j}_{diff} = -\boldsymbol{D} \cdot \nabla n$, in the opposite direction of the advective flux. At equilibrium the net flux must be zero:

$$-n\boldsymbol{M} \cdot (\nabla\Phi) - \boldsymbol{D} \cdot \nabla n = 0, \tag{2.2}$$

but since the potential force is arbitrary and the Boltzmann distribution holds at equilibrium, we have the result

$$\boldsymbol{D} = kT\boldsymbol{M}, \tag{2.3}$$

known as the Einstein-Smoluchowski equation. In the case of spherical particles,

$$\boldsymbol{D} = \frac{kT}{6\pi\eta a}\boldsymbol{I}. \tag{2.4}$$

Equation (2.4) is the famous Stokes-Einstein relation for the diffusivity of a spherical particle in a solvent. Einstein's assertion here is that a small particle of size a placed in a fluid of viscosity η at temperature T will fluctuate due to random impacts from solvent molecules—and these fluctuations of the particle cause it to undergo a random-walk process—it diffuses. Its diffusivity $\boldsymbol{D}$ is driven by the thermal energy kT, which is then dissipated back into the solvent by hydrodynamic drag, $\boldsymbol{I}/6\pi\eta a$. This gives a direct connection between the thermal energy of the solvent and the hydrodynamic drag on a microscopic particle—a statement of the fluctuation-dissipation theorem.

In 1909, Jean-Baptiste Perrin, an experimental physical chemist, sought to prove Einstein's theory (Haw, 2007). He passed light through a suspension of small particles and projected the image onto paper affixed to a wall. Using a pencil, he marked the trajectory of an individual particle at regular time intervals (figure 2.1). He conducted many realizations, and computed the mean-square displacement of a particle, and plotted it as a function of time. He found that indeed the mean-square displacement of a small particle grew linearly in time, in agreement with the process of diffusion—a random walk process that in the instance of the particle, could arise only if many

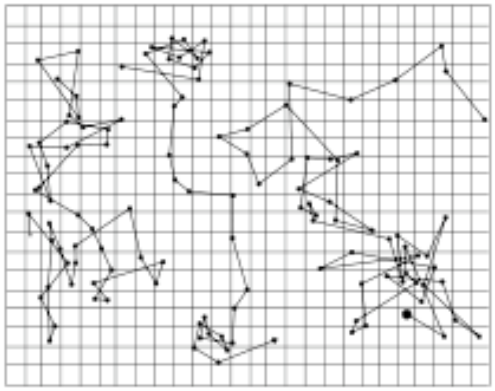

Figure 2.1: Reproduced from the book of Jean-Baptiste Perrin, *Les Atomes* (1914). Three tracings of the motion of colloidal particles of radius 0.53 μm, as seen under the microscope, are displayed. Successive positions every 30 seconds are joined by straight line segments. The mesh size is 3.2 μm.. Caption and image taken from Wikipedia.

random impacts were suffered by the test particle. Perrin published his results in his Ph.D. thesis and in the work "Brownian movement and the molecular reality" (Perrin, 1909). It is generally accepted as the first definitive proof of the existence of the atom.

This result is profound in its simplicity: by just watching a particle move, the existence of the atom was proven. It is as though a particle is a microscope, a lens through which we were able to "see" atoms and molecules for the first time. We shall continue looking through the lens of single-particle motion throughout the course of this work.

Another approach for determining the motion of a microscopic particle is to apply Newton's second law: a dynamic force balance on the particle. In 1908, Paul Langevin wrote down a force balance for a microscopic particle that included a term to account for the random forcing of solvent impacts on the particle (Langevin, 1908):

$$m\frac{d\boldsymbol{U}}{dt} = \boldsymbol{F}^H + \boldsymbol{F}^B, \tag{2.5}$$

where m is the mass of the colloidal particle, $\boldsymbol{U}$ is its instantaneous velocity, $\boldsymbol{F}^H$ is the average interaction between the particle and the solvent, which is the hydrodynamic drag on the particle; and $\boldsymbol{F}^B$ is the random force associated with solvent molecule impacts on the particle. The mean motion of the particle is the first approximation of its interaction with the solvent, based on a key assumption: The "continuum approximation." If the particle size a_p is much larger than that of the solvent a_s, and there are many more solvent particles than colloids (*i.e.* $\phi_s \sim 1$), then a colloid is surrounded by approximately $(a_p/a_s)^3$ solvent molecules (Brady, 2007). This first condition of the continuum approximation indicates that to first order, the colloidal particle interacts with the solvent as a continuum fluid of viscosity η and density ρ. Thus, the solvent is a continuum around the particle, and the hydrodynamic drag can then be written

$$m\frac{d\boldsymbol{U}}{dt} = -6\pi\eta a_p\boldsymbol{U} + \boldsymbol{F}^B(t). \tag{2.6}$$

The solvent molecules are always in thermal motion, and will collide with and impart random forces

to the particle. Its influence on the motion of the colloidal particle is as a random fluctuating force $\boldsymbol{F}^B$. To understand the relationship between the thermal motion of the solvent molecules and the mechanical motion of the colloid, it is useful to examine the time scale over which each executes characteristic motion. The solvent time scale τ_s is the molecular time scale associated with random fluctuations of solvent molecules—the time required to move their size (and thus to collide with a suspended particle). In the liquid state, solvent molecules are very close together and the time required for one to fluctuate its size scales as

$$\tau_s \sim \frac{a_s}{\sqrt{v_s}}. \tag{2.7}$$

Here, a_s is the size, $v_s \sim 3kT/m_s$ is the thermal velocity of a solvent molecule and m_s is the mass of a molecule. For a water molecule, $\tau_s \sim 10^{-13}$ seconds. The time scale for a particle to react to an impact is given by its inertial relaxation time, during which time its momentum can change:

$$\tau_p \sim \frac{m}{6\pi\eta a_p} = \frac{2}{9}\frac{a_p^2}{\nu}\left(\frac{\rho_p}{\rho}\right). \tag{2.8}$$

Here, a_p is the particle size, ν is the kinematic viscosity of the solvent, and ρ_p and ρ_s are the density of the particle and the solvent, respectively. For a particle of size $\frac{1}{2}\mu m$, the time scale is $\tau_p \sim 10^{-7}$ seconds. The particle time scale is much longer than the solvent time scale, and thus many collisions will occur before the colloid can change its momentum. This demonstrates a vast separation in time scales, which can also be seen from (2.8), where $\nu \sim a_s^2/\tau_s$:

$$\frac{\tau_p}{\tau_s} \sim \left(\frac{a_p}{a_s}\right)^2. \tag{2.9}$$

How many solvent particles can impact a colloid in the time τ_s it takes a solvent molecule to move its size? Following the discussion of Brady (2007), the number of solvent molecules $N_{s,coll}$ close enough to impact the colloid over the solvent time scale scales as the number density of solvent particles $n_s = N_s/V$ times the volume V_{coll} around a colloid in which a solvent molecule must reside in order

to impact the colloid in one solvent time step τ_s. Thus the number of impacts a colloid will suffer on the solvent time scale is given by $(N_{s,coll}/\tau_s) * (1\,\tau_s)$ or

$$N_{coll} \sim \left(\frac{a_p}{a_s}\right)^2 \phi_s \quad \text{during } \tau_s, \tag{2.10}$$

where $\phi_s \sim a_s^3 n_s$. A colloid of size $10\,nm$ in water will suffer 10,000 collisions on the solvent time scale. To understand the reaction of the colloidal particle to the solvent impacts, we consider the number of collisions experienced by the particle in the *particle* time scale, $(N_{s,coll}/\tau_s) * (1\,\tau_p)$ or

$$N_{coll} \sim \left(\frac{a_p}{a_s}\right)^4 \phi_s \quad \text{during } \tau_p. \tag{2.11}$$

Thus, for a particle-to-solvent-molecule size ratio of only 10:1, a particle will suffer 10,000 random impacts before it can experience any change in its momentum (Brady, 2007). In turn, the mean response of the particle can be treated from the continuum drag perspective, and the average of the fluctuating force whose individual impacts are random is zero.

While on the time scale of the solvent the Brownian force is zero on average, it is useful to consider the average "size" or amplitude of the Brownian impacts. Since they are random they are instantaneously correlated: $\overline{\boldsymbol{F}^B(t')\boldsymbol{F}^B(t'')} = \boldsymbol{\mathcal{F}}\delta(t'-t'')$, where the overbar indicates an average over the solvent time scale, and $\boldsymbol{\mathcal{F}}$ is the amplitude of the correlation that must be determined. The equation of motion can can be integrated to obtain the instantaneous velocity of the particle, and from this the mean-square velocity (averaged over the solvent time scale) can be obtained. At long times, $t \gg \tau_p$, the memory of the initial velocity and position decays (which means the behavior of the particle does not depend on where it started) while the effect of the separation in time scales persists and is determined by the correlation amplitude $\boldsymbol{\mathcal{F}}$. The kinetic energy of the particle is given by one-half the mass times its mean-square velocity. Now since the temperature of the particle and of the solvent must be equal at equilibrium, thermal energy of the solvent must equal the mechanical energy of the particle. The equipartition theorem states that the solvent's energy (and therefore the particle's energy) must be one-half kT per degree of freedom (which is one for a sphere.) The

correlation amplitude is found as $\boldsymbol{\mathcal{F}} = 2kT(6\pi\eta\, a)\boldsymbol{I}$ for a spherical colloid. This shows that as forces fluctuate, they impart momentum to the particle, and the particle dissipates that momentum back to the solvent through drag. This is a statement of the fluctuation dissipation theorem.

Integrating again obtains the mean displacement, and we find the change in particle position compared to its size:

$$\frac{\Delta\overline{X}}{a_p} \sim \sqrt{\frac{kT\rho_p}{9\pi\eta^2 a_p}} \sim 10^{-3} \tag{2.12}$$

for a $10\,nm$ particle in water. The particle moves about an Angstrom—it has gone nowhere on average, confirming that inertia does not matter in the equation of motion for the particle. Since the left-hand side of (2.6) is now zero and the statistics of the random force are known, it is a simple matter to integrate it twice, square it, and compute its time average to find that at long times,

$$\overline{X(t)X(t)} = 2\frac{kT}{6\pi\eta a}\boldsymbol{I}t. \tag{2.13}$$

Of course the diffusivity is defined as one-half the time rate of change of the mean-square displacement, so Langevin predicted that

$$\boldsymbol{D}_{sphere} \equiv \lim_{t\gg\tau_p} \frac{1}{2}\frac{d}{dt}\overline{X(t)X(t)} = \frac{kT}{6\pi\eta a}\boldsymbol{I}, \tag{2.14}$$

confirming Einstein's result.

The approaches of Perrin and Langevin constitute a "microscopic" view of particle diffusion. The trajectory of an individual particle is followed over time, and its mean-square behavior is computed. Many such realizations of the experiment are made, and an (ensemble) average over realizations gives the average behavior of the particle. Einstein's approach, on the other hand, constitutes a "macroscopic" view, in which a larger collection of particles is considered, and the average behavior is that taken over all the particles in the suspension. The comparison between the macroscopic versus microscopic views will be revisited several times throughout the course of this work.

Although the Langevin equation is helpful for understanding the motion of a single particle, a

macroscopic approach may be more useful for a collection of particles. The probability distribution of particles in space is represented by the Fokker-Planck formalism for particles whose distribution depends on both particle momentum and position. For understanding configuration of a set of particles over time scales long compared to the particle momentum relaxation time, only configuration matters (as shown above). It can be shown that the Fokker-Planck equation then becomes the Smoluchsowski equation (the interested reader may refer to Brady [2007] for a formal derivation.) Einstein derived the Smoluchowski equation (shown above) using a macroscopic approach of the conservation of probability:

$$\frac{\partial P}{\partial t} = -\nabla \cdot \boldsymbol{j}, \tag{2.15}$$

where $\boldsymbol{j}$ is the $N-$particle probability flux and P is the $N-$particle configuration for a suspension of N particles. This expression will be used throughout the course of this work.

2.2 Diffusion regimes

There are three main types of particle diffusion in colloidal dispersions: collective (down-gradient) diffusion, short-time self-diffusion, and long-time self-diffusion. Each corresponds to a distinct physical transport process. The first, collective diffusion, concerns a *macroscopic* process in which the flux of a collection of particles arises due to a macroscopic gradient in their concentration. Here, one considers a dispersion of many particles, of size a say, at number density n in a solvent. A steady, weak concentration gradient $\nabla\phi$ of particles is maintained (where $\phi = 4\pi a^3 n/3$ is the volume fraction of particles.) The probability (number) flux $\boldsymbol{j}$ of particles in this Fickian process is described by

$$\boldsymbol{j} = -\boldsymbol{D}^c(\phi) \cdot \nabla\phi, \tag{2.16}$$

where $\boldsymbol{D}^c$ is the collective diffusivity of the particles. The frame of reference for such macroscopic diffusion is necessarily that of a zero total volume flux.

Self-diffusion concerns the motion of an individual particle relative to the origin. Consider here a quiescent suspension at equilibrium; a single particle is tagged (placed) at the origin at time $t = 0$,

and its motion monitored over time. At very short times, the Brownian motion of the particle allows it to sample positions inside a "cage" of nearest neighbors. The hydrodynamic resistance to its motion is simply the solvent drag—the particle's fluctuations are not large enough to alter the structure of the nearby particle configuration, but the solvent drag is altered by the presence of other background particles. The ability of the tagged particle to wiggle about inside this local region is its hydrodynamic mobility, $\boldsymbol{M}$, and the time-rate of change of its mean-square displacement during this motion is the short-time self-diffusivity, $\boldsymbol{D}_0^S = kT\boldsymbol{M}$, where the mobility is the inverse of the hydrodynamic resistance, $\boldsymbol{M} = \boldsymbol{R}^{-1}$. This self-diffusive motion is found by tracking the detailed kinematics of the tagged particle's motion, in order to obtain the mean of the square of its relative displacement $\boldsymbol{x}'(t) = \boldsymbol{x}(t) - \langle \boldsymbol{x}(t) \rangle$, where $\langle \boldsymbol{x}(t) \rangle$ is its average displacement at time t after many such realizations:

$$\langle \boldsymbol{x}'(t)\boldsymbol{x}'(t) \rangle = 6\boldsymbol{D}_0^S\, t. \tag{2.17}$$

Rallision and Hinch (1986) point out that the time scale t over which this diffusive process occurs is long compared to the momentum relaxation time scale for a particle, $\tau_p \sim m/6\pi\eta a$, but short compared to the time scale over which the tagged particle can move sufficiently to interact with its neighbors, $\tau_H \sim a^2/D_a$, where D_a is the bare diffusion coefficient as given by (2.4). As time proceeds, the particle samples a large enough space to interact with its nearest neighbors, and its motion becomes correlated in time. At times long compared to the interaction time, $t \gg \tau_H$, many such interactions occur, the tagged particle moves into and out of many such local cages, and these interactions de-correlate. Its motion is once again diffusive at long times, and the detailed kinematics of the tagged particle's motion give the *long-time self-diffusivity*:

$$\langle \boldsymbol{x}'(t)\boldsymbol{x}'(t) \rangle = 6\boldsymbol{D}_\infty^S\, t. \tag{2.18}$$

A third perspective of diffusion was proposed by Rallison & Hinch, that of "tracer" diffusion. This perspective plays a central role in our treatment of particle flux in microrheology, and so we shall review their approach in detail here.

Tracer diffusivity: a macroscopic view of self-diffusivity

Let us imagine again an equilibrium suspension of particles of species B say, at volume fraction ϕ_B. Following the approach of Batchelor and Rallision & Hinch (1976; 1986), we suddenly tag a very small fraction of those particles and rename them as species A, where $\phi_A \ll 1$ and $\phi_A \ll \phi_B$. The labeling is done in such a way that there is a gradient in their concentration $\nabla\phi_A$, and hence a Fickian flux of species A. Because species A is dilute and their concentration much smaller than that of the species B, an A particle interacts only with B particles. The motion of species A is therefore unaffected by their gradient, in the sense that their mean drift is zero, and hence their mean-square displacement $\langle \boldsymbol{x}'\boldsymbol{x}' \rangle$ is unchanged from that of the mono-disperse tagged particles above. Thus, the tracer situation is formally identical to the down-gradient diffusion of an infinitely dilute single species. Hence the self-diffusivity of species A can be described in the Fickian (macroscopic) sense but yet evaluated over short and long times. The Fickian flux of species A is given by

$$\boldsymbol{j}_A = -\boldsymbol{D}^A_{tr}(\phi_B, t) \cdot \nabla\phi_A, \tag{2.19}$$

where $\boldsymbol{D}^A_{tr} = \frac{1}{2} d\langle \boldsymbol{x}'\boldsymbol{x}' \rangle / dt$. In the limit of short and long times, Rallison & Hinch show that the tracer diffusivity is the self-diffusivity in the presence of a collection of background bath particles at concentration ϕ_B:

$$\boldsymbol{D}^A_{tr}(\phi_B, t \to 0) = \boldsymbol{D}^S_0(\phi_B) \tag{2.20}$$

$$\text{and} \quad \boldsymbol{D}^A_{tr}(\phi_B, t \to \infty) = \boldsymbol{D}^S_\infty(\phi_B). \tag{2.21}$$

When no species B is present, the short- and long-time self-diffusivities are identical and equal to the bare diffusivity of an A particle alone in a solvent, $\boldsymbol{D}_A$. In the presence of species B at finite concentration ϕ_B, however, the following results are given by Batchelor (1976; 1983) to order ϕ_B:

	with HI	no HI
$\boldsymbol{D}^c(\phi)/D_A$	$1+1.45\phi$	–
$\boldsymbol{D}_0^S(\phi)/D_A$	$1-1.83\phi$	1
$\boldsymbol{D}_\infty^S(\phi)/D_A$	$1-2.1\phi$	$1-2.0\,\phi$

Table 2.1: Tabulation of diffusion coefficients for collective diffusion and short-time and long-time self-diffusion, with and without hydrodynamic interactions (Batchelor, 1976, 1983; Rallison & Hinch, 1986).

A detailed derivation, with physical arguments, of the above result may be found in Appendix A.

2.3 Microrheology

Throughout this work, the theoretical model of nonlinear microrheology is utilized to explore mechanical behavior of colloidal dispersions. As discussed in the Introduction, the motivation for the study of microrheology is its ability to interrogate much smaller-scale systems than is possible with conventional macroscale rheometry. The foundation of theoretical microrheology was put forth by Squires & Brady (2005) and Khair & Brady (2006), in which they proposed that a Brownian probe dragged through a suspension would experience a reduction in its average speed, compared to what its speed would be were it alone in a solvent. As the probe moves through the suspension, it must push neighboring particles out of its way, which reduces the probe's speed. The speed reduction is due to the drag of the background bath particles. The outcome of their work was an analytical expression for the microviscosity; a comparison with the viscosity measured by conventional shear macrorheology showed that microrheology recovers all of the important physics.

Thus far, most work in nonlinear microrheology is focused on the *mean* response of the suspension, and on the microviscosity. In the remainder of this work, we shall explore the *fluctuations* in probe motion, and what these can elucidate about force-induced diffusion and the stress. But before we begin, a brief review of previous work in microrheology will help set the foundation of the current

study.

Solvent drag sets the speed of a single particle translating in Stokes' flow:

$$\boldsymbol{U}^0 = \boldsymbol{M} \cdot \boldsymbol{F}^0, \tag{2.22}$$

where $\boldsymbol{M} = (1/6\pi\eta a)\boldsymbol{I}$ is the mobility of a hard sphere, and $\boldsymbol{F}^0$ is the force required to give the particle a velocity $\boldsymbol{U}^0$. If the same "probe" particle is forced through a solvent containing many suspended microparticles, it must push them aside in order to move through the bath. The background bath particles form a microstructure that hinders the probe's motion, reducing its speed. This speed reduction can be interpreted as the viscous drag of the microstructure. The average probe velocity can be written as (Khair & Brady, 2006)

$$\langle \boldsymbol{U} \rangle = \boldsymbol{U}^0 + \langle \boldsymbol{U}^H \rangle + \langle \boldsymbol{U}^P \rangle + \overline{\langle \boldsymbol{U}^B \rangle}, \tag{2.23}$$

where $\boldsymbol{U}^0$ is the Stokes velocity for the probe alone in a solvent, and the remaining terms are the changes to the Stokes velocity due to hydrodynamic, interparticle, and Brownian contributions to average probe velocity, respectively. The hydrodynamic and Brownian velocities are coupled; disturbance flows due to Brownian motion are coupled to the hydrodynamic velocity field. Brownian motion also makes an indirect contribution in its effect on particle configuration and the subsequent weighting of the average velocities. The specific velocity $\boldsymbol{U}$ is weighted by the probability distribution of background bath particles to form an average velocity $\langle \boldsymbol{U} \rangle$. The distribution of bath particle positions—the microstructure—is governed by the Smoluchowski equation. Let us define the model system of probe plus bath particles dispersed in the solvent, and following the approaches of Squires & Brady (2005) and Khair & Brady (2006), proceed to formulate the Smoluchowski equation governing the evolution of the microstructure as the probe is driven through the bath.

Active, nonlinear microrheology

Consider a system comprising a colloidal dispersion of neutrally buoyant force- and torque-free

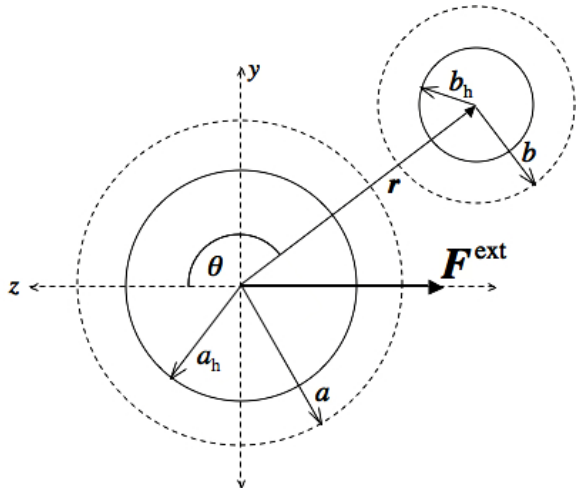

Figure 2.2: Pair interaction for probe and bath particle.

spherical particles, all of size b, suspended in a Newtonian solvent of density ρ and viscosity η. A single Brownian probe, of size a, is driven by a constant external force $\boldsymbol{F}^{ext}$ through the suspension. Owing to the small particle size, the Reynolds number is small, and the fluid motion is governed by Stokes' equations. In general, the probe and bath particles themselves can interact through hydrodynamic and interparticle forces; the simplest model for the interactive force, which shall be adopted here, is the hard-sphere potential. Thusly defined, the colloids exert no force on each other until their surfaces touch, *i.e.* when their separation $r = a + b$. At contact, an infinite potential $V(r)$ prevents their overlap:

$$V(r) = \begin{cases} \infty, & r < a + b, \\ 0, & r > a + b. \end{cases} \tag{2.24}$$

In general, the radii a and b at which the particles exert the hard-sphere force is not the same as their physical or hydrodynamic radii, a_h and b_h, where the no-slip boundary condition is met. Various physical conditions of the colloid or solvent can extend the effective size of the particle beyond the hydrodynamic radius, *e.g.* steric repulsion or an ionic screening layer. The particles then repel each other at their extended, or "thermodynamic" radii, a and b (see figure 2.2.) This approach forms the foundation of the excluded annulus model of Morris & Brady (1996), in which the ratio

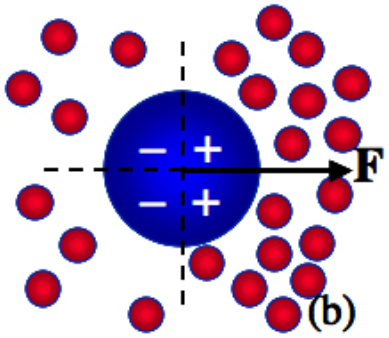

Figure 2.3: Probe particle (blue) forced through a suspension of bath particles (red). The probe must push the bath particles out of its way in order to translate through the bath.

of the two radii, $\lambda_a = a/a_h$ and $\lambda_b = b/b_h$, can be modulated to account for the relative importance of hydrodynamic-to-interparticle forces. When $\lambda_a, \lambda_b \gtrsim O(1)$, the particles are able approach each other closely enough to experience (long-range) hydrodynamic interactions. For $\lambda_a, \lambda_b \to 1$, lubrication interactions also become important. At the opposite extreme of $\lambda_a, \lambda_b \gg 1$, strong interparticle repulsion keeps the particles sufficiently separated that hydrodynamic interactions are negligibly weak.

As the probe is driven through the bath, it distorts the spatial arrangement of bath particles—the suspension microstructure—and drives it from equilibrium (see figure 2.3). The Brownian motion of the bath particles acts to recover the equilibrium configuration, giving rise to an entropic restoring force. The degree to which the microstructure is deformed, and hence its influence on probe motion, depends on the strength with which the probe is forced, $\boldsymbol{F}^{ext}$, compared to the thermal restoring force, kT/b, defining a Péclet number, $Pe_b = F^{ext}/(kT/b)$. The distorted shape of the microstructure also influences hard-sphere and hydrodynamic interactions between probe and bath; together with the entropic restoring force, they hinder the probe's motion through the bath, reducing its average velocity $\langle \boldsymbol{U} \rangle$. Squires & Brady (2005) and Khair & Brady (2006) related this change in probe velocity to an effective microviscosity of the suspension via application of Stokes' drag law.

As discussed above, the average velocity of the probe is comprised of its free Stokes' velocity $\boldsymbol{U}^0$ plus hydrodynamic, interparticle, and Brownian contributions: $\langle \boldsymbol{U} \rangle = \boldsymbol{U}^0 + \langle \boldsymbol{U}^H \rangle + \langle \boldsymbol{U}^P \rangle + \overline{\langle \boldsymbol{U}^B \rangle}$. We review here the derivation of each of these given by Khair & Brady (2006).

Hydrodynamic velocity

The hydrodynamic velocity of a particle subjected to a force $\boldsymbol{F}^{ext}$ in Stokes flow, in the presence of another particle subjected to zero external force is given by

$$\boldsymbol{U}^H = \frac{\boldsymbol{F}^{ext}}{6\pi\eta a} \cdot \left[A_{11}(\lambda r)\boldsymbol{nn} + B_{11}(\lambda r)(\boldsymbol{I} - \boldsymbol{nn}) - \boldsymbol{I}\right], \tag{2.25}$$

where A_{11} and B_{11} are the scalar mobility functions that depend on the separation between a pair of particles (Batchelor & Green, 1972), $\lambda = \lambda_a = \lambda_b$ is the excluded-volume parameter defined above, $\boldsymbol{n}$ is the unit vector along the line of centers of a pair of particles, and $\boldsymbol{I}$ is the identity tensor. In the present model, a single particle is driven through a suspension of same-size particles. Equation 2.25 gives the change in velocity of that particle due to the presence of a second particle. In the dilute limit, only pairwise interactions matter, and so (2.25) describes the change in the hydrodynamic contribution to probe velocity relative to a bath particle. The average hydrodynamic velocity $\langle \boldsymbol{U}^H \rangle$ is a configuration average over all possible pair positions in the suspension. The weighting moment of this average is the pair-distribution function, $g(\boldsymbol{r})$, which is governed by the pair Smoluchowski equation. Thus the hydrodynamic velocity contribution is given by

$$\langle \boldsymbol{U}^H \rangle = \frac{3\phi_b}{4\pi} \frac{1}{6\pi\eta a} \boldsymbol{F}^{ext} \cdot \int \left[A_{11}(\lambda r)\boldsymbol{nn} + B_{11}(\lambda r)(\boldsymbol{I} - \boldsymbol{nn}) - \boldsymbol{I}\right] g(\boldsymbol{r}) d\boldsymbol{r}, \tag{2.26}$$

where $\phi_b = 4\pi b^3 n_b/3$ is the volume fraction of bath particles of size b with number density n_b in the suspension.

The pair Smoluchowski equation,

$$\frac{\partial g}{\partial t} = -\nabla \cdot \boldsymbol{j}, \tag{2.27}$$

governs the evolution of the pair distribution function $g(\boldsymbol{r})$, where the number flux $\boldsymbol{j}$ of bath particles is comprised of advective and diffusive contributions: $\boldsymbol{j} = \boldsymbol{U}g - \boldsymbol{D} \cdot \nabla g$, where $\boldsymbol{U}$ is the probe velocity and $\boldsymbol{D}$ is the relative diffusivity of probe to bath particles. Inserting the flux into (2.27), we obtain

the familiar advection-diffusion equation,

$$\boldsymbol{U}\cdot\nabla g-\nabla\cdot\boldsymbol{D}\cdot\nabla g=0, \tag{2.28}$$

for the steady-state evolution of the microstructure undergoing probe forcing at velocity $\boldsymbol{U}$. A brief derivation of (2.27) and (2.28) is given in §5.3, and a complete, detailed derivation may be found in Squires & Brady (2005). To understand the relative importance of advection (the first term) to diffusion (the second term), we define the Péclet number $Pe = U_0(a+b)/D$, and scale quantities as $r \sim (a+b)$ and $U_0 \sim F^{ext}/6\pi\eta a$ where U_0 is the characteristic probe velocity. Applying these scalings one obtains:

$$\begin{aligned} Pe\,\nabla\cdot(\boldsymbol{U}g)-\nabla\cdot\boldsymbol{D}\cdot\nabla g &= 0, \\ g(\boldsymbol{r}) &\rightarrow 1 \quad \text{as} \quad r\rightarrow\infty, \\ Pe\,\boldsymbol{n}\cdot\boldsymbol{U}g-\boldsymbol{n}\cdot\boldsymbol{D}\cdot\nabla g &= 0 \quad \text{at} \quad r=1. \end{aligned} \tag{2.29}$$

Expressions (2.30) can be solved analytically for all Pe in the absence of hydrodynamic interactions, and numerically otherwise (Squires & Brady, 2005; Khair & Brady, 2006; Zia & Brady, 2010). The result may then be inserted into (2.26) to obtain the average hydrodynamic velocity.

Interparticle force-induced velocity

The average velocity contribution due to particle interactions $\langle \boldsymbol{U}^P \rangle$ depends on the relative motion between a pair of particles. We must begin with the relative mobility of a pair parallel and transverse to their line of centers. This is given by the hydrodynamic functions $G(r)$ and $H(r)$ as (Batchelor, 1970):

$$G(r) = A_{11}(r)-A_{12}(r) \tag{2.30a}$$

$$H(r) = B_{11}(r)-B_{12}(r). \tag{2.30b}$$

The interparticle velocity in the microrheology problem is then given by (Khair & Brady, 2006)

$$\langle \boldsymbol{U}^P \rangle = \frac{1}{6\pi\eta a}\frac{3\phi_b}{4\pi}\int [G(\lambda r)\boldsymbol{nn} + H(\lambda r)(\boldsymbol{I}-\boldsymbol{nn})]\cdot \boldsymbol{F}^P g(\boldsymbol{r})d\boldsymbol{r}. \tag{2.31}$$

Brownian velocity

Khair & Brady (2006) showed that the velocity contribution due to Brownian disturbance flows is given by $\overline{\boldsymbol{U}^B} = -\frac{1}{2}\boldsymbol{D}\cdot\nabla$. The average Brownian velocity is then

$$\langle \overline{\boldsymbol{U}^B} \rangle = -\frac{F^{ext}}{6\pi\eta a}\frac{3\phi_b}{4\pi}Pe^{-1}\int \left[\frac{G(\lambda r)-H(\lambda r)}{r} + \frac{1}{2}\frac{dG(\lambda r)}{dr}\right]\boldsymbol{n}g(\boldsymbol{r})d\boldsymbol{r}. \tag{2.32}$$

The microviscosity

The average-velocity contributions give rise to a velocity that acts in the same direction as the external driving force $\boldsymbol{F}^{ext}$. A natural mechanical interpretation is that these are drag forces—*i.e.*, all contributions to $\langle \boldsymbol{U} \rangle$ beyond the free Stokes' velocity $\boldsymbol{U}^0$ are associated with microstructural drag on the probe. Stokes' drag law relates purely hydrodynamic drag forces on a particle to its velocity; in extension of this idea, Khair & Brady (2006) proposed that the same relationship exists between microstructural drag and velocity. They defined the "effective viscosity" , η^{eff}, via application of Stokes' drag law to the average velocity:

$$\boldsymbol{F}^{ext} = 6\pi\eta a\frac{\eta^{eff}}{\eta}\langle \boldsymbol{U} \rangle. \tag{2.33}$$

The effective viscosity is then given by

$$\frac{\eta^{eff}}{\eta} = \frac{F^0}{6\pi\eta a\langle U \rangle}, \tag{2.34}$$

where $\boldsymbol{F}^{ext} = F^0\hat{\boldsymbol{F}}^{ext}$ and $\langle U \rangle = -\langle \boldsymbol{U} \rangle\cdot\hat{\boldsymbol{F}}^{ext}$. For a dilute bath ($\phi_b \ll 1$), $\langle U \rangle = U^0\left[1 - f_1(Pe)\phi_b + O(f_2(Pe)\phi_b^2\right]$.

The effective viscosity may then be written to $O(\phi_b)$ as

$$\frac{\eta^{eff}}{\eta} \approx 1 + \frac{\eta^{micro}}{\eta} \tag{2.35}$$

where

$$\frac{\eta^{micro}}{\eta} \equiv \frac{F^0}{6\pi\eta a U^0} f_1(Pe)\,\phi_b = f_1(Pe)\,\phi_b\,, \tag{2.36}$$

and the microviscosity has contributions due to hydrodynamic, interparticle, and Brownian drag: $\eta^{micro} = \eta^{micro,H} + \eta^{micro,P} + \eta^{micro,B}$.

The microviscosity is the viscous drag of the particle microstructure—above and beyond the solvent viscosity. In the dilute limit, it is an $O(\phi_b)$ effect, and its magnitude is set by the Péclet number. In the limit of no hydrodynamic interactions ($\lambda_a, \lambda_b \gg 1$), the microviscosity is the average hindrance of the microstructure due to collisions between the probe and the background bath particles. A hard-sphere potential to model interparticle forces was proposed in (2.24); mathematically, the interparticle force is a delta-function at contact: $\boldsymbol{F}^P = -[kT\hat{\delta}(r-2)/(a+b)]\boldsymbol{n}$, where $\hat{\delta}(r-2) = (a+b)\delta(r-2)$. Thus, disturbances to probe velocity due to interparticle forces occur only at contact between probe and bath particle; the integral vanishes elsewhere, and the interparticle velocity becomes

$$\langle \boldsymbol{U}^P \rangle = -\frac{F^{ext}}{6\pi\eta a}\frac{3\phi_b}{4\pi} Pe^{-1} \int \boldsymbol{n} g(\boldsymbol{r}) d\Omega \tag{2.37}$$

for the average hard-sphere velocity disturbance. Here, $d\Omega$ is the element of solid angle. Combining (2.33), (2.35) and (2.37) gives the microviscosity due to hard-sphere collisions, in the limit of no hydrodynamic interactions between particles, which gives:

$$\frac{\eta^{micro,P}}{\eta} = \frac{3\phi_b}{4\pi} Pe^{-1} \hat{\boldsymbol{F}}^{ext} \cdot \int \boldsymbol{n}\, g(1) d\Omega. \tag{2.38}$$

In the limit of no hydrodynamic interactions and particles interacting via a hard-sphere potential, the intrinsic microviscosity is determined solely by the contact value of the pair distribution function. Figure 2.4 shows the microviscosity thus obtained, where it is plotted versus the Péclet number.

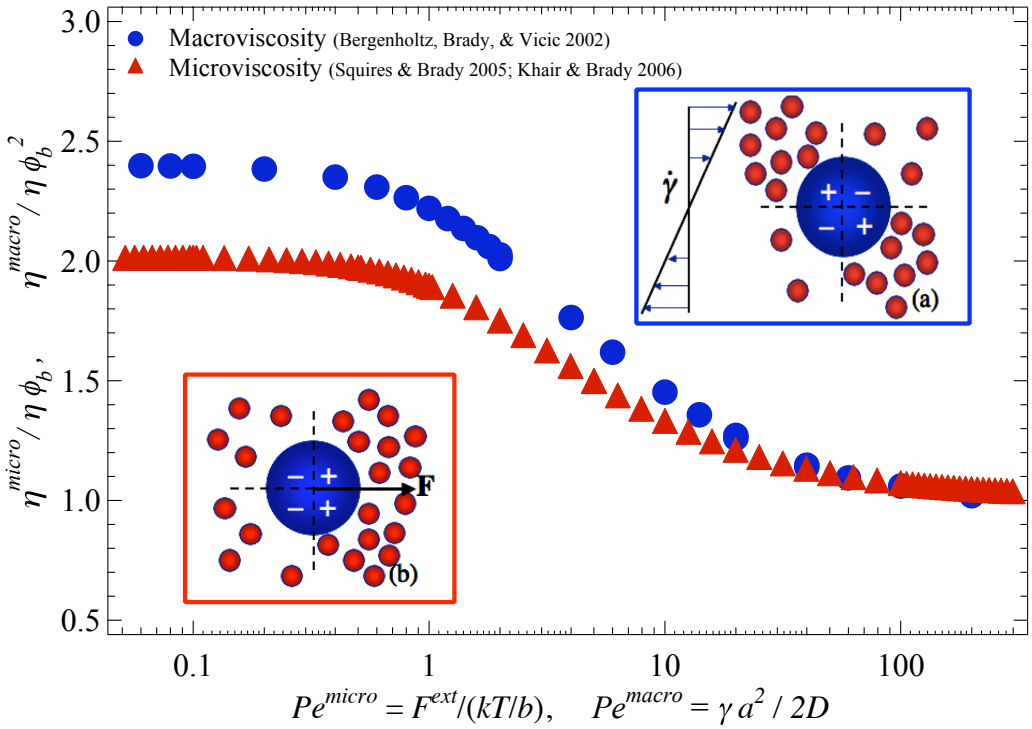

Figure 2.4: The intrinsic viscosity for a dilute suspension, in the absence of hydrodynamic interactions, undergoing: simple shear (filled blue circles) with $Pe = \dot{\gamma}b^2/2D$, where $\dot{\gamma}$ is the shear rate, b the bath particle size, and D the isolated diffusivity of a bath particle (Bergenholtz *et al.*, 2002); and nonlinear microrheology (filled red triangles) (Squires & Brady, 2005; Khair & Brady, 2006), with $Pe = F^{ext}b/kT$, where F^{ext} is the driving force, b the bath particle size, and kT the thermal energy. Insets show a sketch of the corresponding deformed microstructures (a) shear; (b) microrheology.

For very weak forcing, $Pe \ll 1$, the disturbance of the probe is a Pe^2-weak diffusive dipole. The Brownian motion of the bath particles easily repairs the disturbance created by the probe. The thermal restoring force of the bath particles is as strong as probe forcing, and thus the viscous drag dissipates most of the probe's energy. But as the strength of probe forcing is increased, advective forcing becomes stronger than the thermal restoring force of the bath. The Brownian motion of the bath particles is no longer sufficiently fast to dissipate the probe's energy, and they cannot maintain an equilibrium configuration. The probe's energy is thus stored in the compressed configuration of the microstructure and the viscous dissipation weakens. As Pe becomes $O(1)$, a dramatic "force thinning" of the microstructure takes place. The microstructural resistance to probe motion falls off to an $O(1)$ Newtonian plateau as $Pe \to \infty$, as compared to the $O(Pe)$ strength of probe forcing.

But it is important to ask whether the viscosity measured by single-particle forcing recovers all of the same fundamental physical behavior that one obtains through conventional macrorheological

techniques. For the same dilute dispersion subjected to a simple shearing motion, the pair-level intrinsic viscosity is plotted in figure 2.4 (the filled blue circles), against the appropriate Péclet number. A sketch of the deformed microstructure corresponding to each flow is inset in the plot. Clearly the shape of the particle microstructure is different for the two flows. But a comparison between the two sets of data reveal that in both cases, the low-Pe behavior is characterized by an initial Newtonian plateau, the same onset of shear (force) thinning, the same scaling in Pe, and the same terminal Newtonian plateau. The initial quantitative difference in viscosity is to be expected, given the very different microstructures in the two cases. But the agreement is actually quite remarkable: all of the same fundamental physical behavior is recovered by microrheology as is obtained by traditional shear macrorheology.

It should be noted that the scaling in volume fraction ϕ_b is different in the two cases. Both are measuring a pair-level contribution to the viscosity. In macrorheology, pair-level interactions arise at $O(\phi_b^2)$, as two particles must interact in the flow. But in microrheology, interactions are studied in a frame of reference relative to the probe—that is, one of the two particles in a pair is always the probe, and the probe is at the origin of the microstructure. The probability of finding the probe at the origin is unity, and so its interaction with another particle is $O(\phi_b)$. We see no reason why this difference in definition should present any difficulty.

Now that the basic aspects of mean behavior in nonlinear microrheology have been reviewed, along with a review of fluctuations in equilibrium suspensions, we are prepared to continue our discussion with a new focus: non-equilibrium fluctuations.

Fluctuations in nonlinear microrheology

Thus far, the majority of the focus in nonlinear microrheology has been on the *mean* behavior and the effective viscosity. But as was seen in §2.1, *fluctuations* matter in colloidal dispersions. We now turn our attention to fluctuations in probe motion in nonlinear microrheology. They provide important information about the behavior of neighboring particles and, as will be shown, about other material properties such as suspension stress and memory effects. We have also the more

fundamental goal of understanding what the relationship between fluctuation and dissipation *away* from equilibrium reveals about the connection between the macroscopic and microscopic world in complex fluids. We ask the question: What do non-equilibrium fluctuation and dissipation reveal more fundamentally about energy and motion? Avogadro's constant was the sought-after connection during the work of Einstein & Perrin. It establishes a relationship between the macroscopic gas constant $\mathcal{R}$ and Boltzmann's constant k, which connects energy at the atomic level to temperature at the macroscopic level. Perhaps a similar constant away from equilibrium will reveal a connection between an "effective temperature" and particle energies.

Chapter 3

Force-induced diffusion and the microdiffusivity[1]

3.1 Introduction

The motion of active, microscale particles driven through complex fluids is a physical process central to many current scientific problems: vesicle trafficking in cells, artificial nanomotors, and nanotherapeutic drug delivery devices are a few important examples (Janke *et al.*, 2005; Shirai *et al.*, 2005; Heath *et al.*, 2009). The increased demand for knowledge of this small-scale behavior has made microrheology a key step in the understanding, use, and design of such systems. Among the collection of techniques known as microrheology, most involve tracking the movement of a colloidal particle (or set of particles) in order to determine the properties of the surrounding environment (MacKintosh & Schmidt, 1999). There are two main types of particle-tracking microrheology: *passive*—tracking the random motion due to thermal fluctuations—and *active*—applying a constant or oscillatory force to the particles, for example by using optical tweezers or magnetic fields. A detailed comparison can be found in Khair & Brady (2006). Most microrheological work to date has focused on passive microrheology, to obtain linear viscoelastic properties by correlating the random thermally driven displacements of tracers to the complex modulus through a generalized Stokes-Einstein-Sutherland relation—a process which is limited in its scope to equilibrium systems. Yet as noted above, many systems of practical interest are driven out of equilibrium and display (in-

[1]This chapter includes content from our previously published article, Single-particle motion in colloids: force-induced diffusion, by Roseanna N. Zia and John F. Brady, Journal of Fluid Mechanics, Vol. 658 (September 2010), pp. 188-210 Copyright 2010 Cambridge University Press. Reprinted with permission.

deed, rely upon) nonlinear behaviors. Recently a body of work has emerged focusing on this active, nonlinear microrheology regime (Habdas *et al.*, 2004; Squires & Brady, 2005; Meyer *et al.*, 2005; Khair & Brady, 2006; Wilson *et al.*, 2009). In such a system, tracer particles undergo displacements due not only to random thermal fluctuations, but also due to the application of an external force applied directly to the tracer, or "probe." The dispersion is driven out of equilibrium, and as with macrorheology, dynamic responses such as viscosity can be measured. Since the tracer interrogates the material at its own (micro)scale, much smaller samples are required compared to traditional macrorheology, and localized material heterogeneity can be explored. This is a particular benefit for rare biological materials and small systems such as cells. Khair & Brady (2006) recently established the theory that predicts the microviscosity of dilute systems of colloids, and defined the relationship between micro- and macroviscosity—a critical step in the development of microrheology as an experimental tool. Recent experiments confirm the theory (and raise additional questions)(Meyer *et al.*, 2005; Squires, 2008; Wilson *et al.*, 2009).

But in both theory and experiment, the focus thus far has been on the *mean* response of the material—the viscosity—and far less work has been devoted to particle fluctuations that occur due to collisions between the probe and bath particles. As the probe moves through the dispersion it must push neighboring particles out of its way; these collisions induce fluctuations in the probe's velocity, scattering it from its mean path. Is this scattering diffusive? Is it isotropic? How important is the scattering compared to the Brownian diffusion the probe simultaneously undergoes? The answers to these questions are fundamental to understanding the motion of an active microscale particle—important both for scientific and technology considerations. Little work has been published on this topic (Habdas *et al.*, 2004), even though it has major implications for a wide range of technologies beyond material interrogation.

Previous study of particle fluctuations in colloidal *macro*rheology shows that imposing a shearing flow on a suspension enhances particle diffusivity (Leighton & Acrivos, 1987; Morris & Brady, 1996; Brady & Morris, 1997; Breedveld *et al.*, 1998). The imposed shear flow drives the microstructure from equilibrium, giving rise to mechanisms of diffusion not present in a quiescent suspension: a deformed

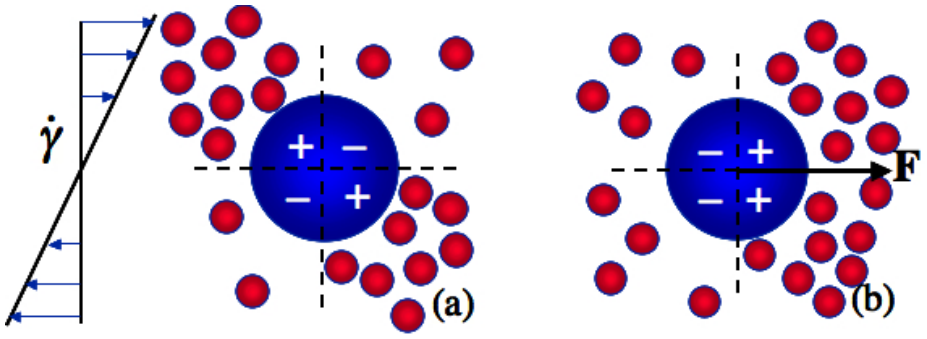

Figure 3.1: Microstructural deformation under (a) macrorheological shear flow, and (b) microrheological forcing. In simple shearing motion (a), bath particles accumulate along the compressional axis and deplete along the extensional axis. A tracer at the origin (the dark sphere) experiences both in-plane and out-of-plane bath-particle gradients. In (b), the (dark) tracer itself deforms the microstructure, accumulating particles on its upstream face and leaving a wake of depletion behind, creating an axisymmetric structure with only longitudinal and transverse components.

microstructure and interparticle collisions. A forced *micro*rheological probe also imposes a flow that drives the suspension from equilibrium, again leading to a deformed microstructure and interparticle collisions—and hence to an analogous force-induced diffusion, or "micro-diffusivity." It is the primary objective of this work to extend the theoretical model of active, nonlinear microrheology to one that is explicit in the fluctuations of the microstructure, and thereby develop expressions for predicting the resultant force-induced diffusion.

It is also useful to ask whether the qualitative agreement between micro- and macroviscosity can be extended to the micro- and macrodiffusivity. Both the shear- and force-induced diffusion grow out of fundamentally similar mechanisms: external forcing causes the tracer to scatter off of the microstructure, rather than wander passively through it. But the directionality and magnitude of the scattering depend on the shape of the deformed microstructure, and this asymmetry is distinct for the two cases, as illustrated in figure 3.1. The idea of whether a direct correlation between macro shear-induced diffusion and micro force-induced diffusion is possible (or even necessary) will be explored in this study, and a comparison between the two sought.

To build up a physical model, we follow the example of Squires & Brady (2005) and consider the motion of a Brownian probe driven by an externally applied force through a dispersion of neutrally buoyant force- and torque-free colloidal particles. The size ratio of probe to bath particle is arbitrary. As the probe particle moves through the suspension it must push neighboring particles out of its way; a buildup of background particle concentration forms in front of the advancing probe and a

deficit or wake trails it. The bath particles (including the probe) undergo Brownian diffusion due to thermal fluctuations of the solvent, which acts to restore the deformed microstructure to an equilibrium configuration. The ratio of advective forcing to entropic restoring force is the Péclet number, $Pe = F^{\text{ext}}/(kT/b)$, where kT is the thermal energy and b the bath-particle size. In the linear response regime ($Pe \to 0$), diffusion of the bath particles dominates. As the probe forcing increases and Pe grows beyond $\sim O(1)$—the active, nonlinear response regime—advection plays an increasingly important role in the shape of the distorted microstructure. Since the details of this shape govern the strength and likelihood of collisions between probe and bath particle, its determination is critical to understanding the resultant force-induced diffusive spread of the probe's trajectory.

The spatio-temporal distribution of bath particles obeys a Smoluchowski equation. Prior treatments of active microrheology formulated the expression for the steady microstructure moving relative to a fixed probe. We extend this approach by considering both the steady microstructure deformation and fluctuations in the microstructure responsible for diffusion of the probe. The resulting Smoluchowski equations are solved for all Pe by a combination of perturbation methods and numerical computation to obtain both the steady microstructure along with a new quantity, the probability-weighted collisional displacements of the probe relative to the bath particles.

In the remaining sections of this paper, we propose and examine an extended model for active, nonlinear microrheology that is explicit in the probe fluctuations, and explore the resultant force-induced diffusion. In §3.3, we formulate the Smoluchowski equation that governs the evolution of the microstructure in physical space, along with kinematic expressions for the probe flux. The latter is comprised of advective and interparticle contributions, and from these the diffusive flux of the probe is extracted and separated into Brownian and flow-induced components. To make analytical progress an assumption of diluteness is made. In §3.4 the Smoluchowski equation is separated into steady and fluctuating components, completing the formulation of the problem. In the first part of §3.5 the case of asymptotically weak probe forcing, $Pe \ll 1$, is studied. Regular perturbation expansions are sufficient to obtain the $O(\phi_b)$ correction to the long-time self-diffusivity, which corresponds to passive

diffusion: $D \sim D_a(1-2\phi_b)$, where ϕ_b is the (dilute) volume fraction of bath particles and D_a is the diffusivity of an isolated probe (Batchelor, 1976). Higher orders in $\phi_b Pe$ are required in order to find the first effect of the forcing on particle self-diffusion and we proceed to $O(\phi_b Pe^2)$ whereupon the problem becomes singular, which requires the use of matched asymptotic expansions. In the second part of §3.5 we shift focus to the opposite extreme of very strong probe forcing, or $Pe \gg 1$, and the nonlinear response of the microstructure is exposed. This limit is also singular with a boundary layer at the probe surface. To solve for probe fluctuations at arbitrary values of the Péclet number, a numerical solution is required, and a finite-difference scheme is employed to this end in the last portion of §3.5. In §3.6 we present an alternative solution of the problem based upon measurements of the probe's displacements obtained by Brownian dynamics simulation, presented juxtaposed to the Smoluchowski results. §3.7 is devoted to a comparison of microdiffusivity to the macrodiffusivity (theory and experiments). Throughout, we consider a simplified model that neglects hydrodynamic interactions between particles; this simplification affords insight into the basic physics of diffusive behavior arising from interparticle forcing, but could be extended to include other interparticle forces such as hydrodynamic interactions; the approach also offers a direct solution to related problems such as self-propelled objects. The study is concluded with a discussion in §3.8, including a brief discussion of hydrodynamic interactions, self-propulsion, and non-spherical shapes.

3.2 Scaling predictions

Scaling arguments are useful for predicting the behavior for extreme values of the Péclet number. For random walk processes, the diffusivity scales as:

$$D \sim \frac{l^2}{\tau}\,, \tag{3.1}$$

where l is the size of a probe step, and τ is the de-correlation time. For very weak forcing, $Pe \ll 1$, Brownian diffusion dominates the motion, so the timescale is $\tau \sim (a+b)^2/D_a$, where D_a is the self-diffusivity of an isolated probe particle of size a. In this linear response regime, $l \sim Pe(a+b)$.

The number of diffusive steps depends on the number of bath-particle collisions; thus, for very small Pe, the microdiffusivity should scale quadratically in the forcing and linearly in volume fraction of bath particles ϕ_b:

$$D^{\text{micro}} \sim Pe^2 \phi_b D_a \,, \quad Pe \ll 1 \,. \tag{3.2}$$

For large forcing, $Pe \gg 1$, the timescale is now advective, $\tau \sim (a+b)/U$, the probe can move $l \sim (a+b)$ in that time, and the force-induced microdiffusivity should scale linearly with the Péclet number and in volume fraction of bath particles:

$$D^{\text{micro}} \sim Pe\, \phi_b D_a \,, \quad Pe \gg 1 \,. \tag{3.3}$$

3.3 Theoretical framework

The theoretical framework of active microrheology was developed in chapter 2, and is reviewed briefly here. A single Brownian probe particle of radius a is dragged by a constant external force $\boldsymbol{F}^{\text{ext}}$ through a dispersion of colloidal particles, all of size b, which are immersed in a solvent of density ρ and viscosity η. The importance of fluid inertia relative to the viscous shearing forces is characterized by the Reynolds number, $Re = \rho U a/\eta$, where U is the characteristic velocity of the moving probe, and for micron-sized probes $Re \ll 1$ so that the fluid mechanics are governed by Stokes flow. The advective forcing of the probe acts to deform the microstructure of the bath, while the Brownian motion of the bath particles counteracts it in an attempt to restore equilibrium. This interplay drives fluctuations in the probe's velocity that give rise to diffusive behavior. The primary goals of this section are to examine the dispersive contributions to the probe's flux relative to the bath, to formulate the expression for the force-induced component, and to show that the force-induced dispersive motion is indeed diffusive.

We shall assume a system of particles for which $\lambda_a, \lambda_b \gg 1$, where hydrodynamic interactions are negligible compared to interparticle and thermal forces, and particles that interact via a hard-sphere potential (cf chapter 2, figure 2.2 & equation 2.24). This model captures the essential features of the

dispersive process while keeping the analyses as simple as possible; hydrodynamics will only make a quantitative difference and are discussed briefly in §3.8.

We consider the probe amid a dispersion of $N-1$ bath particles in a configuration $\boldsymbol{x}_N$. The distribution of particles is given by an $N-$particle probability density, $P_N(\boldsymbol{x}_1, \boldsymbol{x}_2, ..., \boldsymbol{x}_N; t)$, which obeys a Smoluchowski equation:

$$\frac{\partial P_N}{\partial t} + \sum_{i=1}^{N} \nabla_i \cdot \boldsymbol{j}_i = 0, \tag{3.4}$$

where the sum is over all particles in the dispersion, and the flux of particle i is given by

$$\boldsymbol{j}_i = \boldsymbol{U}_i P_N(\boldsymbol{x}_N; t) - \sum_{j=1}^{N} \boldsymbol{D}_{ij} \cdot \nabla_j (\ln P_N(\boldsymbol{x}_N; t) + V_N/kT) P_N(\boldsymbol{x}_N; t). \tag{3.5}$$

Here, kT is the thermal energy, $\boldsymbol{D}_{ij} = kT\boldsymbol{M}_{ij}$ is the relative Brownian diffusivity between particles i and j, and $\boldsymbol{M}_{ij}$ is the mobility tensor relating the velocity of particle i to the force exerted on particle j. The first term on the right hand side of (5.5) is the advective flux of particle i with velocity $\boldsymbol{U}_i$; the second term is the flux due to entropic gradients in the microstructure; and $\boldsymbol{D}_{ij} \cdot (\nabla_j V_N/kT) P_N$ gives the flux of particle i due to the forcing of interactive potential with particle j.

In the dilute limit, only pair interactions are important, and the probability P_N in equations (5.4) and (5.5) reduces to the pair probability of finding the probe at position $\boldsymbol{x}_1$ and a bath particle at position $\boldsymbol{x}_2$. To analyze the relative flux between probe and bath, it is convenient to change to a frame of reference moving with the probe, placing the probe at $\boldsymbol{z} = \boldsymbol{x}_1$, and a bath particle at $\boldsymbol{r} = \boldsymbol{x}_2 - \boldsymbol{x}_1$. The pair Smoluchowski equation becomes:

$$\frac{\partial P_2(\boldsymbol{z}, \boldsymbol{r}\,; t)}{\partial t} + \nabla_z \cdot \boldsymbol{j}_a + \nabla_r \cdot (\boldsymbol{j}_b - \boldsymbol{j}_a) = 0; \tag{3.6}$$

the subscripts a and b refer to the probe and bath particle, respectively. We are interested in the flux of the probe relative to *any* other particle, and so we integrate $P_2(\boldsymbol{z}, \boldsymbol{r}; t)$ over all possible positions of a bath particle, to obtain the single-particle Smoluchowski equation for the probe particle. Applying

the divergence theorem and noting that relative flux is zero at contact and at infinity, we have

$$\frac{\partial P_1(\boldsymbol{z}\,;t)}{\partial t} + \nabla_z \cdot \langle \boldsymbol{j}_a \rangle = 0, \tag{3.7}$$

where $\langle \boldsymbol{j}_a \rangle \equiv \int \boldsymbol{j}_a d\boldsymbol{r}$. The unbounded domain of the probe makes a transformation to Fourier space convenient. Taking the Fourier transform, denoted by $\widehat{\ }$, of the Smoluchowski equation (3.7) yields

$$\frac{\partial \hat{P}_1(\boldsymbol{k}\,;t)}{\partial t} + i\boldsymbol{k} \cdot \langle \hat{\boldsymbol{j}}_a \rangle = 0, \tag{3.8}$$

where the average flux $\langle \hat{\boldsymbol{j}}_a \rangle$ from (5.5) has also been transformed to Fourier space:

$$\langle \hat{\boldsymbol{j}}_a \rangle = (\boldsymbol{U}_a - i\boldsymbol{k}D_a)\, \hat{P}_1(\boldsymbol{k};t) + D_a \int \nabla_r \hat{P}_2(\boldsymbol{k},\boldsymbol{r};t) d\boldsymbol{r}. \tag{3.9}$$

Here, $\boldsymbol{U}_a = \boldsymbol{F}^{\text{ext}}/6\pi\eta a$ is the the probe velocity due to the imposed constant external force, $D_{11} \equiv D_a$ the probe self-diffusivity, i the imaginary unit, and the angle brackets $\langle\ \rangle$ denote an ensemble average over all possible suspension configurations. $\hat{P}_2(k,\boldsymbol{r}\,;t)$ and $\hat{P}_1(k\,;t)$ are the Fourier transforms of $P_2(\boldsymbol{z},\boldsymbol{r}\,;t)$ and $P_1(\boldsymbol{z}\,;t)$, respectively.

The last term in equation (3.9) preserves explicitly the effect of bath particles on the probe. In order determine to the average probe flux, the distribution of the bath relative to the probe must be determined. To this end we define the structure function $g(\boldsymbol{k},\boldsymbol{r}\ t)$:

$$\hat{P}_2(k,\boldsymbol{r}\,;t) \equiv n_b g(k,\boldsymbol{r}\,;t) \hat{P}_1(k\,;t)\ , \tag{3.10}$$

where n_b is the undisturbed number density of bath particles far from the probe.

Expression (3.10) is similar to the familiar definition of the pair-distribution function in physical space, $P_2(\boldsymbol{z},\boldsymbol{r}\,;t) = n_a n_b\, g(\boldsymbol{z},\boldsymbol{r}\,;t)$ (since $\boldsymbol{z}$ is the origin, it is typically omitted). But $g(k,\boldsymbol{r}\,;t)$ is not simply the Fourier transform of $g(\boldsymbol{z},\boldsymbol{r}\,;t)$. Rather, we have defined *in Fourier space* the microstructure $g(\boldsymbol{k},\boldsymbol{r};t)$ where the $\boldsymbol{k}$-dependence explicitly preserves fluctuations of the probe relative to the

origin.

Note also that $g(\boldsymbol{k},\boldsymbol{r},t)$ is *not* to be confused with the structure factor, $S(\boldsymbol{z},\boldsymbol{q},t)=\mathcal{F}_r[P_2(\boldsymbol{z},\boldsymbol{r},t)]$, corresponding to a Fourier transform with respect to the separation vector $\boldsymbol{r}$ between the probe and bath particle. Indeed, we solve for the distribution of bath particles relative to the probe in physical (real) space $\boldsymbol{r}$. The Fourier transform variable $\boldsymbol{k}$ is with respect to the absolute position of the probe, $\boldsymbol{z}$. To determine the diffusive motion of the probe one imagines a concentration gradient of a dilute collection of probes; these physical-space gradients correspond to algebraic multiples of the wave vector, $\boldsymbol{k}$, in Fourier space. The probe flux down this concentration gradient is influenced by the interaction with bath particles distributed according to $g(\boldsymbol{k},\boldsymbol{r},t)$, a distribution that must be determined for all $\boldsymbol{r}$.

Combining equations (3.9) and (3.10) we obtain for the steady average probe flux:

$$\langle\hat{\boldsymbol{j}}_a\rangle=\left[\boldsymbol{U}_a-D_a i\boldsymbol{k}+n_b D_a\int\nabla_r g(\boldsymbol{k},\boldsymbol{r})d\boldsymbol{r}\right]\hat{P}_1(\boldsymbol{k}). \tag{3.11}$$

For the long-time self-diffusion of the probe, we consider the short wave vector (long length-scale) limit and expand $g(\boldsymbol{k},\boldsymbol{r})$ for small $\boldsymbol{k}$, corresponding to a weak gradient in the "concentration of probes":

$$g(\boldsymbol{k},\boldsymbol{r})=g_0(\boldsymbol{r})+i\boldsymbol{k}\cdot\boldsymbol{d}(\boldsymbol{r})+\ldots\,, \tag{3.12}$$

which immediately yields the two terms governing the scattering of the probe: the steady microstructure, $g_0(\boldsymbol{r})$, and the probability-weighted displacement of the probe, $\boldsymbol{d}(\boldsymbol{r})$—*i.e.* the likelihood of a collision and the strength and direction of the probe displacement upon collision, respectively. Inserting this into the expression for probe flux yields

$$\langle\hat{\boldsymbol{j}}_a\rangle=\left(\left[\boldsymbol{U}_a+n_b\,D_a\int\nabla g_0(\boldsymbol{r})d\boldsymbol{r}\right]-D_a i\boldsymbol{k}\cdot\left[\boldsymbol{I}-n_b\int\nabla_r\boldsymbol{d}(\boldsymbol{r})d\boldsymbol{r}\right]\right)\hat{P}_1(\boldsymbol{k}), \tag{3.13}$$

in which $\boldsymbol{I}$ is the identity tensor. Examination of (3.13) reveals the effect of the bath particles on both the mean ($O(1)$) and fluctuating ($O(\boldsymbol{k})$) response of the overall suspension. The first bracketed

term gives the probe's average speed through the fluid: $\boldsymbol{U}_a$ is reduced by the entropic reactive force of the microstructure, as given by the integral term. This reduction in probe speed due to the suspended particles was used by Squires & Brady (2005) to define the microviscosity. Recalling that $i\boldsymbol{k}$ terms represent diffusion, the second bracketed group gives the *effective* diffusivity of the probe: the third term its free Brownian diffusion, plus an increment due to interactions with the bath. This increment corresponds to hard-sphere interactions between probe and bath that scatter the probe's mean path. From a phenomenological perspective, the effect of the bath particles is to reduce the mean velocity of the probe, and to increase the diffusive spread of its trajectory—the effective diffusivity. Defining the second bracketed group as the effective diffusivity of the probe and integrating by parts we obtain:

$$D^{\text{eff}} \equiv D_a \left[I - n_b \oint_{r=a+b} \boldsymbol{n}\boldsymbol{d}\, dS \right], \tag{3.14}$$

where $\boldsymbol{n}$ is the unit surface normal pointing outward from the probe.

In the limit $Pe \to 0$, the entropically hindered diffusion of a particle in a dilute suspension without hydrodynamic interactions must be recovered, $D^{\text{eff}} = D^s_\infty = D_a(1-2\phi_b)$ (Batchelor, 1976), for $a/b = 1$. Motivated by this fact, we denote the corresponding displacement field for the unforced probe $\boldsymbol{d}_{\text{entropic}} \equiv \boldsymbol{d}(Pe{=}0)$. Hence, we express the total displacement field as a sum of entropic and "mechanical" contributions:

$$\boldsymbol{d} = \boldsymbol{d}_{\text{entropic}} + \boldsymbol{d}', \tag{3.15}$$

where $\boldsymbol{d}'$ is the probe fluctuation over and above that for hindered passive diffusion. As we show below, $\boldsymbol{d}_{\text{entropic}}$ contributes $-2\phi_b D_a$ to the effective diffusivity, so we write

$$\boldsymbol{D}^{\text{eff}} = D_a \boldsymbol{I}\,(1-2\phi_b) + \boldsymbol{D}^{\text{micro}}, \tag{3.16}$$

where we have defined

$$\boldsymbol{D}^{\text{micro}} \;\equiv\; n_b D_a \oint \boldsymbol{n}\,\boldsymbol{d}'\, dS\,. \tag{3.17}$$

The effective diffusivity of a tracer particle is its bare diffusivity, $D_a\boldsymbol{I}$, minus the entropic hindrance of the bath, $2\phi_b D_a\boldsymbol{I}$, *plus* an enhancement due to mechanical scattering by the other bath particles, $\boldsymbol{D}^{\text{micro}}$. The force-induced microdiffusivity is proportional to the number density of bath particles, the isolated probe self-diffusivity, and to the first moment of the hard-sphere deflections.

It remains only to obtain the steady microstructure $g_0(\boldsymbol{r})$ and the first fluctuation correction, $\boldsymbol{d}'(\boldsymbol{r})$.

3.4 Non-equilibrium microstructure: Smoluchowski solution

The goal of this section is to formulate an expression governing the evolution of the microstructure, $g(\boldsymbol{k},\boldsymbol{r})$. The Smoluchowski equation governing the pair probability in Fourier space gives the evolution of the fluctuating microstructure:

$$\frac{\partial \hat{P}_2}{\partial t} + \nabla_r\cdot[U_r - D_r\nabla_r]\,\hat{P}_2 + D_a ik\cdot\nabla_r\,\hat{P}_2 + ik\cdot\hat{\boldsymbol{j}}_a = 0, \tag{3.18}$$

where we have defined the relative Brownian diffusivity between the probe and the bath particle, $D_r \equiv D_a + D_b$ and $U_r \equiv U_a - U_b$. With the definition of $g(\boldsymbol{k},\boldsymbol{r})$ in equation (3.10) and substituting (3.8) in (3.18) we have to leading order in diluteness, at steady state:

$$\nabla_r\cdot[U_r - D_r\nabla_r]\,g + 2D_a ik\cdot\nabla_r g = 0, \tag{3.19}$$

$$\boldsymbol{n}\cdot[U_r g - D_r\nabla_r g + D_a ik\,g] = 0 \quad \text{at} \quad r = a+b, \tag{3.20}$$

$$g \sim 1 \quad \text{as} \quad r\to\infty, \tag{3.21}$$

in which conservation requires a no-flux boundary condition at contact and there is no long-range order. The equations are made dimensionless by scaling quantities as

$$r \sim a+b, \qquad U \sim F^{\text{ext}}/6\pi\eta\, a \qquad D \sim D_a + D_b = \frac{kT}{6\pi\eta}\left(\frac{1}{a}+\frac{1}{b}\right), \tag{3.22}$$

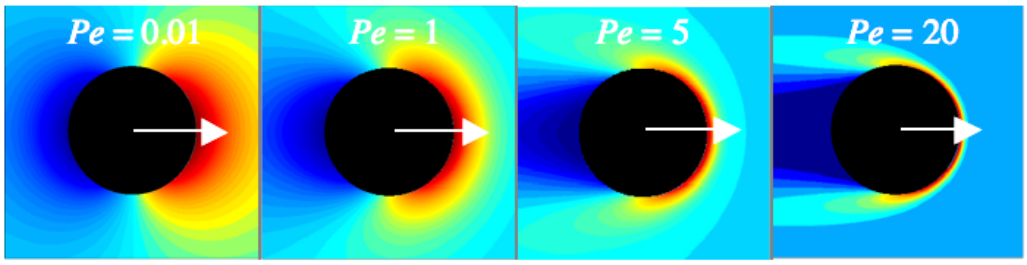

Figure 3.2: Theoretical predictions for the deformed microstructure around a moving probe particle in the absence of hydrodynamic interactions at the pair level. The test particle is moving to the right and there is a buildup of background particle density in front (red) of the probe and a deficit (dark blue) in the trailing wake (Squires & Brady, 2005).

and together with of the expansion (3.12) of $g(\boldsymbol{k},\boldsymbol{r})$, the steady microstructure obeys

$$\nabla^2 g_0 - Pe\, u\cdot\nabla g_0 = 0, \tag{3.23}$$

$$n\cdot[\nabla g_0 - Pe\, u\, g_0] = 0 \quad \text{at } r=1, \tag{3.24}$$

$$g_0 \sim 1 \quad \text{as } r\to\infty, \tag{3.25}$$

where u is the unit vector parallel to probe forcing. Squires & Brady (2005) have solved this problem analytically for all $Pe = F^{\text{ext}}/(kT/b)$. A contour plot in figure 3.4 shows the perturbed steady microstructure g_0 for a range of Pe.

The expression governing the probability-weighted displacement also forms an advection-diffusion equation, but is forced by gradients in the steady microstructure:

$$\nabla^2 d - Pe\, u\cdot\nabla d = \beta\nabla g_0, \tag{3.26}$$

$$n\cdot(\nabla d - Pe\, u\, d) = \tfrac{1}{2}\beta g_0 \quad \text{at} \quad r=1, \tag{3.27}$$

$$d \sim 0 \quad \text{as} \quad r\to\infty, \tag{3.28}$$

where $\beta \equiv 2/(1+a/b)$. Hence the displacement field $\boldsymbol{d}$ is coupled to g_0. In the next section the coupled system is solved analytically in the limit of small and large Pe, and numerically for arbitrary values of the Péclet number.

3.5 Analytical results

Low*-Pe *Limit

For small Péclet number, Brownian diffusion of the bath particles easily repairs the deformation of the microstructure caused by the probe's motion. Since the bath is hardly displaced from equilibrium, we approach the solution with a perturbation expansion in small Pe. Recalling equations (3.23)–(3.25), however, it is apparent that the problem is singular: at some distance $\rho \sim rPe$ from the probe, advection is as important as diffusion. The domain is divided into two regions, and matched asymptotic expansions yield the expression for the steady microstructure g_0 to $O(Pe^2)$:

$$g_0(\boldsymbol{r}; Pe) = 1 - \frac{1}{2}\boldsymbol{u}\cdot\frac{\boldsymbol{r}}{r^3}Pe + \frac{1}{4}\left(\frac{1}{r} - \frac{1}{3}\boldsymbol{uu}\colon\left[\frac{\boldsymbol{I}}{r^3} - 3\frac{\boldsymbol{rr}}{r^5}\right] - \boldsymbol{uu}\colon\frac{\boldsymbol{rr}}{r^3}\right)Pe^2, \tag{3.29}$$

which agrees with the solution that Squires & Brady obtained to $O(Pe)$, which we have extended here to $O(Pe^2)$.

A similar method is applied to equations (3.26)–(3.28) to obtain the fluctuation field. The Pe^0 term of the expansion of $\boldsymbol{d}$ yields the solution

$$\boldsymbol{d}_{\text{entropic}} \equiv \boldsymbol{d}^{(0)} = -\frac{1}{4}\beta\frac{\boldsymbol{r}}{r^3}, \tag{3.30}$$

which gives

$$D^{\text{eff}}(Pe{=}0) = D_a\left[1 - \frac{1}{2}\left(1 + a/b\right)^2\phi_b\right], \tag{3.31}$$

which, for equal probe and bath-particle size, recovers the long-time self diffusivity of a sphere in a dilute dispersion reported by Batchelor (1976), $D^{\text{eff}}(Pe{=}0) = D^s_\infty = D_a(1 - 2\phi_b)$. Since there is no flow at $Pe{=}0$, this $O(\phi_b)$ correction is due to the entropic hindrance of the bath.

It is interesting to note that the $O(1)$ solution for $\boldsymbol{d}$ is the same as the $O(Pe)$ solution for g_0. In fact the problems for g_0 and $\boldsymbol{d}$ are identical in the limit $Pe \to 0$. In the linear response regime, whether the forcing is by external means, g_0, or by thermal fluctuation, $\boldsymbol{d}$, the resulting mobility reduction or diffusivity—kT times the mobility—is the same.

At the next order in Pe, we resolve the vector d into scalar components parallel and transverse to the direction of the probe's velocity, $\boldsymbol{d}_{\parallel} = d_z \boldsymbol{u}$, $\boldsymbol{d}_{\perp,x} = d_x e_x$ and $\boldsymbol{d}_{\perp,y} = d_y e_y$. The $O(\phi_b Pe)$ fluctuation makes no contribution to the microdiffusivity—in keeping with scaling predictions, since $\boldsymbol{nd}^{(1)} \sim \boldsymbol{u}\cdot\boldsymbol{nnn}$ and the displacement of a sphere has no coupling to odd tensors.

Proceeding to the next order in Pe, the singular nature of the problem becomes evident, as the solution by regular perturbation expansion fails to decay to zero far from the probe. An asymptotic expansion in the inner region is matched to the solution in the outer region, giving the proper far-field condition for the inner solution. The first correction to the fluctuation that gives rise to microdiffusive behavior is then:

$$\begin{aligned} d_{\parallel}^{(2)} &= \beta\left[-\frac{13}{48} - \left(\frac{67}{360}\frac{\boldsymbol{r}}{r^3} - \frac{11}{480}\left[3\frac{\boldsymbol{r}}{r^5} - 5\boldsymbol{uu}\colon\frac{\boldsymbol{rrr}}{r^7}\right]\right)\cdot\boldsymbol{u}\right] \\ &\quad -\beta\left[\frac{13}{144}\left(\left[\frac{\boldsymbol{r}}{r^3} - 3\boldsymbol{uu}\colon\frac{\boldsymbol{rrr}}{r^5}\right] - \frac{1}{96}(41\frac{\boldsymbol{r}}{r} - 15\boldsymbol{uu}\colon\frac{\boldsymbol{rrr}}{r^3})\right)\cdot\boldsymbol{u}\right], \qquad (3.32) \\ d_{\perp}^{(2)} &= \beta\left\{-\frac{7}{80r^2} + \frac{13}{48}\boldsymbol{uu}\colon\frac{\boldsymbol{rr}}{r^4} + \frac{11}{480}\left[\frac{1}{r^4} - 5\boldsymbol{uu}\colon\frac{\boldsymbol{rr}}{r^6}\right] + \frac{5}{32}\left[1 - \boldsymbol{uu}\colon\boldsymbol{rr}\right]\boldsymbol{r}\cdot e_y\right\}, \qquad (3.33) \end{aligned}$$

which yields for the microdiffusivity in the limit of $Pe \ll 1$ (plotted in figure 3.5):

$$\begin{aligned} D_{\parallel}^{\text{micro}} &= \frac{79}{180}\left(1 + \frac{a}{b}\right)^2 D_a\, Pe^2 \phi_b, \qquad (3.34) \\ D_{\perp}^{\text{micro}} &= \frac{11}{60}\left(1 + \frac{a}{b}\right)^2 D_a\, Pe^2 \phi_b. \qquad (3.35) \end{aligned}$$

When forced very weakly though a dilute suspension, a probe particle diffuses with its bare diffusivity D_a, minus an entropic hindrance due to the presence of the bath particles that scales as $\phi_b D_a$, plus an enhancement due to hard-sphere collisions with the bath particles—characteristic of Taylor dispersion for particles in a bulk flow. As predicted by scaling arguments in the Introduction, in the low-Pe limit, the force-induced enhancement to the diffusion is quadratic in the forcing; it is also linear in the volume fraction of bath particles, ϕ_b, and anisotropic, preferentially diffusing along the direction of forcing (as compared to the transverse direction) by a factor of 2.39.

High*-Pe *Limit

For very large Péclet number, the shape of the microstructure in front of the probe is deformed into two distinct regions: an outer region in which advection dominates diffusion and the microstructure is undisturbed, and an inner region—a $1/Pe-$thin boundary layer that forms on the upstream face of the probe—where diffusion balances advection. A $Pe-$long wake of particle deficit forms behind the probe, where probability for a probe/bath-particle collision is small. The particles that reside inside the boundary layer provide the most probability for a strong hard-sphere deflection of the probe (cf figure 3.4). Inside the boundary layer, a coordinate rescaling $R = (r-1)Pe \sim O(1)$ preserves the diffusive term, properly reflecting the physics of the inner region and allowing satisfaction of the no-flux condition at contact. A singular perturbation expansion in powers of Pe^{-1} then obtains the deflection field in the boundary layer on the upstream face of the probe, $\pi/2 \leq \theta \leq \pi$:

$$d_{\parallel} = -\frac{\beta}{12}\frac{\boldsymbol{u}\cdot\boldsymbol{n}}{(\boldsymbol{u}\cdot e_\theta)^2}\left(1+(\boldsymbol{u}\cdot\boldsymbol{n})^3\right)e^{Pe(r-1)u\cdot n}Pe + O(1), \tag{3.36}$$

$$d_{\perp} = -\frac{\beta}{12}(\boldsymbol{u}\cdot\boldsymbol{n})(\boldsymbol{u}\cdot e_\theta)(\boldsymbol{n}\cdot e_y)e^{Pe(r-1)u\cdot n}Pe + O(1), \tag{3.37}$$

where $\boldsymbol{u}\cdot\boldsymbol{n} \leq 0$, θ is the angle between $\boldsymbol{u}$ and the normal $\boldsymbol{n}$ and and $\boldsymbol{e}_\theta$ is a unit vector in the direction of θ. As expected from earlier scaling arguments, the microdiffusivity is linear in the forcing when $Pe \gg 1$:

$$D_{\parallel}^{\text{micro}} = \frac{1}{4}\left(1+\frac{a}{b}\right)^2\left(\ln 2 - \frac{1}{4}\right)D_a\,Pe\,\phi_b + O(1), \tag{3.38}$$

$$D_{\perp}^{\text{micro}} = \frac{1}{32}\left(1+\frac{a}{b}\right)^2 D_a\,Pe\,\phi_b + O(1). \tag{3.39}$$

As in the low-Pe limit, the large Pe microdiffusivity is also transversely anisotropic, with a longitudinal-to-transverse preference of approximately 7/2. The effect of the hard-sphere collisions is a $Pe-$large diffusive scattering of the probe's trajectory.

The high Pe analytical results are shown in figure 3.5 alongside those for small Pe. When scaled

with the volume fraction of bath particles and the probe's bare diffusivity D_a, the asymptotic limits of $Pe \ll 1$ and $Pe \gg 1$ form a framework to guide the analysis for intermediate values of the Péclet number, which is developed in the next section.

Numerical solution for arbitrary Pe

To obtain the fluctuating microstructure over the full range of Pe, a numerical solution of the full Smoluchowski equations (3.23)–(3.25) and (3.26)–(3.28) is required. The radial coordinate is rescaled with Pe^{-1} to obtain the stretched coordinate $R = Pe(r-1)$. Because the flow is axisymmetric about the line of external forcing, derivatives of g_0 and $\boldsymbol{d}'$ in the azimuthal angle are zero.

A central difference scheme is used to discretize gradients over the two-dimensional domain. Once a boundary layer forms, *i.e.* beyond $Pe \gtrsim O(1)$, the radial gradients in the microstructure are almost entirely confined to the boundary layer. As Pe continues to grow and the boundary layer thins, a grid point concentration function that varies with Pe increases the density of grid points close to contact, yet retains sufficient resolution far from the probe to capture the physics throughout the upstream domain. The difference coefficients and operators for both radial and angular directions are compactly arranged into first- and second-order sparse matrices. The solutions for the steady and fluctuating pair-distribution function are then obtained in MATLAB using a LAPACK iterative banded solver.

The steady microstructure is solved first (figure 3.4), and the gradients ∇g_0 used to drive for the fluctuation field $\boldsymbol{d}'$. Contour plots for the deflection field are shown in figures 3.3 and 3.4; the anisotropy is evident. The longitudinal fluctuations show that at very small Pe (similar to $Pe=0.01$ in the figure), the fluctuations form a dipole about the probe, with highest probability of a strong kick at the upstream face of the probe, and decaying as $\sim 1/r^2$. As the Péclet number is increased, the boundary layer thins (similar to $Pe = 20$ in figure 3.3), and strong kicks to the probe result from particles swept into the boundary layer on the front of the probe. Particles diffuse and weakly advect around the probe, the boundary layer detaches and a wake forms behind it—resulting in strong fore-aft asymmetry of probe fluctuations.

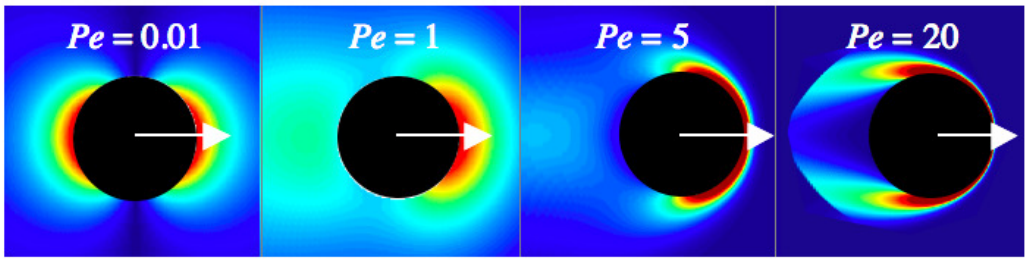

Figure 3.3: The fluctuation field longitudinal to probe forcing. Blue areas indicate regions of weak or no deflection; red areas indicate probability of strong deflection.

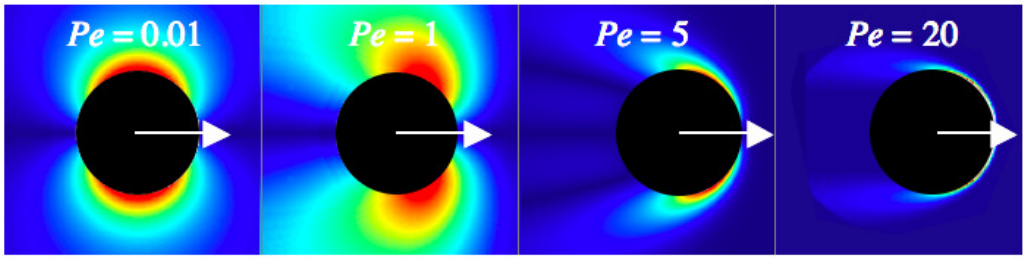

Figure 3.4: The fluctuation field transverse to probe forcing. Blue areas indicate regions of weak or no deflection; red areas indicate probability of strong deflection.

The transverse probe fluctuation field is shown in figure 3.4; for very weak forcing (similar to $Pe = 0.01$ in the figure), the region of highest probability for a strong deflection is at $\theta = \pi/2$, with the distribution mirrored across the axis of symmetry. The resulting probe deflection is perpendicular to its mean motion. As Pe is increased, the probability of a lateral deflection is confined to the boundary layer.

The first moment of the fluctuation is numerically integrated over the surface of contact between probe and bath to obtain the microdiffusivity for a range of $0.01 < Pe < 1000$, as shown in figure 3.5. For very weak and very strong forcing, the numerical solution matches the analytical asymptotes.

Note that two sets of asymptotes are shown for $Pe \gg 1$ in figure 3.5. The straight asymptotes correspond to the high Pe microdiffusivity as given by equations (3.38) and (3.39). Recall that for the large Pe analytical solution we found $\boldsymbol{d}$, the *total* fluctuation field, rather than that due to force-induced collisions only, $\boldsymbol{d}'$ (cf equation 3.15). This is asymptotically correct for $\boldsymbol{D}^{\text{micro}}$ as $Pe \to \infty$. But $\boldsymbol{D}^{\text{micro}}$ is defined in terms of $\boldsymbol{d}'$ and therefore to be consistent, we should use $\boldsymbol{d}'$ rather than $\boldsymbol{d}$—which gives the curved asymptote. For large values of the Péclet number the two coincide.

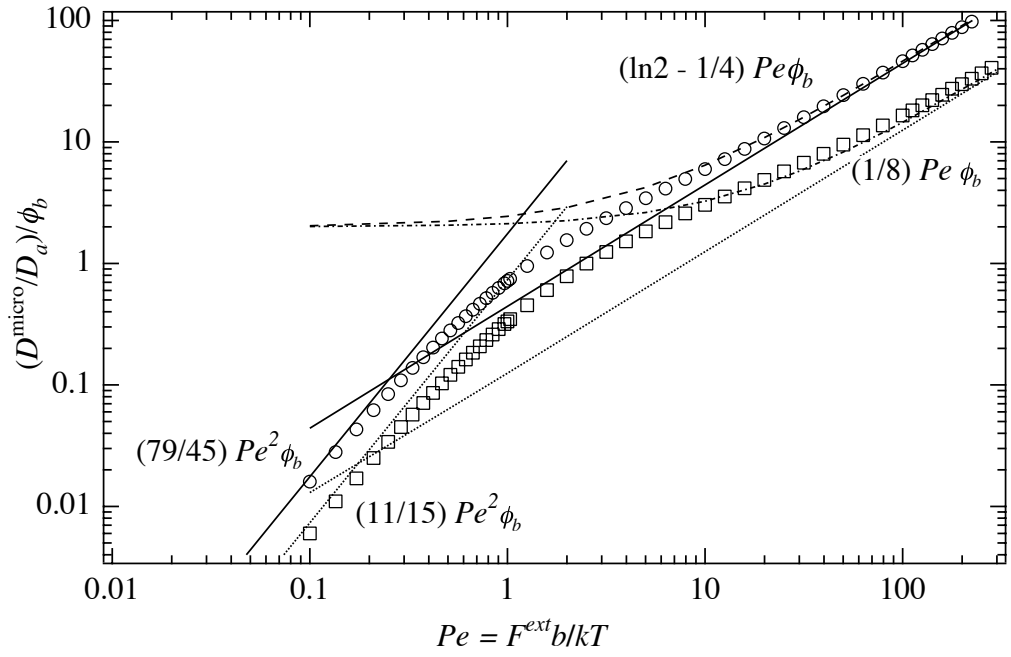

Figure 3.5: The force-induced diffusivity D^{micro}, scaled with the probe bare diffusivity D_a and the volume fraction of bath particles, ϕ_b. Analytical solution for asymptotically small and large forcing are shown by solid lines (longitudinal) and dotted lines (transverse). Curved asymptotes exclude the entropic contribution (dashed for longitudinal; dash-dot for transverse). Open symbols represent the numerical solution of the full Smoluchowski equation (circles for the longitudinal microdiffusivity, squares for the transverse microdiffusivity.)

3.6 Brownian dynamics simulation

The dynamics of probe and bath-particle motion are governed by the Langevin equation, a force balance that includes Brownian, external, hydrodynamic, and other interparticle forces. In the present case this equation reads:

$$\mathbf{0} = \boldsymbol{F}^H + \boldsymbol{F}^{\text{ext}} + \boldsymbol{F}^B + \boldsymbol{F}^P, \tag{3.40}$$

where the left hand side is zero because inertia is not important in colloidal dispersions. A probe of size a is placed among a randomly distributed bath of particles of size b. The hydrodynamic force is given by $\boldsymbol{F}^H = -6\pi\eta a\boldsymbol{U}$ and the external force $\boldsymbol{F}^{\text{ext}} = \mathbf{0}$ for all particles except the probe. The

external force is prescribed, and the other forces in equation (6.1) are given by

$$\overline{\boldsymbol{F}^B} = 0 \qquad \overline{\boldsymbol{F}^B(0)\boldsymbol{F}^B(t)} = 2kT(6\pi\eta a_i)\boldsymbol{I}\delta(t), \quad \text{and} \tag{3.41}$$

$$\boldsymbol{F}^P = \boldsymbol{F}^{HS}. \tag{3.42}$$

Here, the overbar denotes a time average and $\delta(t)$ is the Dirac delta function; $a_i \equiv a$ for the probe, and $a_i \equiv b$ for a bath particle. This expression is integrated over a time step Δt and solved for the total displacement in the first term. At each time step in the simulation the particle positions are updated with a Brownian step and in the case of the probe, an externally forced step. The hard-sphere displacement due to a collision between probe and bath particle is added next; since the hard-sphere force is singular—non-zero at contact only—special treatment is needed. To this end we use a modified "potential free" algorithm (Heyes & Melrose, 1993; Carpen & Brady, 2005), in which overlaps resulting from the external and Brownian steps are corrected along the line of centers of the two particles. For a complete description of Brownian dynamics of active microrheology, see Carpen & Brady (2005).

Dilute suspension

A dilute bath can be achieved in two ways: first, a single bath particle and a single probe can be placed in the simulation cell, and many many simulations run in order to obtain a statistically large number of interparticle collisions. Alternatively, very many "ideal-gas" bath particles can be placed in the cell with one probe—*i.e.* only probe/bath-particle collisions occur, and the bath particles simply pass through each other. Thus an individual time step contains only one deterministic and one Brownian step—for each particle in the cell—but it could contain zero, one, or several hard-sphere displacements, depending on the number of bath particles within one step of contacting the probe. Since the bath particles do not directly see each other, they have no size except when they encounter the probe. It is their number concentration n_b, the contact length scale $(a + b)$, and the Brownian diffusivities D_a and D_b that govern the system dynamics. Varying the value of ϕ_b

thus provides a means to compress the time required to obtain a sufficient number of collisions for statistical analysis, and should have no effect on probe diffusivity (although this turns out not to be precisely the case, as we show below). To this end, "volume fractions" of bath particles from $0.1 \leq \phi_b \leq 0.9$ were tested.

Simulations were conducted with values of the Péclet number ranging from 0.1 to 100, volume fractions $\phi_b = 0.1, 0.3, 0.5, 0.7,$ and 0.9, and $a/b = 1$. On average, a hard-sphere collision occurs during approximately two percent of the total number of time steps. Hence to obtain sufficient resolution of the data, a set of 480 simulations of 10^6 time steps each was run for each Pe and for each ϕ_b. The overall displacement of the probe, $\boldsymbol{x}(t)$, was recorded at each time step.

The *effective* diffusivity of of the probe $\boldsymbol{D}^{\text{eff}}$ is obtained from the time rate of change of the mean-square displacement of the probe according to

$$D^{\text{eff}}(t) = \frac{1}{2}\frac{d}{dt}\langle\, x'(t)\; x'(t)\,\rangle, \tag{3.43}$$

where $x' \equiv x(t) - \langle\, x(t)\,\rangle$ and the angle brackets $\langle\,\rangle$ denote an ensemble average over time and over all simulations. A plot of the probe's average mean-square displacement versus time is shown in figure 3.6, where it can be seen that at long times $\langle \boldsymbol{x}'\boldsymbol{x}' \rangle$ grows linearly in time—confirming that the force-induced dispersion of the probe is indeed diffusive, with a constant diffusivity.

To determine the effect of external forcing on the probe's diffusivity, the effective diffusivity in the absence of flow, *i.e.* at $Pe \equiv 0$, is subtracted from $\boldsymbol{D}^{\text{eff}}$ to yield the force-induced diffusion $\boldsymbol{D}^{\text{micro}}$:

$$\boldsymbol{D}^{\text{micro}} = \boldsymbol{D}^{\text{eff}} - \boldsymbol{D}^{\text{eff}}(Pe{=}0), \tag{3.44}$$

which corresponds to equation (3.16) defined in the theory. Results are plotted in figure 3.7, where $\boldsymbol{D}^{\text{micro}}$ is made dimensionless with probe self-diffusivity, D_a, and scaled with the volume fraction of bath particles ϕ_b.

For $\phi_b = 0.1$, the Brownian dynamics data match the theoretical solution over the full range of Pe, but the data for other values of ϕ_b do not collapse together as expected. The data follow the

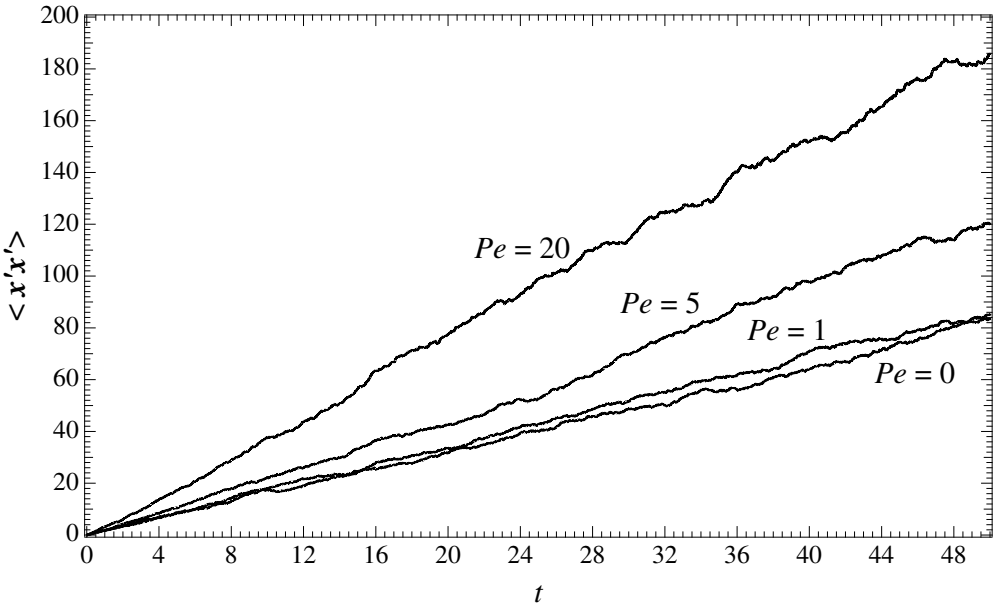

Figure 3.6: Longitudinal mean-squared displacement of the probe, as a function of time via Brownian dynamics simulation. Volume fraction of bath particles shown is $\phi_b = 0.1$. Displacements are made dimensionless as $(a + b)$; time is scaled with the correlation time τ, where $\tau \sim a^2/D_a$ for $Pe \leq 1$ and $\tau \sim a/U$ for $Pe > 1$. Each curve is an ensemble average over 480 simulations.

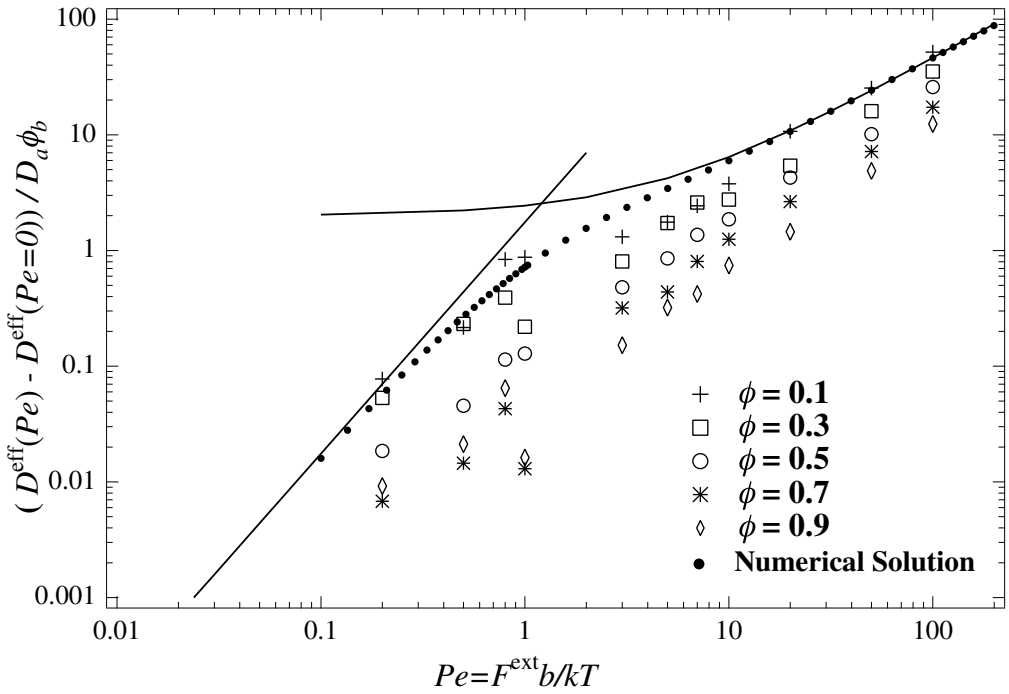

Figure 3.7: Microdiffusivity via Brownian dynamics simulation with ideal gas bath, $a/b = 1$, no hydrodynamic interactions, and ϕ_b as shown in legend. Plotted with analytical and numerical solutions of the Smoluchowski equation (longitudinal direction only is shown.) Solution of Smoluchowski equation is shown by solid asymptotes (analytical results) and filled circles (numerical results). Error bars are on the order of marker size; each marker represents a set of 480 simulations.

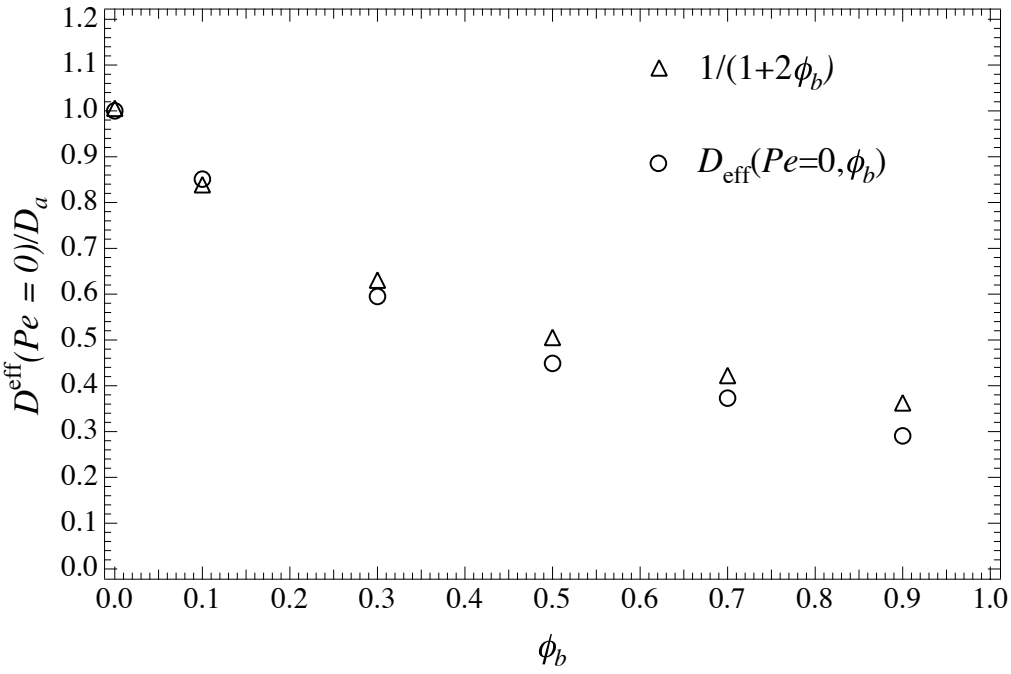

Figure 3.8: Effective diffusivity of the unforced probe for various concentrations of bath particles (probe to bath-particle size ratio taken to be unity.) Circles (◯) are results measured via Brownian dynamics simulation; triangles (△) correspond to theory, $D^s_\infty = 1/(1+2\phi_b)$. Error bars are on the order of marker size; each marker represents a set of 480 simulations.

same qualitative trend, but for $\phi_b > 0.1$ lie beneath the numerical solution, indicating a dependence on volume fraction—even though the bath is modeled as an ideal gas. This surprising result can be understood by noting that the bath particles' motion is correlated via their interactions with the probe. Although the bath particles do not interact directly, a probe/bath-particle collision changes the position of the probe relative to the other nearby particles, giving rise to a correlation between the bath particles. That this correlation must exist can be seen from the dilute, pairwise expression for the equilibrium long-time self-diffusivity of a probe equal in size to the bath particles, $D^s_\infty = (1-2\phi_b)D_a$. This result predicts a *negative* diffusion coefficient for $\phi_b > 0.5$ if only pairwise interaction were important. Clearly the correlated behavior via interaction with the probe is critical even though the bath particles are an ideal gas. In figure 3.8 we show the actual long-time self-diffusivity of the probe as determined by Brownian dynamics simulation. Also shown in the figure is a theoretical prediction for D^s_∞ which follows from the approach of Brady (1994), who determined the long-time self-diffusivity of hard spheres in concentrated suspensions as

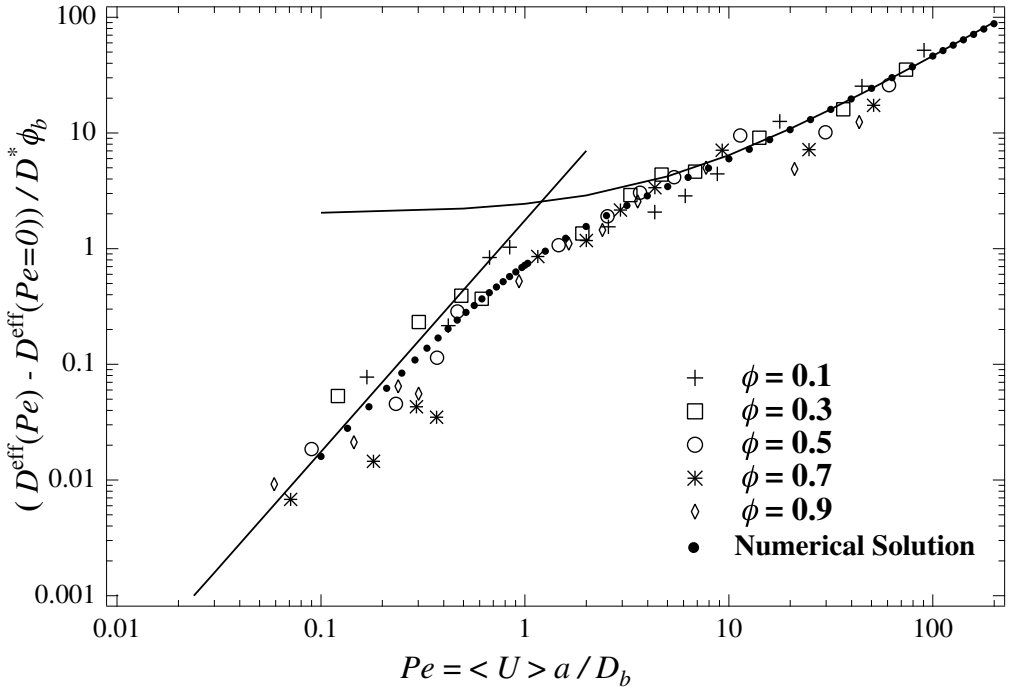

Figure 3.9: Brownian dynamics simulation data, shown with analytical (solid lines) and numerical solution (filled circles) of the Smoluchowski equation (longitudinal). The force-induced microdiffusivity, D^{micro}, is scaled with volume fraction of bath particles, ϕ_b and made dimensionless with D^*, which corresponds to D^s_∞ for $0 \leq Pe \leq 20$ and to D_a for $Pe > 20$. It is plotted against the effective Péclet number, which reflects the correlation of the bath particles. Error bars are on the order of marker size; each marker represents a set of 480 simulations.

$$D^s_\infty(\phi_b) = D_a[1 + 2\phi_b g_0(2;\phi_b)]^{-1}. \tag{3.45}$$

For ideal-gas bath particles the equilibrium pair-distribution function at contact is $g_0 = 1$, and we have

$$D^s_\infty(\phi_b) = D_a \frac{1}{(1 + 2\phi_b)}, \tag{3.46}$$

which is in reasonable agreement with the results from Brownian dynamics simulations in figure 3.8 (where $a/b \sim O(1)$).

The correlated collisions make the bath more resistive to the motion of the probe as evidenced by the smaller long-time self-diffusivity—in the linear response regime the diffusivity and the resistance to external forcing are the same—and so what is important is the *actual* probe speed $\langle U \rangle$ rather than the imposed external force in setting the Péclet number. The probe perturbs the microstructure with this average speed. Away from the probe, the bath particles again form an ideal gas, and

restore the microstructure under their own Brownian motion, which is unhindered. This gives an effective Péclet number:

$$Pe^{\text{eff}} = \frac{\langle U \rangle \, a}{D_b}, \tag{3.47}$$

where D_b is the bare diffusivity of the bath particles away from the probe and $\langle U \rangle$ is the average probe velocity determined by simulation.

The scaling of D^{micro} with the isolated probe diffusivity D_a (the vertical axis in figure 3.7) emerged from the kinematic expression for probe flux, equation 5.5, where the diffusive flux of the probe was assumed to depend on unhindered probe diffusion. But for small Pe the probe forcing should be proportional to D^s_∞ rather than D_a as the deformation to the microstructure is sensitive to the correlated bath-particle behavior. At very large Pe (when the boundary layer is thin) the unhindered forcing, D_a, is appropriate. We apply this rescaling of the Péclet number over the full range of Pe, and of D^{micro} for $0 \leq Pe \lessapprox 20$, as seen in figure 3.9. The Brownian dynamics results now collapse onto the theoretical results in a universal curve for $a/b = 1$.

3.7 Comparison to macrodiffusivity

Previous studies of particle motion in macrorheology show that imposing a shear flow on a colloidal dispersion increases particle diffusivity (Leighton & Acrivos, 1987; Morris & Brady, 1996; Brady & Morris, 1997; Breedveld *et al.*, 1998). In the non-colloidal regime, the dispersivity of a sphere falling through a neutrally buoyant suspension at low Reynolds number and high Péclet number has also been studied both analytically (Davis & Hill, 1992) and experimentally (Abbot, Graham, Mondy & Brenner, 1997). It is of interest to seek comparison between such macroscale behavior and the results of this investigation.

Both shear-induced macrodiffusivity and force-induced microdiffusivity result from the scattering of a tracer, or probe, particle by the deformed microstructure. Brady & Morris (1996; 1997) determined the shear-induced long-time diffusion tensor $\boldsymbol{D}^{\text{macro}}$ for weak shearing and strong shearing. Both $\boldsymbol{D}^{\text{micro}}$ and $\boldsymbol{D}^{\text{macro}}$ scale as $\sim O(\phi_b Pe)$ for $Pe \gg 1$. At small values of the Péclet number,

the dependence of force-induced diffusion on Pe changes in both micro and macro cases as the correlation timescale becomes diffusive; while the former scales as $\sim O(\phi_b Pe^2)$, the latter scales as $\sim O(\phi_b Pe^{3/2})$—reflecting the different symmetry and forcing of the two microstructures. Further, in both flows the distorted bath microstructure is *asymmetric* (cf figure 3.1) which gives rise to an anisotropic diffusion tensor. Brady & Morris (1997) also showed that the shear-induced diffusion tensor could be directly related to the bulk stress tensor for the suspension, and its anisotropy to the normal stress differences—a hallmark of the rheological behavior of far-from equilibrium complex fluids. We have shown that the microdiffusivity tensor is anisotropic as well; the notion of normal stress differences in the context of active microrheology is an intriguing one, and this connection should be further explored.

The settling of a non-Brownian ball through a neutrally buoyant quiescent suspension of non-colloidal spheres is the macroscale analogue of our model at very high Pe (in the falling-ball regime, the Péclet number is very large due to particle size). The dispersion of the ball's trajectory arises due to many uncorrelated hydrodynamic interactions with the background suspended balls. Davis & Hill (1991) determined theoretically the hydrodynamic diffusivity of a falling ball in the dilute limit for all size ratios a/b. For size ratio of order unity, they give the hydrodynamic diffusivity as

$$\frac{D^H_{\text{theory}}}{Ua} \approxeq 1.33 \left(\frac{b}{a}\right)^2 \phi_b. \tag{3.48}$$

Here, $U = F^{\text{grav}}/6\pi\eta a$ is the Stokes velocity of the falling ball, F^{grav} is the net force due to gravity, η is the solvent viscosity, and the superscript H denotes the hydrodynamic diffusivity. Mondy and coworkers (1997) conducted experiments in which they measured the dispersion of a ball of size a as it fell through a suspension of balls of size b, for several volume fractions ϕ_b and a range of probe-to-background ball size ratios, a/b. At the smallest volume fraction measured, $\phi_b = 0.15$, for $O(1) \lesssim a/b \lesssim O(10)$ they found the diffusivity of the falling ball to be

$$\frac{D^H_{\text{meas}}}{\langle U \rangle a} = 1.067 \left(\frac{b}{a}\right)^{1.93^{+0.53}_{-0.26}} \phi_b, \tag{3.49}$$

where the error shown corresponds to 95% confidence limits, and $\langle U \rangle$ is the average vertical speed of the falling ball. We recall the $O(Pe)$ result for the parallel microdiffusivity from §3.5:

$$\frac{D^{\text{micro}}_{\text{theory}}}{\langle U \rangle a} = \frac{1}{4}\left(\ln 2 - \frac{1}{4}\right)\left(\frac{b}{a}\right)\left(1 + \frac{a}{b}\right)^2 \phi_b, \tag{3.50}$$

The hydrodynamic interactions, particularly the near-field lubrication interactions, between the non-colloidal spheres produce a dependence on size ratio that is qualitatively different than the size ratio dependence in the case of no hydrodynamic interactions considered in this work. Hydrodynamic interactions can be included in the theory developed here and is left for a future study. However, the same scaling in Pe_b and ϕ_b is obtained.

3.8 Conclusions

We have extended the model of active, nonlinear microrheology to account for fluctuations in probe motion. A dilute colloidal dispersion of hard spheres through which a Brownian probe is driven by a constant external force was studied. Collisions between the probe and bath particles were shown to drive a long-time diffusive spread of the probe's trajectory—a force-induced diffusion, or "microdiffusivity." The microdiffusivity increases the probe's long-time self-diffusion. In the limit $Pe \to 0$, D^{micro} scales quadratically: $D^{\text{micro}} \sim Pe^2 \phi_b D_a$. At the opposite extreme where $Pe \to \infty$ the microdiffusivity is linear in the forcing, $D^{\text{micro}} \sim Pe \phi_b D_a \sim (F^{ext}/\eta)\phi_b$, and the force-induced diffusion dominates the spread of the probe's trajectory.

For all values of Pe, it was found that the dependence of the microdiffusivity on the volume fraction of bath particles, ϕ_b, is not strictly linear even when only pairwise interactions are considered and the bath particles are an ideal gas. The motion of the bath particles becomes correlated via their interactions with the probe, and when $\phi_b \gtrsim 0.1$, the effect of the correlation becomes important. A key effect of bath-particle correlation is a reduction in the mean speed of the probe; since now $\langle U \rangle$ is the speed with which the microstructure is perturbed, the appropriate Péclet number is given

by $Pe^{\text{eff}} = \langle U \rangle a/D_b$. Similarly, the diffusive flux of the probe is hindered by the bath particles at small Pe, but for for larger Pe its relaxation through the boundary layer is set by its bare diffusion coefficient D_a. The microdiffusivity should then be made dimensionless by D^s_∞ for $0 \leq Pe \lessapprox 20$ and by its bare diffusivity D_a for $Pe \gtrapprox 20$, where it is proposed that $D^s_\infty = D_a/(1 + 2\phi_b)$ accounts for the correlation. A re-scaling of all Pe for $\phi_b > 0.1$ that reflects this physical process collapses the data onto a single curve given by the dilute theory, as shown in figure 3.9. This correlated behavior of the bath particles raises the issue of excluded volume interactions between the bath particles, a subject that merits further study.

It was found that for all Pe, neglecting hydrodynamic interactions, the microdiffusivity is proportional the scale factor $(1 + a/b)^2$. In the limit of a small probe, $a/b \to 0$, this factor reduces to unity and the microdiffusivity scales with Pe and ϕ_b as expected. However, when a/b is large, the analysis predicts a microdiffusivity that grows as $(a/b)^2$. This result is counter to what one would expect, because very small bath particles should produce correspondingly small effects. There are two sources for this behavior. The first is the neglect of hydrodynamic interactions between the probe and the bath particles. A large probe would appear as a rigid surface to the small bath particles and it may be a poor approximation to have neglected the long-range hydrodynamic interactions. The other contributor to the apparent paradox is the way we have stated the standard (macro)rheological condition for diluteness: $\phi_b \ll 1$ dictates only that the typical distance between bath particles must be small. But in microrheology, for the *probe* to move through a dilute bath requires that the probe encounter only one bath particle at a time. The probe's contact area scales as a^2, and the number of colliders n_b within one collision distance, b, must be small; that is, a shell of thickness b around the probe can contain at most one bath particle at any given time in order to assure that only pair-collisions occur: $n_b a^2 b \ll 1$. Hence the diluteness condition is more properly stated as $\phi_b (a/b)^2 \ll 1$. With this constraint, the microdiffusivity, *e.g.* at large Pe, is $D^{\text{micro}} \sim (a/b)^2 \phi_b D_a Pe$ and remains small for $a/b \gg 1$.

Next, a comparison between tracer motion in a sheared suspension and probe motion in active microrheology showed that both flows give rise to an enhancement to long-time self-diffusivity.

Further, for both systems the asymmetry of the deformed microstructure produces an anisotropic diffusion tensor, which prompts the question of normal stress differences. Understanding the close qualitative relationship between macrodiffusivity and microdiffusivity and their connection to normal stress differences can enable the use of the latter as a material interrogation technique—*e.g.* the measurement of the long-time self-diffusion of the probe may yield normal stresses, a subject of a future study.

The comparison between falling-ball rheometry in the dilute limit and active microrheology in the dual limit $Pe \to \infty$, $\phi_b \ll 1$ shows that in both regimes the diffusivity of the probe scales linearly in both the forcing and the volume fraction of bath particles. A key physical difference between the two problems is that the falling-ball dispersivity is a purely hydrodynamic phenomenon, whereas our model for active microrheology excludes all but hard-sphere mechanical interactions. This difference manifests in the dependence of force-induced diffusion on probe/background-particle size ratio a/b. The effect of hydrodynamic interactions between colloidal particles is not expected to change the scaling in Pe or ϕ_b, but is likely to yield a different dependence on particle size ratio.

Indeed, an important area for future study is how hydrodynamic interactions affect the force-induced diffusion. When hydrodynamic interactions are important, the probe flux changes; its ensemble average (equation 3.9) now contains an additional term, $\boldsymbol{R}_{FU}^{-1}\cdot\boldsymbol{F}^P\hat{P}_1$. As before, the terms in the average probe flux can be arranged to more readily identify the physical process associated with each one (cf equation 3.13.) The new hydrodynamic contribution appears in the first bracketed term, which is a coefficient of the probability density $\hat{P}_1$—hydrodynamics affect the probe's *average* speed. And since the bare diffusion tensor for the probe, $\boldsymbol{D}_a$, now depends on relative positions of probe and bath particles, it remains inside the integrals in equation 3.13. This gives only a geometric scale-factor difference in the general expression for the effective diffusivity, 3.14. Now for large Pe, hydrodynamic interactions also *qualitatively* alter the deformed microstructure; the scaling of g_0 in Pe varies in the presence of hydrodynamic interactions. In the so-called "pure hydrodynamic" limit, $a/a_h \equiv 1$ (Khair & Brady, 2006), the scaling becomes $g_0 \sim Pe^{0.78}$, and varies continuously up to $g_0 \sim Pe$ for $a/a_h \to \infty$; a similar qualitative change in Pe-scaling is expected for the deflection

field. Thus the presence of hydrodynamic interactions will give rise to a quantitative change in the bare diffusion coefficient, and at high Pe, a qualitative change in the deflection field $\boldsymbol{d}$ (cf equations 3.26-3.28.) Since the microdiffusivity is the first moment of the deflection field at contact, its scaling in Pe is expected to change accordingly. And as noted above, significant qualitative changes in the size-ratio-dependence (not in Pe) can occur at high-Pe in the case of disparate probe/bath-particle size ratio.

Often the particles studied experimentally have a shape that deviates from that of a sphere—sometimes significantly so. An ellipsoidal-type probe particle in a dispersion of spherical bath particles can be studied, where an external force is applied through the probe's center. The new length scales added by the minor and major axes of the probe gives rise to a *quantitative* difference in the diffusivity—the size dependence of the diffusivity would reflect the new length scales. One would also need to consider the importance of rotational diffusion. As the probe moves through the bath, the angle its major axis forms with the line of action of the external force changes. For small Pe, all orientations are equally likely; the rotational diffusion would make the probe act as a "sphere" of size R_{avg}, the rotational average of the major and minor axes, and thus still give the same forcing (dipolar microstructural disturbance.) The scaling in Pe is identical, since the flow is the same. At high Pe, rotational diffusion is slow compared to advection, and one expects the probe particle to attain a stable orientation with its major axis transverse to the forcing, as found by Khair & Brady (2008) for a constant-velocity ellipsoidal-type probe. They also found that the perturbation to the microstructure scales linearly in Pe for $Pe \gg 1$ in the absence of hydrodynamics, and so the scaling in Pe remains the same. For intermediate values of Pe, in the case of constant forcing, rotational diffusion matters. But one would predict that a balance in kicks from bath particles would again align the probe transverse to the flow as at high Pe. Thus the contribution to the diffusion coefficient is at most a *geometric* scaling of the size dependence.

An important outcome of this work is its general applicability to a wider class of problems. Thus far we have studied the diffusive motion of a particle moving due to an *externally applied* force through a bath of other particles. Many systems of interest, however, consist of self-propelled

objects; biological microswimmers are important examples. Can such motion be related to that of the externally forced particle studied here? In fact, it turns out that the results obtained here are the same as those one would obtain for many self-propelled particles. What is important is the relative motion of the probe to the bath particles, so if one can neglect hydrodynamic interactions, the results in the case of a microscale swimmer would be *identical* to those obtained in this study (with Pe based on U_{probe} rather than an external force.) A self-propelled object must be torque- and force-free, so if the object is a swimmer, velocity decays as $\sim 1/r^2$. Thus, neglecting hydrodynamic interactions may be a reasonable approximation. In the case of electrophoretic motion, the velocity disturbance decays as $\sim 1/r^3$ and neglecting hydrodynamics is an even better approximation. (Including hydrodynamics would make only a *quantitative* difference, as discussed above.) The solution presented for the microdiffusivity is therefore applicable to a very wide range of problems in which hydrodynamic interactions can be neglected—both externally forced and self-propulsive systems. Important future work includes experimental verification of this idea; development of theory for general-shape swimmers; and extension to groups of swimmers or propelled objects. The crowded interior of a cell also provides a fascinating opportunity to combine the effects of a concentrated bath with self-propulsion to study the motion of objects diffusing through the intracellular fluid.

Several other interesting questions remain. We have investigated the steady-state behavior of the suspension, but studying its transient behavior is as yet unexplored. Other open questions include the connection of diffusivity to normal stress differences, and the "continuum" limit for large size ratios $a/b \gg 1$. Notwithstanding, the simplifications invoked in the model thus far provide important conclusions about the fluctuating motion of a tracer particle in the active, nonlinear microrheology regime. That this motion is diffusive, with a simple dependence on few parameters, and widely applicable to a range of problems may open new techniques for researchers in material science, the biosciences, and nanoscale technology.

Chapter 4

The stress tensor via nonlinear microrheology

4.1 Introduction

One of the primary objectives of traditional macroscale rheology is to understand and characterize the relationship between strain rate and material stress, which is carried out by imposing a bulk shearing motion on a sample of material. In our investigation here, material behavior is studied through the framework of nonlinear *micro*rheology—in which a Brownian "probe" particle is driven through a complex fluid, and its motion tracked in order to infer the mechanical properties of the embedding material. Probe motion through the dispersion distorts the microstructure; the character of this deformation, and hence its influence on probe motion, depends on the strength with which the probe is forced, F^{ext}, compared to thermal forces, kT/b, defining a Péclet number, $Pe = F^{ext}/(kT/b)$, where kT is the thermal energy and b the bath-particle size. It was shown in chapters 2 and 3 that the material viscosity and the diffusivity can be determined by monitoring the mean and fluctuating motion of the probe. But no such simple technique has yet been put forth to determine suspension stress in microrheology, nor to define the microrheological stress constitutively in terms of material properties, *e.g.* the viscosity. Recent approaches in nonlinear microrheology were able to produce only a scalar evaluation of the stress due to the axisymmetric geometry surrounding the probe. But it has been proposed in previous studies of equilibrium suspensions that diffusion is driven by stress gradients (Einstein, 1906; Batchelor, 1976; Brady & Morris, 1997). If such a

connection can be made in nonlinear microrheology, then the mean-square displacement of the probe can be used to determine the stress tensor. Further, by simply monitoring the mean and mean-square motion of a probe, one can determine the full rheological picture of a material: viscosity, diffusivity, and the stress. In the previous chapter, it was shown that in nonlinear microrheology, collisions between probe and bath particles give rise to force-induced diffusion, or "microdiffusivity." Further, it was found that the microdiffusivity tensor is transversely anisotropic (Zia & Brady, 2010); a simple connection between stress and diffusivity would then provide a measure of normal stress *differences*. The goal of the present investigation is to develop a theoretical framework for defining an analytical expression for the stress in terms of particle migration and diffusion.

It has previously been proposed that stress gradients drive diffusion in suspensions. Einstein proposed this idea in his model of Brownian motion, and asserted that gradients in the osmotic pressure drive diffusion (1906). A brief review of his famous thought experiment is given in chapter 2. In a slightly different approach, Batchelor (1976) showed that gradients in the chemical potential are the driving force for diffusive flux in single- and multispecies (near) equilibrium suspensions. Connecting the two approaches yields the simple prediction that gradients in the stress in colloidal dispersions drive diffusion, $\partial \boldsymbol{\Sigma}/\partial n \sim \boldsymbol{D}$, where $\boldsymbol{\Sigma}$ is the stress, $\boldsymbol{D}$ is the diffusion tensor, and n is the number density of particles. If this relation holds true for non-equilibrium suspensions, then as alluded to in the introductory chapter (chapter 1), simply watching the motion of a single particle would yield an extraordinary amount of information: stress, viscosity, and diffusion. It is the primary goal of this chapter to propose a proper form for this expression and from it, determine an analytical relationship between stress gradients and particle migration and diffusion. But more deeply, an understanding of the implications this raises about the fluctuation-dissipation relation in *non*-equilibrium systems is sought.

The remainder of this chapter is constructed as follows: We begin in §4.2 with a brief review of traditional approaches taken in describing suspension stress. In such approaches, the details of particle distribution must be known in order to determine stress in general systems, although powerful approximations such as the Carnahan-Starling equations of state are valid for systems not close to

maximum packing (1969; 1971). In §4.3, a macroscopic approach is introduced. Here, a connection between macroscopic driving forces and diffusion is made: Gradients in the chemical potential are shown to drive Fickian diffusion. Because thermodynamics connects the osmotic pressure and the chemical potential, diffusion can also be interpreted as due to osmotic pressure gradients—which supports the notion that stress gradients drive diffusion. The general relationship between suspension stress $\boldsymbol{\Sigma}$ and diffusion $\boldsymbol{D}$ is proposed: $\partial\boldsymbol{\Sigma}/\partial n \propto \boldsymbol{D}$, where n is the number density of particles in the suspension. We seek then to understand if this relation is valid in non-equilibrium systems. Next, in §4.4 we apply the simple relation above to a test case: nonlinear microrheology. Qualitatively the agreement is good throughout the full range of Pe. But quantitative differences between the known and predicted values for the diffusivity indicate that the simple approach taken does not fully account for the behavior of the particles. The primary difference between the models considered by Einstein and Batchelor, and our nonlinear microrheology model is the difference between an equilibrium and a non-equilibrium system. The former can be described by an equation of state, while the latter must be described by an equation of *motion*. The relevant equation of motion is a momentum balance.

A momentum balance over the particles is proposed in §4.5, in which the divergence of the stress balances body forces on the particles. In order to determine the constitutive form for the relevant body forces, the momentum balance is applied to the equilibrium cases of diffusion at infinite dilution and for concentrated suspensions. The known results are recovered when the body force is constitutively modeled to account for diffusive flux. The next objective is to apply the momentum balance to non-equilibrium systems. The nonlinear microrheology test case is revisited, in two modes: the first, constant-velocity mode which recovers the microviscosity (cf chapter 2), and points up the fact that advective flux of particles may play a role in gradient-driven particle migration. Secondly, the case of constant-external force nonlinear microrheology is considered. In this system particles migrate due to diffusion and also due to being advected by the mean flow. This leads to a constitutive model for the body forces in the momentum balance, in which it is asserted that fluctuation and dissipation associated with diffusion and viscous drag characterize

the particle migration driven by stress gradients. The resulting analytical relationship between stress, diffusion, and viscous drag confirms that stress gradients drive diffusive and advective flux in non-equilibrium systems. The normal stress, normal stress differences, and the osmotic pressure are obtained analytically for small and large Pe, and numerically for the full range of Pe. The results are given in §4.6, where they are compared to the stress derived via a traditional microscopic (Smoluchowski) approach and to measurements obtained via Brownian dynamics simulation. In section §4.8 the new theory is compared to the stress in a dilute dispersion of colloids undergoing simple shear. The study is concluded in §4.9 with a discussion.

4.2 Microscopic analysis

A familiar colligative property of suspensions is the osmotic pressure Π. The osmotic pressure is the particles' contribution to the total pressure in the suspension—solvent plus fluid. In an incompressible fluid, the absolute value of the fluid pressure p_f has no equation of state—it is decoupled from the density and the temperature. But the particle pressure Π depends on state variables such as the temperature. It can be thought of as the partial pressure of the particles; their thermal fluctuations give rise to pressure in the fluid analogously to the way atoms in a gas or fluid create pressure on the walls of an enclosing container. The equation of state for the particles is given in terms of the osmotic pressure; in such a canonical ensemble of particles, a treatment by statistical mechanics gives the osmotic pressure as the partial derivative of the Helmholtz free energy with respect to volume, at constant temperature T and particle number N. For a suspension of particles at number density n, interacting via a pair-potential V at particle separations r,

$$\Pi = nkT - \frac{2\pi}{3} n^2 \int_0^\infty r^3 \, g(\boldsymbol{r}) \frac{dV}{dr} dr \tag{4.1}$$

where $g(\boldsymbol{r})$ is the pair-distribution function (McQuarrie, 1976; Brady, 1993*a*). For a suspension of hard spheres that do not interact hydrodynamically, the hard-sphere potential suffices to characterize particle interactions; the potential of interaction is zero for $r > 2a$ where a is the size of the

particles, and an infinite potential prevents particle overlap for $r < 2a$. For repulsive hard spheres, $V(r) = kT\delta(r-2)$ where $\delta(r)$ is the Dirac delta function. The hard-sphere model for the interparticle force gives an average interparticle $\langle \boldsymbol{\Sigma}^P \rangle$ stress as

$$\langle \boldsymbol{\Sigma}^P \rangle = -nkT \left(1 + \frac{3}{\pi}\phi \int \boldsymbol{nn}\, g(1) d\Omega \right), \tag{4.2}$$

where $\boldsymbol{n}$ is the unit surface normal pointing outward from a particle, $g(1)$ is the pair-distribution function at contact (the pair-distribution function $g(\boldsymbol{r})$ describes the radial pair arrangements around a test particle), $d\Omega$ is the element of solid angle, and the angle brackets signify the volume average, $\langle \cdot \rangle = \int \cdot dV$. In consequence, the osmotic pressure in such a suspension is given by

$$\frac{\Pi}{nkT} = 1 + 4\phi\, g(1), \tag{4.3}$$

where $\phi = 4\pi a^3 n/3$ is the volume fraction of particles, $g(2)$ is the pair-distribution function at contact, and the first term is the osmotic pressure at infinite dilution (McQuarrie, 1976; Brady, 1993*a*).

An alternative approach with which the reader may be familiar was advanced by several workers in the late fifties and sixties, utilizing a virial series expansion to obtain the osmotic pressure of a hard-sphere fluid at equilibrium. To do so they derived the compressibility $Z \equiv \Pi V/nkT$, where V is the volume and Π is the osmotic pressure. Carnahan & Starling (1969) proposed a geometric series for this virial expansion, with the following result:

$$Z = \frac{\Pi V}{nkT} = \frac{1 + \phi + \phi^2 - \phi^3}{(1-\phi)^3}, \tag{4.4}$$

known as the Carnahan-Starling equation of state. In the case of a dilute system at equilibrium, since $g^{eq}(1) \approx 1$, the Carnahan-Starling equation of state becomes

$$\frac{\Pi}{nkT} = 1 + 4\phi\, g^{eq}(1), \tag{4.5}$$

which is identical to (4.3). However, (4.4) is invalid in very concentrated suspensions where it fails to predict the divergence of the viscosity. It is also an equation of state, applicable to equilibrium systems only. In the end, the microscopic approach requires the computation of the pair-distribution function $g(\boldsymbol{r})$ from the appropriate governing equation in order to obtain the stress analytically to be generally applicable. An alternative approach is considered next.

4.3 Macroscopic view of suspension stress

In Chapter 2, we reviewed several different perspectives on diffusion, each related to a distinct physical transport process. Collective diffusion is a macroscopic process of down-gradient or Fickian diffusion; alternatively, self-diffusivity is a microscopic process detected by tracking the trajectory of individual particles over time. But self-diffusion can also be viewed from a macroscopic, or Fickian, perspective: one can imagine "tagging" a set of particles in a dispersion in such a manner that there is a weak spatial gradient in the tagged species; the down-gradient diffusion of these particles relative to the remaining untagged particles is equivalent to their self-diffusivity from the microscopic (individual trajectory) perspective (Batchelor, 1976; Rallison & Hinch, 1986). Previously, diffusive flux has been related to gradients in the chemical potential and in the osmotic pressure (Einstein, 1906; Batchelor, 1976). We shall review these briefly next, with a view towards applying them more generally as a way to determine stress in a non-equilibrium system. The benefit of such an approach is that rather than needing to know the details of the entire particle microstructure $g(\boldsymbol{r})$, a connection between diffusion and stress would allow the determination of the latter by simply monitoring particle mean-square displacement. In particular, the macroscopic approach taken in determining the diffusion tensor in microrheology (cf chapter 3) would then allow the determination of stress tensor by monitoring the mean-square displacement of a *single* particle.

Gradient-driven diffusion

In his theory on the diffusion of small particles (1906), Einstein asserted that gradients in the osmotic pressure are the driving force of diffusive flux in dilute suspensions. The central assumption in his

approach is the existence of thermodynamic equilibrium between solvent and particles. Assuming a Fickian (macroscopic) process, he deduced the diffusion coefficient for a spherical particle (a detailed discussion of the Einstein approach can be found in chapter 2.) The outcome was an elegant and powerful relationship:

$$\boldsymbol{D} = kT\boldsymbol{M}, \tag{4.6}$$

where $\boldsymbol{D}$ is the diffusivity, k is Boltzmann's constant, T is the temperature, and $\boldsymbol{M}$ is the hydrodynamic mobility of the microscopic particle—the inverse of the hydrodynamic drag coefficient. For spherical particles,

$$\boldsymbol{D} = \frac{kT}{6\pi\eta a}\boldsymbol{I}, \tag{4.7}$$

the familiar Stokes-Einstein relation giving the diffusivity of a spherical particle in a solvent. Here, η is the solvent viscosity and a is the particle size. This simple expression connects thermodynamics and hydrodynamics—or more fundamentally, fluctuation and dissipation. But how can this result be connected to the osmotic pressure of the suspension of small particles?

Reconsidering Einstein's thought-experiment, Batchelor (1976) showed that the driving force for collective, or down-gradient, diffusivity of particles in a suspension is the gradient in chemical potential μ. The advective flux $\boldsymbol{j}_{adv} = -n\boldsymbol{M}\nabla\mu$ due to the external potential is the diffusive flux $\boldsymbol{j}_{diff} = -\boldsymbol{D}\cdot\nabla n$:

$$\boldsymbol{D}^c\cdot\nabla n = n\boldsymbol{M}^c\cdot\nabla\mu, \tag{4.8}$$

where the superscript c indicates the down-gradient, collective diffusivity $\boldsymbol{D}^c$, and $\boldsymbol{M}^c$ is the corresponding mobility. Now the chain rule gives $\nabla\mu = (\partial\mu/\partial n)\nabla n$; substituting this into the equation above gives for $\boldsymbol{D}^c$

$$\boldsymbol{D}^c = n\boldsymbol{M}^c\frac{\partial\mu}{\partial n}. \tag{4.9}$$

Equation (4.9) indicates that a number-density gradient in the chemical potential is the driving force for macroscopic *collective* diffusion. But the argument due to Einstein for a suspension at infinite dilution showed that equivalently, osmotic pressure gradients drive diffusion. Can the same

connection be made here for non-dilute systems? Let us examine equation (4.9) more closely—in particular, the mobility $\boldsymbol{M}^c$—to see.

Because gradient diffusion is the same as sedimentation (Batchelor, 1972), the mobility in equation (4.9) is defined by the sedimentation coefficient $K(\phi)$: $\boldsymbol{M} = K(\phi)/6\pi\eta a\boldsymbol{I}$ for spheres. When particles are close enough to interact hydrodynamically (*i.e.* the volume fraction of particles $\phi = 4\pi a^3 n/3$ is not small), down-gradient particle diffusion drives a backflow of fluid in order to conserve volume (Batchelor, 1972; Russel & Glendinning, 1981; Brady, 2011). In addition, one must properly account for the chemical potential gradient acting on the fluid. Moving this fluid force onto the particles so that the fluid is force-free gives

$$\boldsymbol{D}^c = \frac{K(\phi)}{6\pi\eta a}\frac{n}{1-\phi}\frac{\partial \mu}{\partial n}\boldsymbol{I}, \tag{4.10}$$

where $K(\phi)$ is the sedimentation coefficient (Batchelor, 1972). Batchelor also showed that when the number of solvent molecules is much larger than the number of colloidal particles that the connection between the gradient in chemical potential and the osmotic pressure is given by

$$n\frac{\partial \mu}{\partial n} = kT(1-\phi)\left(1+O(\phi)\right). \tag{4.11}$$

Now let us return to the Einstein's idea that osmotic pressure gradients drive diffusion. We know that for a dilute dispersion, $\Pi = nkT(1+4\phi)$, and so $\partial\Pi/\partial n = kT(1+8\phi) \approx kT$. The general expression (4.6) for the diffusivity is $\boldsymbol{D} = kT\boldsymbol{M}$, and so we may write $n\partial\mu/\partial n = \partial\Pi/\partial n$, which gives

$$\boldsymbol{D} = \boldsymbol{M}\frac{\partial \Pi}{\partial n}, \tag{4.12}$$

which corresponds to Einstein's original argument that osmotic pressure gradients drive diffusive flux. Recall that Π is the negative of one-third the trace of the stress tensor, $\boldsymbol{\Sigma}$. This prompts us

to propose a more general form of (4.12):

$$\boldsymbol{D} = -\boldsymbol{M} \cdot \frac{\partial \boldsymbol{\Sigma}}{\partial n}. \tag{4.13}$$

Here, the stress tensor $\boldsymbol{\Sigma}$ describes the stress in the particle phase, a natural outcome of the fact that the osmotic pressure is the particle contribution to suspension pressure. Equation 4.13 implies that stress gradients drive collective diffusion. Rearranging, we have

$$\frac{\partial \boldsymbol{\Sigma}}{\partial n} = -\boldsymbol{M}^{-1} \cdot \boldsymbol{D},$$

assuming the existence of $\boldsymbol{M}^{-1}$. However, it is possible that number density gradients orthogonal to ∇n are associated with number-density variation in chemical potential in (4.8). Such gradients make no contribution to the flux in the direction of ∇n, but may make a contribution to the osmotic pressure. A more general form of (4.13) would then include an isotropic tensor, $\boldsymbol{P}$ say:

$$\boldsymbol{D} = -\boldsymbol{M} \cdot \left(\frac{\partial \boldsymbol{\Sigma}}{\partial n} + \frac{\partial \boldsymbol{P}}{\partial n} \right). \tag{4.14}$$

If we also include the contribution to the osmotic pressure

$$\frac{\partial \boldsymbol{\Sigma}}{\partial n} = -\boldsymbol{M}^{-1} \cdot \boldsymbol{D} - \frac{\partial \boldsymbol{P}}{\partial n}. \tag{4.15}$$

This inspires us to ask whether this macroscopic approach can be shown to be valid for non-equilibrium suspensions in general. In order to test this idea, the simplest approach is to apply our result (4.13) directly to a specific non-equilibrium case: nonlinear microrheology.

4.4 Stress-induced diffusion in nonlinear microrheology

In §4.3 we asserted a simple relationship between stress gradients and diffusion in an equilibrium suspension, equation 4.12. In this section a test case is studied: active nonlinear microrheology, as

outlined in the model system described in chapters 2 and 3, in which a probe of size a is driven by an external force $\boldsymbol{F}^{ext}$ through an otherwise quiescent suspension of bath particles of size b. We consider a dilute bath, $\phi_b = 4\pi b^3 n_b/3 \ll 1$ in which the volume fraction of probes is comparatively small ($\phi_a \ll \phi_a$). As discussed in chapter 2, a weak gradient in probes, ∇n_a, allows the macroscopic analysis of their fluctuations. The proposed non-equilibrium stress-diffusion equation is

$$\frac{\partial \boldsymbol{\Sigma}}{\partial n_a} = -\boldsymbol{R} \cdot \boldsymbol{D}^{micro}, \tag{4.16}$$

where $\boldsymbol{R} = \boldsymbol{M}^{-1}$ is the hydrodynamic resistance tensor and $\boldsymbol{D}^{micro}$ is the probe microdiffusivity (cf chapter 3 and Zia & Brady (2010)). For hard spherical probes of size a, the resistance tensor coupling force to translation in the absence of hydrodynamic interactions is is given by $\boldsymbol{R} = 6\pi\eta a \boldsymbol{I}$. Straightforward integration of (4.16) then gives the probe-phase stress:

$$\frac{\boldsymbol{\Sigma}}{n_a kT} = -\boldsymbol{D}^{micro}. \tag{4.17}$$

To evaluate the validity of the expression (4.17), the left-hand side, $\boldsymbol{\Sigma}/n_a kT$, is computed via the Smoluchowski equation and (4.2); it is found to be in excellent agreement with measurements obtained by Brownian dynamics simulation as shown in §4.7. It is compared to the right-hand side, $\boldsymbol{D}^{micro}$ (cf chapter 3.) Both the left- and right-hand sides of (4.17) are plotted in figures 4.1 and 4.2, where the diagonal elements of each tensor are shown. The agreement between the two approaches is fair; while qualitative agreement is good over the entire range of forcing, the results disagree quantitatively. At high Pe the right-hand side under-predicts the diffusive flux driven by stress gradients, and over-predicts it at small Pe in the longitudinal direction. The quantitative under-prediction at high Pe does not seem too severe, but at small Pe, the prediction of anisotropic diffusive flux does not match the behavior of the stress tensor, which is nearly isotropic at $Pe \ll 1$, while $\boldsymbol{D}^{micro}$ is $\sim O(Pe^2)$ and anisotropic. Evidently the flux produced by stress gradients is not fully accounted for by the expression (4.16). One could be content here with the strong qualitative agreement; but the missing flux may contain important information.

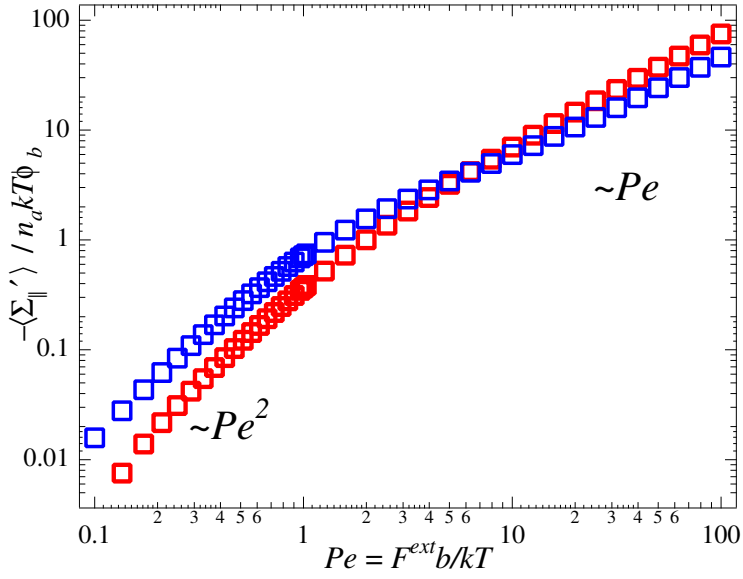

Figure 4.1: Longitudinal normal stress Σ_{zz} normalized by $n_a kT$ and volume fraction ϕ_b (cf figure 2.2). Red open squares represent the micromechanically derived stress, the left-hand side of (4.17); blue open squares represent the right-hand side of (4.17).

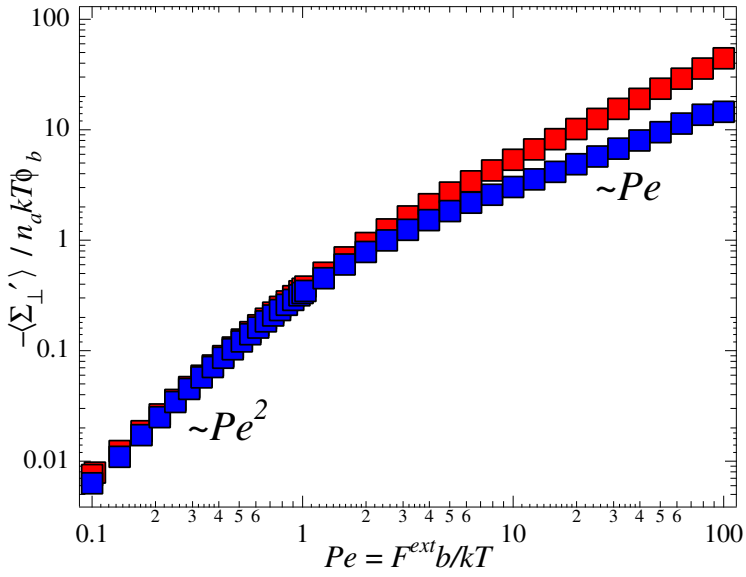

Figure 4.2: Transverse normal stress $\Sigma_{xx} = \Sigma_{yy}$, normalized by $n_a kT$ and volume fraction ϕ_b (cf figure 2.2). Red filled squares represent the micromechanically derived stress, the left-hand side of (4.17); blue filled squares represent the right-hand side of (4.17).

Equation (4.17), which can be viewed as a constitutive relation for particle-phase stress, offers some insight into what might have been missed. Constitutive expressions for the stress typically contain both normal stress (*e.g.* dynamic pressure, Reynolds stress) as well as deviatoric (viscous) stress associated with flow. For example, simple shearing of a dilute suspension gives a constitutive

expression for the stress that includes hydrostatic fluid pressure, osmotic pressure, and importantly, deviatoric terms characterized by viscous stresses. It is natural to expect an analogous deviatoric/viscous term to appear in the case of a microrheological flow as well. While expression (4.17) contains a pressure term—diffusive stress—it does not contain a deviatoric term—viscous stress.

In simply applying the expression derived for an *equilibrium* system, no explicit accounting was taken for the effects of flow. The mismatch of actual and predicted diffusive flux may be due to a flow-induced (*i.e.* deviatoric) flux. In the case of a shear flow, deviatoric stresses are viscous stresses, and act in shear (off-diagonal elements in the stress tensor). But in extensional and microrheological flows, viscous flow stresses are normal. In light of these contributions, perhaps the proper perspective is that stress gradients drive particle *migration*—which may include both diffusive and advective particle flux. With this in mind, we revisit the analysis which led to the stress-diffusion relation (4.16) that in turn led to (4.17).

4.5 Stress-induced migration

While the gradient-driven diffusion predicted by the simple approach of extending the equilibrium stress-diffusion relation (4.16) is qualitatively correct, it under-predicts diffusion at high Pe and over-predicts it at low Pe. Evidently, stress gradients in flowing suspensions produce additional flux of a type not accounted for in (4.16). A brief phenomenological analysis of (4.16) as a constitutive relation hints that stress gradients may drive not just diffusive flux, but viscous (advective) flux as well. Here we examine the assumptions made in arriving at (4.16), and in so doing, attempt to discover whether other forms of particle flux are indeed relevant.

The development used to arrive at (4.16) was based on an assumption of equilibrium—the motion of particles was governed by an equation of *state*. However, for non-equilibrium systems, an equation of *motion* describes the appropriate conserved quantity: momentum. Let us directly examine the stress state in the particles, by thinking about a momentum balance on the particle phase.

Momentum analysis

We propose a simple momentum balance of the form of Cauchy's equation of motion,

$$\rho \frac{D\boldsymbol{U}}{Dt} = \nabla \cdot \boldsymbol{\sigma} + \boldsymbol{f}^{ext}, \tag{4.18}$$

where ρ is the density, D/Dt is the material derivative, $\boldsymbol{U}$ is the velocity, $\boldsymbol{\sigma}$ is the stress tensor, and $\boldsymbol{f}^{ext}$ is any externally applied body force applied point-wise in the medium. The importance of fluid inertia relative to the viscous forces is characterized by the Reynolds number, $Re = \rho U a/\eta$, where U is the characteristic velocity of the moving probe, and for micron-sized probes $Re \ll 1$ so that the fluid mechanics are governed by Stokes flow and the left-hand side of (4.18) can be neglected. If we consider only the stress in the particle phase, $\boldsymbol{\Sigma}$, an interactive force between the particles and the embedding material appears as an additional body force $\boldsymbol{f}^{int}$. The momentum balance becomes

$$\nabla \cdot \boldsymbol{\Sigma} = -\boldsymbol{f}^{ext} - \boldsymbol{f}^{int}, \tag{4.19}$$

in a frame of reference relative to the fluid. For a suspension at infinite dilution, we may model the stress and the interactive force constitutively as $\boldsymbol{\Sigma} = -nkT\boldsymbol{I}$ and $\boldsymbol{f}^{int} = -6\pi\eta\, a\, n\boldsymbol{U}$, respectively. In the absence of density gradients, the left-hand side of (4.19) is zero and the balance becomes

$$\boldsymbol{f}^{ext} = -6\pi\eta\, a\, n\boldsymbol{U}, \tag{4.20}$$

recovering Stokes' drag on a spherical particle. Alternatively, we may consider a dilute suspension in which a density gradient of particles is present; in the absence of any external force, we have

$$\begin{aligned} \nabla \cdot \boldsymbol{\Sigma} &= -\boldsymbol{f}^{int} && (4.21)\\ &= n\boldsymbol{R} \cdot \boldsymbol{U}^{int} && (4.22)\\ &= \boldsymbol{R} \cdot \boldsymbol{j}^{int}, && (4.23) \end{aligned}$$

where $\boldsymbol{R} = \boldsymbol{M}^{-1}$ is the hydrodynamic resistance of the particles. The probability flux of particles is given by $\boldsymbol{j} = n\,\boldsymbol{U}$; taking a Fickian perspective, we may write the flux constitutively as $\boldsymbol{j} = -\boldsymbol{D}\cdot\nabla n$. Since $\nabla\cdot\boldsymbol{\Sigma} = -kT\nabla n$, we have

$$\boldsymbol{D} = \frac{kT}{6\pi\eta\, a}, \tag{4.24}$$

recovering Einstein's result for infinitely dilute suspensions.

The next step is to determine if the momentum balance approach recovers known behavior for concentrated suspensions. To this end, we consider now a suspension of colloids of arbitrary volume fraction ϕ, in which a concentration gradient of particles ∇n is present, but there is no externally applied force. The momentum balance on the particles proposed above gives $\nabla\cdot\boldsymbol{\Sigma} = -\boldsymbol{f}^{int} = \boldsymbol{R}\cdot\boldsymbol{j}$. Again assuming a Fickian model for the flux, and applying the chain rule to the derivative, we obtain

$$\boldsymbol{D} = -\boldsymbol{M}\cdot\frac{\partial\boldsymbol{\Sigma}}{\partial n}. \tag{4.25}$$

Batchelor determined the collective diffusion tensor in such systems in terms of the collective mobility $\boldsymbol{M}$ and the gradient in the chemical potential μ (1976):

$$\boldsymbol{D} = \boldsymbol{M}\frac{n}{1-\phi}\frac{\partial\mu}{\partial n}, \tag{4.26}$$

where the factor $1/(1-\phi)$ arises due to a transfer from the fluid reference frame to a zero volume-flux reference frame. Thus we have

$$\frac{\partial\boldsymbol{\Sigma}}{\partial n} = -\frac{n}{1-\phi}\frac{\partial\mu}{\partial n} = -\frac{1}{1-\phi}\frac{\partial\Pi}{\partial n}\boldsymbol{I}. \tag{4.27}$$

Shifting back to the fluid frame of reference obtains $\partial\boldsymbol{\Sigma}/\partial n = -\partial\Pi/\partial n\boldsymbol{I}$, indicating that the momentum balance recovers the known collective diffusivity. Now the question becomes, can our momentum-balance approach be applied for general non-equilibrium suspensions?

Momentum balance approach for constant-velocity nonlinear microrheology

The results above indicate that a momentum balance on particles in a suspension can recover several key results: single-particle diffusion, Stokes' drag on a single particle, and collective diffusion in concentrated suspensions. Here we shall apply our momentum analysis to a basic non-equilibrium problem of interest: Constant-velocity nonlinear microrheology.

In active, nonlinear microrheology, a Brownian probe is driven by an externally applied force through a dispersion of neutrally buoyant force- and torque-free colloidal particles (cf chapter 2). As the probe particle moves through the suspension it must push neighboring particles out of its way; a buildup of background particle concentration forms in front of the advancing probe and a deficit or wake trails it. The bath particles undergo Brownian diffusion due to thermal fluctuations of the solvent, which acts to restore the deformed microstructure to an equilibrium configuration. The character of the external driving force may be a constant imposed velocity, a constant applied force, or a combination of the two modes. In the first mode, external forcing is applied such that the velocity of the probe remains constant—*e.g.* the probe may be held by laser tweezers in a very stiff optical trap (Meyer *et al.*, 2005), as the dispersion is translated past it at constant speed. Because the probe's velocity is constrained to be constant, it does not undergo Brownian diffusion, nor does it experience force-induced diffusion due to collisions with the background bath particles. The proper Péclet number defining the flow is then $Pe = U\,a/D_b$, where D_b is the diffusivity of the bath particles. In our macroscopic model for connecting probe self-diffusivity to gradients in probe-particle number density (cf chapter 2), this mode is equivalent to selecting the A particles such that $\nabla n_a = 0$. We have for the momentum balance:

$$\boldsymbol{f}^{ext} = -\boldsymbol{f}^{int}, \tag{4.28}$$

As discussed in earlier chapters, in nonlinear microrheology, the effective viscosity η_{eff} is defined (cf chapter 2) according to the relation $(\boldsymbol{f}^{ext}/6\pi\eta a) = (\eta_{eff}/\eta)\langle \boldsymbol{U}\rangle$, where $\langle \boldsymbol{U}\rangle$ is the reduced probe velocity due to structural drag, and η^{eff} is the effective viscosity of the suspension—solvent and

particles. Insertion into (4.28) gives

$$\boldsymbol{f}^{int} = -6\pi\eta a \frac{\eta_U^{eff}}{\eta}\langle \boldsymbol{U}\rangle. \tag{4.29}$$

where the effective viscosity for a dilute bath is η_U^{eff}/η (cf chapter 3). Evidently, *the interactive force can be advective in nature*, and here is due to the viscous drag of the solvent plus particles. The coefficient of the velocity on the right-hand side of (4.29) is nothing more than the effective hydrodynamic drag due to advection on a constant-velocity probe:

$$\boldsymbol{R}_{adv,U} \equiv 6\pi\eta\, a \frac{\eta_U^{eff}}{\eta}\boldsymbol{I}. \tag{4.30}$$

Here, we have used the subscript U to indicate constant-velocity mode. Without fluctuations in probe motion, probe-number density gradients do not arise, and the flux of the probe is simply its mean motion relative to the fluid, which is a combination of solvent drag and microstructural drag. But what if fluctuations in probe motion are allowed?

Momentum balance approach for constant-force nonlinear microrheology

In chapter 3, the model for constant force nonlinear microrheology was developed. In contrast to the constant-velocity mode of probe forcing (discussed above), here the probe can fluctuate and diffuse as it moves through the bath. Such fluctuations are modeled macroscopically by allowing a gradient in the probe phase, ∇n_a. The momentum balance (4.19) now becomes

$$\nabla\cdot\boldsymbol{\Sigma} = -\boldsymbol{R}\cdot\frac{\eta_F^{eff}}{\eta}\langle\boldsymbol{U}\rangle - \boldsymbol{f}^{int}, \tag{4.31}$$

where the equivalence of the drag to the external force has been inserted, $\boldsymbol{f}^{ext}/6\pi\eta a = (\eta_F^{eff}/\eta)\langle\boldsymbol{U}\rangle$ and the subscript F denotes constant external force mode. The task at hand now is to model the interactive force in the constant-force case. The previous cases considered thus far—equilibrium and collective diffusion, and the constant-velocity external force case—we expect that $\boldsymbol{f}^{int}$ will have

both diffusive and advective contributions (or more fundamentally, they are associated with fluctuation and dissipation.) In the current system, we must allow for both fluctuational and dissipative interactive forces, *e.g.* diffusive and viscous (advective):

$$\boldsymbol{f}^{int} = \boldsymbol{f}_{adv} + \boldsymbol{f}_{diff}. \tag{4.32}$$

The advective contribution is considered first. The difference between constant-velocity and constant-force microrheology must be accounted for in the momentum balance. Physically, this difference can be understood in the following way: When the probe is constrained to move at a constant velocity through the suspension, it must plow bath particles out of its way without any change in its speed. In the constant-force mode, where the probe's velocity can fluctuate, the resistance to probe motion by the bath is not as great, because the probe can adjust its speed when encountering regions of relatively higher or lower volume fraction, and move around them. A reduction in the viscous drag results from the probe's ability to fluctuate, which results in a change in the hydrodynamic mobility of the probe. The interactive force in the constant-velocity and constant-force cases then differ by this fluctuating contribution which we shall denote as $\boldsymbol{f}_{adv,U'}$. We may compare the difference in general form as follows:

$$\boldsymbol{f}_{adv} = \begin{cases} \boldsymbol{f}_{adv,U}, & U^{ext} = \text{const.}, \\ \boldsymbol{f}_{adv,U} + \boldsymbol{f}_{adv,U'}, & F^{ext} = \text{const.} \end{cases} \tag{4.33}$$

The constitutive forms for the steady and fluctuating terms in (4.33) can be understood from the perspective of a mobility versus resistance formulation of the constant constant-force versus constant-velocity modes. In Stokes' flow hydrodynamics the relations $\boldsymbol{F} = \boldsymbol{R} \cdot \boldsymbol{U}$ and $\boldsymbol{U} = \boldsymbol{M} \cdot \boldsymbol{F}$ reflect the fact that when the imposed velocity is given and the resultant force is sought the problem is a "resistance problem," whereas when a force is imposed and the resultant velocity sought, the problem is a "mobility problem." Solving the latter for the force gives the interactive force in terms of the resultant velocity: $\boldsymbol{f}_{adv} = n_a \boldsymbol{M}_{adv}^{-1} \langle \boldsymbol{U} \rangle$. Here, the resistance $\boldsymbol{M}_{adv}^{-1}$ comprises the

steady contribution $\boldsymbol{R}_{adv,U}$ and a fluctuating contribution which we shall denote $\boldsymbol{R}'_{adv}$. Inserting the equality $\boldsymbol{M}^{-1}_{adv} = \boldsymbol{R}_{adv,U} - \boldsymbol{R}'_{adv}$ into the advective interactive force obtains

$$\boldsymbol{f}_{adv} = -n_a \left(\boldsymbol{R}_{adv,U} - \boldsymbol{R}'_{adv}\right) \cdot \langle \boldsymbol{U} \rangle \qquad (F^{ext} = \text{const}). \tag{4.34}$$

The minus sign indicates that the drag is reduced. The advective portion of the interactive force may then be written as $\boldsymbol{f}^{int,adv} = n_a(\boldsymbol{R}_{adv,U} - \boldsymbol{R}'_{adv}) \cdot \langle \boldsymbol{U} \rangle$. Following the result of (4.30) obtains

$$\boldsymbol{f}^{int}_{adv} = -n_a(\boldsymbol{R}\frac{\eta^{eff}_U}{\eta} - \boldsymbol{R}'_{adv}) \cdot \langle \boldsymbol{U} \rangle, \tag{4.35}$$

where $\boldsymbol{R}$ is the drag on an isolated probe, $\boldsymbol{R} = 6\pi\eta\, a\boldsymbol{I}$. Here we have been careful to note that

$$\frac{\eta^{eff}_F}{\eta} \neq \frac{\eta^{eff}_U}{\eta}, \tag{4.36}$$

a point which is discussed in detail in chapter 5.

The diffusive contribution is considered next: Diffusive flux away from equilibrium will correspond to both the equilibrium diffusivity plus the force-induced diffusion, or microdiffusivity. The simplest approach is then to constitutively model the diffusive forces as was done in the previous sections, as $\boldsymbol{f}^{int,diff} = \boldsymbol{R} \cdot \boldsymbol{D}^{eq} \cdot \nabla n_a + \boldsymbol{R} \cdot \boldsymbol{D}^{micro} \cdot \nabla n_a$. Now, we recall from earlier discussions of equilibrium suspensions that particle fluctuations in suspensions are associated with an isotropic osmotic pressure. Is there an similar isotropic non-equilbrium contribution? Should the pressure not increase as particle fluctuations become stronger? But the diffusion tensor in microrheology is anisotropic; should an isotropic "pressure" term, $\boldsymbol{f}^p$, be included? We propose that this is so, and revisit it in detail below. Then the diffusive interactive force is modeled as

$$\boldsymbol{f}^{int,diff} = \boldsymbol{R} \cdot \boldsymbol{D}^{eq} \cdot \nabla n_a + \boldsymbol{R} \cdot \boldsymbol{D}^{micro} \cdot \nabla n_a + \boldsymbol{f}^p. \tag{4.37}$$

Inserting the advective interactive force (4.35) and the diffusive interactive force (4.37) into the

momentum balance (4.31) then gives

$$\nabla \cdot \boldsymbol{\Sigma} = n_a \boldsymbol{R} \cdot \langle \boldsymbol{U} \rangle \left(\frac{\eta_U^{eff}}{\eta} - \frac{\eta_F^{eff}}{\eta} \right) - n_a \boldsymbol{R}' \cdot \langle \boldsymbol{U} \rangle - \boldsymbol{R} \cdot \left[\boldsymbol{D}^{eq} + \boldsymbol{D}^{micro} \right] \cdot \nabla n_a + \boldsymbol{f}^p. \qquad (4.38)$$

where the first term in (4.35) was obtained in (4.30). We now address the proposed non-equilibrium, isotropic "pressure" term, $\boldsymbol{f}^p$. As noted above, thermal fluctuations of particles in a suspension can be viewed in analogy to gas particles that collide with the walls that enclose them. Their kinetic energy, which in the case of spheres is also their thermal energy, determines the pressure of these collisions. The osmotic pressure of particles in a solvent also exert a pressure on fictitious walls that enclose them; their thermal energy kT determines how vigorously they fluctuate, and hence the osmotic pressure goes up and down with increasing or decreasing temperature. But what can be said about the "effective temperature" when the particles are agitated by non-thermal forces? The fluctuation that drives agitation of the probe is the force-induced diffusion, $\boldsymbol{D}^{micro}$; we propose that it contributes an isotropic pressure to the suspension, and the corresponding force points in the direction of the gradient: $\boldsymbol{f}^p = -tr[\boldsymbol{D}^{eff}/3]\boldsymbol{I} \cdot \nabla n_a$, where the effective diffusivity is the equilibrium and force-induced values, $\boldsymbol{D}^{eff} = \boldsymbol{D}^{micro} + \boldsymbol{D}^{eq}$. Inserting this into the momentum balance obtains:

$$\nabla \cdot \boldsymbol{\Sigma} = n_a \boldsymbol{R} \cdot \langle \boldsymbol{U} \rangle \left(\frac{\eta_U^{eff}}{\eta} - \frac{\eta_F^{eff}}{\eta} \right) - n_a \boldsymbol{R}' \cdot \langle \boldsymbol{U} \rangle - \boldsymbol{R} \cdot \left[\boldsymbol{D}^{eq} + \boldsymbol{D}^{micro} \right] \cdot \nabla n_a - \frac{1}{3} tr[\boldsymbol{D}^{eff}] \boldsymbol{I} \cdot \nabla n_a. \quad (4.39)$$

In the limit of a dilute suspension the effective viscosity is given as the sum of the solvent viscosity plus an $O(\phi_b)$ correction due to the drag of the bath particles, $\eta^{micro}\phi_b$ which is made dimensionless with the solvent viscosity η. Squires & Brady (2005) and Khair & Brady (2006) defined this via Stokes' drag law in terms of the average interparticle contribution to the velocity (cf chapter 2). Squires & Brady also noted that the microviscosity in the constant-velocity case is twice that of the constant-force case, $\eta_U^{micro} = 2\eta_F^{micro}$. In the dilute limit, our momentum balance then becomes

$$\nabla \cdot \boldsymbol{\Sigma} = n_a \frac{\eta_F^{micro}}{\eta} \phi_b \boldsymbol{R} \cdot \langle \boldsymbol{U} \rangle - n_a \boldsymbol{R}' \cdot \langle \boldsymbol{U} \rangle - \boldsymbol{R} \cdot \left[\boldsymbol{D}^{eq} + \boldsymbol{D}^{micro} \right] - \frac{1}{3} tr[\boldsymbol{D}^{eff}] \boldsymbol{I} \cdot \nabla n_a. \qquad (4.40)$$

Applying the chain rule gives

$$\left[\frac{\partial \boldsymbol{\Sigma}}{\partial n_a} = \frac{n_a Pe\, D_a}{b}\left(\frac{\eta_F^{micro}}{\eta}\phi_b \boldsymbol{R} - \boldsymbol{R}'\right)\cdot \hat{\boldsymbol{u}}\boldsymbol{v} - \boldsymbol{R}\cdot\left[\boldsymbol{D}^{eq} + \boldsymbol{D}^{micro}\right] - \frac{1}{3}tr[\boldsymbol{D}^{eff}]\boldsymbol{I}\right]\cdot \nabla n_a. \quad (4.41)$$

where $\hat{\boldsymbol{u}}$ is a unit vector in the direction of probe forcing and $\boldsymbol{v} \equiv \nabla n_a/(\nabla n_a \cdot \nabla n_a)$ is the component of the advective flux term in the direction of the density gradient, and scales as $1/|\nabla n_a|$. The steepness of this gradient can be approximated by a Fickian scaling, where $\boldsymbol{j}$ is the particle flux:

$$\begin{aligned} \nabla n_a &\sim \frac{j}{D(Pe)} \\ &\sim \frac{n_a U}{D(Pe)} \\ &\sim \frac{n_a Pe\, D_a}{D(Pe) b}, \end{aligned} \quad (4.42)$$

where $D(Pe)$ is the coefficient of the force-induced diffusion and corresponds to $\boldsymbol{D}^{micro}/\phi_b$. Inserting this scaling into the momentum balance obtains

$$\frac{\partial \boldsymbol{\Sigma}}{\partial n_a} = kT\frac{\boldsymbol{D}^{micro}}{D_a}\cdot\left(\frac{\eta_F^{micro}}{\eta}\boldsymbol{I} - \frac{\boldsymbol{R}'}{6\pi\eta\, a\, \phi_b}\right) - \boldsymbol{R}\cdot\left[\boldsymbol{D}^{eq} + \boldsymbol{D}^{micro}\right] - \frac{1}{3}tr[\boldsymbol{D}^{eff}]\boldsymbol{I}. \quad (4.43)$$

Finally, we wish to determine the reduced microstructural drag $\boldsymbol{R}'$ effected by probe fluctuations. As $Pe \to \infty$, the total drag of the microstructure is $O(1)$, which gives the estimate that in the limit of a dilute bath, $\boldsymbol{R}'/6\pi\eta\, a \sim \phi$. Inserting this into the momentum balance gives

$$\frac{\partial \boldsymbol{\Sigma}}{\partial n_a} = kT\frac{\boldsymbol{D}^{micro}}{D_a}\left(\frac{\eta_F^{micro}}{\eta} - 1\right) - \boldsymbol{R}\cdot\left[\boldsymbol{D}^{eq} + \boldsymbol{D}^{micro}\right] - \frac{1}{3}tr[\boldsymbol{D}^{eff}]\boldsymbol{I}. \quad (4.44)$$

Since the non-equilibrium, gradient-driven flux is of interest, let us subtract off the equilibrium stress, which gives the non-equilibrium stress gradient $\boldsymbol{\Sigma}'$. A rearrangement of terms then gives

$$\frac{\partial \boldsymbol{\Sigma}'}{\partial n_a} = -\boldsymbol{R}\cdot\boldsymbol{D}^{micro} + kT\frac{\boldsymbol{D}^{micro}}{D_a}\left(\eta_F^{micro} - 1\right) - kT\frac{tr(\boldsymbol{D}^{micro})}{3D_a}\boldsymbol{I}. \quad (4.45)$$

The presence of stress gradients drives fluctuations that have a direct effect and an indirect effect. The direct effects are the the force-induced diffusion, the first term in (4.45), and the pressure increase in the third term. The indirect effect is the "softening" of the suspension—the negative contribution in the second term. Because it reduces viscous drag, the suspension can be viewed as softer. (But an alternate view can consider that less viscous dissipation means more elastic response; whether the entropic spring is stiffer or not is a different question, to be addressed in chapter 5.)

Evidently, number-density gradients in the stress drive diffusive flux, advective flux, and an increase in isotropic particle pressure. Integration of (4.45) with respect to number density of probes gives

$$\frac{\boldsymbol{\Sigma}'}{n_a kT} = -\frac{\boldsymbol{D}^{micro}}{D_a} + \left(\eta^{micro} - 1\right)\frac{\boldsymbol{D}^{micro}}{D_a} - \frac{tr(\boldsymbol{D}^{micro})}{3D_a}\boldsymbol{I}. \tag{4.46}$$

Here we see that the stress tensor $\boldsymbol{\Sigma}'/n_a kT$ is given by a sum of fluctuational (diffusive) terms and dissipative (viscous) terms, along with an "effective temperature" driven by the strength of the flow. As shown in chapters 2 and 3, each term on the right-hand side of (4.46) can be determined by monitoring the mean motion or the mean-square motion of a single probe particle forced through a dispersion of bath particles of volume fraction ϕ_b. [1]

The power of the simple analytical relation (4.46) is twofold: first, the ability to obtain the full stress tensor, along with the effective viscosity and the probe diffusivity, from two measurements. Secondly, and perhaps more importantly, is the fact that the stress reflects a balance between fluctuation and dissipation *away* from equilibrium. This idea will be explored further in the concluding section.

Momentum balance approach for sedimentation

We consider here a dispersion of particles of a single species, A say, subjected to an imposed gradient in their number density due to the application of an external potential Φ. This system is equivalent to the case of a single species sedimenting under the gravitational potential (Batchelor, 1972). The

[1] It should be noted here that $\boldsymbol{\Sigma}'$ represents the stress measured by collisions between the probe and bath particles. One should also ask what contribution to the stress is made by non-equilibrium interactions between the bath particles themselves. The latter contribution should scale as $O(\phi_b^2)$ which is small in the case of a dilute bath. In order to study this contribution it was measured in by Brownian dynamics simulation and is discussed in §4.8.

equation of motion for the particles is

$$\begin{aligned} \nabla \cdot \boldsymbol{\Sigma} &= \boldsymbol{f}_{int} \\ &= -\boldsymbol{R} \cdot \boldsymbol{D}^c \cdot \nabla n_a. \end{aligned} \tag{4.47}$$

Since there is no imposed flow, the particle flux is diffusive. Here, the superscript c indicates that in this macroscopic process, since only a single species is present, the only diffusive mechanism present is the collective motion of the particles. By the chain rule, $\nabla \cdot \boldsymbol{\Sigma} = \nabla n_a \partial \boldsymbol{\Sigma} / \partial n_a$; applying this to (4.47) and solving for $\boldsymbol{D}^c$ obtains

$$\boldsymbol{D}^c = \boldsymbol{M} \cdot \frac{\partial \boldsymbol{\Sigma}}{\partial n_a}. \tag{4.48}$$

Even in the absence of hydrodynamic interactions between particles, the collective sedimentation of particles drives a volume-conserving backflow of fluid. This backflow hinders particle motion (cf chapter 2); the mobility $\boldsymbol{M} = \boldsymbol{R}^{-1}$ of the particles is given by the no-hydrodynamics sedimentation coefficient (Russel & Glendinning, 1981): $\boldsymbol{M} = (1 - 5\phi_A)/(6\pi\eta a)$. Recalling from the Carnahan-Starling equation of state for a single species that $\partial \boldsymbol{\Sigma}_A / \partial n_a = -kT(1+8\phi_A)\boldsymbol{I}$ (Carnahan & Starling, 1969), and inserting this and $\boldsymbol{M}$ into (4.48) gives

$$\boldsymbol{D}^c = \boldsymbol{D}_a(1 + 3\phi_A). \tag{4.49}$$

Equation 4.49 gives the (new) result for the effective diffusion coefficient for sedimenting colloids in the absence of hydrodynamic interactions. Evidently a suspension sediments more quickly when the particles do not interact hydrodynamically (recall the corresponding with-hydro result, $\boldsymbol{D}^c = \boldsymbol{D}_a(1 + 1.45\phi_A)$.

4.6 Analytical results

The macroscopic analysis of the particle stress in a suspension was developed in the previous section, with a particular interest in the stress in nonlinear microrheology. An explicit analytical expression

was derived that predicts the stress from an analysis of particle flux driven by stress gradients. The results from this new approach are plotted and discussed below, compared to Brownian dynamics simulations in §4.7, and then compared to the stress tensor in dilute suspensions undergoing a bulk shearing motion in §4.8.

Normal stresses, normal stress differences, and the osmotic pressure

In order to test the new constitutive expression—and indeed the idea that stress gradients drive particle flux—the right-hand side of (4.46) is plotted in figures 4.3 and 4.4, along with the left-hand side computed via the Smoluchowski equation (cf §4.2). Agreement is very good; accounting for ad-

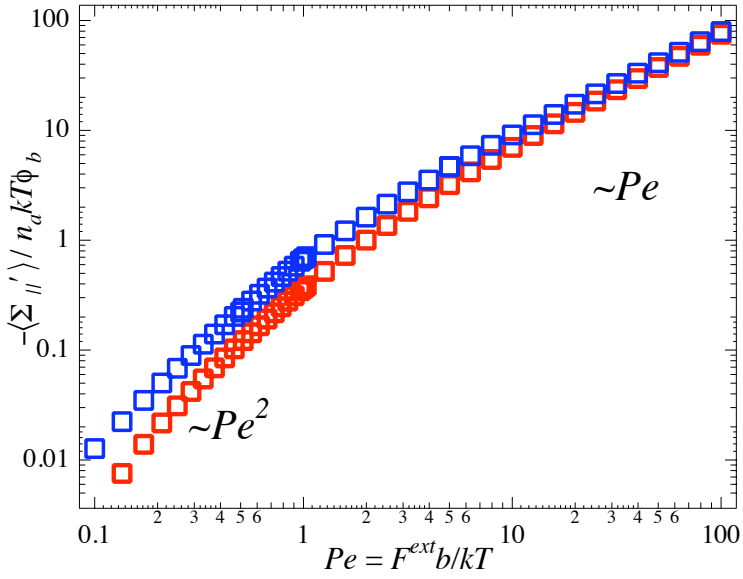

Figure 4.3: Longitudinal normal stress Σ_{zz} normalized by $n_a kT$ and volume fraction ϕ_b (cf figure 2.2). Red open squares represent the micromechanically derived stress (§4.2); blue open squares represent the right-hand side of (4.46).

vective flux in the model yields qualitative and quantitative agreement between the new macroscopic approach and the micromechanically derived stress (§4.2). The importance of the advective contribution is most easily seen by comparing figures 4.3 and 4.4, which reflect the advective contribution, to figures 4.1 and 4.2, in which it has been neglected.

For strong probe forcing, the non-equilibrium stress scales linearly in the forcing, $-\Sigma'/nkT\phi_B \sim Pe$, and is larger in the direction along the line of forcing than transverse to it—confirming the presence of normal stress differences. For weak probe forcing, the flow-induced stress scales quadratically

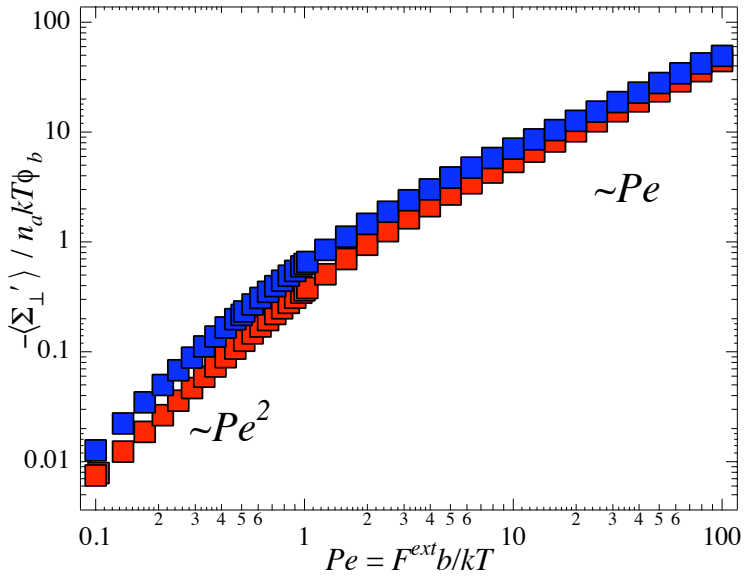

Figure 4.4: Transverse normal stress $\Sigma_{xx} = \Sigma_{yy}$ normalized by $n_a kT$ and volume fraction ϕ_b (cf figure 2.2). Red filled squares represent the micromechanically derived stress (§4.2); blue filled squares represent the right-hand side of (4.46).

in the forcing, $-\Sigma'/nkT\phi_B \sim Pe^2$.

Normal stress differences are important in the context of single-particle forcing in many physical systems; they may cause soft particles, *e.g.* sub-cellular organelles, to elongate—or even rupture. We recall that the normal stress differences are defined by

$$N_1 \equiv \Sigma_{zz} - \Sigma_{yy} \tag{4.50}$$

$$N_2 \equiv \Sigma_{yy} - \Sigma_{xx}, \tag{4.51}$$

where z is the direction of probe forcing, and x and y are the two orthogonal axes. According to (4.46), the first normal stress difference is

$$\frac{N_1}{n_a kT\phi_b} = -\frac{D_\parallel^{micro} - D_\perp^{micro}}{D_a\phi_b} + \frac{D_\parallel^{micro} - D_\perp^{micro}}{D_a\phi_b}(\eta^{micro} - 1) \tag{4.52}$$

and the second normal stress difference is zero:

$$\frac{N_2}{n_a kT\phi_b} = 0. \tag{4.53}$$

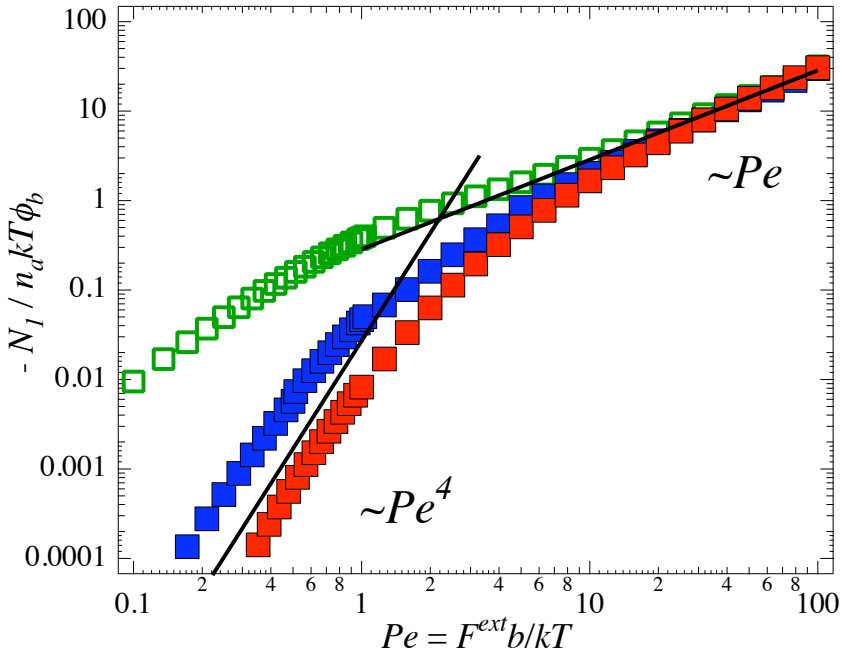

Figure 4.5: First normal stress difference N_1 for a dilute dispersion of hard-sphere colloids normalized by $n_a kT$ and volume fraction ϕ_b. Filled red squares represent the micromechanically derived stress (§4.2); filled blue squares represent the right-hand side of (4.52). For comparison, the open green symbols represent the initial theory (the right-hand side of (4.17).)

Figure (4.5) shows a comparison of the right-hand side of (4.52) compared to the left-hand side, again computed via the micromechanically derived stress (§4.2. For comparison, the original simple theory (the right-hand side of (4.17)) is shown in green in the same plot. Agreement is much improved. For strong forcing, N_1 scales linearly in the forcing Pe. For weak forcing, $Pe \ll 1$, Brownian motion easily restores isotropy to the microstructure around the probe, and N_1 vanishes as Pe^4 as $Pe \to 0$. Due to the axisymmetric structure around the probe, the second normal stress difference is zero for all Pe.

While normal stress differences indicate how a soft object might elongate, the osmotic pressure indicates how a compressible object might shrink or expand. The osmotic pressure is the trace of the stress tensor; the corresponding non-equilibrium contribution is $\Pi'/n_a kT = -\boldsymbol{I} : \boldsymbol{\Sigma}'/3$, which gives

$$\frac{\Pi'}{n_a kT\phi_b} = \frac{D_{\parallel}^{micro} + 2D_{\perp}^{micro}}{D_a \phi_b}\left[\frac{4}{3} - \eta^{micro})\right]. \tag{4.54}$$

The osmotic pressure is plotted as a function of the imposed force in figure 4.6, alongside the

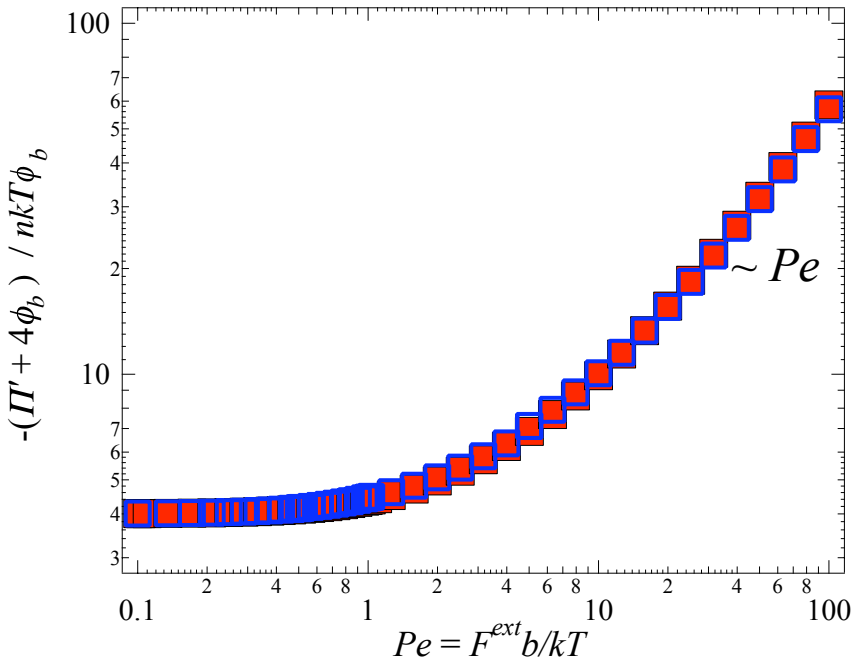

Figure 4.6: Osmotic pressure Π normalized by $n_a kT$ and volume fraction ϕ_b, for a dilute bath of hard spheres with no hydrodynamic interactions. Red filled squares represent the micromechanically derived stress (§4.2); blue open squares represent the right-hand side of (4.54).

statistical mechanics results. Agreement is excellent, and indicates an $O(Pe)$ growth in osmotic pressure at large Pe. Expression 4.54 shows that the osmotic pressure may be determined by monitoring mean and mean-square probe motion.

Expression 4.46 applies to the nonlinear microrheology of a dilute dispersion of colloids, but the arguments used to derive it are sufficiently general as to allow inclusion of other parameters that drive microstructural deformation and migration, *e.g.* electrostatic or hydrodynamic interactions. One need only determine the mean and mean-square motion of a probe in order to determine viscosity, diffusivity, and the full stress tensor.

4.7 Brownian dynamics simulation

An alternative approach to studying particle behavior in a colloidal suspension is to examine the detailed dynamics of individual particle motion. The Brownian dynamics simulation method was described in chapter 3 in §3.6. Following the same programme here, the non-equilibrium contribution

to the particle stress due to a collision is $\langle \boldsymbol{\Sigma}' \rangle = -n_a \langle \boldsymbol{r}\boldsymbol{F}^P \rangle$, where $\boldsymbol{r}$ is the distance between the probe and a bath particle and the angle brackets $\langle \cdot \rangle$ indicate an average of the value over the duration of the simulation. The hard-sphere collision particle stresslet $-\boldsymbol{r}\boldsymbol{F}^P$ was measured at each time step, and averaged over the steady-state simulation. Here, $\boldsymbol{r}$ is the collisional displacement along the line of centers of the probe and colliding bath particle. Simulations were conducted for a range of Pe and volume fraction ϕ_b, with thirty simulations per parameter combination. The average stress for each simulation was then averaged over all 30 simulations.

The first normal stress difference, $\langle N_1 \rangle = n_a \langle (r_z F_z - r_y F_y) \rangle$ is plotted in figure 4.7 as a function of Pe. At small values of the Péclet number, the measured result for N_1 is close to zero in average value. The second normal stress difference $\langle N_2 \rangle = n_a \langle (r_y F_y - r_x F_x) \rangle$, where we recall that z is the direction of constant external force, is found to vanish on average. The results agree well with the theory. The average osmotic pressure, $\langle \Pi \rangle = n_b \langle (r_x F_x + r_y F_y + r_z F_z) \rangle / 3$ is plotted in figure 4.8 , where again we find close agreement between the two theory approaches (microscopic and macroscopic), and the measurements obtained via Brownian dynamics.

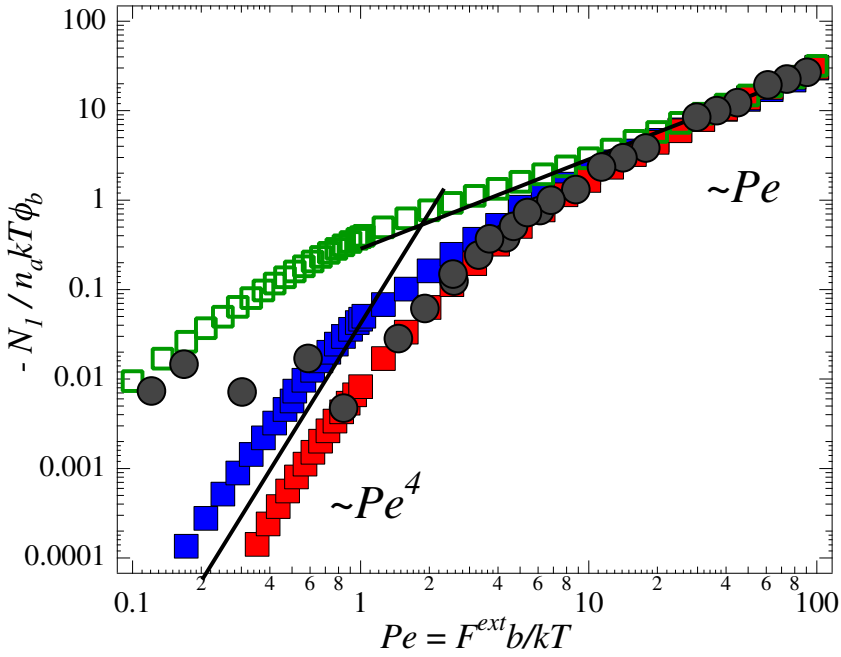

Figure 4.7: First normal stress difference, $N_1/n_a kT\phi_B$. Brownian dynamics simulation results are the black filled circles (each represents 280 simulations; error bars are on the order of marker size.) Red filled squares represent the micromechanically derived stress (§4.2); blue filled squares represent the right-hand side of (4.52). For comparison, the green open squares represent the initial theory (the right-hand side of (4.17).)

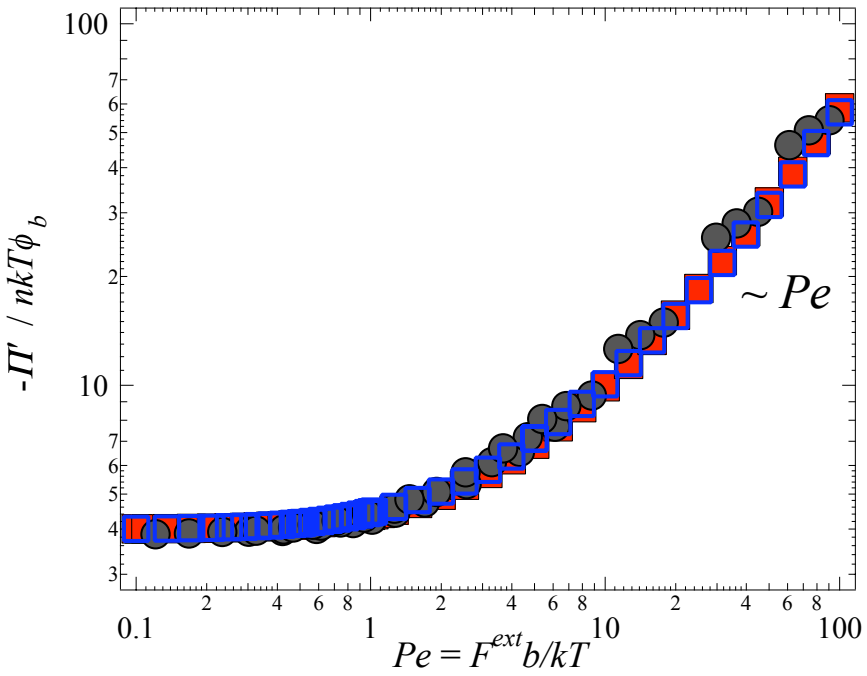

Figure 4.8: Osmotic pressure, $\Pi/n_a kT\phi_b$. Brownian dynamics simulation results are the black filled filled circles (each represents 280 simulations; error bars are on the order of marker size.) Red filled squares represent the micromechanically derived stress (§4.2); blue open squares represent the right-hand side of (4.54).

4.8 Comparison to shear macrorheology

There have been numerous previous studies of normal stresses in colloidal dispersions for bulk motion such as simple shear and extensional flows. Theoretical investigations of suspensions undergoing simple shear were conducted analytically by Brady & Vicic (1995) for small Pe, with and without hydrodynamic interactions; by Brady & Morris (1997) at large Pe for suspensions with and without hydrodynamic interactions; and numerically for dilute dispersions at arbitrary Pe, with and without hydrodynamic interactions. Brownian dynamics simulations for dilute and concentrated suspensions were conducted by Foss & Brady (2000a). The effect of hydrodynamic interactions was studied via Stokesian dynamics simulation by Foss & Brady (2000b) for a dispersion undergoing simple shear, and by Sami (1996) in the case of an extensional flow. Their findings can be summarized as follows:

1. In a study of low-Pe behavior, Brady & Vicic (1995) found that the first contribution to non-Newtonian behavior in a suspension undergoing shear in the absence of hydrodynamic interactions is found at $O(Pe^2\phi^2)$, in the both the normal stress differences and the vis-

cosity (shear-thinning). The first contributions are found as $N_1/nkT \sim Pe^2\phi^2 > 0$, and $N_2/nkT \sim Pe^2\phi^2 < 0$. A range of volume fractions was studied. They also studied the effects of hydrodynamic interactions. In comparing the limits $\lambda \to \infty$ and $\lambda \to 1$ (cf chapter 2) they were able to examine the relative contributions of interparticle forces and hydrodynamic forces to particle density around a test particle. As expected, when $\lambda \to \infty$ hydrodynamic interactions have little effect. But when $\lambda \to 1$, the relative contributions due to HI and interparticle forces to key components of the microstructure varies spatially. While far from a test particle HI play a less dominant role, near a test particle they play a dominant role. They propose that this effect is due to the balance between advection and diffusion, and not due to lubrication.

2. For the limit of very strong shear, Brady & Morris (1997) extended the study of dilute suspensions. Employing a "radial balance approximation" , they determined the shear-induced diffusion tensor, and proposed the connection that $\partial\boldsymbol{\Sigma}/\partial\phi \propto \boldsymbol{D}$ is valid away from equilibrium. They predicted that $N_1/nkT = 0$ and $N_2/nkT\phi^2 = -(16Pe/15)\pi(a_h/a)$, where a_h/a is defined in figure 2.2. In the limit of no hydrodynamics, this predicts that the second normal stress difference vanishes as well, and hence that normal stress differences do not arise at high Pe without hydrodynamic interactions between particles. As noted by Bergenholtz *et al.*, however, the proper definition of the volume fraction with the thermodynamic, rather than hydrodynamic, radius shows that this term remains.

3. Over the full range of Pe, the numerical study of Bergenholtz *et al.* (2002) investigated normal stresses with and without hydrodynamic interactions. At low Pe, their results confirmed those of Brady & Vicic (1995): Normal stress differences do indeed arise in the absence of hydrodynamic interactions, because hard-sphere repulsion allows particles to cross streamlines, giving rise to random motion and breaking the reversibility required in Stokes' flow. In contrast to the findings of Brady & Morris (1997), however, at high Pe they found that $N_1/nkT\phi^2 \sim Pe > 0$ and $N_2/nkT\phi^2 \sim Pe < 0$, with $N_2/nkT\phi^2 \to -12\pi Pe/5$ as $Pe \to \infty$. The disagreement in N_1 between the two studies is likely a result of the radial balance approximation employed by Brady & Morris (1997); evidently, angular gradients in the microstructure make an impor-

tant contribution to both the diffusion tensor and the stress tensor, even in the absence of hydrodynamic interactions. This notion is supported by our finding that the microdiffusivity is strongly dependent on angular gradients (cf chapter 3). One important feature is that when hydrodynamic interactions are present, the first normal stress difference changes sign near $Pe \sim 100$; this is because the hydrodynamic contributions to N_1 are negative for all Pe, due to the strong extensional forces required to pull particles apart against lubrication forces as particles are advected downstream from a test particle.

4. For suspensions undergoing shear, without hydrodynamic interactions, Foss & Brady (2000*a*) conducted Brownian dynamics simulations over a range of volume fraction ($0.40 < \phi < 0.55$). While the low-Pe behavior is consistent with that found by the studies discussed above, one distinguishing new feature emerged in their study: the formation of ordered "strings" of particles in high-Pe shear of Brownian suspensions. The appearance of these long-range structures bias the number of collisions in the velocity direction versus the velocity-gradient and vorticity directions, thus giving rise to strong positive increases in both N_1 and N_2 for large Pe.

5. Foss & Brady continue their simulation investigations of sheared suspensions, now considering the effect of hydrodynamic interactions, via Stokesian dynamics simulation (2000*b*). Their results are largely consistent with those of Bergenholtz *et al.* (2002).

6. Extensional viscosity was studied by Sami (1996) via Stokesian dynamics simulations for concentrated suspensions. Here, analogously to the present study, normal stresses and their differences are related to the viscosity and to microstructural asymmetry. Because the normal stress differences are linear in the extensional viscosity, his results also predict the first normal stress difference, where he finds that $N_1/nkT\phi \sim Pe$ for large Pe.

We begin our comparison between normal stresses in nonlinear microrheology versus macrorheology with the most direct comparison: the study by Bergenholtz *et al.* of the normal stresses in dilute dispersions hard spheres undergoing simple shear. Figure 4.9 shows a comparison between

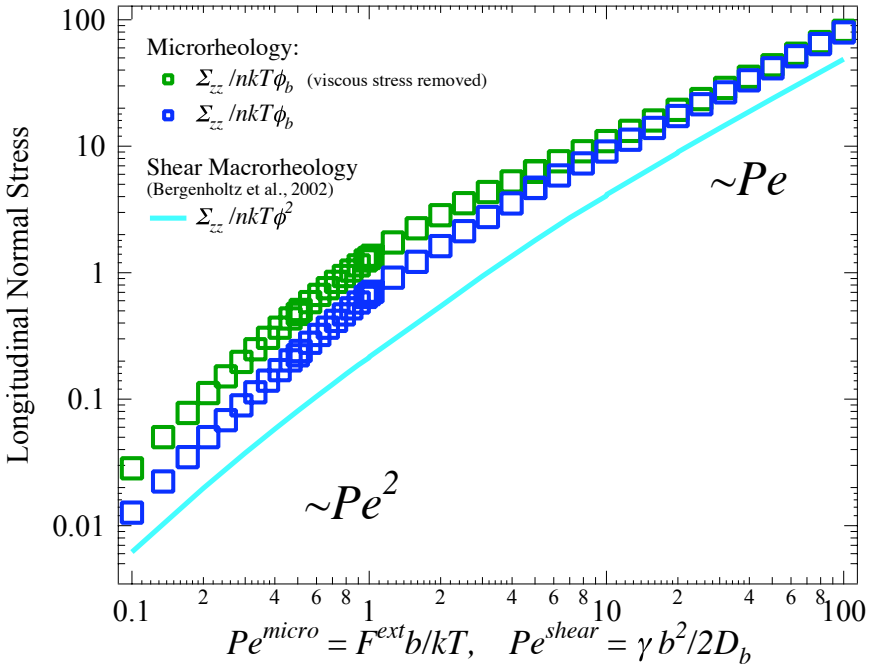

Figure 4.9: Macro versus microrheology: Normal stress on the plane normal to the flow direction. Cyan solid line by Bergenholtz *et al.* (2002) for simple shear of dilute colloidal dispersion of hard spheres. Blue open squares are for nonlinear microrheology, the right-hand side of (4.46). Green open squares are for nonlinear microrheology (equation 4.46), *where the viscous stress has been removed.*

the normal stress on the plane normal to the flow direction. Two sets of data for microrheology are shown: blue open squares reflect the full equation 4.46; green open squares have the viscous contribution to the normal stress removed. Comparison between macro and micro with the full micro-stress tensor reveal strong agreement at large Pe, but different scaling in Pe at low Pe. The fundamental difference between the stress tensor components in macro versus micro is that in macro, all viscous stresses are in the off-diagonal components, whereas in micro, viscous stresses are normal. One can take the approach here that to make a "like" comparison, the viscous stress should be included in both, or in neither. To this end, the viscous contribution is removed from the microrheology stress, as shown by the green squares. Comparing these to the macro results indicates the same scaling in Pe over the full range of Pe. There is still quantitative disagreement at small Pe.

Next, we make a comparison between the normal stresses on the plane transverse to the flow, as shown in figure 4.10. The first major difference between micro and macro is, of course, the difference in symmetry properties between the two flows. In the case of microrheology, the structure around

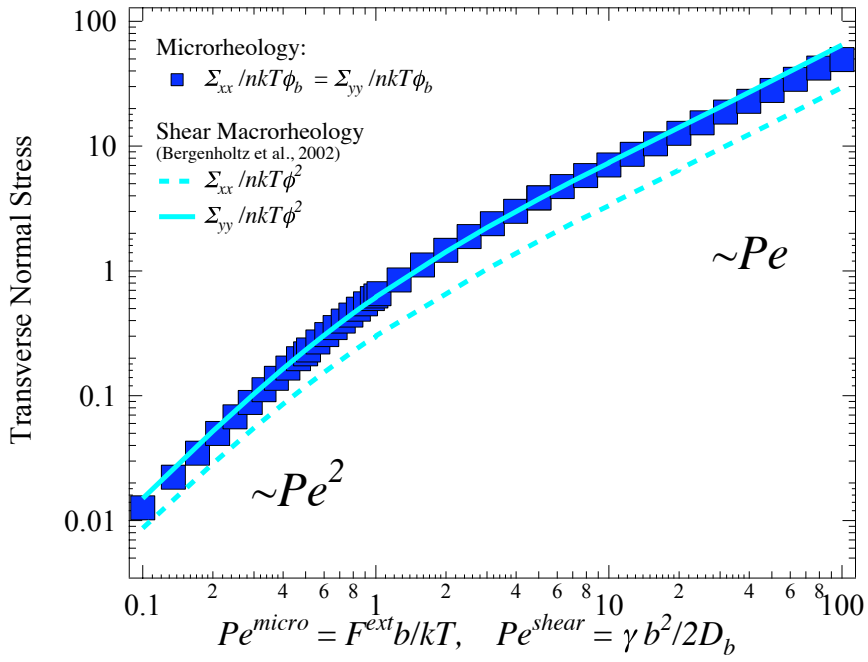

Figure 4.10: Macro versus microrheology: Normal stress on the plane transverse to the flow direction. Cyan lines are numerical results by Bergenholtz *et al.* (2002) for simple shear of dilute colloidal dispersion of hard spheres (solid line: velocity-gradient direction; broken line: vorticity direction). Blue filled squares are for nonlinear microrheology (equation 4.46).

the probe is axisymmetric, and so there is no distinction between any direction orthogonal to the flow. On the other hand, in macrorheology, the structure around a tracer is skew symmetric, the the stress on a plane along the velocity-gradient direction is different than that along the vorticity direction (Bergenholtz *et al.*, 2002). The plot shows that despite this rather fundamental difference, the similarity between micro and macro is very strong. The same scaling in Pe is evident for the full range of Pe, and quantitative agreement between micro and the macro stress is strong. Of course, the major outcome of the quantitative difference gives a qualitatively different second normal stress difference—it is zero in microrheology, and $O(Pe)$ in macrorheology.

The first normal stress difference, however, has much stronger similarity for the two flows. Figure 4.11 gives a plot of the first normal stress difference for micro and macro flows. The cyan solid line represents data for macrorheology Bergenholtz *et al.* (2002); the green open squares reflect the full equation (4.52), while the blue filled squares are the same result but with the viscous stress (the second term in equation 4.27) removed, as was done above for the longitudinal normal stress. Agreement between all three sets of data is good at high Pe, where viscous stress does not matter for

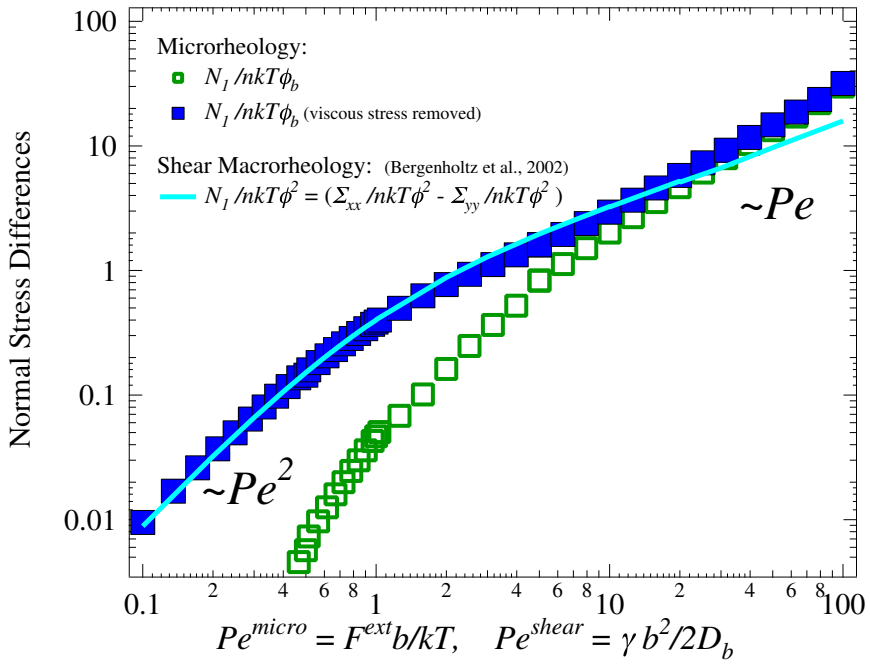

Figure 4.11: Macro versus microrheology: Normal stress differences. Cyan solid line represents numerical results by Bergenholtz *et al.* (2002) for simple shear of dilute colloidal dispersion of hard spheres. Blue filled squares are are for nonlinear microrheology (4.52); green open squares: Equation (4.52) minus viscous stress.

the microrheology tensor. But at moderate and low Pe, agreement between macro and micro (4.52) is poor. Again noting that viscous stresses are not present in the macrorheology normal elements, a comparison between macro and microrheology N_1 without the viscous normal stress is shown. Here, agreement is excellent. For strong forcing, the N_1 scales linearly in Pe.

The final comparison between the two flows is the behavior of the osmotic pressure, which for a dilute bath is plotted in figure 4.12. For the microrheology results, the full stress tensor (equation 4.54) is used. Here, we see strong qualitative and quantitative agreement for the full range of Pe. For strong forcing, the osmotic pressure scales linearly in Pe. It is interesting that the agreement in behavior for the osmotic pressure is so strong, when the stress tensor components themselves showed at least quantitative disagreement above. In order to understand why this agreement exists, it is useful to consider the mathematical underpinning of the osmotic pressure: It represents the invariants of the stress tensor. Although one flow is axisymmetric (micro) and the other flow is skew symmetric (macro), a rotation of quadrants makes their structures nearly identical. And because the stress is the second moment of the microstructure, the sign does not change in such a transformation.

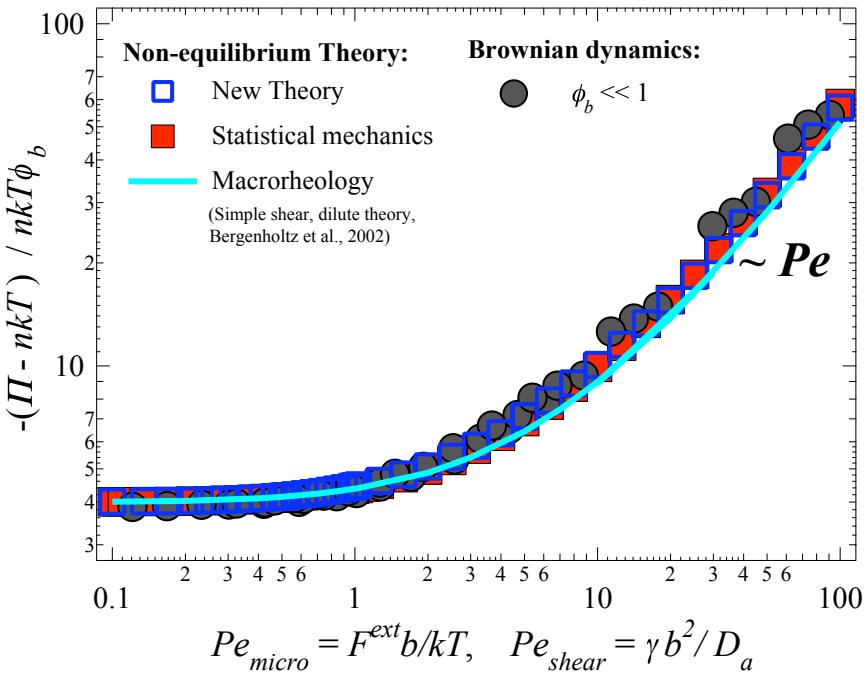

Figure 4.12: Macro versus microrheology (dilute system): Osmotic pressure. Legend as in figure 4.8, plus: cyan solid line shows numerical results by Bergenholtz *et al.* (2002) for simple shear of dilute colloidal dispersion of hard spheres.

Further, a diagonalization of the macro stress tensor using its eigenvalues would move the viscous stress components to the diagonal; because the eigenvalues are preserved in such a transformation, the osmotic pressure reflected in the transformed macro stress tensor should bear strong similarity to that of the micro stress tensor, due to the similar structures. This view may also contribute understanding as to why the overall agreement between microrheology and macrorheology is so strong, at least in the absence of hydrodynamic interactions.

Probe/bath-particle interactions versus bath/bath-particle interactions

Up to now, we have examined the non-equilibrium particle stress by driving the bath from equilibrium with a probe particle, and measuring the collisions suffered by the probe due to interactions with the bath particles. In §4.5 it was proposed that in a dilute bath, interactions between bath particles would make an $O(\phi_b^2)$ contribution to the non-equilibrium osmotic pressure, which is small for a dilute bath; hence, the stress obtained by probe-bath interactions gives an accurate measurement of particle-phase pressure.

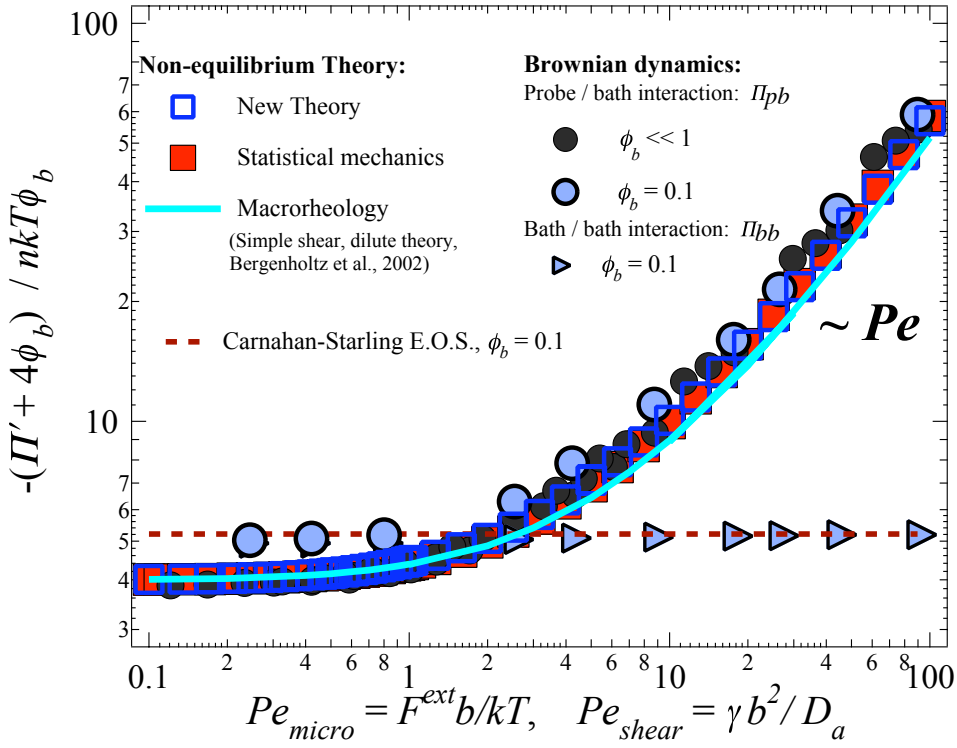

Figure 4.13: Comparison of contribution to osmotic pressure due to bath-bath collisions (light blue filled flags, BD simulation) versus probe-bath collisions (legend as in 4.12) and to the osmotic pressure in a dilute bath of hard spheres undergoing simple shear (cyan solid line). Red broken line: equilibrium osmotic pressure via Carnahan-Starling equation of state at $\phi_b = 0.1$. Other symbols defined as in figure 4.7.

To investigate this idea, Brownian dynamics simulations were conducted in which the bath particles interact via excluded volume interactions. Simulations were run at a volume fraction of bath particles $\phi_b = 0.1$. The stress measured by probe/bath-particle collisions, $\langle \boldsymbol{\Sigma} \rangle / n_a kT\phi_b$, and that for bath/bath-particle collisions, which shall be denoted $\langle \boldsymbol{\Sigma} \rangle_{bb} / n_b kT\phi_b$, was measured. The osmotic pressure thus obtained, as a function of Pe, is shown alongside those for the dilute bath, in figure 4.13. For reference, the equilibrium osmotic pressure predicted by the Carnahan-Starling equation of state (Carnahan & Starling, 1969) is shown on the plot for a volume fraction $\phi_b = 0.1$.

As predicted by the scaling argument, the equilibrium osmotic pressure is higher for a bath of interacting particles than for the dilute case. While the osmotic pressure measured by the probe, $\Pi / n_a kT$, increases linearly with Pe, the osmotic pressure due to the bath/bath-particle interactions, denoted $\Pi_{bb} / n_b kT$, when averaged over all the bath particles, remains at the equilibrium value regardless of Pe. This reflects the fact that most of the bath particles interact with each other due

to Brownian motion only, where the probe and bath particles interact due to the external forcing. In order to understand if this reflects what would be expected from traditional macrorheology experiments, the dilute theory results for a bath undergoing simple shear (Bergenholtz *et al.*, 2002) are plotted alongside the microrheology results in figure 4.13. It should be noted, however, that the presence of hydrodynamic interactions can result in qualitatively different behavior of the stress—including a Pe-dependent change in sign. Examination of this effect is left for future work.

4.9 Conclusions

We have presented a new approach for understanding and determining the stress in a dispersion of colloidal particles. Inspired by the equilibrium connection between osmotic pressure gradients and diffusion, it was proposed that diffusion is driven by stress gradients in non-equilibrium suspensions as well. Previous work has connected gradients in number density and chemical potential to collective diffusion (Einstein, 1906; Batchelor, 1972); these treatments applied to equilibrium Brownian suspensions. This idea holds appeal in that the simple measurement of mean-square displacement would then provide a measurement of suspension stress. It was thus proposed that the relation $\partial \boldsymbol{\Sigma}/\partial n \propto \boldsymbol{D}$ holds for non-equilibrium suspensions. The corresponding equation $\boldsymbol{\Sigma} = -\boldsymbol{R} \cdot \boldsymbol{D}$ was evaluated for the case of nonlinear microrheology; the right-hand side of this relation is the force-induced diffusion, $\boldsymbol{D}^{micro}$, and the resistance tensor is $\boldsymbol{R} = 6\pi\eta a \boldsymbol{I}$. The left-hand side was computed as the second moment of the microstructure g, where g is governed by a pair Smoluchowski equation. The agreement between the extension of the equilibrium macroscopic approach and the micromechanical (Smoluchowski) approaches was fair; the scaling dependence on Pe was strong but quantitative agreement was not as good. Taking a phenomenological view of the stress tensor, it was noted that the effect of viscous forces was not accounted for in $\boldsymbol{\Sigma}$. Underlying assumptions for the model were examined to determine where physical processes may have been neglected. The primary feature of the equilibrium model limiting its generalization to non-equilibrium systems is that it was derived from an equation of state; non-equilibrium systems must be described by an equation of motion.

Cauchy's momentum balance was presented as the equation of motion of the suspension, where the inertial and time-dependent terms were discarded due to a vanishingly small Reynolds number. To consider the particle stress only, an additional body-force term, the interactive force, was introduced to account for the effect of the remaining medium on the particles. Several cases were examined in which the constitutive form of the interactive force corresponded to the relevant transport process. For equilibrium suspensions subjected to a particle-density gradient but no external body forces, Fickian diffusion was taken as the constitutive model for the flux due to the interactive force. Then, for no gradients but with an external body force—constant-velocity nonlinear microrheology—it was found that the interactive force is the mean advective drag of the microstructure. This important result indicates that advective, as well as diffusive, flux should be considered in the non-equilibrium system.

Before moving on to consider a more general system—the presence of both an external body force and particle-density gradients—it was noted that the thermal agitation of particles that gives rise to the isotropic osmotic pressure at equilibrium will also be present away from equilibrium. But the probes scatter more actively off of the microstructure, and intuitively, this increased agitation should lead to a higher isotropic particle pressure. That is, it should have the effect of an increased "effective temperature" in the suspension. Particle fluctuations due to scattering increase as flow strength increases, and so it was proposed that this Pe-dependent isotropic pressure be constitutively modeled by the trace of the flow-induced diffusion tensor.

Next, the case of constant-force nonlinear microrheology was considered, where the probe velocity can fluctuate. The freedom to fluctuate gives the probe the ability to adjust its speed when encountering regions of higher or lower density. The hindrance of the microstructure is reduced compared to the constant-velocity case, which has the effect of weakening the viscous resistance to it motion. On average, probe fluctuations thus give rise to an increment in advective flux, over the flux produced by a constant-velocity motion. That is, stress gradients drive advective flux of the probe.

This can be understood from the perspective of a mobility versus resistance formulation of the

constant constant-force versus constant-velocity modes. Constant-velocity microrheology is given by a *resistance* formulation, $\boldsymbol{F} = \boldsymbol{R} \cdot \boldsymbol{U}^{ext}$, whereas when constant-force microrheology is represented by a *mobility* formulation, $\boldsymbol{U} = \boldsymbol{M} \cdot \boldsymbol{F}^{ext}$. When there are no fluctuations in a dilute hard-sphere suspension with no hydrodynamic interactions, $\boldsymbol{R} = \boldsymbol{M}^{-1}$. But when fluctuations matter, $\boldsymbol{R} \neq \boldsymbol{M}^{-1}$. The hydrodynamic resistance in the constant-force problem is the same as the constant-velocity drag minus the contribution due to fluctuations. Their difference is the reduction in the resistive force, or, if you will, the presence of an advective force in the opposite direction of viscous drag forces. The effect of the fluctuations is the same as if a certain steady force acted on the bath, that in the constant-force mode, balances the fluctuations of the probe. My view of this as a "fictitious force" is directly inspired by the same view taken by Batchelor of the thermodynamic force (1976). In the limit of a dilute suspension, the strength of this force is $O(\phi_b)$. The final result was an analytical expression for particle stress in terms of a sum of fluctuational (diffusive) and dissipative (viscous) contributions. This powerful result shows that by simply measuring the mean and mean-square motion of a probe particle driven through a suspension, one can determine the viscosity, the diffusivity, and the stress. An isotropic pressure term gives the "effective temperature" of the suspension.

Before going on to a comparison of the new theory to known micromechanical results, the case of sedimentation was evaluated. The collective diffusion coefficient in the absence of hydrodynamic interactions was determined, which we believe is a new result.

The total flux predicted by the new theory was compared to known results obtained via a micromechanical approach (cf §4.2) and with a measurement of the stress via Brownian dynamics simulations. The normal stress differences were compared with the three approaches; agreement was excellent. For large Pe, the first normal stress difference was shown to scale linearly in the forcing and in the volume fraction of bath particles, $N_1/nkT \sim Pe\,\phi_b$. For very weak forcing, $Pe \ll 1$, N_1 vanishes as $\sim O(Pe^4)$ because the Brownian motion of the bath particles easily restores deformation caused by the probe's motion, and isotropy dominates the structure. Due to the axisymmetry of the microstructure about the axis of forcing, the second normal stress difference $N_2 = 0$ for all Pe.

The osmotic pressure was computed via the new theory, and was also compared to the statistical mechanics and Brownian dynamics results; agreement was excellent here as well. For large Pe, the osmotic pressure was shown to scale linearly in the forcing and in the volume fraction of bath particles. For very weak forcing, $Pe \ll 1$, the total non-equilibrium osmotic pressure Π asymptotes to the the value predicted by the Carnahan-Starling equation of state (Carnahan & Starling, 1969).

To give a physical picture of the importance of these measurements, one can imagine a soft particle, such as an organelle inside the cell, or such as a bubble, placed in a suspension. If the particle is compressible, then forcing it through the medium will cause it to shrink or expand—and possibly burst—due to the particle pressure. If the particle is soft, the normal stress differences that arise due to forcing will elongate it—possibly causing rupture. These effects have important implications in the consideration of nanoparticle drug delivery and the escape of viruses from the endosomal pathway, for example.

Microrheology need not—in fact should not—be viewed as a microscale version of traditional shear rheology. However, one can always ask whether the measurements obtained via microrheology correspond in a meaningful way with the bulk measurements obtained by shear macrorheology. For example, Khair & Brady (2006) demonstrated that the microviscosity recovers all of the important phenomenological behavior of a dilute colloidal dispersion under flow, for same-size particles—the same scaling in Pe, the same onset of shear thinning and thickening, and in the limit of negligible hydrodynamics, the same terminal Newtonian plateau. In §4.8, we compared the osmotic pressure results for microrheology with the dilute theory of Bergenholtz *et al.* (2002), and found that the osmotic pressure measured by single-probe forcing matches quite well with the dilute shear rheology theory. This is actually somewhat surprising, if one considers the dependence of stress on the contact value of the microstructure. The deformed microstructures of the two flows—simple shear and microrheology—are markedly different. One important difference became evident in the comparison of the individual elements of the stress tensors. Here, the match between the parallel and perpendicular diagonal elements of the stress tensor in macrorheology contains no viscous stress: viscosity is strictly deviatoric in simply sheared suspensions. In contradistinction, viscous stress in

microrheology is normal, and must appear on the diagonal of the stress tensor. When the viscous stress was removed from the new theoretical prediction (cf equation 4.52), very good agreement between the first normal stress difference in micro versus macrorheology was found.

It is interesting that the agreement in behavior for the osmotic pressure is so strong, when the stress tensor components themselves showed quantitative disagreement. The excellent agreement between micro and macro for the osmotic pressure can be argued physically: The shear microstructure is skew symmetric about a test particle, while for microrheology it is axisymmetric. But if one refers to the microstructural sketches of simple shearing versus microrheology in figure 2.4, one can imagine rotating the upper left quadrant of the shear microstructure to the upper right quadrant; the structures are then strikingly similar. Since the sign change would not matter in the second moment of this structure, it is not surprising then that at least the osmotic pressure is the same. This can also be understood in terms of the properties of eigenvalues. The osmotic pressure represents an invariant of the stress tensor. A diagonalization of the macro stress tensor using its eigenvalues would move the viscous stress components to the diagonal; because the eigenvalues are preserved in such a transformation, the osmotic pressure reflected in the transformed macro stress tensor should bear strong similarity to that of the micro stress tensor, due to the similar structures. This view may also contribute understanding as to why the overall agreement between microrheology and macrorheology is so strong, at least in the absence of hydrodynamic interactions.

An additional important consideration in the comparison of micro to macrorheology is the fact that microrheological flows are not viscometric: they do not produces statistically homogeneous flows and microstructures. The microstructure around a driven probe is statistically different than the structure away from the probe. The question then arises whether the suspension properties sampled by the probe reflect the bulk properties of the medium, as is the case in macrorheology. A similar concern arises in falling-ball rheometry. It has been proposed that the probe-phase stress is not the only contributor to overall particle-phase stress—that interactions between the bath particles themselves make a significant contribution. A simple scaling analysis shows that bath/bath-particle interactions contribute only to $O(\phi_b^2)$, a negligible contribution for a dilute bath—and as shown in

§4.8, the probe-bath measurement evidently matches dilute shear theory quite well. Nonetheless, one must carefully consider contributions to osmotic pressure due to collisions between the bath particles themselves. Brownian dynamics simulations for single-probe forcing, in a bath of interacting background particles. The contribution to stress due to bath/bath particle interactions was monitored, and found not to deviate from the equilibrium osmotic pressure. Thus we conclude that forcing the probe through the suspension and computing the stress on the probe phase gives an accurate account of non-equilibrium stress in the absence of hydrodynamic interactions.

The effect of hydrodynamic interactions between particles was not considered in this study. These are expected to produce a qualitative effect at high Pe, as lubrication interactions between particles induce shear thickening in the suspension. We expect the same stress-migration relation to hold, but with different scaling in Pe for strong forcing in lubrication limit, where the scaling of the microviscosity in the microstructure is now less than unity (Khair & Brady, 2006). When hydrodynamics become important, additional changes in the scaling of probe- to bath-particle size ratio will also become important, as these may strongly affect the microdiffusivity (Davis & Hill, 1992; Zia & Brady, 2010). One effect also not considered here was that of higher concentration of bath particles, with and without hydrodynamic interactions. The same stress-migration relation should still be valid, but with a quantitative difference due to the effect of concentration (in the absence of hydrodynamics). A change in scaling of the diffusion tensor to reflect the long-time self-diffusivity may be sufficient to account for this change (Brady, 1993*b*).

In conclusion, we find a new fundamental relationship between stress gradients and particle migration in colloidal dispersions away from equilibrium. This relationship accurately predicts normal stresses, osmotic pressure, and normal stress differences in nonlinear microrheology when compared to benchmark theory and to dynamic simulation results. The results are found to be consistent with those found in traditional shear macrorheology. Importantly, the analytical relationship derived allows that two simple measurements, mean and mean-square motion, can reveal everything of rheological importance about a complex fluid: Viscosity, diffusivity, and stress can now be measured by making only two measurements. This is a significant amount of information gleaned just from

watching a single particle move. We propose that the constitutive expression for the stress thus obtained is in fact a non-equilibrium form of the Stokes-Einstein relation, in which stress is the balance between fluctuation and dissipation. The fact that the balance is nonzero points toward a storage of energy in the microstructure, which will be explored further in the next chapter.

Returning to Einstein's thought experiment, we recall that his test particle, or probe, was the "microscope" through which he looked in order to "see" the motion of atoms and molecules—indeed, to verify their existence (cf chapter 2). He proposed that if a liquid were indeed composed of atoms, then the motion of a small particle suspended in the fluid would move with the same random trajectories as the solvent atoms. Combining the theories of kinetics, diffusion, and thermodynamics, he proved that the diffusive motion of a small particle is indeed evidence of the existence of the atom. This is a profound conclusion, drawn by simply watching a particle move in liquid. Perrin confirmed the theory with measurement in 1909, and from this work, Avagadro's number was determined. We have sought to follow this example, and watch a particle move in a complex fluid—but now, for a system that is not at equilibrium. By studying fluctuations *away from equilibrium*, we have discovered an analogous non-equilibrium relation between fluctuation and dissipation—and that the balance between the two is stored in the material stress. What can this tell us more fundamentally about energy and motion? Avogadro's constant is a scaling factor that connects the macroscopic and microscopic views of matter. As such, it connects other physical constants and properties (Avagadro, 1811). For example, it establishes a relationship between the macroscopic gas constant $\mathcal{R}$ and Boltzmann's constant k, which connects energy at the atomic level to temperature at the macroscopic level. It allows the ideal gas equation of state to be stated in terms of the properties of molecules rather than the experimental constant $\mathcal{R}$. Here we have stated the equation of motion of an "ideal gas" of particles in terms of the properties of the individual particles and of the system. We related the energy density of the particles (the stress) to "effective temperature," at the macroscopic level. As we look toward the future, this leaves open an intriguing question: Can we formulate a more universal way to define temperature?

Chapter 5

Nonlinear viscoelasticity in colloidal dispersions: Energy storage and release in nonlinear microrheology

5.1 Introduction

Most work thus far in nonlinear microrheology has focused on steady dynamic behavior, and has established the relationship between steady-state microstructural mechanics and transport properties such as the diffusivity, viscosity, and stress. Transient behavior has also been studied in the near-equilibrium, linear-response regime, via its connection to low-amplitude oscillatory probe forcing and the complex modulus. Such studies show that for very weak forcing, the microstructural response that drives stress (and relaxation) is indistinguishable from equilibrium fluctuations. The connection can be viewed from the perspective of Green-Kubo linear response theory (Green, 1954; Kubo, 1966): While the shear stress in an equilibrium system is zero on average, Brownian motion drives fluctuations that produce small perturbations in microstructural isotropy, which give rise to temporary shear stresses. These stresses decay in time, and the shear stress autocorrelation function, $\boldsymbol{C}_s(t) = \langle \boldsymbol{\sigma}(t)\boldsymbol{\sigma}(0)\rangle$, is the memory kernel that describes this decay. Stress relaxation is memory decay: As correlation weakens, memory of past fluctuations is being lost. Green-Kubo theory relates the autocorrelation functions for stress and velocity to transport coefficients—the

viscosity and the diffusivity, respectively. The connection between the diffusivity and the velocity autocorrelation function $\boldsymbol{C}_v(t) = \langle \boldsymbol{v}'(t)\boldsymbol{v}'(0)\rangle$ is an important example of the fluctuation-dissipation theorem (Kubo, 1966). It can be measured experimentally, and can be derived analytically by enforcing the equipartition theorem. Green-Kubo theory can also be generalized to describe linear viscoelastic behavior in colloidal dispersions (Nägele & Bergenholtz, 1998). Here, analytical determination of the velocity autocorrelation function requires that one define a memory kernel for the material. The memory kernel in weakly non-equilibrium viscoelastic systems is often modeled by a frequency-dependent complex exponential; the exponential character weights recent events much more strongly than those in the distant past—the farther back in time, the less memory of how the microstructure was arranged. The complex character describes the phase-response of a viscoelastic material: In-phase response is elastic, and out-of-phase response is viscous. However, it is known and shall be shown below that in colloidal dispersions the relaxation is *not* exponential; rather, memory decays algebraically (Russel, 1981).

Relaxation and memory have been studied thoroughly in equilibrium colloidal dispersions. Thermal fluctuation (diffusion) of a single particle in a solvent is dissipated back into the solvent via viscous drag (Einstein, 1906; Perrin, 1909). This decay of particle momentum due to viscous drag occurs on the order of 10^{-7} seconds (cf chapter 2); from a microscopic perspective, memory loss is instantaneous [for a discussion of relaxation on the solvent time scale, see *e.g.* Russel (1981); Hocquart & Hinch (1983)]. But a single particle diffusing through a dispersion of other particles deforms the suspension, giving rise to stresses that relax on time scales longer than the individual-particle momentum relaxation time scale. This relaxation time scale can be probed via low-amplitude oscillatory shearing motion. The infinite-frequency limit corresponds to the shortest relaxation time scale of the dispersion, and it was found that the stress decays as $t^{-1/2}$ at very short times (in the absence of hydrodynamic interactions) (Lionberger & Russel, 1994; Brady, 1993*b*). Brady (1993*b*) obtained the frequency-dependent viscosity in concentrated suspensions by analyzing diffusion (rather than stress). He proposed that the short- and long-time self-diffusivity should be related to the complex viscosity via a frequency-dependent Stokes-Einstein relation. At short times (high frequency), a dif-

fusing tracer does not disturb the microstructure, and hence the dissipation of its motion is purely hydrodynamic in origin and corresponds to the high-frequency complex viscosity. At long times (low frequency), the particle (weakly) deforms the microstructure as it migrates from one local "cage" of nearest-neighbors to another; Brady argued that the disturbance of the particle is equivalent to very weak steady shear. The stress due to long-time diffusive behavior must therefore decay as $t^{-7/2}$, due to the quadrupolar disturbance associated with the linear flow, where the dissipative mechanism is the zero-frequency (steady) shear viscosity.

While Brady showed that the limits of short-time and long-time diffusive behavior probe the infinite-frequency and zero-frequency viscous responses, respectively, equilibrium thermal fluctuations of a tracer particle excite *all* frequency response modes in a suspension. Khair & Brady (2005) determined the linear response of a suspension at arbitrary frequency from the approach of small-amplitude oscillatory microrheology.

These previous studies form a body of work that describes the temporal decay of microstructural memory in equilibrium suspensions, and in suspensions undergoing small-amplitude deformations. Yet the results give little insight into nonlinear behavior: how a suspension evolves from one limit to the other, *i.e.* how the microstructure and stress transition between equilibrium and nonlinear steady state. Little theoretical work has been devoted thus far to the study of stress formation and relaxation in strongly non-equilibrium systems.

Elastic behavior in suspensions arises due to the presence of a deformed particle microstructure. Mechanically, particles accumulate in space because they hinder each other's movement along a streamline. When flow is stopped, the compressed structure relaxes over time. Statistically, two particles pushed together and then released will be driven apart by Brownian motion—the gradient in their distribution gives rise to an entropic force that acts to make uniform their spatial distribution. This entropic-spring effect applies to suspensions of many particles as well. Applying a load to a suspension deforms it, restricting the number of available configuration states of the particles. The reduction in their entropy exacts a free-energy penalty; this energy density is stored in the particle configuration and results in an increase in suspension stress. Removal of the load allows the particles

to seek a uniform distribution, which releases the stored energy and reduces suspension stress. Some of this energy release is elastic: A tracer particle used to deform the suspension would "spring back" some distance as the entropic spring energy is released. But some of the energy is dissipated viscously into the solvent. The degree to which each of these mechanisms contributes to stress formation and relaxation is not yet understood.

Previous experimental studies of transient non-equilibrium behavior in suspensions, including startup and cessation flows, show that different forces contribute to suspension stress and viscosity—*e.g.* hydrodynamic, interparticle, and Brownian forces—and give rise to distinct relaxation processes. For example, Mackay & Kaffashi (1995); Kaffashi *et al.* (1997) studied the decay of stress immediately after the cessation of imposed strain-rate on a sheared suspension; they found that the hydrodynamic stress decays instantaneously, as it must—the hydrodynamic stress is proportional to the imposed strain-rate, and thus must vanish in the absence of flow. Watanabe and coworkers (1996*a*; 1996*b*) analyzed stress development and relaxation in sudden startup and cessation of shearing flow, and found both short- and long-time relaxation modes. While these studies certainly show that stress relaxes via multiple transport processes, a clear understanding of *how* those processes dissipate energy has not yet been achieved.

The goal of this study is to understand the basic physical aspects of structural development and relaxation in colloidal dispersions, and the mechanisms by which microstructural memory forms and decays. Microstructural and transport properties have been studied extensively at equilibrium and at steady-state away from equilibrium, where transport properties depend on the extent to which the microstructure is deformed. In microrheology, the strength with which the probe is forced, F^{ext}, compared to thermal forces, kT/b, governs the behavior and defines the Péclet number, $Pe = F^{ext}/(kT/b)$, where kT is the thermal energy and b is the bath-particle size. But the *transition* from equilibrium (frame (a) in figure 5.1) to steady state (frame (b) in figure 5.1), and the relaxation back to equilibrium when flow is shut off (frame (c) in figure 5.1) is not nearly as well studied. Here we study the evolution of stress and microstructure over time from the perspective of single-particle forcing and the microrheology framework. Structural and stress behavior during startup

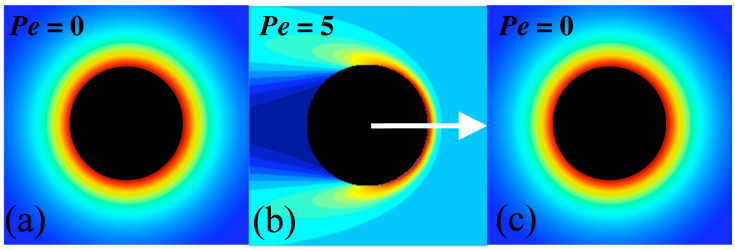

Figure 5.1: Contour plot of microstructure around the probe, in the plane passing through the origin of the probe. Red and yellow indicate strong and moderate probability accumulation respectively; dark blue and light blue indicate strong and moderate depletion respectively. Black is excluded volume around probe. (a) Prior to startup of the flow, the microstructure is at equilibrium. (b) Long after flow startup, the steady-state structure forms; here, for $Pe = 5$, a $1/Pe-$thin accumulation layer forms on the upstream face of the probe, and a depletion wake trails it. (c) Long after flow cessation, the Brownian motion of the bath particles restores the equilibrium microstructure around the probe.

and cessation of an imposed flow will be examined in the nonlinear regime, where the structure is driven far from equilibrium. The foundation of our approach has already begun: In chapter 4, we investigated the relationship between stress, fluctuation, and dissipation away from equilibrium. We saw that the stress is given by the balance between non-equilibrium fluctuations and viscous relaxation in nonlinear microrheology. The strength of advective forces relative to diffusive forces—the Péclet number—is equivalently a ratio of diffusive to advective time scales. It sets the time scale over which the microstructural disturbance persists; Pe is thus a memory parameter in nonlinear flows—it indicates how long the microstructure "remembers" the disturbance caused by the probe's motion. It should therefore play an important role in our understanding of stress development and relaxation.

In microrheology, the force/velocity relationship is analogous to the stress/strain-rate relationship in macrorheology. We expect both approaches to yield the same qualitative information about about structural evolution and relaxation. In this study, we will monitor probe motion following sudden startup and cessation of the application of external forcing to the probe. The work is carried out analytically and by dynamic simulation.

The remainder of this chapter is set out as follows: In §5.2 a scaling argument is advanced to predict the early-time behavior of the viscosity (force) during startup of flow. These scaling predictions provide a framework to guide analytical and numerical work; the corresponding physical arguments provide insight into the basic physics at play during stress formation and relaxation.

A formal theoretical framework is developed in §5.3 in which the time-dependent evolution of the microstructure is formulated. The connection between time-dependent viscosity and microstructure is given. An important distinction between "constant-force" and "constant-velocity" microrheology is reviewed; the forcing mode plays an important role in microstructural evolution at steady state (Squires & Brady, 2005) and makes a quantitative difference in the magnitude of the steady-state microviscosity. Its role in structural formation is explored in §5.3. The transient microstructure is solved analytically using a combination of asymptotic analysis (§5.4 and §5.5) and numerical methods (§5.6). Transient microviscosity is then measured via Brownian Dynamics simulation in §5.7, for both constant-force and constant-velocity regimes. The microviscosity at long times after startup is compared to the theory predictions of Squires & Brady (2005), and to the dynamic simulation of steady-state microrheology of Carpen & Brady (2005). The work is also compared to analogous results for sheared suspensions undergoing startup and cessation (Foss & Brady, 2000*b*) in §5.8. The chapter is concluded with a discussion of results and implications in §5.9.

5.2 Scaling predictions

Prior to formulating and solving the detailed problem, scaling arguments can provide insight into the fundamental physical aspects of system behavior. At flow startup, it takes time for the probe to realize that there is a boundary—the boundary is infinitely far away. The information about the probe's disturbance propagates into what initially appears to be, from the probe's perspective, an infinite domain. Space and time cannot be separated, which is characteristic of diffusive propagation, where error functions describe the behavior. We expect the initial microviscosity η^{micro}/η to grow as

$$\frac{\eta^{micro}(t)}{\eta} \sim \left(\frac{t}{\tau_{rel}}\right)^{1/2}, \quad t \to 0 \quad \text{(startup)}. \tag{5.1}$$

Here, η^{micro} is the viscous drag of the particles (cf chapter 2), η is the viscosity of a pure solvent, and τ_{rel} is the diffusive relaxation time scale: $\tau_{rel} \sim a^2/D$.

At the other extreme, when the flow is shutoff, forced advection ceases and diffusion dominates

the behavior. For strong forcing prior to shutoff, the probe initially sees only the boundary layer and diffuses (the remainder of the bath is infinitely far away); this highly local process is one-dimensional inside the boundary layer, and thus the scaling is a 1D diffusive monopole ($\simeq t^{-1/2}$). As the probe continues to relax into the microstructure, it becomes a fully 3D diffusive monopole ($\simeq t^{-3/2}$). Finally, at very long times, the probe undergoes equilibrium fluctuations and disturbs the suspension with a diffusive dipole ($\simeq t^{-5/2}$), and thus,

$$\frac{\eta^{micro}(t)}{\eta} \sim \left(\frac{t}{\tau_{rel}}\right)^{-5/2}, \quad t \to \infty \quad \text{(cessation)}. \tag{5.2}$$

5.3 Theoretical framework

Force and stress evolution: Transient microviscosity

We shall consider the same model system detailed in chapter 2 by figure 2.2: a suspension of colloids interacting via a hard-sphere potential (equation 2.24), neglecting hydrodynamic interactions. In §2.3, we reviewed the derivation of the microviscosity—the microstructural drag of bath particles that reduces probe velocity as it travels through the bath, above and beyond the solvent drag—following Squires & Brady (2005) and Khair & Brady (2006). In the dilute case of this model, the microviscosity is related, via Stokes' drag law, to the reduction in probe speed due to its collisions with the bath particles. The expression for the microviscosity may also be written as a more general time-dependent expression:

$$\frac{\eta^{micro}(t;Pe)}{\eta} = \frac{3}{4\pi} Pe^{-1} \hat{\boldsymbol{F}}^{ext} \cdot \int \boldsymbol{n}\, g(1,t;Pe) d\Omega. \tag{5.3}$$

Here, the microstructure and hence the viscosity are evolving in time, t. The pair-distribution function is now a function of time. In order to determine how the viscosity evolves from equilibrium to steady state, the time-dependent Smoluchowski equation must be solved in order to obtain $g(\boldsymbol{r},t;Pe)$. This is where we shall begin.

Structural evolution: Transient microstructure

We consider the probe amid a dispersion of $N-1$ bath particles in a configuration $\boldsymbol{x}_N$. The distribution of particles is given by an $N-$particle probability density, $P_N(\boldsymbol{x}_1, \boldsymbol{x}_2, ..., \boldsymbol{x}_N; t)$, which obeys a Smoluchowski equation:

$$\frac{\partial P_N}{\partial t} + \sum_{i=1}^{N} \nabla_i \cdot \boldsymbol{j}_i = 0, \tag{5.4}$$

where the sum is over all particles in the dispersion and the flux of particle i is given by

$$\boldsymbol{j}_i = \boldsymbol{U}_i P_N(\boldsymbol{x}_N; t) - \sum_{j=1}^{N} \boldsymbol{D}_{ij} \cdot \nabla_j (\ln P_N(\boldsymbol{x}_N; t) + V_N/kT) P_N(\boldsymbol{x}_N; t). \tag{5.5}$$

Here, kT is the thermal energy, $\boldsymbol{D}_{ij} = kT\boldsymbol{M}_{ij}$ is the relative Brownian diffusivity between particles i and j, and $\boldsymbol{M}_{ij}$ is the mobility tensor relating the velocity of particle i to the force exerted on particle j. The first term on the right hand side of (5.5) is the advective flux of particle i with velocity $\boldsymbol{U}_i$; the second term is the flux due to entropic gradients in the microstructure; and $\boldsymbol{D}_{ij} \cdot (\nabla_j V_N/kT) P_N$ gives the flux of particle i due to the forcing of interactive potential with particle j.

In order to obtain a closed expression for the pair-distribution function, it is necessary to neglect interactions of order three and higher—that is, to integrate the Smoluchowski equation (5.5) over $N-2$ configurational degrees of freedom. This restricts the theory to the dilute limit where the volume fraction of bath particles is small, $\phi_b \ll 1$, permitting only pair-collisions between probe and bath. Following the example of Squires & Brady (2005), the probability P_N in equations (5.4) and (5.5) reduces to the pair probability of finding the probe at position $\boldsymbol{x}_1$ and a bath particle at position $\boldsymbol{x}_2$. To analyze the relative flux between probe and bath, it is convenient to change to a frame of reference moving with the probe, placing the probe at $\boldsymbol{z} = \boldsymbol{x}_1$, and a bath particle at $\boldsymbol{r} = \boldsymbol{x}_2 - \boldsymbol{x}_1$. Then the pair probability is given by the conditional probability of separation $\boldsymbol{r}$ between probe and bath particle, given the probe is at the origin, times the probability of finding the probe at the origin: $P_2(\boldsymbol{z}, \boldsymbol{r}) = P_{1/1}(\boldsymbol{r}|\boldsymbol{z}) P_1(\boldsymbol{z})$. Now because the conditional probability is defined as $P_{1/1}(\boldsymbol{r}|\boldsymbol{z}) = n_b g(\boldsymbol{r})$, where n_b is the number density of bath particles, the pair Smoluchowski

equation becomes

$$\frac{\partial g}{\partial t} + \nabla \cdot (\boldsymbol{U}_r g) = \nabla_r \cdot \boldsymbol{D}_r \cdot (g \nabla_r V/kT + \nabla_r g), \tag{5.6}$$

where we have defined the relative Brownian diffusivity between the probe and the bath particle, $D_r \equiv D_a + D_b$ and $U_r \equiv U_b - U_a$. For a suspension of hard spheres in the absence of hydrodynamic interactions, the above equation becomes

$$\frac{\partial g}{\partial t} + \boldsymbol{U} \cdot \nabla g = D_r \nabla^2 g. \tag{5.7}$$

The strength of the external forcing compared to the restoring entropic force defines the Péclet number:

$$Pe = \frac{U_0(a+b)}{D}, \tag{5.8}$$

where the length scale is set by $r \simeq (a+b)$, $D \sim D_r$, and the characteristic velocity U_0 is set by the Stokes velocity of an isolated probe. Thus the evolution of the microstructure is given by

$$\frac{\partial g}{\partial \hat{t}} + Pe\, \boldsymbol{u} \cdot \nabla g = \nabla^2 g, \tag{5.9}$$

where $\boldsymbol{u}$ is the unit vector antiparallel to probe forcing, and time has been scaled diffusively: $\hat{t} = t/(a+b)^2/D_r$.

Because we are interested in changes in the microstructure, it is useful to consider the microstructural perturbation f defined by $g(\boldsymbol{r}, t; Pe) = 1 + f(\boldsymbol{r}, t; Pe)$. At the boundaries, the hard spheres require a no-flux condition at contact, and there is no long-range order in the suspension. For flow startup, the sudden onset of forcing appears as an advective term at $t = 0$ in the no-flux condition. Applying these two boundary conditions, the governing equations become

$$\begin{aligned} \frac{\partial f}{\partial \hat{t}} + Pe\, \boldsymbol{u} \cdot \nabla f &= \nabla^2 f, \\ \boldsymbol{n} \cdot \nabla f &= Pe\, \boldsymbol{u}\, f H(\hat{t}) \quad \text{at } r = 1, \\ f &\sim 0 \qquad\qquad \text{as } r \to \infty, \end{aligned} \tag{5.10}$$

where $H(\hat{t})$ is the Heaviside function that turns on the flow. The microstructure is initially undisturbed, *i.e.* $f(\boldsymbol{r}, 0) = 0$.

When the probe force is removed, the advective forcing terms vanish:

$$\begin{aligned} \frac{\partial f}{\partial \hat{t}} &= \nabla^2 f, \\ \boldsymbol{n} \cdot \nabla f &= 0 \qquad \text{at } r = 1, \\ f &\sim 0 \qquad \text{as } r \to \infty, \\ f(r, 0) &= f_0^{SS}(Pe), \end{aligned} \tag{5.11}$$

where the initial condition for microstructural relaxation is the steady-state microstructure prior to removal of the external force.

Constant-external force versus constant-external velocity

Active microrheology experiments are carried out by two main approaches: driving the probe with a constant external force—*e.g.* with magnetic tweezers (Habdas *et al.*, 2004)—or holding the probe fixed in an optical trap and moving the bath past it at a constant velocity—*e.g.* with laser tweezers (Meyer *et al.*, 2005). In the former case (Mode 1), the applied probe force remains constant while its velocity fluctuates and, as a result, the probe experiences a collision-induced diffusive spread of its trajectory [cf chapter 3, Zia & Brady (2010)]. In the latter case (Mode 2), the velocity is held constant and cannot fluctuate in magnitude or direction, and hence cannot diffuse—it experiences a fluctuating force instead. The theoretical framework for nonlinear microrheology was first developed by Squires & Brady (2005). The model is based on an interpretation of the average probe velocity as the effective viscosity of the suspension (cf chapter 2), where the average is taken over all possible configurations of the microstructure. They presented the solution for the constant-force microstructure and the corresponding effective viscosity. Although they did not calculate the constant-velocity microstructure explicitly, they propose that the Mode-2 viscosity should be twice that of Mode-1 viscosity. They based this proposal on a scaling argument justified physically as follows: as the probe moves through the bath, it encounters variations in local bath-particle density.

In Mode 1, since probe velocity can fluctuate, the probe can "wiggle" around and adjust its speed if it reaches a more dense or less dense region. On the other hand, in Mode 2 the probe velocity cannot change, and it must "bulldoze" through the suspension regardless of fluctuations in local density. Squires & Brady proposed that this difference is captured by the scaling of the diffusivity. Recall from equation (5.8) that the Péclet number is defined as $Pe = U_0(a+b)/D$, where D is the appropriate diffusive scaling. In Mode 1, the proper diffusive scaling is the relative diffusivity D between a pair of particles:

$$D_F \sim D_a + D_b = \frac{kT}{6\pi\eta}\left(\frac{1}{a}+\frac{1}{b}\right) \quad \text{(constant force)}, \tag{5.12}$$

where $D_a = kT/6\pi\eta a$ and $D_b = kT/6\pi\eta b$ are the isolated diffusivities of a probe and a bath particle, respectively, and D is the relative velocity scale. But in Mode 2, since the probe cannot diffuse, the proper diffusive scaling is that of the bath particles, which can diffuse:

$$D_U \sim D_b = \frac{kT}{6\pi\eta b} \quad \text{(constant velocity)}. \tag{5.13}$$

For a probe-to-bath-particle size ratio $a/b = 1$, we have that $D_F = 2D_U$, with the same ratio for the effective viscosity. These scaling arguments apply to the limit of no hydrodynamic interactions. This prediction will be evaluated in the Brownian-dynamics simulation of the startup flow, by comparing the long-time steady-state solution for the two modes. These results will be compared to the steady-state theory prediction of Squires & Brady, and to the steady-state Brownian dynamics simulations of Carpen & Brady (2005).

5.4 Analytical solutions: Flow startup

Low-Pe *limit*

In steady nonlinear microrheology the perturbation to the microstructure due to weak probe forcing is $f(\boldsymbol{r}) = -Pe\, h(r;Pe)\boldsymbol{u}\cdot\boldsymbol{n}$, where h vanishes quadratically in the radial coordinate r, and for

the steady case is independent of time. Here, $\boldsymbol{u}$ is the unit vector antiparallel to the direction of probe forcing and $\boldsymbol{n}$ is the unit surface normal (Squires & Brady, 2005; Khair & Brady, 2006; Zia & Brady, 2010). Proposing this general form for the solution, and noting that the evolution of the microstructure is convenient to analyze in frequency space, a Fourier-Laplace transform for the small-Pe solution inserted into (5.10) gives the governing equations as an ODE in frequency space with appropriate boundary conditions:

$$\begin{aligned} \frac{1}{s^2}\frac{\partial}{\partial s}\left(s^2\frac{\partial \hat{f}}{\partial s}\right) - \frac{2}{s^2}\hat{f} - i\alpha\,\hat{f} &= 0, \\ \frac{\partial \hat{f}}{\partial r} + \frac{1}{2}\sqrt{\frac{\pi}{2}}\left[\frac{1}{i\omega} - \pi\delta(\omega)\right] &= 0 \quad \text{at } r = 1, \\ \hat{f} &\sim 0 \quad \text{as } r \to \infty. \end{aligned} \tag{5.14}$$

Here, the transform variable ω has been scaled diffusively as above. With the substitution of variable $z = (i\alpha)^{1/2}$, (5.14) is the modified spherical Bessel differential equation with $n = 1$:

$$z^2\hat{f}'' + 2z\hat{f}' - (z^2+2)\hat{f} = 0, \tag{5.15}$$

which admits the exact solution (Brady, 1993*b*)

$$\hat{f}(r,\omega) = \frac{2}{r^2}\exp[\sqrt{i\alpha}(1-r)]\left[\frac{1+z_0 r/2}{1+z_0+z_0^2/2}\right]\left(\pi\delta(\omega)+\frac{1}{i\omega}\right), \tag{5.16}$$

with $z_0 = 2(i\alpha)^{1/2}$; growing solutions are prohibited by the boundary condition at infinity. To compute the frequency-space microviscosity, the microstructure at contact ($r = 1$) is required:

$$\hat{f}(1,\omega) = 2\left[\frac{1+\sqrt{s}/2}{1+\sqrt{s}+s/2}\right]\left(\pi\delta(is)+\frac{1}{s}\right), \tag{5.17}$$

where we have substituted the Laplace variable $s = i\alpha$. Inserting this expression into (5.3) and inverting the transform gives the transient microviscosity:

$$\frac{\eta^{micro}(t)}{\eta} = -4\mathcal{L}^{-1}\left[2\frac{1+\sqrt{s}/2}{1+\sqrt{s}+s/2}\right]\left(\pi\delta(is)+\frac{1}{s}\right). \tag{5.18}$$

Equation 5.17 can inverted numerically in MATHEMATICA (Valko & Abate, 2002). The transient microviscosity thus obtained is plotted in figure 5.2, in the limit of weak forcing (small Pe). The analytical solution is plotted alongside the very early-time behavior predicted by scaling arguments. The microviscosity increases in time very rapidly after the onset of probe forcing, and then asymptotes to a steady-state value. The long-time limit is compared below in table 5.1 to the small-Pe steady-state values computed by Squires & Brady (2005) and Khair & Brady (2006).

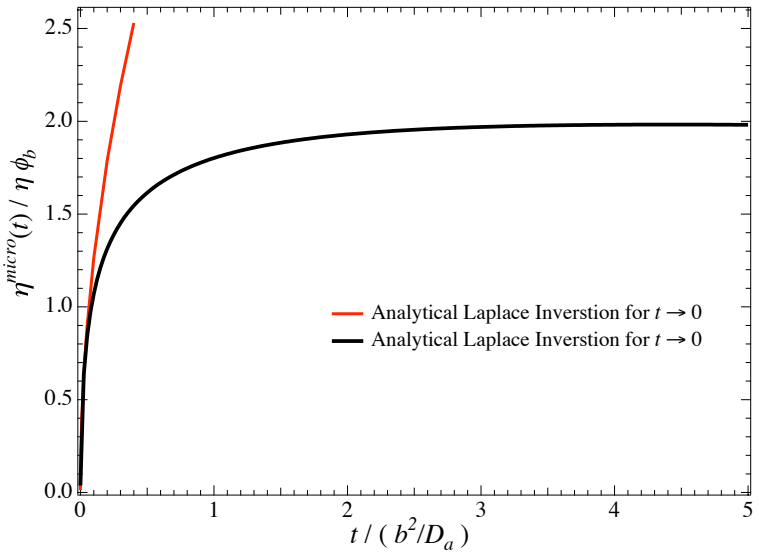

Figure 5.2: Startup of probe forcing for small Pe. Solution obtained via numerical inversion of the Laplace-space solution in (5.18). As $\hat{t} \to \infty$, the microstructure reaches steady state and the viscosity asymptotes to its steady value.

At very early times during startup, or as $s \to \infty$, expression (5.18) becomes

$$\frac{\eta^{micro}(s\to\infty)}{\eta} \sim \frac{1}{s(1+\sqrt{s})} \sim \frac{1}{s}, \tag{5.19}$$

or, since $s = (i\alpha)^{1/2}$, where $\alpha = \omega b^2/D = b^2/tD$,

$$\frac{\eta^{micro}(\hat{t})}{\eta} \sim \hat{t}^{1/2} \quad \text{as} \quad t \to 0. \tag{5.20}$$

The early-time behavior is shown in the log-log plot shown in figure 5.3. At very early times, the scaling prediction from the previous section agrees with the results of the asymptotic analysis above.

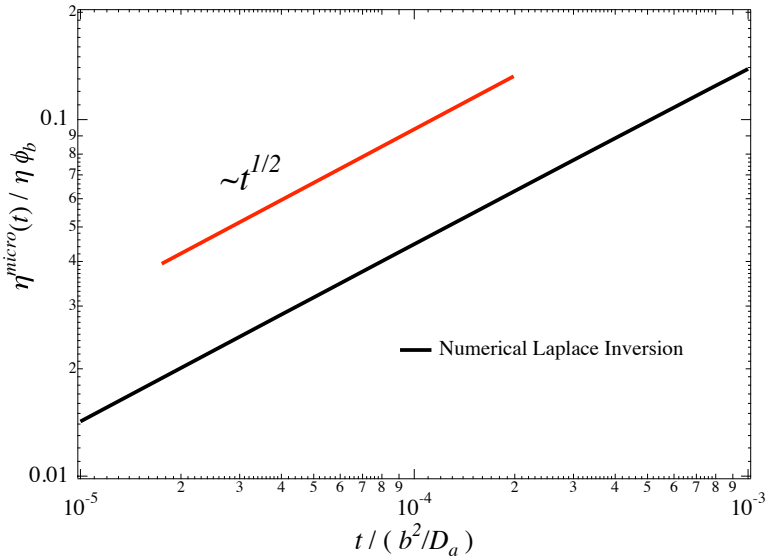

Figure 5.3: Startup of probe forcing: The initial increase in the viscosity scales at early times as $\sim \hat{t}^{1/2}$ for small Pe. In the limit of very short times, the scaling of the microviscosity is the square root of time, as predicted by scaling arguments in §5.2.

High-Pe *limit*

For strong probe forcing ($Pe \gg 1$), the *steady-state* shape of the microstructure in front of the probe is deformed into two distinct regions: an outer region in which advection dominates diffusion and the microstructure is undisturbed, and an inner region—a $1/Pe$-thin boundary layer that forms on the upstream face of the probe—where diffusion balances advection. A Pe-long wake of particle deficit forms behind the probe where probability for a probe/bath-particle collision is small. The particles that reside inside the boundary layer provide the most probability for a strong hard-sphere deflection of the probe (cf figure 3.4). The presence of a defined boundary layer characterizes the attainment of steady state. Although at early times the microstructure boundary layer has not yet

formed, here we explore the idea that since the early structure is confined in time and space to a very small region around the the origin in both coordinates, a "boundary layer" rescaling in both coordinates may capture the proper physics of microstructural development.

Inside the boundary layer, a coordinate rescaling $R = (r-1)Pe \sim O(1)$ preserves the diffusive term, properly reflecting the physics of the inner region and allowing satisfaction of the no-flux condition at contact. The appropriate scaling for time is the characteristic diffusive time; but here, all of the probe diffusion takes place inside the boundary layer of thickness $\delta \sim (a+b)/Pe$, and so time is scaled as $t \sim \delta^2/D$. The governing equation inside the boundary layer then becomes

$$\frac{\partial g}{\partial \hat{t}} + \frac{\partial^2 g}{\partial R^2} + \left(Pe^{-1} - \cos\theta\right)\frac{\partial g}{\partial R} - Pe^{-1}\sin\theta\frac{\partial g}{\partial \theta} = 0, \tag{5.21}$$

where θ is the polar angle as defined in figure 2.2. We have neglected terms of $O(Pe^{-2})$ and smaller, and all quantities are dimensionless. Following Brady & Morris, we make the "radial balance" approximation (1997): We assume that gradients in θ may be neglected; then for large Pe the resulting governing equations become, after taking a Laplace transform:

$$\begin{aligned} \frac{\partial^2 \hat{f}}{\partial R^2} + \left[Pe^{-1} - \cos\theta\right]\frac{\partial \hat{f}}{\partial R} - s\,\hat{f} &= 0, \\ \frac{\partial \hat{f}}{\partial R} - \cos\theta\left(\hat{f} + \frac{1}{s}\right) &= 0 \quad \text{at} \quad R = 0, \\ \hat{f} &\sim 0 \quad \text{as} \quad R \to \infty. \end{aligned} \tag{5.22}$$

The $O(Pe^{-1})$ term must be retained in order to satisfy the boundary condition at $R \to \infty$. This initial value problem has an exact solution, and upon inverting, one obtains

$$f(\hat{t}) = \frac{1}{2}\left[(1 - Pe\cos\theta)\mathrm{Erf}\left(-\frac{\sqrt{\hat{t}}(Pe\cos\theta - 1)}{2Pe}\right) + (Pe\cos\theta + 1)\left(\exp(\frac{\cos\theta\hat{t}}{Pe})\mathrm{Erfc}\left(\frac{\sqrt{\hat{t}}(Pe\cos\theta + 1)}{2Pe}\right) - 1\right)\right]. \tag{5.23}$$

This expression is then inserted into (5.3) and integrated numerically to obtain the transient microviscosity. The results are plotted in figure 5.4. The microviscosity increases very rapidly after the onset of probe forcing, and then asymptotes to a steady value. The long-time microviscosity is

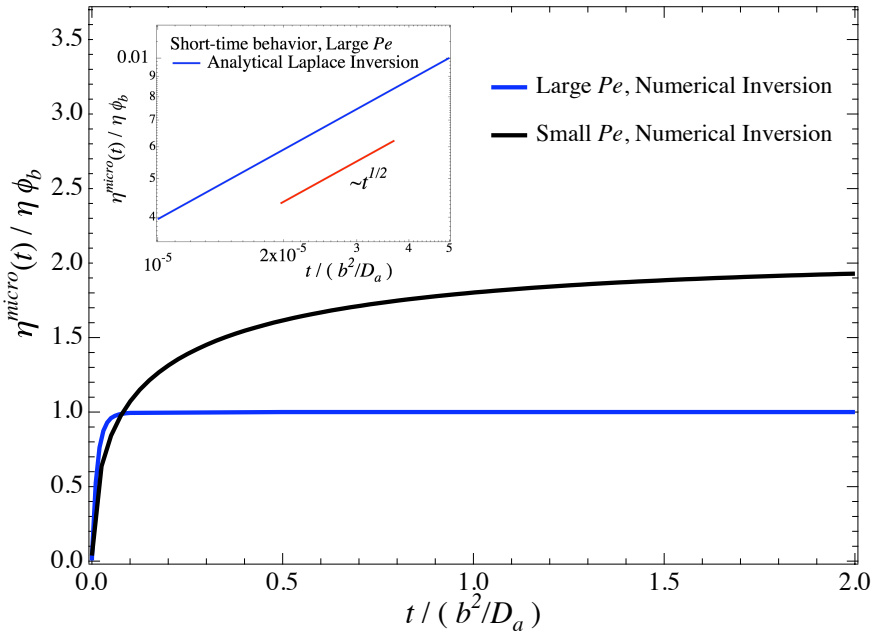

Figure 5.4: Startup of probe forcing: Comparison of $Pe \to \infty$ (blue line) to $Pe \to 0$ (black line) behavior. Early time behavior shown in inset. Time non-dimensionalized on the boundary-layer thickness, and is independent of Pe. Solution obtained via analytical inversion of the Laplace-space solution in (5.23). As $\hat{t} \to \infty$, the microstructure reaches steady state and the viscosity asymptotes to its steady value.

compared below in table 5.1 to the high-Pe steady-state values computed by Squires & Brady (2005) and Khair & Brady (2006). The early-time behavior can be seen more clearly in the log-log plot inset in the figure where again, the microviscosity grows with the square root of time. Importantly, the early-time behavior of the transient microviscosity is the same for small Pe and large Pe. The Péclet number is a measure of how strongly the microstructure is deformed from the equilibrium state. One interpretation of the Pe-independence is that it gives a measure of the time required for the probe to realize that it is not alone in the bath—and to interact with the surrounding microstructure. The duration of this regime is then the fundamental time scale of the microstructure.

5.5 Analytical Solution: Flow Cessation

When the probe force is removed the advective forcing terms vanish from the Smoluchowski equation:

$$\begin{aligned} \nabla^2 f - \frac{\partial f}{\partial \hat{t}} &= 0, \\ \frac{\partial f}{\partial r} &= 0 \quad \text{at } r = 1, \\ f &\sim 0 \quad \text{as } r \to \infty, \\ f(r,0) &= f_0^{SS}(Pe), \end{aligned} \tag{5.24}$$

where the initial condition for microstructural relaxation is the steady-state microstructure $f_0^{SS}(Pe)$ prior to removal of the external force. Although the external force has been removed, *the effect of previous forcing is still stored in the compressed microstructure.* The initial condition sets the initial decay of viscosity and stress; we examine this behavior in the limit of very weak and very strong forcing prior to flow shutoff.

Low-Pe *limit*

Just before the flow is turned off, the suspension is at steady state in the linear response regime; equation 5.24 gives the forced diffusion problem just after flow is shut off. This problem can be solved by separation of variables.

High-Pe *limit*

For very strong forcing, in order to make analytical progress, we make the "radial-balance approximation" proposed by Brady & Morris (1997), neglecting gradients in polar angle. For a large-Pe flow prior to shutoff, the initial condition of the microstructure is characterized by a thin boundary layer on the upstream face of the probe, and a deficit wake trailing the probe. Inside the boundary layer, a coordinate rescaling $R = (r-1)Pe \sim O(1)$ preserves the balance between diffusion and advection present prior to shutoff. The appropriate scaling for time is the characteristic diffusive time; but here, all of the probe diffusivity will take place inside the boundary layer of thickness

$\delta \sim (a+b)/Pe$, and so time is scaled as $t \sim \delta^2/D$. To leading order in Pe the governing equations inside the boundary layer then become, upon taking a Laplace transform,

$$\begin{aligned} \frac{\partial^2 \hat{f}}{\partial R^2} - s\,\hat{f} &= f_0^{SS}, \\ \frac{\partial \hat{f}}{\partial R} &= 0 \quad \text{at } R = 0, \\ \hat{f} &\sim 0 \quad \text{as } R \to \infty. \end{aligned} \tag{5.25}$$

Upon inversion, the solution at contact is given by

$$f(\tau) = -f_{SS}(0)\left[\exp((\cos^2\theta)\,\tau)\mathrm{Erfc}(\cos\theta\sqrt{\tau})\right]. \tag{5.26}$$

Insertion into equation (5.3), we have for the microviscosity

$$\frac{\eta^{micro}(\tau)}{\eta} = \frac{3}{4\tau}\left[e^{\tau}\mathrm{Erfc}(\sqrt{\tau}) + 2\sqrt{\frac{\tau}{\pi}} - 1\right], \tag{5.27}$$

where $\tau \equiv Pe^2\hat{t}$. The results are plotted in figure 5.5 for a range of Pe. There is an initially rapid decay of the stress at very short times, followed by slower long-time decay—indicating two relaxation modes. It is also evident that the higher the pre-cessation Pe, the faster the relaxation. It may seem counterintuitive that a more strongly deformed microstructural disturbance decays faster than a weakly deformed one. But physically, the probe need only diffuse the length of the boundary layer in order to relieve contact stress—as was seen in equation 5.3. That diffusive distance scales as Pe^{-1}, so the higher the Péclet number, the faster the initial relaxation.

At long times after shutoff, $\eta(\hat{t} \to \infty)/\eta \sim \hat{t}^{-1/2}$; this is shown more clearly in figure 5.6. But in our scaling predictions, the cessation behavior should transition from 1D monopolar ($\hat{t}^{-1/2}$) to 3D monopolar ($\hat{t}^{-3/2}$) to dipolar ($\hat{t}^{-5/2}$). Evidently the radial-balance approximation, which discarded polar gradients in microstructure, does not fully capture the long-time behavior of the suspension.

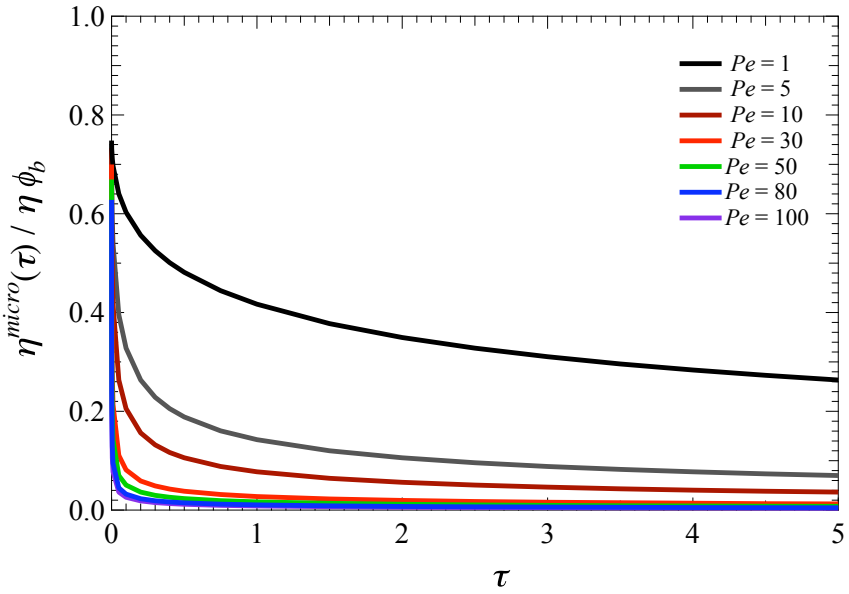

Figure 5.5: Cessation of probe forcing: initially, the viscosity drops rapidly from its steady-state value, and then decays more slowly at longer times. Time τ is scaled on the boundary-layer thickness

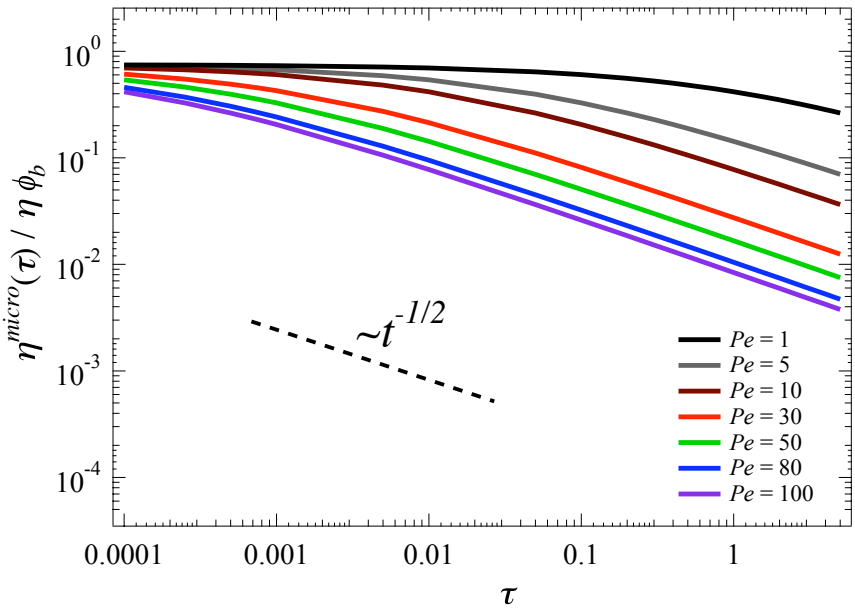

Figure 5.6: Log-log plot of post-cessation viscosity. At long times, the decay scales as $\hat{t}^{-1/2}$.

5.6 Numerical solution for arbitrary Pe

To obtain the transient microstructure over the full range of Pe, a numerical solution of the Smoluchowski equations (5.10) and (5.11) is required. Here, gradients are discretized utilizing a second-

order finite-difference scheme. The discretization grid must account for the evolving shape of the microstructure in both space and time. In order to properly capture the spatial gradients inside the boundary layer, we follow the method of Khair & Brady (2006). Here, the radial coordinate is rescaled with Pe^{-1} to obtain the stretched coordinate $Y = Pe(r-1)$. Because the flow is axisymmetric about the line of external forcing, derivatives of $g(\boldsymbol{r})$ in the azimuthal angle are zero. Defining $x \equiv 1 + Y/Pe$, we have for the governing equations at startup:

$$\begin{aligned} Pe^{-2}\frac{\partial f}{\partial \hat{t}} &= \frac{\partial^2 f}{\partial Y^2} + Pe^{-1}\frac{2}{x}\frac{\partial f}{\partial Y} + \frac{Pe^{-2}}{x^2\sin\theta}\frac{\partial}{\partial\theta}\left(\sin\theta\frac{\partial f}{\partial\theta}\right) - \cos\theta\frac{\partial f}{\partial Y} + Pe^{-1}\frac{\sin\theta}{x}\frac{\partial f}{\partial\theta}, \quad (5.28)\\ \frac{\partial f}{\partial Y} &= \cos\theta(f+1) \quad \text{at} \quad Y = 0,\\ f &= 0 \qquad\qquad\quad \text{as} \quad Y \to \infty,\\ f &= 0 \qquad\qquad\quad \text{at} \quad \hat{t} = 0. \end{aligned}$$

For flow cessation, the time-dependent diffusion equation (5.11) becomes

$$\begin{aligned} Pe^{-2}\frac{\partial f}{\partial \hat{t}} &= \frac{\partial^2 f}{\partial Y^2} + Pe^{-1}\frac{2}{x}\frac{\partial f}{\partial Y} + Pe^{-2}\frac{1}{x^2\sin\theta}\frac{\partial}{\partial\theta}\left(\sin\theta\frac{\partial f}{\partial\theta}\right), \quad (5.29)\\ \frac{\partial f}{\partial Y} &= 0 \qquad\qquad \text{at} \quad Y = 0,\\ f &= 0 \qquad\qquad \text{as} \quad Y \to \infty,\\ f &= f_0^{SS}(\boldsymbol{r}, Pe) \quad \text{at} \quad \hat{t} = 0. \end{aligned}$$

A central difference scheme is used to discretize spatial gradients over the two-dimensional domain. Once the boundary layer forms, the radial gradients in the microstructure are almost entirely confined to the boundary layer. As Pe continues to grow and the boundary layer thins, a grid point concentration function that varies with Pe increases the density of grid points close to contact, yet retains sufficient resolution far from the probe to capture the physics throughout the upstream domain (Bergenholtz *et al.*, 2002). The difference coefficients and operators for both radial and angular directions are compactly arranged into first- and second-order sparse matrices, and the discretized

PDE takes on the form

$$\boldsymbol{M} \cdot \boldsymbol{f} = \dot{\boldsymbol{f}}, \tag{5.30}$$

where $\boldsymbol{f}$ is the solution array for all grid points, $\dot{\boldsymbol{f}} \equiv \partial \boldsymbol{f}/\partial \hat{t}$, time is scaled on the boundary layer thickness, and $\boldsymbol{M}$ is the super-matrix containing the coefficient and finite-difference matrices that operate on the solution $\boldsymbol{f}$. The solution for the homogeneous (*i.e.* time-independent) pair-distribution microstructure $f_0^{SS}(Pe)$ is obtained by solving (5.30) with the left-hand side equal to zero. The boundary condition at contact results in a non-trivial solution. The homogeneous problem was solved in Chapter 3 utilizing MATLAB and a LAPACK iterative banded solver. To obtain the transient microstructure over the full range of Pe during startup and cessation, we recognize that each row in (5.30) is a linear ordinary differential equation in time. The Method of Lines is used to solve this system of initial value problems, and is implemented using MATLAB's ODE45 solver. Time is discretized automatically using the Jacobian of the matrix $\boldsymbol{M}$.

Formation of the steady microstructure: startup behavior

We begin by solving the startup problem, where the initial condition is an unperturbed microstructure. Figure 5.7 gives a plot of the microviscosity just after startup, for a dilute dispersion of equally sized spheres, driven by a same-size probe particle. Time is scaled diffusively. The structure and the stress evolve together, at first diffusively regardless of Pe; but at longer times, the higher the Péclet number, the faster the approach to steady state. A comparison between the steady-state value for the microviscosity (Squires & Brady, 2005; Khair & Brady, 2006) is shown in Table 5.1.

Pe	$\eta_{SS}^{micro}/\eta\phi_b$	$\eta^{micro}(\hat{t}\to\infty)/\eta\phi_b$	% error
1	1.88	1.9	+1.1%
5	1.48	1.48	0%
10	1.32	1.29	−2.3%
30	1.14	1.05	−7.9%
50	1.10	1.00	−10%
80	1.07	0.97	−9.4%
100	1.06	0.89	−19%

Table 5.1: Comparison of long-time value of transient microviscosity obtained in this study to the steady-state value obtained from solving the steady probe-motion problem (Squires & Brady, 2005; Zia & Brady, 2010).

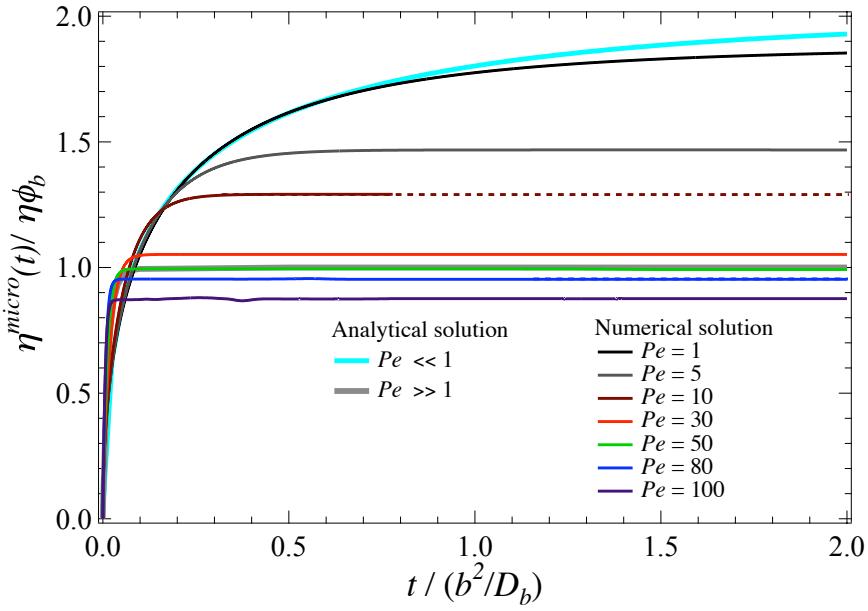

Figure 5.7: Startup of probe forcing: The initial increase in the viscosity is steep and appears independent of Pe. The probe's disturbance then propagates via collisions with the bath particles and the structure begins to form. As $\hat{t} \to \infty$, the microstructure reaches steady state and the viscosity asymptotes to its steady value. (dashed lines indicate manual extension of data based on asymptotic value.)

For moderate values of Pe, the agreement is excellent. As Pe becomes large, the long-time transient value under-predicts the steady-state value. The source of this error is numerical; since the identical discretization was used for the steady-state solution and the homogeneous solution, the error arises in the solution of the initial-value problem, which is a very stiff equation. As Pe increases the rise from equilibrium to steady state is much steeper in time. The MATLAB function ODE45 was used, which is a general ODE solver; however, other functions within MATLAB have been optimized for stiff equations, such as ODE15 . Such equations utilize multistep discretization that control both stability and error propagation through the Jacobian. The drawback is that such methods can be computationally very expensive. A reduced error may be obtained by utilizing a stiff solver. At the opposite limit of small Pe, was taken in selecting a sufficient number of grid points in the small-Pe regime: The discretization is second-order, so a sufficiently large number of grid points was selected in order to avoid generating an additional (erroneous) diffusive forcing in the governing equations. The early transient behavior is shown in figure 5.8. The transient microviscosity at short times scales as $\eta^{micro}(\hat{t})/\eta \sim \hat{t}^{1/2}$. This result agrees with the analytical solution for short times, and with

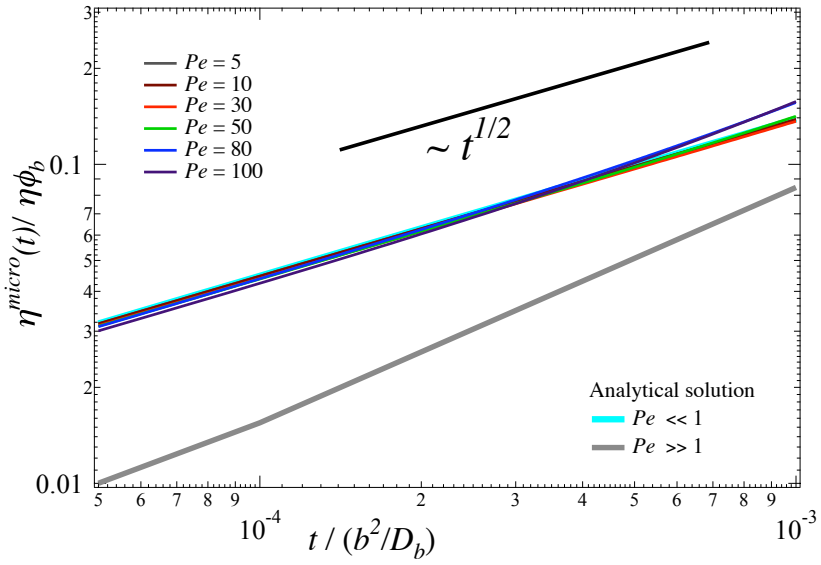

Figure 5.8: Startup of probe forcing: At very short times, a log-log plot reveals the $\hat{t}^{1/2}$ scaling of the viscosity, regardless of Pe.

the scaling prediction of §5.2.

At short times, the propagation of force through the microstructure is $1D$ monopolar. The probe sees only the local structure, which is so compressed in time that it appears locally planar in time. As the probe explores longer time regions, it interacts with the structure, and is when the Péclet number becomes relevant because the structure is disturbed. The curves for various Pe start to separate as the structure forms. The disturbance is communicated through the suspension by particle collisions—at higher Pe, the probe moves farther in a given time and thus propagates the disturbance more quickly. Force-thinning behavior observed in steady-state suspensions is evident, as the long-time plateau decreases with Pe.

Relaxation of microstructure and stress: cessation behavior

Here we explore how the stress decays with time when the external force is removed. How long does it take for the suspension to come to rest? The decay in viscous force after shutoff is plotted in figure 5.9. An initially rapid decay of the stress at very short times is followed by a slower long-time decay—indicating at least two relaxation modes. The rate of decay also varies with the initial condition: the higher the pre-cessation Pe, the faster the relaxation. While it seems counterintuitive that a more

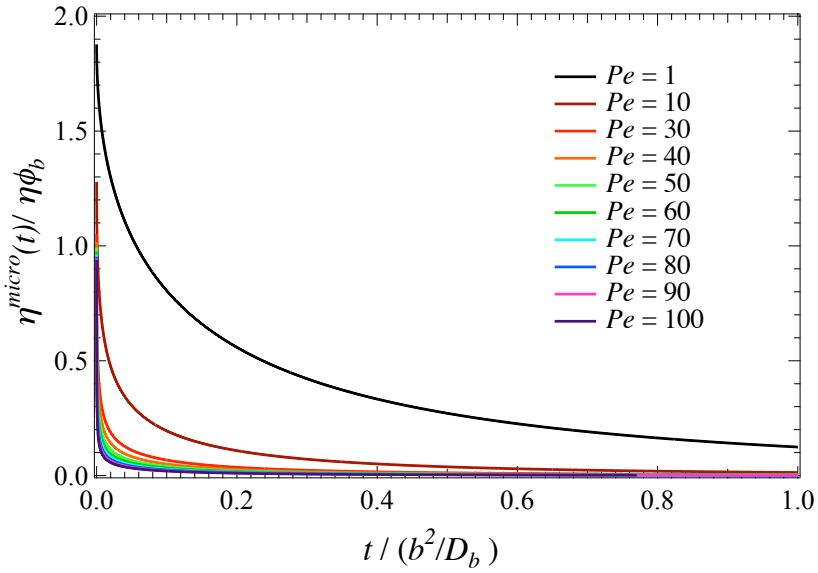

Figure 5.9: Flow cessation: Viscosity drops rapidly from its steady-state value. The rate at which the viscosity and stress relax increases with increasing Pe—the initial relaxation is due to the motion of the probe through the boundary layer of thickness $\delta \sim (a+b)/Pe$. The structure continues to relax more slowly at long times.

strongly deformed microstructural disturbance would decay faster than a weakly deformed one, the microstructure explains the behavior: the probe need only diffuse the length of the boundary layer in order to relieve contact stress—as was seen in equation 5.3. That diffusive distance scales as Pe^{-1}, so the higher the Péclet number, the faster the initial relaxation.

The relaxation over several time scales corresponds to distinct physical processes. For very short times, the time scale for relaxation is set by the boundary layer of thickness $\delta \sim (a+b)/Pe$, and so $\tau \sim \delta^2/D_r$, where D_r is the relative diffusivity between the probe and a bath particle. Nearly all probe force relaxation occurs during this process, owing to the dependence of the bath-particle drag on the contact value of the microstructure. At longer times the Brownian diffusion of the bath particles acts to close the Pe-long wake on a time scale set by how long it takes a bath particle to move its size: $\tau \sim b^2/D_b$. In this long-time limit as structural isotropy is restored, the majority of the microstructural relaxation occurs with very little change in probe speed.

In figure 5.10, the transient microviscosity has been multiplied by the Péclet number, which collapses the curves for all Pe onto one curve at long times. The decay in viscosity and suspension stress can evidently be made independent of the initial condition, indicating loss of memory of the

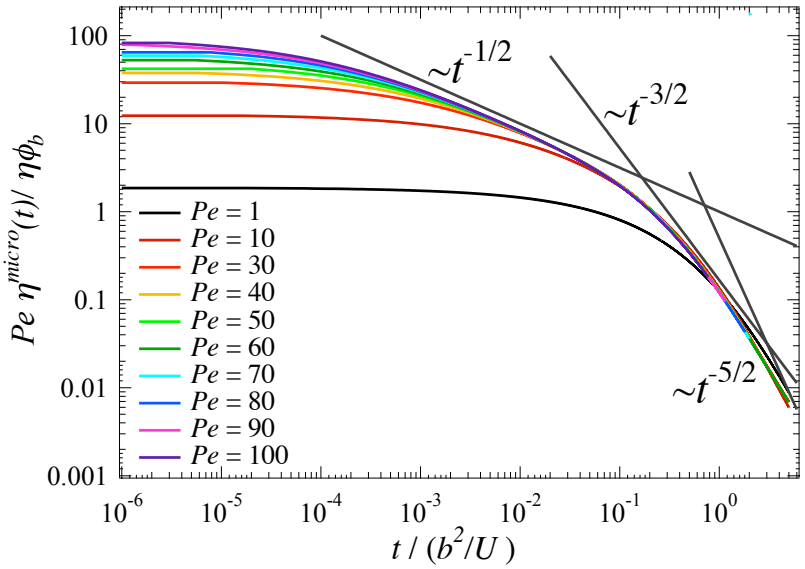

Figure 5.10: Flow cessation: Viscosity plotted on advective time scale, where U was the velocity of the probe prior to shutoff. All lines collapse together at long times, indicating the loss of memory of the initial condition.

previous structure. The long-time decay follows several distinct scalings, corresponding to the relaxation of the probe into the surrounding microstructure. The initial decay is through the boundary layer; this highly local process is one-dimensional inside the boundary layer, and thus the scaling is a 1D diffusive monopole ($\sim t^{-1/2}$). As the probe continues to relax into the microstructure, it becomes a fully 3D diffusive monopole ($\sim t^{-3/2}$). Finally, at very long times, the probe undergoes equilibrium fluctuations and disturbs the suspension with a diffusive dipole ($\sim t^{-5/2}$). In contrast to the radial-balance approximation made in the analytical solution, the numerical solution includes angular gradients that now reveal the full relaxation behavior expected from physical arguments.

5.7 Brownian dynamics simulation

An alternative approach to studying particle behavior in a colloidal suspension is to examine the detailed dynamics of individual particle motion. In chapter 3 we discussed the Brownian dynamics numerical algorithm for simulating individual particle motion in a Newtonian solvent. Continuing with the same approach, here the particle velocity was monitored and the transient microviscosity then computed as outlined in chapter 2 via application of Stokes' drag law. We study not only

the evolution of the microviscosity as it evolves from equilibrium to steady state and then relaxes back to equilibrium—but more importantly, an understanding of *how* this evolution is connected to structural changes in the bath is sought. To this end, each plot of the transient microviscosity is accompanied by a series of "density snapshots"—instantaneous images of the microstructure at key points of change in the viscosity.

To obtain the transient microviscosity, the particle velocity $\boldsymbol{U}^P$ (cf chapter 2) was measured at each time step and averaged over simulations to obtain an ensemble, time-dependent average. The particle density was also measured (in a frame of reference moving with the probe) in a one-diameter-thick slice of the simulation cell parallel with the direction of probe forcing, passing through the probe center. Color scheme in the density plots is set for maximum contrast; blue areas correspond to regions of particle-center depletion, while red and yellow regions correspond to areas of high and moderate particle-probability accumulation respectively. The density measurement was taken at eight selected times as noted in each caption (the times are labeled on the graph and on each density snapshot with circled numbers). Each corresponds to a specific time in the startup or cessation of the flow. All data are an ensemble average over 18,000 simulations.

Constant-external force

We begin with a study of the transient viscosity as measured by the drag on a probe being driven by a constant external force. Figure 5.11 gives a plot of the results, for a volume fraction $\phi_b = 0.35$ and a range of Pe. The accompanying "density snapshots" in figure 5.12 are for $Pe = 30$, $\phi_b = 0.35$. Probe forcing is initiated at $\hat{t} = 0$, and continues for one diffusive time step. The force is then instantaneously removed at $\hat{t} = 1$.

Before the flow is turned on, the microstructure is at equilibrium. The probe motion is started and the equilibrium microstructure is destroyed (snapshot 1). Particles collide and propagate the stress, and as steady state is approached, the boundary-layer shape characteristic of high-Pe flows emerges (snapshots 3 and 4). The curves agree with the theoretical results shown in figure 5.7, and the long-time asymptotes are in excellent agreement with the steady-state values tabulated in table 5.1. Force-thinning behavior observed in steady-state suspensions is evident, as the long-time

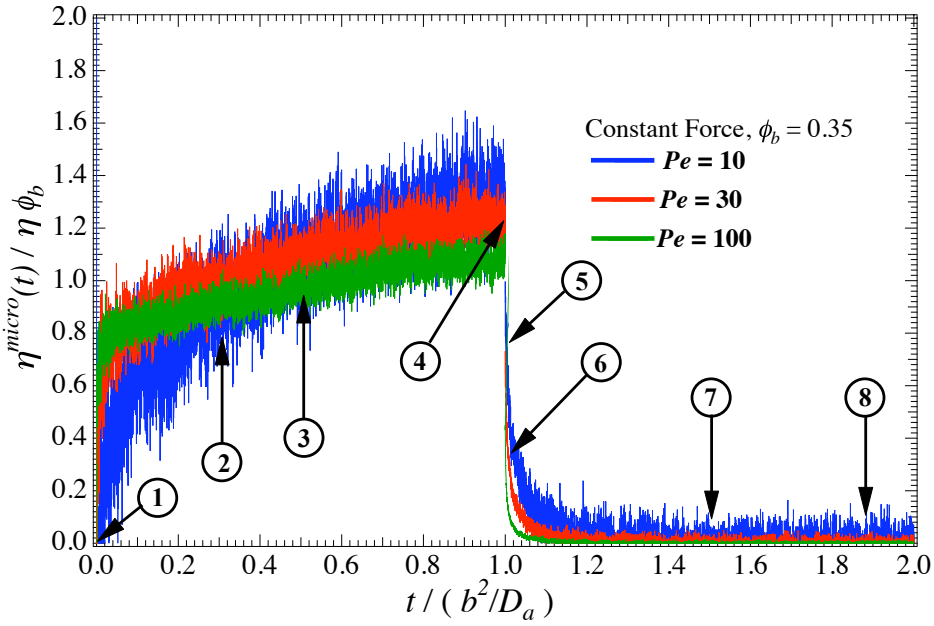

Figure 5.11: Brownian dynamics simulation results: Transient microviscosity as a function of time, for a probe driven by a constant external force through the bath at various values of Pe for volume fraction $\phi_b = 0.35$. The microviscosity is the $O(\phi_b)$ viscous drag due to hard-sphere collisions with background bath particles. Forcing starts at $\hat{t} = 0$ and is shut off at $\hat{t} = 1$.

plateau decreases with Pe.

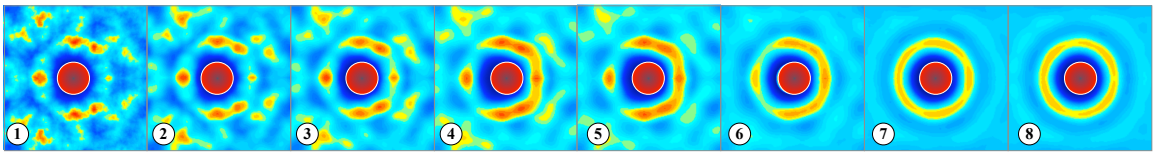

Figure 5.12: Density plot: time-evolution of the microstructure for constant force; $Pe = 30$; $\phi_b = 0.35$ at: $\hat{t}_1 = 0+$; $\hat{t}_2 = 0.2$; $\hat{t}_3 = 0.5$; $\hat{t}_4 = 1.0$; $\hat{t}_5 = 1.01$; $\hat{t}_6 = 1.2$; $\hat{t}_7 = 1.5$; $\hat{t}_8 = 1.9$. Data correspond to red trace in figure 5.11.

After steady state has been reached in the simulation, the probe forcing is turned off (point 4 in figure 5.11), while particle velocity continues to be monitored. As seen in the change from point 4 to point 5, over a very small time scale the majority of the stress relaxes. As time continues (points 7 and 8) the stress changes very little, but the microstructural relaxation continues for a much longer time (snapshots 7 and 8), via the Brownian motion of the bath particles.

Figures 5.13, 5.14, and 5.15 show a comparison of how the microstructural density evolves and relaxes at $Pe = 30$, for a range of volume fractions. The density plots indicate that perhaps the wake has not fully formed within one diffusive time step for the higher-density suspensions—the wake has not fully broken the ring of nearest neighbors in the downstream region of the probe—and

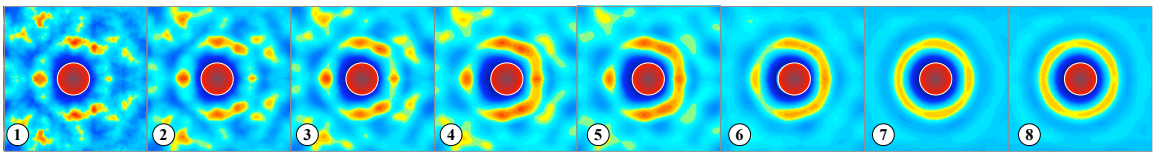

Figure 5.13: Density plot: time-evolution of the microstructure for constant force; $Pe = 30$; $\phi_b = 0.35$ at: $\hat{t}_1 = 0+$; $\hat{t}_2 = 0.2$; $\hat{t}_3 = 0.5$; $\hat{t}_4 = 1.0$; $\hat{t}_5 = 1.01$; $\hat{t}_6 = 1.2$; $\hat{t}_7 = 1.5$; $\hat{t}_8 = 1.9$. Data correspond to cyan trace in figure 5.16.

possibly that the time to reach steady state increases with a more dense suspension.

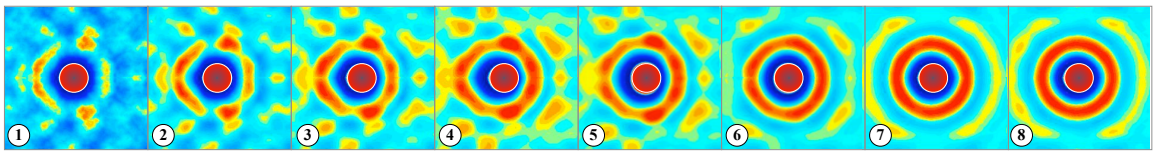

Figure 5.14: Density plot: time-evolution of the microstructure, constant force; $Pe = 30$; $\phi_b = 0.40$ at: $\hat{t}_1 = 0+$; $\hat{t}_2 = 0.2$; $\hat{t}_3 = 0.5$; $\hat{t}_4 = 1.0$; $\hat{t}_5 = 1.01$; $\hat{t}_6 = 1.2$; $\hat{t}_7 = 1.5$; $\hat{t}_8 = 1.9$. Data correspond to red trace in figure 5.16.

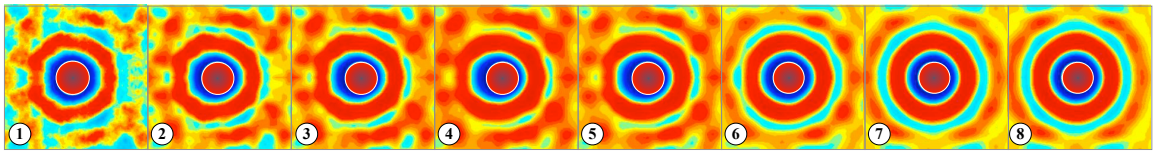

Figure 5.15: Density plot: time-evolution of the microstructure for constant force; $Pe = 30$; $\phi_b = 0.45$ at: $\hat{t}_1 = 0+$; $\hat{t}_2 = 0.2$; $\hat{t}_3 = 0.5$; $\hat{t}_4 = 1.0$; $\hat{t}_5 = 1.01$; $\hat{t}_6 = 1.2$; $\hat{t}_7 = 1.5$; $\hat{t}_8 = 1.9$. Data correspond to blue trace in figure 5.16.

The effect of volume fraction on the formation stress is shown in figure 5.16, which shows the transient viscosity at $Pe = 30$ for a range of volume fractions ϕ_b. Normalizing the viscosity by ϕ_b collapses the data onto one curve as $\hat{t} \to \infty$. The curves remain distinct at early startup times, however. The initial slope between points 1 and 2 on the plot is steeper for higher volume fraction. This behavior supports the idea that stress propagation occurs by particle collisions: The travel distance for a collision is shorter in a more dense suspension. By way of an analogy to solid mechanics, the speed c of a stress wave through a material increases with the stiffness of the material: $c \sim \sqrt{E/\rho}$, where E is the stiffness and ρ the mass-density. In our colloidal suspension, the result indicates that a more dense suspension is initially "stiffer." At longer times, a comparison of the curves for $\phi_b = 0.35$ and $\phi_b = 0.40$ indicates that steady state is reached faster for the more dense suspension, because the slope of the former is still nonzero. The behavior for $\phi_b = 0.45$ is similar to that for $\phi_b = 0.40$. This contradicts the conclusion drawn from visual inspection of the density plots; there, we said that because the symmetry of the ring of nearest neighbors (the red ring)

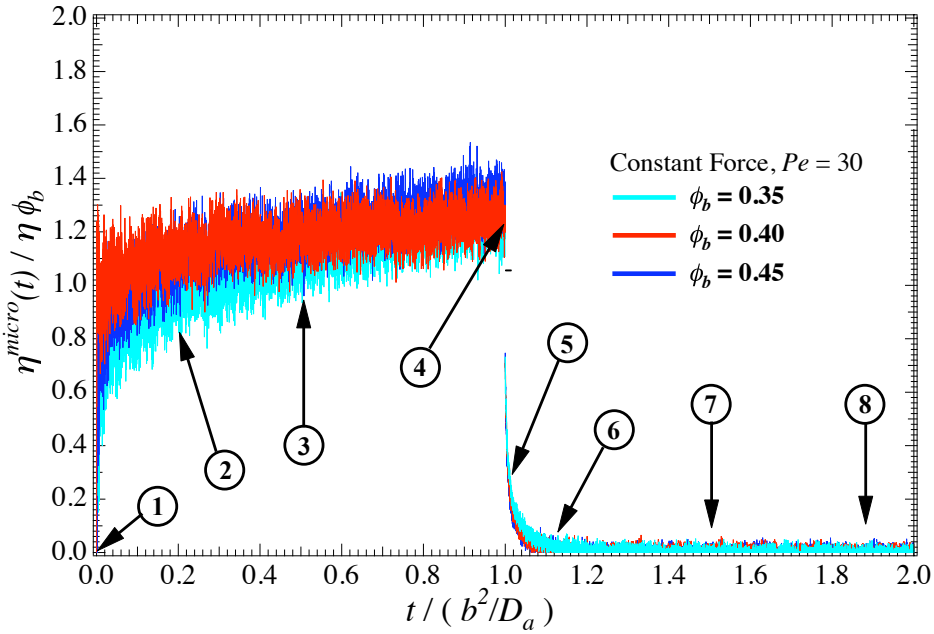

Figure 5.16: Transient microviscosity as a function of time, for a probe driven by a constant external force through the bath at $Pe = 30$ for various volume fractions of bath particles. The microviscosity is the $O(\phi_b)$ viscous drag due to hard-sphere collisions with background bath particles. Forcing starts at $\hat{t} = 0$ and is shut off at $\hat{t} = 1$.

was less fully broken in the higher volume-fraction plots, that steady state may be delayed. The apparent contradiction between the two may indicate that boundary-layer formation is the more critical feature of steady-state viscosity than is depletion-wake formation.

The position of the probe was also monitored during the simulation. Figure 5.17 is a plot of the absolute probe position, as a function of time, for $Pe = 30$, $\phi_b = 0.35$. During startup, two distinct slopes can be seen (denoted by the grey solid lines next to the startup curve): Initially rapid motion, after which the probe slows down as the microstructure develops; a boundary layer forms on the probes upstream face, and the bath thickens to its steady-state value.

Importantly, the probe travels backwards immediately after cessation ($1 \leq \hat{t} \lesssim 1.2$), as seen in figure 5.17. The suspension remembers configurations from the past for a finite period of time; removal of the force allows the probe to return to a previous configuration. This motion reveals *nonlinear elasticity* in colloidal dispersions. Such behavior is common in entangled polymers and other topologically hindered materials. But its presence in a suspension of spherical colloids is evidence of the entropic origin of nonlinear viscoelasticity. As the force on the probe presses into an

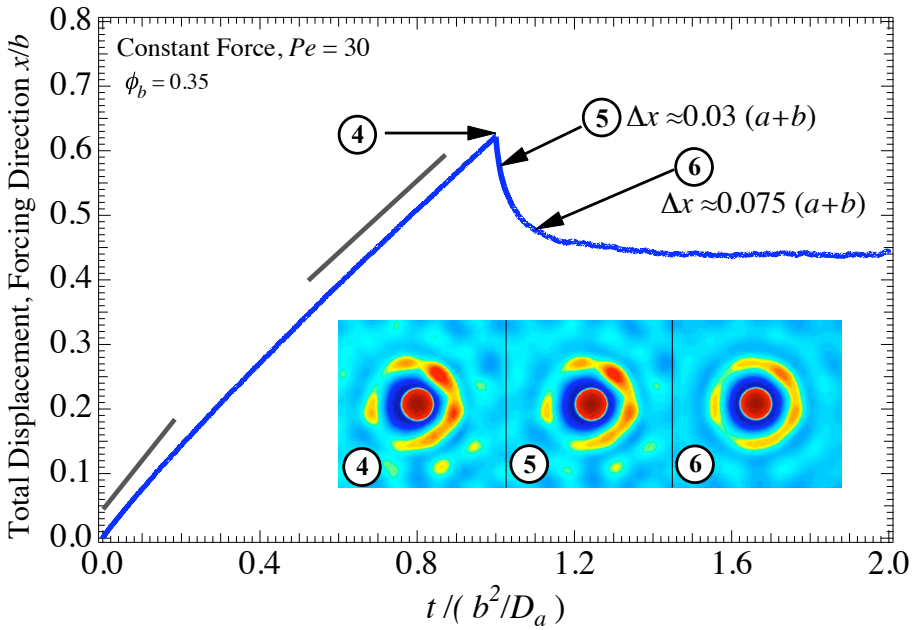

Figure 5.17: Displacement of the probe as a function of time (blue line), during startup and cessation of probe forcing. Grey lines indicate difference in startup slope from intermediate time versus long time. Data shown are for constant-external force. Forcing starts at $\hat{t} = 0$ and is shut off at $\hat{t} = 1$.

upstream region of bath particles, it compresses their configuration. Upon release of the external force, the structure springs back, like a mechanical return spring, and pushes the probe backwards. This entropic elasticity is the return of the free-energy density stored in the microstructure. Stress in hard-sphere dispersions is therefore a measure of its ability to store free energy. In contradistinction, a single particle in pure fluid dissipates all of its energy on any time scale longer than its momentum relaxation time.

We recall from figure 5.11 that the majority of the *stress* in the suspension relaxes very quickly upon shutoff; it was proposed that the mechanism for this relaxation was the motion of the probe backward through the boundary layer. For $Pe = 30$, the back-travel should be approximately the boundary-layer thickness $\delta \sim (a+b)/Pe \approx 0.033$. A coarse measurement of the "slope" of the back-travel region in figure 5.17 indicates that the initial back-travel distance is approximately $0.03(a+b)$, at which point much of the stress has relaxed. As the microstructure continues to relax, the probe back-travels for a total of $\Delta x \approx 0.075(a+b)$. The corresponding density plots showing the probe in red and the microstructure around it are inset in the figure. The stress relaxation, travel distance,

boundary-layer thickness, and density plots appear to agree. The initial back-travel shows that much of the stress relaxation is due to the separation of the probe from the boundary layer. The remainder arises due to the entropic relaxation of the microstructure around the probe. What is the entropic force associated with the release of the free energy during relaxation? The entropic force $F^{entropic}$ is thermal, and then should scale as $kT/\Delta x$, or

$$F^{entropic} \approx 13.3\frac{kT}{a+b}, \tag{5.31}$$

for the total back-travel of the probe ($\Delta x \approx 0.075(a+b)$). In the limit of a very small probe, the entropic force is approximately $F^{entropic} \approx 6.7kT/b$. In the limit of a very large probe, the bath particles diffuse very quickly and close the boundary layer before the probe can travel backwards into the wake—hence it should experience no back-travel, and $F^{entropic}/(kT/b) \to 0$.

Constant-external velocity

In this section, we investigate transient microrheology behavior when the probe is constrained to travel at a constant velocity $\boldsymbol{U}$ (Mode 2), rather than being driven by a constant external force (Mode 1) as in the previous section. The difference in the two forcing modes has interesting dynamical consequences. Because the Mode-2 probe cannot fluctuate, it cannot diffuse around other particles. It must push them out of its way, which may lead to a larger accumulation of particles in the boundary layer, and a longer depletion wake. In addition, spikes and dips in the force may arise in order to maintain constant velocity. In contrast, a constant-force probe will adjust its velocity if it encounters regions of higher or lower density. A higher boundary-layer density will lead to higher viscous drag. Squires & Brady (2005) proposed that the two modes would lead to different drag; they solved for the constant-force microviscosity and predicted a doubling of the Mode-2 steady-state microviscosity, where the factor of two comes their diffusive scaling argument discussed earlier.

Figure 5.18 gives a plot of the transient microviscosity in the case of a probe being driven at constant-velocity through a suspension for a range of Pe, at volume fraction of background bath particles $\phi_b = 0.35$. The steady-state viscosity is indeed larger than the Mode 1 values (cf figure

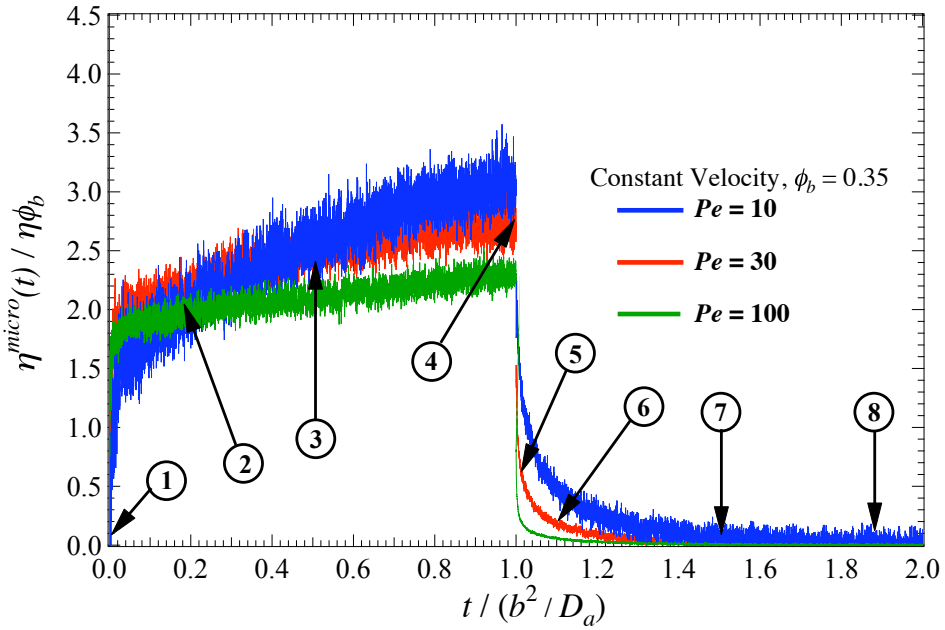

Figure 5.18: Transient microviscosity as a function of time, for a probe traveling at constant velocity through the bath for various Pe, volume fraction $\phi_b = 0.35$. The microviscosity is the $O(\phi_b)$ viscous drag due to hard-sphere collisions with background bath particles; in the case of constant-velocity forcing, although the probe velocity does not fluctuate, the velocity due to hard-sphere collisions does. Forcing starts at $\hat{t} = 0$ and is shut off at $\hat{t} = 1$.

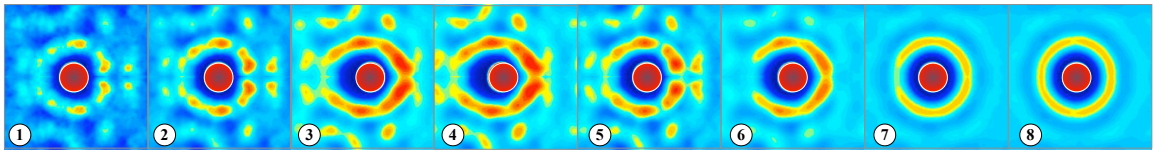

Figure 5.19: Density plot: time-evolution of the microstructure for constant velocity; $Pe = 30$; $\phi_b = 0.35$ at: $\hat{t}_1 = 0+$; $\hat{t}_2 = 0.2$; $\hat{t}_3 = 0.5$; $\hat{t}_4 = 1.0$; $\hat{t}_5 = 1.01$; $\hat{t}_6 = 1.2$; $\hat{t}_7 = 1.5$; $\hat{t}_8 = 1.9$. Data correspond to red trace in figure 5.18.

5.13). Force-thinning behavior is evident, as the steady-state viscosity decreases with Pe. For $Pe = 100$, the simulation results are excellent agreement with the prediction by Squires & Brady that $\eta_U^{micro} = 2\eta_F^{micro}$. The agreement is good for smaller Pe, with measured values approximately 10% higher than the Squires & Brady prediction. Because the volume fraction here is clearly not dilute ($\phi_b = 0.35$), some disagreement is expected. The data are also compared in the following section with the results of Carpen & Brady (2005), who conducted Brownian dynamics simulations at steady state and compared the steady value of the constant-force versus constant-velocity microviscosity. In snapshots 3, 4, and 5 of figure 5.19, the particle accumulation (shown in red and yellow) on the upstream face of the probe is higher and the trailing wake (depletion shown in blue and dark blue)

more pronounced as compared to the corresponding Mode-1 plots (figure 5.13). This structure is consistent with the notion of the Mode-2 probe as a "bulldozer" that pushes particles out of its way without slowing down. Evidently the consequence is a higher viscous resistance.

It should be pointed out that the long-time region of the startup curves do not appear to have reached a plateau. If the simulations have not yet reached steady state at $\hat{t} = 1$, a longer startup time may reveal higher yet asymptotes. Alternatively, if the long-time region were to decay at longer times to the predicted steady value, the non-monotonic behavior would agree with similar overshoot observations in constant strain-rate startup in sheared suspensions (Foss & Brady, 2000*a*,*b*).

When the flow is shut off, the stress relaxation is markedly slower for smaller pre-cessation Pe than for higher Pe. But the mechanism for relaxation is different in the case of constant-velocity forcing, although the dependence on boundary-layer thickness is the same. Here, the probe's velocity is constrained to be zero at shutoff. It cannot diffuse to relax through the boundary layer. In consequence, stress relaxation occurs only via the Brownian diffusion of the bath particles out of the boundary layer. For higher Pe, the boundary layer is more concentrated but thinner; the higher the Péclet number, the shorter the distance that must be traversed by the bath particles in order to relieve the stress.

The effect of volume fraction on startup and cessation behavior is illustrated in figure 5.20, for constant velocity at $Pe = 30$. Importantly, scaling the viscosity with volume fraction ϕ_b does not collapse the data onto one curve for the startup regime, as it did in in the constant-force regime (cf figure 5.16). Insight into this qualitative difference in behavior can be gained by examining the evolving microstructure. Again this is related to the "bulldozer" analogy for the constant-velocity probe; as ϕ_b increases, a Mode-1 probe can adjust its velocity easily in more dense regions, but a Mode-2 probe cannot. In consequence, more particles accumulate on the upstream face of the probe. The viscosity is determined by the microstructure at contact, so higher concentrations increase viscous drag. Recall that the microstructural density increases both with volume fraction and with forcing, $g(\phi; Pe)$. A re-scaling of Pe with the long-time self-diffusivity for concentrated suspensions may achieve a universal curve.

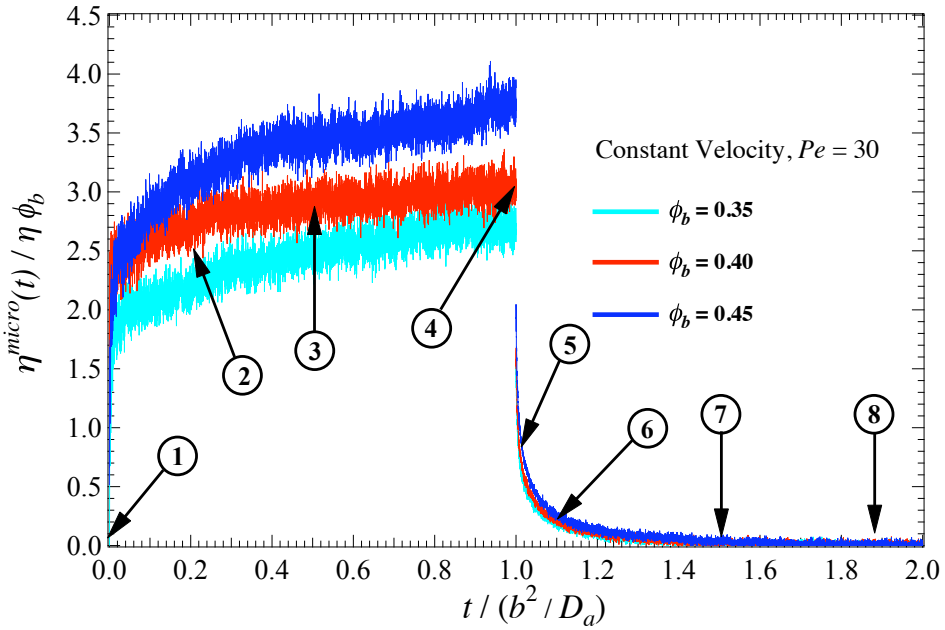

Figure 5.20: Transient microviscosity as a function of time, for a probe traveling at constant velocity through the bath at $Pe = 30$ for various volume fractions of bath particles. The microviscosity is the $O(\phi_b)$ viscous drag due to hard-sphere collisions with background bath particles; in the case of constant-velocity forcing, although the probe velocity does not fluctuate, the velocity due to hard-sphere collisions does. Startup at $\hat{t} = 0$ and is shut off at $\hat{t} = 1$.

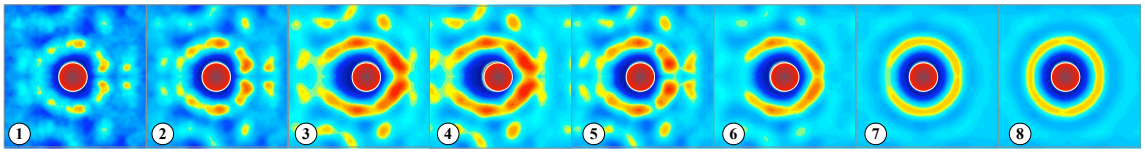

Figure 5.21: Density plot: time-evolution of the microstructure, constant velocity; $Pe = 30$; $\phi_b = 0.35$ at: $\hat{t}_1 = 0+$; $\hat{t}_2 = 0.2$; $\hat{t}_3 = 0.5$; $\hat{t}_4 = 1.0$; $\hat{t}_5 = 1.01$; $\hat{t}_6 = 1.2$; $\hat{t}_7 = 1.5$; $\hat{t}_8 = 1.9$. Data correspond to cyan trace in figure 5.20.

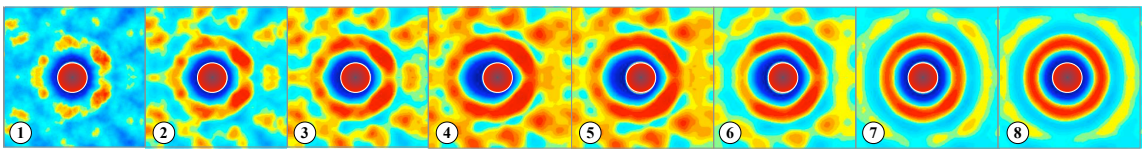

Figure 5.22: Density plot: time-evolution of the microstructure, constant velocity; $Pe = 30$; $\phi_b = 0.40$ at: $\hat{t}_1 = 0+$; $\hat{t}_2 = 0.2$; $\hat{t}_3 = 0.5$; $\hat{t}_4 = 1.0$; $\hat{t}_5 = 1.01$; $\hat{t}_6 = 1.2$; $\hat{t}_7 = 1.5$; $\hat{t}_8 = 1.9$. Data correspond to red trace in fig. 5.20.

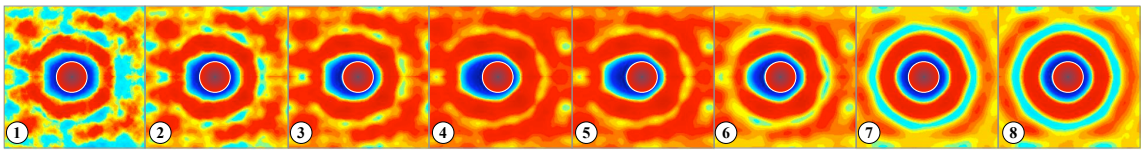

Figure 5.23: Density plot: time-evolution of the microstructure, constant velocity; $Pe = 30$; $\phi_b = 0.45$ at: $\hat{t}_1 = 0+$; $\hat{t}_2 = 0.2$; $\hat{t}_3 = 0.5$; $\hat{t}_4 = 1.0$; $\hat{t}_5 = 1.01$; $\hat{t}_6 = 1.2$; $\hat{t}_7 = 1.5$; $\hat{t}_8 = 1.9$. Data correspond to blue trace in fig. 5.20.

Effect of forcing mode: Constant force versus constant velocity

In the previous section it was shown that the transient microviscosity attains a steady-state value that decreases with Pe, increases with volume fraction ϕ_b, and exhibits a factor of two difference depending on whether the mode of probe forcing is a constant applied force or is an imposed constant velocity. The long-time behavior thus agrees with the steady-state theory results of Squires & Brady (2005) and Khair & Brady (2006), and the dynamic simulation results of Carpen & Brady (2005). In this section we continue this comparison the viscosity-doubling behavior. In figure 5.24, a plot

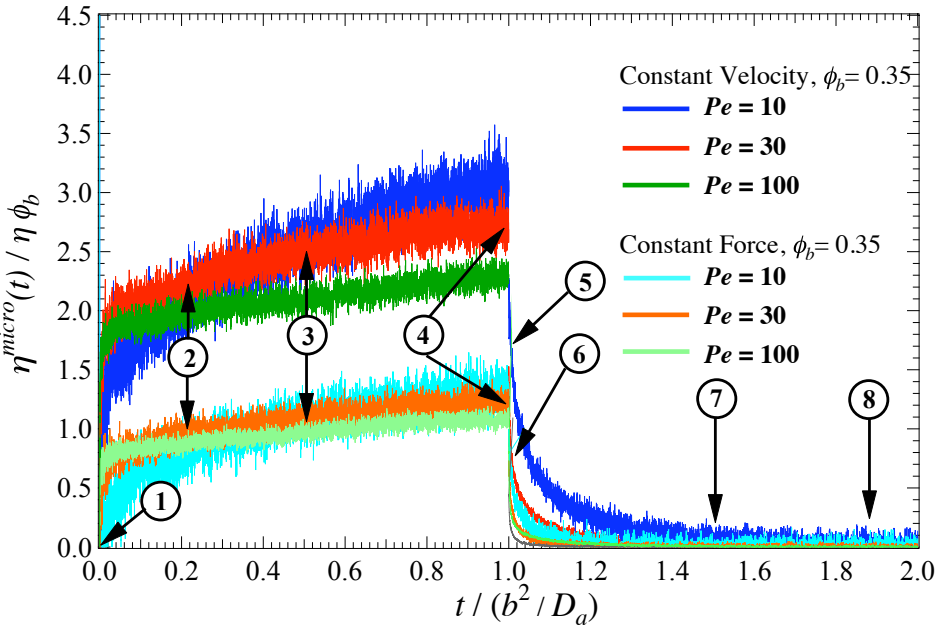

Figure 5.24: Transient microviscosity as a function of time, for Mode 1 (constant force) and Mode 2 (constant velocity) probe forcing, for three values of Pe and volume fraction $\phi_b = 0.35$. The microviscosity is the $O(\phi_b)$ viscous drag due to hard-sphere collisions with background bath particles. Forcing starts at $\hat{t} = 0$ and is shut off at $\hat{t} = 1$.

of the microviscosity during startup and cessation for a range of Pe and with volume fraction $\phi_b = 0.35$showing a direct comparison between the transient microviscosity when measured by the two different forcing modes: constant imposed velocity (Mode 2, the top three curves) and constant external force (Mode 1, the bottom three curves). The approximate doubling of the long-time viscosity in Mode 2 can be understood from a microstructural perspective by comparing it to the density plots in figure 5.25. At long times after startup (snapshot 4) the boundary layer of mode 2 (top row) appears to be wider and more dense than that of the corresponding frame below it in

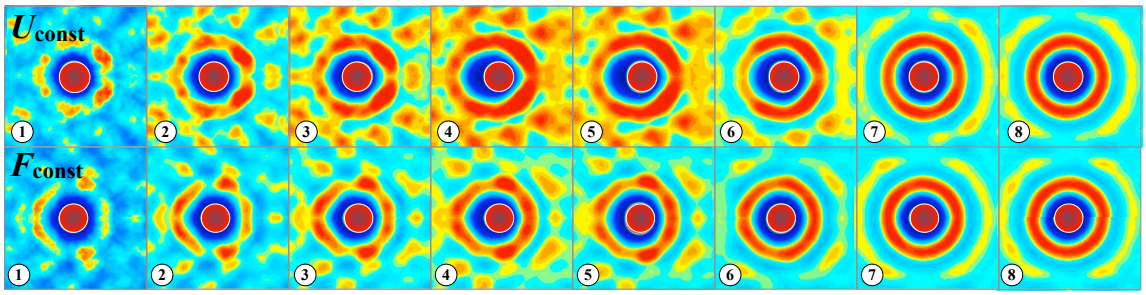

Figure 5.25: Constant force versus constant velocity: time-evolution of the microstructure with $Pe = 30$; $\phi_b = 0.40$ at: $\hat{t}_1 = 0+$; $\hat{t}_2 = 0.2$; $\hat{t}_3 = 0.5$; $\hat{t}_4 = 1.0$; $\hat{t}_5 = 1.01$; $\hat{t}_6 = 1.2$; $\hat{t}_7 = 1.5$; $\hat{t}_8 = 1.9$.

Mode 1. Recalling the dependence of the microviscosity on the contact microstructure in equation 5.3, it is easy to see the connection between higher boundary-layer density and higher viscosity.

After shutoff, comparison between the two sets of curves in figure 5.24 shows that relaxation of the stress has a qualitative dependence on whether the forcing mode is constant-velocity or constant-force. The freedom of the probe to fluctuate and "wiggle"around in the microstructure not only reduces viscous drag, but also allows a faster stress relaxation. Evidently, velocity fluctuations can relieve non-equilibrium stress in colloidal dispersions. This makes sense physically, in that the ability to move in response to a force generally alleviates the applied stress.

If at a given Pe, for each forcing mode the probe carries the same energy, there is a difference in how much of that power is stored in microstructural rearrangement and how much is dissipated through fluctuations. More energy is stored in the more compressed microstructure under constant-velocity forcing. Although this may seem to contradict the fact that the constant-velocity mode has a higher viscosity, *i.e.* its motion is more dissipative, we must be careful to scale Pe with the proper diffusivity, which is half of that for constant-force mode.

It can also be seen that the longer wake in the constant-velocity mode takes longer to close than in the case of constant force. Wake closure occurs only via the Brownian diffusion of bath particles laterally into the wake. The length of the wake does not matter. However, the stronger anisotropy of the microstructure in Mode 2 gives rise to a longer time for particles to distribute randomly around the probe.

The small quantitative disagreement between predicted and measured steady-state microviscosity

may reflect a different scaling for a more concentrated suspension. Alternatively, it is possible that the simulations run here did not reach steady state by the time the flow was shut off and, that if allowed to continue, the curve would flatten and decay to the steady-state value. If such non-monotonic behavior exists, it would be evidence of "overshoot" behavior measured by dynamic simulation in constant strain-rate macrorheology (Foss & Brady, 2000*b*). Another possibility is that the scaling prediction does not apply to suspensions at the high volume fractions shown. To determine if this is the case, results for suspensions at lower concentration should collapse together when scaled by ϕ_b.

5.8 Comparison to macrorheology

In microrheology, the force/velocity relationship is analogous to the stress/strain-rate relationship in macrorheology. Both approaches should yield the same qualitative information about about structural evolution and relaxation. Previous theoretical studies of transient suspension behavior were conducted by Foss & Brady (2000*a*; 2000*b*). Brownian dynamics and Stokesian dynamics simulations of suspensions undergoing shear flow were conducted, and the startup and cessation flow regimes studied. Their findings included the same $t^{1/2}$ scaling of early startup flow, along with shear-thinning behavior for the long-time asymptotic value of the macroviscosity. An important qualitative feature of the startup regime in transient macrorheology is an overshoot behavior of the macroviscosity. Their plots of viscosity versus time shows marked non-monotonic behavior during the transition from early-time to long-time behavior. The effect is more pronounced for moderate Pe, and nearly vanishes at high Pe. This phenomenon has not yet been observed in our studies of transient microviscosity. However, as was noted above, this behavior may be responsible for the higher-than-expected long-time viscosity in the constant-velocity regime. Continuation of the startup flow for a longer duration may reveal if one diffusive time step is sufficient for moderate Pe. If the microstructure is in fact still evolving, the viscosity may continue to grow, or may decay to the predicted value. Foss & Brady also found similar behavior in the cessation regime, where advective scaling collapses all the data onto a single curve at long times.

5.9 Conclusions

The formation and relaxation of non-equilibrium stress in colloidal dispersions was studied using the framework of nonlinear microrheology. In this approach a dilute dispersion of hard colloids is driven far from equilibrium by the motion of an externally forced Brownian probe particle. In order to explore time-dependent behavior of the structure and stress, the velocity and displacement of the probe were monitored after sudden startup of the flow, for one diffusive time step. Forcing was then abruptly removed, and monitoring of probe displacement and velocity were continued after shutoff as the suspension relaxed. In microrheology, the force/velocity relationship is analogous to the stress/strain-rate relationship in macrorheology, and so it is expected that the probe velocity yields the same qualitative information about about structural evolution and relaxation. Probe velocity is related to force via the microviscosity, as defined using Stokes' drag law. The behavior of transient microviscosity thus gives insight into the basic physical aspects of structure and stress formation in the suspension. The work combines analytical and numerical techniques, along with dynamic simulation.

During the startup of the flow, the microstructure evolves initially as a one-dimensional monopole in time, and the viscosity grows as $\hat{t}^{1/2}$. Importantly, the early-time behavior of the transient microviscosity is the same regardless of the strength of probe forcing. Since the Péclet number is a measure of how strongly the microstructure is deformed from the equilibrium state, one interpretation of the early-time Pe-independence is that it gives a measure of the time required for the probe to realize that it is not alone in the bath—and to interact with the surrounding microstructure. The duration of this regime is then the fundamental time scale of the microstructure. As the probe encounters more particles, it slows down, and eventually the drag on the probe asymptotes to a long-time steady value. The force-thinning characteristic of hard-sphere suspensions was seen in the the decrease in steady-state viscosity with Pe. Analytical and numerical results and Brownian dynamics simulation measurements were in good agreement. These values also agreed with the steady-state values reported by Squires & Brady (2005), Khair & Brady (2006), and Carpen & Brady (2005).

After the forcing is removed, the motion of the probe and suspension does not cease instan-

taneously. It was found that the suspension has several relaxation time scales: The stress decays quickly at first, and then continues to decay more slowly over longer time scales. The rate of initial decay depends on the state of the microstructure just before the flow was stopped; the higher the value of the Péclet number, the more rapid the initial decay. While this behavior is found for both constant-force and constant-velocity forcing modes, the underlying mechanism differs for the two cases. For the former, both the probe and the bath particles can diffuse and relax through the boundary layer to relieve stress; whereas in the latter case, only the bath particles can diffuse resulting in a slower stress relaxation. In either case the stress-relaxation time depends on the boundary-layer thickness. These results are consistent with similar findings by Foss & Brady (2000*a*; 2000*b*).

It was found that a colloidal dispersion of hard spheres exhibits nonlinear viscoelastic behavior when the configuration of its microstructure is deformed. A plot of the absolute position in the fixed-force case reveals that the probe travels backwards upon removal of the applied force: The suspension remembers its previous configuration for a time. While such behavior is well-known in polymeric and other topologically hindered materials, this is interesting behavior in a suspension of isotropic particles interacting only through short-range steric hindrance. Some of the energy of the probe's motion is evidently stored as free energy in the compressed configuration of bath particles; it is entropic in origin (not enthalpic), and this is the origin of non-equilibrium suspension stress. An interesting question that arises here is whether the entropic spring force $F^{entropic}$ (cf equation 5.31) can be derived analytically from first principles; at steady state, the microstructure is a statically distorted structure, and this force may be given by $F^{entropic} \sim kT\nabla \log g$.

During the relaxation process, the gradient in the free energy does useful work, giving the probe a net displacement. A coarse graphical measurement of the back-travel slope indicates that the majority of the stress relaxation occurs when the probe relaxes out of the boundary layer, as predicted earlier. The total back-travel of the probe was used to estimate the magnitude of the entropic force associated with the entropic "spring"return. It was found to scale as approximately $13kT$ for same-size probe and bath particles. The limiting behavior of the proposed analytical estimate of the entropic force (equation 5.31) was computed for a very large and very small probe; it was found that

the strength of the entropic spring is halved for a small probe, and vanishes for a very large probe. This behavior corresponds to the exclusion of particle centers from the region occupied by the probe, and the entropic penalty this exacts for the distribution of bath particles. Importantly, energy of the entropic "return spring" is less than the energy put into the suspension, which for $Pe = 30$ is approximately $30kT$. Some of the energy is dissipated. Over long times the Brownian motion of the bath particles dissipates the stored free energy viscously, which is the underlying mechanism for long-time stress relaxation.

A comparison was made between constant-force and constant-velocity regimes (Modes 1 and 2, respectively). Brownian dynamics simulations confirm the steady-state prediction by Squires & Brady that $\eta_U^{micro} \sim 2\eta_F^{micro}$. Brownian dynamics simulation of steady-state microrheology by Carpen & Brady (2005) found similar values for the viscosity as the long-time startup results in this study. Physically, in Mode 2 the probe velocity cannot fluctuate, which results in a larger accumulation of bath particles in the boundary layer and thus a stronger resistance to probe motion. The time to reach steady state in constant-velocity mode may also be longer; the time required to sample all configurations of the microstructure is apparently longer, due to the need to encounter many different spikes and dips in density. In other words, the microstructure has a stiffer response to constant-velocity interrogation, reflecting the entropic origin of the "spring" constant. This finding agrees with the results of the previous chapter, in which the stress in a suspension is found to be reduced in the case of a probe that can fluctuate as it is driven through the bath.

One consequence of the stiffer response in Mode 2 is a stronger sensitivity to bath-particle concentration. The time scale for particles to get out of the probe's way is reduced, and increasing their local density further reduces this time window and increases the stiffness of the suspension. This may prove a useful technique for measuring volume fractions in suspensions. The wake structure is quantitatively different for the two modes; the longer wake structure in constant-velocity mode drives a longer relaxation time, as the Brownian motion of the bath particles has a larger wake to heal.

The comparison between transient nonlinear macrorheology and microrheology shows that in

both cases, the early stress evolution scales with the square root of time, and shows the same shear (force) thinning over a range of Pe (Foss & Brady, 2000a). The relaxation showed similar dual relaxation time scales, and in both cases, the long time relaxation behavior collapsed onto a single curve, indicating that memory of the initial condition is lost. A key difference between the two studies was found in the transition from short to long times in the startup regime. In macrorheology, the constant strain-rate startup flow reveals non-monotonic behavior in the suspension stress. An overshoot precedes the long-time plateau, which becomes less pronounced as Pe is increased. This behavior may be explained by the formation of temporary local structure around the tracer particle, which gets stripped away by the flow as the boundary layer forms. No such overshoot behavior was found in our studies. However, it was noted that the constant-velocity simulations may not have yet reached steady state when the flow was shut off. Simulations with longer startup duration may elucidate this further.

Several questions remain. The effect of hydrodynamic interactions was not included in this study. When these interactions are important, shear thickening occurs for large Pe, which will change the steady-state plateau. A study involving hydrodynamic interactions during startup may yield insight into the time scales at which the Brownian and hydrodynamic contributions to viscosity can contribute. The presence of a Brownian stress relaxation may be measured, but the hydrodynamic stress will decay instantaneously after flow shutoff. The mechanisms that underlie the constant-force versus constant-velocity probe regimes should be studied with a view toward the force fluctuations that arise during constant-velocity motion. While the velocity-velocity autocorrelation gives insight into diffusivity, what can we learn from force-force correlation? The ratio a/b of probe size was taken to be unity for this study. It would be interesting to explore the parameter space of variable size ratio, and understand its contribution to relaxation time scales. A qualitative change is not expected, except when hydrodynamic interactions are important. Notwithstanding, the simplifications used in this study provide important insight into the fundamental physical aspects of stress propagation, free-energy storage, and nonlinear viscoelasticity in colloidal dispersions. That this behavior is found for a suspension of simple spherical particles is important in revealing the entropic nature of energy

storage as stress density in a complex fluid, and may have implications in a wide range of research problems.

Finally, we return to the idea that probe motion is a window through which we can view the connection between fluctuation and dissipation. We have asked the question: What can non-equilibrium fluctuation and dissipation tell us more fundamentally about energy and motion? Avogadro's constant was the sought-after connection during the work of Einstein & Perrin. It establishes a relationship between the macroscopic gas constant $\mathcal{R}$ and Boltzmann's constant k, which connects energy at the atomic level to temperature at the macroscopic level. In chapter 4, we found that a stirred suspension can be characterize by an "effective temperature." Here we have discovered that stress relaxation away from equilibrium depends strongly on the probe's ability to fluctuate. Although power input by the probe must all be dissipated, it takes time to do so. The temporary storage of energy—the stress—results again in increased "effective temperature." In this sense, particle fluctuations may provide a new way to define temperature in complex fluids.

Chapter 6

Dual-probe microrheology: Non-equilibrium depletion flocculation

6.1 Introduction

Depletion interactions have long been a topic of study in colloidal dispersions. From a practical standpoint, aggregation, flocculation, and sedimentation are phenomena important to the production, use, and storage of complex fluids. The influence of depletion interactions on particle aggregation has implications for processing, storage, and handling of complex fluids. For example, suspended microparticles in paint that give it tint must remain in suspension long enough for application to a surface; bitter-tasting phenolic compounds in wine are often removed by sedimentation prior to bottling; and the treatment of wastewater and purification of industrial slurries are critical to recovering clean water and safely storing toxic waste. Other examples include microscopically small systems, in which depletion interactions may influence the formation and stability of bacterial colonies and biofilms, or the formation of critical aggregations inside the cell, for example. From a theoretical standpoint, the phenomenon of depletion interactions has been studied for many decades. In the 1950's, Asakura & Oosawa (1954) identified the underlying mechanism for one form of aggregation, namely, that due to depletion interactions. They considered a pair of plates in a dilute solution of smaller particles, where the plates are separated by a distance smaller than the background particle size. Because the gap excludes the presence of the background particles, there is a region of pure

solvent between them and a region of finite concentration everywhere else. A gradient in the free energy thus arises, due to the restriction of particle positions in configuration space. The free-energy gradient produces a force that acts on the plates. This force points down-gradient, producing a net attraction between the plates. From a statistical perspective, the plates want to migrate into the depleted region to make uniform the distribution of particles in space. Asakura & Oosawa show that the driving force for this phenomenon in equilibrium systems is a gradient in the osmotic pressure. While much study has been devoted to equilibrium depletion interactions (see, for example Russel *et al.* (1989)), Limited work has been devoted to the exploration of such interactions in non-equilibrium systems.

Theoretical studies were conducted by (Khair & Brady, 2005) for a pair of particles translating along their line of centers through a colloidal dispersion at constant velocity. Carpen & Brady (2005) also studied the same arrangement by dynamic simulation; in both studies, it was found that for certain separation distances between the probes, the wake of depletion of the first particle increased the mobility of the trailing probe, due to the reduced number of bath particles upstream from the trailing probe. Carpen & Brady also studied the interactive force between a pair of probe particles translating transverse to their line of centers at constant velocity through a colloidal dispersion. They found that an interactive force arises between them that varies from attractive to repulsive, depending on their separation and on the Péclet number. Cordova-Figueroa & Brady studied non-equilibrium, osmotic force-driven motion of a single probe particle (2008), in an osmotic motor arrangement. They conclude that a non-uniform osmotic pressure gives rise to non-equilibrium force on the motor particle. An interesting question to ask here is how two side-by-side motors would interact; would the osmotic pressure gradient lead to depletion interactions? This is a particularly interesting case because no external force is present.

In this work, we continue the investigation of non-equilibrium depletion interactions by dynamic simulation. We study the interactive force between a pair of equally sized probes driven at constant velocity $\boldsymbol{U}$ through an otherwise quiescent suspension of colloidal particles. As the probes travel through the suspension, they drive the microstructure out of equilibrium. The character of the

microstructure surrounding the probes is determined both by the distance R by which the two probes are separated and by the strength of the external forcing, $Pe = Ua/D_b$, where U is the constant probe velocity and D_b the diffusivity of the bath particles. Osmotic pressure gradients develop as the microstructure is deformed, giving rise to an interactive force between the probes. This force is studied for a range of Pe and R, by Brownian dynamics simulation.

In particular, the goal of our study is to understand more clearly the physical mechanisms underlying the interaction, and the evidently qualitative dependence on Pe. The model comprises two hard spheres separated by a fixed distance translating at fixed velocity perpendicular to their line of centers, through a bath of same-size colloids. The probes cannot diffuse or drift at fixed velocity; in order to move through the bath, each probe must displace particles that are in its path. The force required to hold the probes at fixed velocity will be monitored. When the region between the probes excludes the bath particles, we expect the probes to tend to drift into the gap. When the excluded volume grows to allow bath particles to gain entry into the gap, a competition for volume between probe and bath particle should arise, producing repulsive forces on the probes. The importance of the entropic nature of equilibrium depletion flocculation away from equilibrium is not known and will be studied. The interactive force between the probes will be studied for a range of center-to-center spacings, and for a range of Pe.

The remainder of this chapter is organized as follows: In §6.2, the model system for two-probe microrheology is outlined, followed by a description of the Brownian dynamics simulation method in §6.3. The interactive force between the probes is measured in the simulation, and these are presented and discussed in §6.4, along with plots of the microstructural density evolution. Comparisons to equilibrium depletion interactions are made. The study is concluded with a discussion in §6.5.

6.2 Model system

The model system is nearly identical to the system outlined in chapter 2; previously, a single Brownian probe particle of size a was driven by an external force through a sea of spherical colloids of size b suspended in a Newtonian solvent. Here, rather than a single probe, two particles are

forced through the suspension. Figure 6.1 illustrates the system, where the two probes are driven at constant velocity $\boldsymbol{U}$ through the bath. They are separated by a distance R, and they translate in the direction perpendicular to their line of centers. For convenience, we shall take the size ratio to be unity: $a/b = 1$. We shall restrict our attention to the hard-sphere limit and to the limit

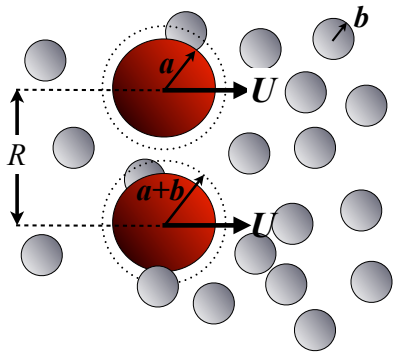

Figure 6.1: Sketch of model system: two probe particles of size a (red) are forced at constant velocity $\boldsymbol{U}$ in the direction perpendicular to their line of centers, through a suspension of colloids of size b (grey). The probe centers are separated by a distance R.

of no hydrodynamic interactions (cf chapter 2). This model captures the essential features of the dispersive process while keeping the analyses as simple as possible.

6.3 Simulation method

The approach taken here to studying particle behavior in a colloidal suspension is to examine the detailed dynamics of individual particle motion. The dynamics of probe and bath particle motion are governed by the Langevin equation, a force balance which includes external, hydrodynamic, interparticle, and random Brownian forces. In the present case this equation reads:

$$\boldsymbol{m} \cdot \frac{d\boldsymbol{U}}{dt} = \boldsymbol{F}^H + \boldsymbol{F}^B + \boldsymbol{F}^P + \boldsymbol{F}^{ext}, \tag{6.1}$$

where the left hand side is zero because the particle Reynolds number is small. Here, the external force $\boldsymbol{F}^{ext} = \boldsymbol{0}$ for all particles except the two probes. The equation is then integrated over a time step Δt as outlined in chapter 3 to obtain the displacement equation, which governs the displacement of each particle during the simulation due to external, Brownian, and interparticle forces.

To begin the simulation, the cell is populated with two probes of size a which are placed among a random distribution of bath particles of size b at number density n_b and volume fraction $\phi_b = 4\pi b^3 n_b/3$. A continuum Newtonian solvent of viscosity η and density ρ is modeled implicitly in the governing equation (6.1). The cell is replicated periodically to simulate an infinite domain. As illustrated in figure 6.2, the two probes are placed on the mid-plane of the cell (marked by the dashed line) and flank the centerline with respect to their separation R.

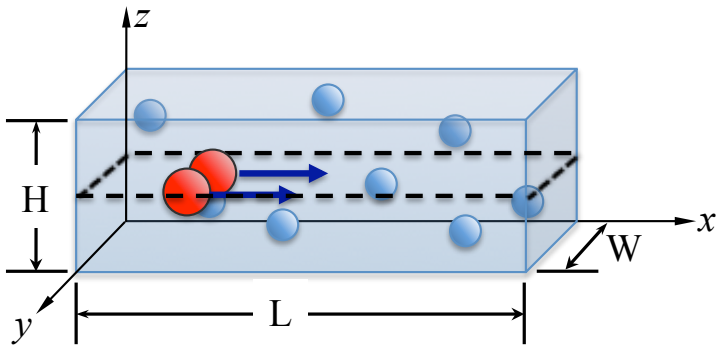

Figure 6.2: Sketch of simulation cell for Brownian dynamics simulation of dual-probe microrheology.

In the current study, the probes are constrained to travel with constant velocity $\boldsymbol{U}$, which means that the probes receive no Brownian displacement—or rather, that each Brownian kick to a probe is countered with an equal and opposite restraining force (displacement). Hard-sphere collisions with the bath particles also produce displacements of the two probes; in order to maintain constant probe velocity, an equal but opposite force is exerted by a probe that exactly balances each hard-sphere collision. The sum of these counteraction forces are recorded at each time step for each probe. The resultant force vector has three Cartesian components, $\boldsymbol{F}_a = F_x\boldsymbol{e}_x + F_y\boldsymbol{e}_y + F_z\boldsymbol{e}_z$, with origin and directions as indicated in figure 6.2. The x-component of the force may be interpreted as the drag force of the bath on the probe, and hence used to measure the suspension microviscosity (cf chapter 2). The y-component is the force required to keep the distance R between the probes fixed. The average Brownian contribution to $\langle F_y \rangle$ must be zero, where the average is over the duration of the simulation. The remainder of $\langle F_y \rangle$ can then be interpreted as the interactive force between the probes. The third Cartesian component, $\langle F_z \rangle$, is purely Brownian in origin and must be zero on

average.

The dimensions of the simulation cell are set to accommodate the prescribed number and volume fraction of bath particles. For the two-probe arrangement, special care must be taken to assure that that the periodic images of probes do not interact. Thus, the height and width (dimensions H and W in the figure) must allow for a sufficient decay in structure around each probe, so that the distribution of particles is uniform at the midpoint between periodic images. The required width depends weakly on the volume fraction of bath particles, but strongly on the degree of probe forcing. The required cell width decreases as Pe increases, because the microstructural disturbance caused by the probe becomes confined to a boundary layer, as is shown in the next section. However, as Pe is increased, the length of the trailing wake, which is Pe long, increases. The simulation cell must therefore be sufficiently long (the dimension L in the figure) to allow the periodic images of the probe to enter fully random structure at steady state. Several values of the dimensionless probe separation distance $\hat{R} = R/2a$ were evaluated:

$$\hat{R} \in [2.0, 2.5, 3.0, 3.5, 4.0, 4.25, 4.5, 5.0]. \tag{6.2}$$

A range of Pe was studied as well:

$$Pe \in [0, 0.1, 0.5, 1, 3, 5, 7, 10, 20, 30, 50, 100]. \tag{6.3}$$

Thirty simulations were conducted for each combination of Pe and $\hat{R}$.

The interactive probe force is measured at each time step, and at the end of the simulation, the Cartesian force vector is recorded in two ways: firstly, the force is recorded as a function of time, $\boldsymbol{F}_a(t)$ throughout the simulation. In addition a time-average force $\langle \boldsymbol{F}_a \rangle$ is recorded, where the angle brackets signify an average over all time steps after the suspension has reached steady state. Steady state is estimated to have been reached after ten diffusive time steps when $Pe < 1$ and after one advective time step when $Pe \geq 1$.

6.4 Results

To maintain constant velocity, a force must be applied to each probe to counter the Brownian and interparticle impacts they suffer as they travel through the suspension. Here the force is averaged over the span of a single simulation, and then averaged over all 30 simulations. The interactive force between the two probes is the y-component of the vector, as shown in the sketch in figure 6.3.

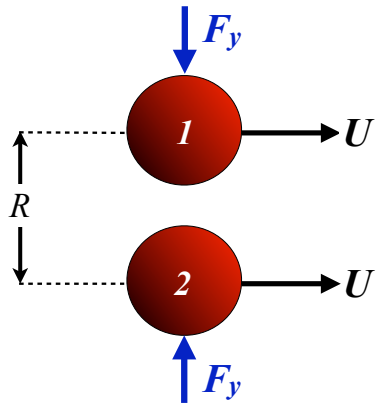

Figure 6.3: Definition sketch for orientation of two probes: separation distance R, equal velocities $\boldsymbol{U}$ perpendicular to their line of centers. Blue arrows are oriented such that attraction between the probes corresponds to a negative F_y for probe 1 and a positive F_y for probe 2. Repulsion corresponds to opposite signs for each. Probes are identified as 1 and 2 for clarity.

Interactive force between the driven probes: Attraction and repulsion

Figure 6.4 gives the y-component of the interactive force between probes, made dimensionless with the Stokes drag $6\pi\eta aU$ and scaled with the volume fraction of bath particles. The sign convention is set by the location of the origin in the simulation cell: Attractive forces between the probes correspond to negative values of F_y for probe 1 and positive F_y for probe 2 (cf figure 6.3). Repulsion corresponds to opposite signs for each.

As can be seen in the figure, the probes experience a range of qualitative behavior: when they are closer, they tend to attract. As their fixed separation becomes larger, a repulsive force develops between them. As R exceeds approximately 4.25 radii, they no longer interact. The value of R at which the attractive-to-repulsive transition occurs varies with Pe. As the strength of probe forcing increases, the transition from attractive to repulsive behavior shifts to the left. A smaller separation

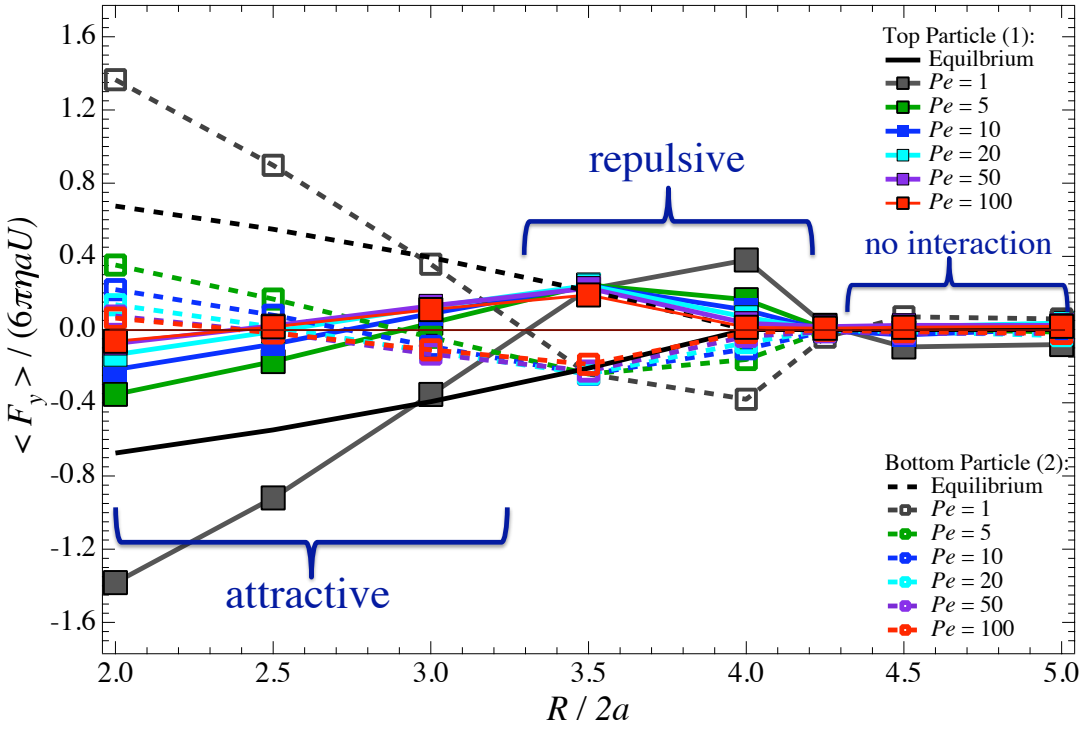

Figure 6.4: Total depletion force F_y (scaled on the Stokes drag $6\pi\eta\, a\, U$) as a function of Pe, plotted for a range of particle separations $\hat{R}$. Error bars on order of marker size.

allows the probes to repel at higher Pe, which indicates that attractive behavior is a Brownian or thermal mechanism, and vanishes as Brownian motion becomes less important to suspension dynamics. To study this behavior is more closely the plots are separated into three regimes of interaction: mostly attractive, mostly repulsive, or mostly neutral regimes.

The "mostly attractive" regime is plotted in figure 6.5, where the interactive force is plotted now as a function of Pe, for several values of the separation $\hat{R}$. When the probes are separated by less than 3.5 radii, they attract strongly for weak to moderate forcing. When Pe is small, Brownian motion of the background bath particles gives rise to osmotic pressure that acts normally on the probes, except in the depleted region—and the probes migrate into the depleted volume. The closer the probes, the steeper the osmotic pressure gradient, and the stronger the attraction. As Pe grows, Brownian motion weakens, effectively cooling the suspension. The osmotic force of the bath particles becomes weak compared to the external driving force, and the attraction weakens. Simultaneously, a concentration of bath particles builds up in the cleft between the two probes, increasing the osmotic

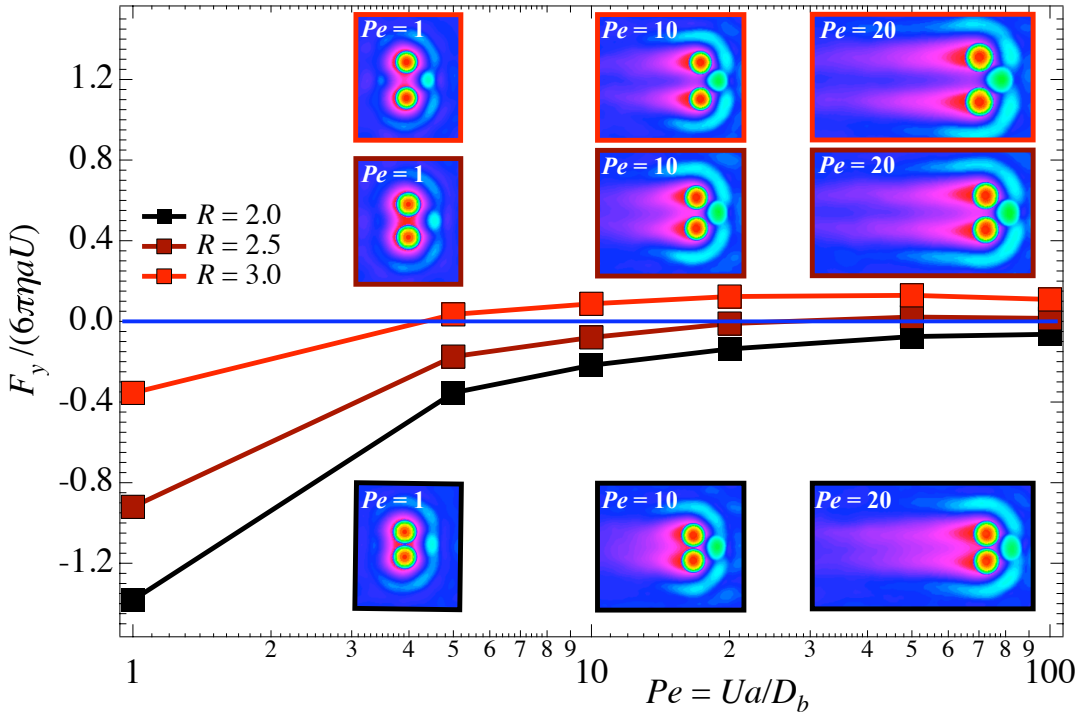

Figure 6.5: Attractive regime: non-equilibrium depletion force (scaled with the Stokes drag $6\pi\eta\, a\, U$) as a function of Pe, studied over range of particle separations $\hat{R}$. Error bars on order of marker size. Insets: average bath-particle density around the probes, in a frame of reference moving with the probes. Color scale is set for maximum contrast.

force on "inboard" surfaces of the probes (see figure 6.6). At $Pe \sim 10$, the depletion force nearly

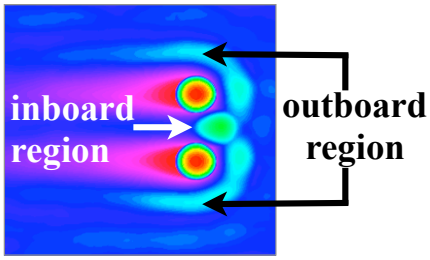

Figure 6.6: Inboard and outboard regions of two probes.

balances that of the particles at the tip of the gap; the interactive force becomes nearly neutral. As Pe becomes large, bath particle accumulation in the cleft become stronger, giving rise to weak repulsion.

When the probes are separated by three to four radii (figure 6.7), background bath particles start to penetrate the gap between the probes. Insets in the plot show the average bath-particle density around the probes, in a frame of reference moving with the probes. Beyond $Pe \sim O(1)$, particles are

advected into the depleted region, as can be seen in the inset density plots. The osmotic pressure gradient around the probes is weakened, reducing their attraction. In addition, the bath particles in the gap between the probes take up residence in the boundary layer that forms between them. There, advection balances diffusion and the bath particles can only escape by diffusing through the gap. While inside this boundary layer, the particles exert an osmotic pressure on the probes due to hard-sphere collisions. The probes repel each other. As the separation become large enough for an entire bath particle to pass unrestricted between the probes, repulsion weakens.

For probe separation larger than two full diameters (figure 6.8), bath particles pass between the probes as easily as around them. Probes receive as many kicks on the "inboard"surfaces as they receive on the surfaces that face away from each other (the "outboard"surfaces in figure 6.6) which results in a neutral interactive force.

Figures 6.9 and 6.10 show this transformation of the microstructure around the probe—the former, with the separation between the probes held constant at $\hat{R} = 0.35$ and in order of increasing

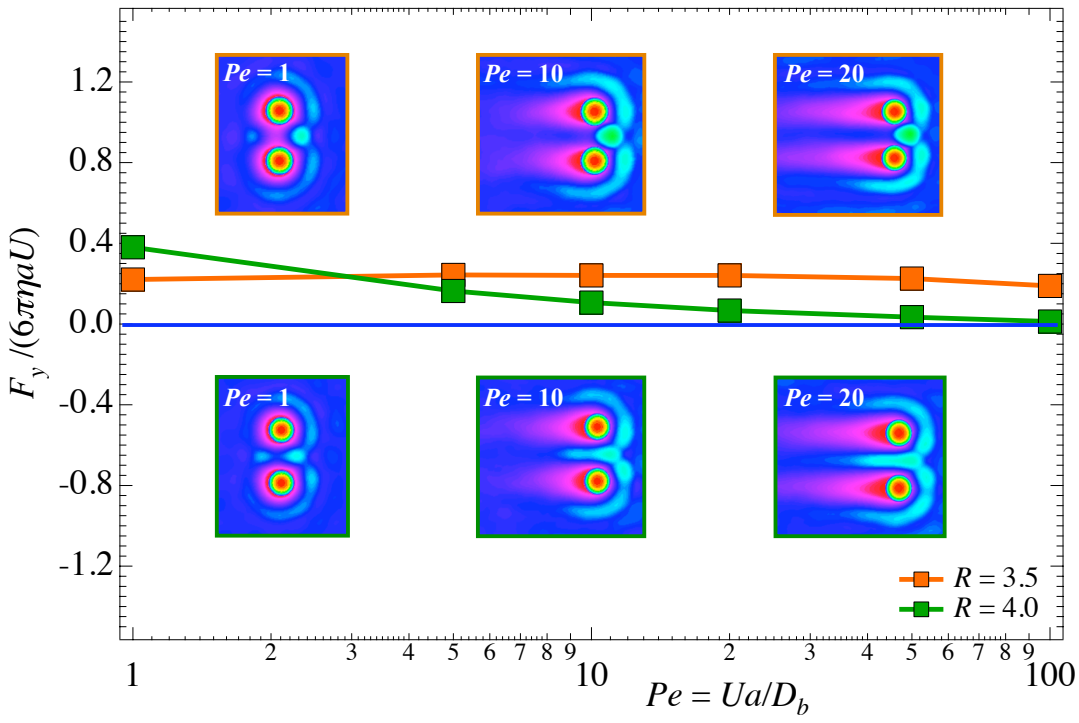

Figure 6.7: Repulsive regime: Non-equilibrium depletion force (scaled with the Stokes drag $6\pi\eta\, a\, U$) as a function of Pe, studied over range of particle separations $\hat{R}$. Error bars on order of marker size. Insets: average bath-particle density around the probes, in a frame of reference moving with the probes. Color scale is set for maximum contrast.

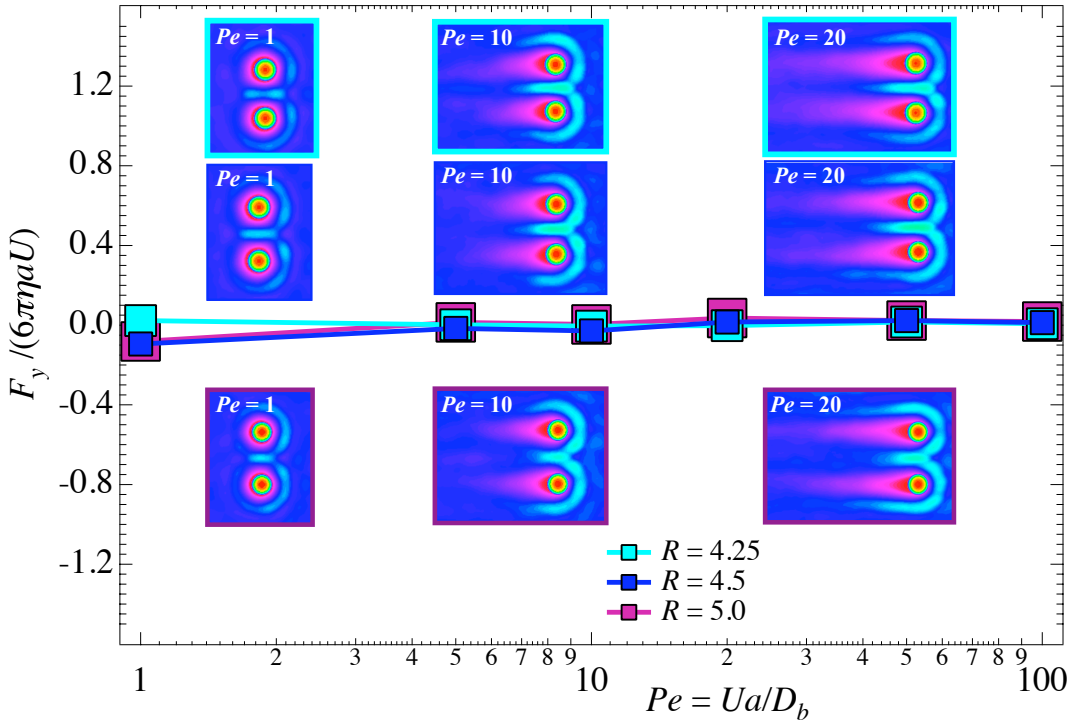

Figure 6.8: Neutral regime: Non-equilibrium depletion force (scaled with Stokes drag $6\pi\eta a$) as a function of Pe, studied over range of particle separations $\hat{R}$. Error bars on order of marker size. Insets: average bath-particle density around the probes, in a frame of reference moving with the probes. Color scale is set for maximum contrast.

external force. In the latter, the external force is held constant at $Pe = 10$, while the separation distance is varied.

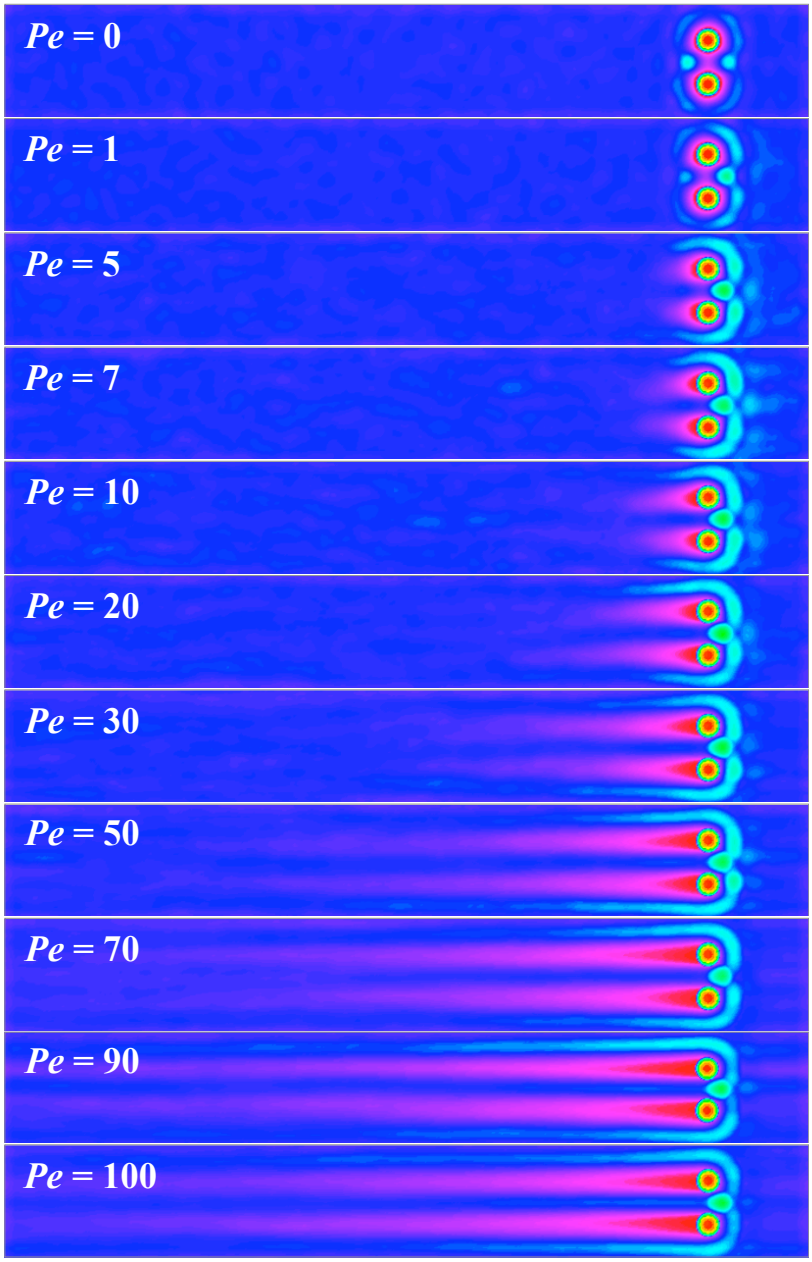

Figure 6.9: Density plot: evolution of the bath-particle microstructure for constant separation $\hat{R} = 3.5$ and volume fraction $\phi_b = 0.35$ and $0 \leq Pe \leq 100$. Data correspond to orange trace in figure 6.7.

The evolution of the microstructure in figure 6.9 elucidates the qualitative behavior of the interactive force. At $Pe = 0$ and $Pe = 1$, the red area indicating particle depletion surrounds the probes and illustrates a depletion volume between them. As Pe is increased, the red color gives way to blue, indicating increasing density of particles between the probes, and the onset of repulsive interactions.

In figure 6.10, the external forcing is held constant while the particle separation is varied, as in

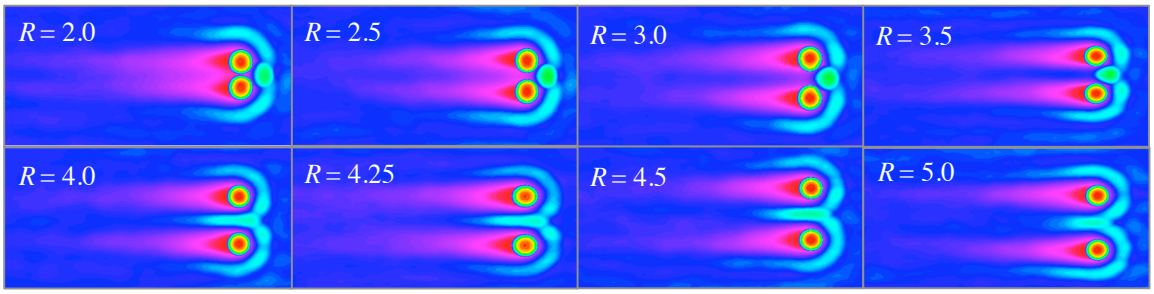

Figure 6.10: Density plot: evolution of the bath-particle microstructure for constant $Pe = 10$ and volume fraction $\phi_b = 0.35$ and $2 \leq \hat{R} \leq 5.0$. Data correspond to blue trace in figure 6.4.

the force plot 6.4. The boundary-layer structure up until $\hat{R} = 2.5$ is confined to the outboard region of the probes—as though the two probes are one—and a small depletion volume (red color) between them gives rise to attraction. As separation is increased, the bath particles enter the gap; from the spacing of $3.0 < \hat{R} < 4.25$, the intruding bath particles form a cleft that cannot fully penetrate the gap between the probes, and a repulsive force results. As $\hat{R}$ increases further, a full boundary-layer structure is formed around each of the particles, until they effectively move as separate particles and do not interact significantly.

A comparison to equilibrium depletion flocculation

As discussed in the Introduction to this chapter, Asakura & Oosawa identified the mechanism underlying depletion flocculation of objects immersed in a dilute suspension of particles that arises when the objects are separated by a distance smaller then the suspended particles (1954). The osmotic force that drives the objects together is derived from the gradient in the free energy of the suspension: the osmotic pressure gradient. Figure 6.11 shows a sketch of one such arrangement, when the submerged objects and suspended background particles are spheres of size a and size b, respectively. Applying the result of Asakura & Oosawa to this system, we obtain, for the attractive force:

$$\boldsymbol{F}^{depl} = -n_b kT \oint_{depl} \boldsymbol{n}\, dS \tag{6.4}$$

$$= -n_b^{\infty} kT\pi \left[(a+b)^2 - \left(\frac{r}{2}\right)^2\right] \hat{\boldsymbol{r}}, \quad a < \frac{r}{2} < (a+b) \tag{6.5}$$

$$= \boldsymbol{0}, \quad \frac{r}{2} > (a+b), \tag{6.6}$$

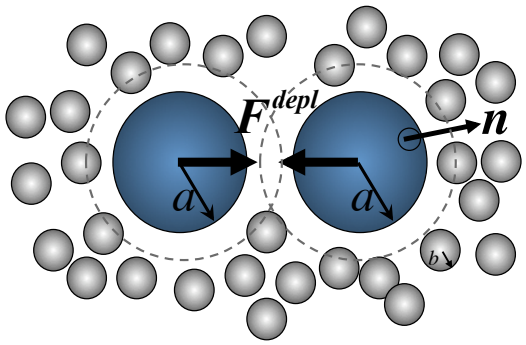

Figure 6.11: Equilibrium depletion flocculation: two particles of size a (blue) are held at fixed position in a suspension of colloids of size b (grey). The probe centers are separated by a distance r.

where $\boldsymbol{n}$ is the unit surface normal and $\hat{\boldsymbol{r}}$ is the unit vector along the line of centers of the immobile spheres. This force is shown in figure (6.4) as a black solid line and black dotted line. It is of interest to understand the qualitative and quantitative behavior of the non-equilibrium portion of the interactive force—that is, the effect above and beyond the equilibrium attraction.

In figure 6.12, the equilibrium depletion force $\langle \boldsymbol{F}^{depl} \rangle = \langle \boldsymbol{F}_y(Pe = 0) \rangle$ is subtracted from the total interactive force $\langle \boldsymbol{F}_y(Pe) \rangle$, and the resultant is scaled with the Stokes' drag $6\pi\eta\, a\, U$. It is plotted as a function of the strength of external force, for a range of separations $\hat{R}$. Two regions

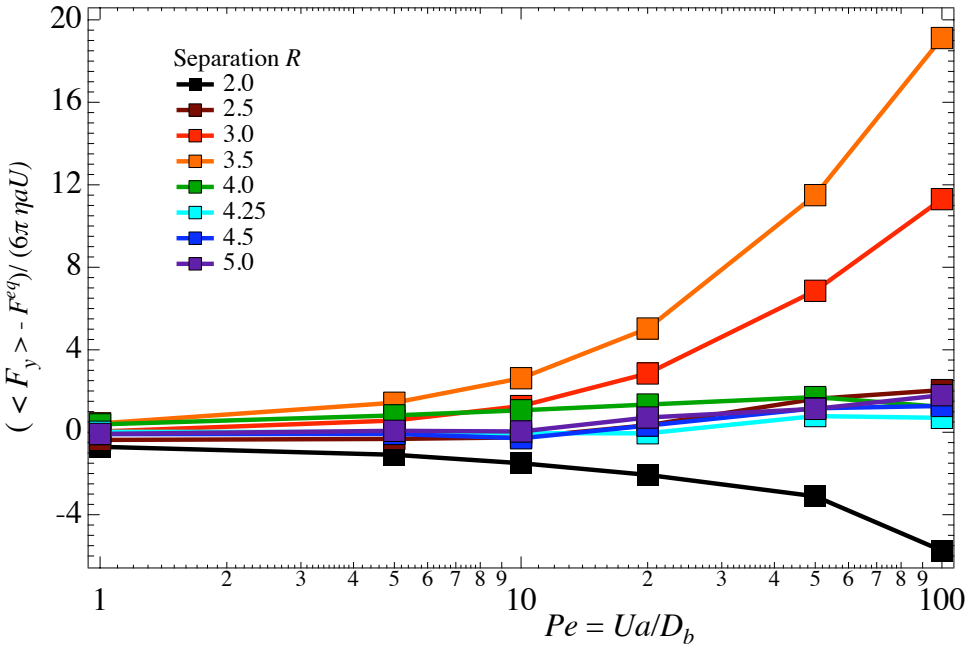

Figure 6.12: Non-equilibrium portion of the total depletion interaction force, as a function of Pe, for a range of particle separations $\hat{R}$.

can be observed on the plot. In the first region, where $Pe \lesssim 10$, the interactive forces are weakly repulsive, except in the case of two probes at contact; for $\hat{R} = 2.0$, the interaction is uniformly attractive, regardless of the value of Pe. For non-contacting probes, the attraction is $\sim O(1)$ for moderate Pe. No matter how strong the forcing, when $\hat{R} = 2$, there are always more kicks on the outboard surfaces of the probes than on the inboard surfaces where they face each other. As Pe increases, the probes are close enough to interact and to allow accumulation of bath particles between them become strongly repulsive ($3.0 \lesssim \hat{R} \lesssim 4.0$). Attraction between probes separated by less than the critical separation $\hat{R} \approx 4.0$ can be fitted with Pe^{γ}, where γ is yet to be determined.

Two key results are to be gleaned from the data in figure 6.12. Firstly, depletion attraction is strictly entropic in origin. This is evidenced by the fact that without the equilibrium contribution to the interactive force between the probes, it is always repulsive. Secondly, the contact behavior indicates that the non-equilibrium repulsion interaction is due strictly to collisions between bath particles and probes on the surfaces in the depleted region.

6.5 Conclusions

Depletion interactions in equilibrium suspensions are an area of both practical and heuristic interest. While such interactions have many important technology implications—ranging from industrial slurries to household liquids to foodstuffs—they play a more fundamental role in science: they provide another lens through which we can indirectly view the world at a much smaller scale. Asakura and Oosawa (1954) recognized the entropic origin of depletion interactions between a pair of particles in an equilibrium solution of smaller macromolecules. Placing the particles close enough to exclude the macromolecules from the space between them gives rise to a gradient in the osmotic pressure. This in turn produces a down-gradient flux of the two particles into the gap between them. The underlying entropic mechanism for this motion is the tendency for a set of Brownian particles to migrate so as to make uniform their statistical distribution in space. But is the interactive mechanism always strictly entropic in origin? Does it play a role in non-uniform microstructures which are deformed due to non-equilibrium forcing? In this study, answers to these questions were sought, along with

an understanding of how interactive forces between particles evolve when the suspension is not at equilibrium.

The interactive force between a pair of particles in a colloidal dispersion was studied using the framework of dual-probe nonlinear microrheology. In this approach, a pair of Brownian probes is driven through a colloidal dispersion. As the probes move through the bath, they suffer Brownian impacts from the solvent as well as collisions with the dispersed bath particles. In order to examine what, if any interactive force arises between the probes, they were driven at a constant velocity transverse to their line of centers through the bath. The force required to maintain constant velocity was monitored and, in particular, the force required to keep them at fixed distance from each other was studied. For two probes initially separated infinitely far apart, it was found that as the probes are brought closer together they first repel and then attract.

The distance at which the probes transition from repulsive behavior to attractive behavior decreases with Pe, the strength of the forcing. That is, as the suspension warms up (decreasing Pe), the entropic attraction between the probes extends for larger separations. But regardless of Pe, when the distance between probe surfaces is larger than their diameter, no net force is required to maintain their relative position, other than the force required to prevent Brownian diffusion. The probes no longer interact.

The equilibrium contribution to the interactive force was subtracted from the total interactive force. Here, we found that except for two touching probes, the non-equilibrium part of the interactive force is always repulsive regardless of Pe. This confirms the assertion that depletion interaction in such a system is a strictly entropic phenomenon. In the system studied here, the the non-equilibrium interaction arose due to hard-sphere collisions between the probes and bath particles. The hard-sphere force scales thermally as $\sim kT$, as does the entropic force. However, the deformation of the microstructure gives rise to more frequent collisions. As Pe increases, the collisional contribution overtakes the entropic contribution, causing a transition from attractive to repulsive behavior.

Several questions remain. The first concerns the influence of hydrodynamic interactions between particles. In this study, hydrodynamic interactions were neglected in order to gain insight into the

structural physics at play. But hydrodynamics can give rise to lubrication interactions in strong flows, for example, which tend not only to keep particles farther apart, but keeps particles attached to each other in downstream extensional flow due to lubrication interactions. The formation of doublets and doubled doublets and so on can give rise to shear banding and shear thickening. In the case of nonlinear microrheology, would it be possible also to see strong depletion interactions in the presence of a flow, thus reversing the attraction / repulsion transition? This could lead to stability of colloidal gels under strong flows, for example.

Our study assumed only same-size probe and bath particles. The effect of a large or small probe/bath-particle size ratio changes the osmotic pressure gradient as seen by the probe—can this also delay the onset of the repulsive regime? And finally, how does the interactive force change when the particles are self-propelled, *e.g.* an osmotic motor—how would two side-by-side motors interact, and could this be used to stabilize them rotationally?

Chapter 7

Conclusions

The motion of microscopic particles in liquids provides a window through which scientists have long studied the connection between thermal agitation and macroscopic thermodynamic properties. Einstein's famous 1906 thought experiment provided the first macroscopic connection between fluctuation and dissipation—thermodynamics and hydrodynamics—in complex fluids. A simple connection between a measurable fluctuation—diffusion—and energy dissipation—viscosity—was given by the Stokes-Einstein relation. It was found that the response that drives stress is indistinguishable from thermal fluctuations. In 1909, Perrin conducted one of the first particle-tracking experiments, setting the stage for modern-day microrheology. Einstein's analytical relationship and Perrin's experimental approach are used widely in the modern-day interrogation of complex media, and have even been generalized to a frequency-dependent, linear-viscoelastic relation. But this approach is limited by its very nature to equilibrium systems.

In order to study dynamic response properties of a material, a much different approach has traditionally been taken: Rather than examine the motion of a single particle, a bulk motion is imparted to the material of interest. Macroscale rheology is the traditional approach taken in the study of dynamic response properties of materials driven far from equilibrium. But for microscopically small systems, such macroscopic techniques often cannot access the dynamic behavior of interest, either because one is interested in microscale variation in properties, or the material is rare and unavailable in sufficient quantities for macroscopic testing, or because the force driving the system from equilibrium acts over very small length scales.

Active, nonlinear microrheology is one approach to interrogating the dynamic response properties of microscopically small systems: A Brownian "probe" (or set of probes) is driven through a complex fluid, and its motion tracked in order to infer the mechanical properties of the embedding material. With no external forcing the probe and background particles form an equilibrium microstructure that fluctuates thermally with the solvent. Probe motion through the dispersion distorts the microstructure; the character of this deformation, and hence its influence on probe motion, depends on the strength with which the probe is forced, F^{ext}, compared to thermal forces, kT/b, defining a Péclet number, $Pe = F^{ext}/(kT/b)$, where kT is the thermal energy and b the bath-particle size. Both the mean and the fluctuating motion of the probe are of interest. Recent studies showed that the reduction in mean probe speed gives the effective material viscosity. But the velocity of the probe may also fluctuate due to collisions with the suspended particles, causing the probe to undergo a random walk process. In our work here, it was shown that the long-time mean-square fluctuational motion of the probe is diffusive and the microdiffusivity of the forced probe was determined for the full range of Péclet number.

Previous work in microrheology defined a scalar viscosity; however, a tensorial expression for the suspension stress in microrheology was still lacking. The notion that diffusive flux is driven by gradients in particle-phase stress leads to the idea that the microdiffusivity can be related directly to the suspension stress, and that anisotropy in the diffusion tensor reveals normal stress differences. While the particle-phase stress tensor can be determined as the second moment of the deformed microstructure, in this study a connection was made between diffusion and stress gradients, and an analytical expression for particle-phase stress as a function of the microdiffusivity and microviscosity obtained, which is in excellent agreement with the micromechanical theory, simulation results, and the results of traditional macroscopic rheology. Simply tracking the mean and mean-square motion reveals the diffusivity, the viscosity, and the full stress tensor. Importantly, we have found that much of the rheologically important information about a material can be obtained by simply *watching a single particle move.*

In the study of suspension stress, it was also found that fluctuations in probe motion reduce

the viscous drag of the microstructure on the probe. The freedom to fluctuate gives the probe the ability to adjust its speed when encountering regions of higher or lower density. The hindrance of the microstructure is reduced, which has the effect of weakening the viscous resistance to its motion. On average, probe fluctuations thus give rise to an increment in advective flux, over the flux produced by a constant-velocity motion. That is, stress gradients drive advective flux of the probe. This can be thought of in terms of the fact that the constant-velocity problem is formulated hydrodynamically as a resistance problem: $\boldsymbol{F} = -\boldsymbol{M} \cdot \boldsymbol{U}$, whereas the constant-force mode is a mobility problem: $\boldsymbol{U} = -\boldsymbol{R} \cdot \boldsymbol{F}$. When there are no fluctuations $\boldsymbol{M} = \boldsymbol{R}^{-1}$ for a dilute hard-sphere suspension. But when fluctuations matter, $\boldsymbol{M} \neq \boldsymbol{R}^{-1}$. Their difference is the reduction in the resistive force, or, if you will, the presence of an advective force in the opposite direction of viscous drag forces. The effect of the fluctuations is the same as if a steady force acted on the bath, that in the constant-force mode, balances the fluctuations of the probe. My view of this as a "fictitious force" is inspired directly by the same view taken by Batchelor of the thermodynamic force (1976). It was also found that the non-equilibrium osmotic pressure can be viewed as a purely mechanical quantity—and that a stirred suspension can be characterized by an "effective temperature," which can give a purely mechanical definition of the temperature.

By studying fluctuations *away from equilibrium*, we have discovered a non-equilibrium relation between fluctuation and dissipation—and that the balance between the two is stored in the material stress. What can this tell us more fundamentally about energy and motion? In order to explore this further, we studied the evolution of stress and microstructure in a colloidal dispersion, by tracking transient probe motion during startup and cessation of a strong flow.

During the startup of the flow, it was found that the early-time behavior of the transient micro-viscosity is the same regardless of the strength of probe forcing, and that the microstructure evolves initially as a one-dimensional diffusive monopole in time as $\hat{t}^{1/2}$. The reason for this behavior is that it takes time for the probe to realize that it is not alone in the bath and to interact with the surrounding microstructure. The duration of this regime is then the fundamental timescale of the microstructure. After the forcing is removed, the motion of the probe and suspension does not cease

instantaneously. It was found that the suspension has several relaxation timescales: The probe's speed decays quickly at first, and then decays more slowly over longer timescales. The rate of initial decay depends on the state of the microstructure just before the flow was stopped; the higher the value of the Péclet number, the more rapid the initial decay. This behavior is in keeping with the prediction that much of the microstructural stress relaxation occurs when the probe and bath particles relax away from each other through the boundary layer. Since the initial distance that must be traveled is the width of the boundary layer, which scales as Pe^{-1}, stronger forcing prior to cessation leads to faster recovery after cessation. In the case of a constant-velocity probe, this initial relaxation takes longer due in part to a wider boundary layer: Since the probe cannot fluctuate, it acts as a "bulldozer" and piles up a larger density of particles on its upstream face. Both the particle density and boundary layer width are increased as compared to the constant-force mode. In addition, since the probe cannot diffuse, the only mechanism for relaxation is the diffusion of the bath particles—the diffusion is reduced by half compared to the constant-force mode and so the initial relaxation takes longer. Analytical and numerical results, and simulation measurements were in good agreement.

It was also found in the transient study that a colloidal dispersion of hard spheres exhibits nonlinear viscoelastic behavior. Upon release of the external force, the probe travels backwards in the bath due to the entropic force of the compressed microstructure—the suspension remembers its previous configuration for a time. While such behavior is well-known in polymeric and other topographically hindered materials, this is interesting behavior in a suspension of isotropic particles interacting only through short-range steric hindrance. Some of the energy of the probe's motion is evidently stored as free energy in the compressed configuration of bath particles; it is entropic, and *this is the origin of non-equilibrium suspension stress.* While the power input by the probe must all be dissipated, it takes time to do so, and the lag time allows energy storage in the form of material stress. Importantly, the available energy of the entropic "return spring" is less than the energy put into the suspension over the same time interval, which for $Pe = 30$ is approximately $30kT$. Some of the energy is dissipated. Over long times the Brownian motion of the bath particles dissipates the

stored free energy viscously, which is the underlying mechanism for long-time stress relaxation.

Entropic and osmotic forces play an important role in suspensions in other contexts as well. Depletion interactions in (near) equilibrium systems arise due to such forces. In order to study more closely the effects of these forces away from equilibrium, studies of the the interactive force between a pair of particles driven through a suspension were conducted. The force required to maintain a fixed distance between the probe particles was monitored as they were driven at constant velocity transverse to their line of centers through a dispersion. It was found that the depletion attraction between the probes competes with a non-equilibrium repulsion due to the osmotic pressure distribution around the probes. Both the entropic attraction and the osmotic repulsion act only when the probes are separated by less than five diameters; beyond this separation, they act as though alone in the dispersion. When the two are close enough to interact, it was observed that the osmotic force due to hard-sphere collisions is strictly repulsive; the depletion interaction is purely an entropic phenomenon. The competition between the two is won by mechanical forces as Pe increases and the osmotic force of collisions dominates the osmotic force of the entropic depletion.

Up to this point we have found that nonlinear microrheology is an important framework for understanding the fundamental physics of non-equilibrium suspension dynamics, and that it also provides a technique for rheological interrogation of much smaller scale systems than can be accessed by traditional rheological approaches.

But microrheology need not—in fact should not—be viewed as a microscale version of traditional shear rheology. However, we explored whether the measurements obtained via microrheology correspond with the bulk measurements obtained by shear macrorheology. Khair & Brady (2006) demonstrated that the microviscosity recovers all of the important phenomenological behavior of a dilute colloidal dispersion under flow, for same-size particles—the same scaling in Pe, the same onset of shear thinning and thickening, and in the limit of negligible hydrodynamics, the same terminal Newtonian plateau. In §4.7, we compared the osmotic pressure and stress tensor components for microrheology with the dilute theory of Bergenholtz *et al.* (2002), and found that the an excellent match for the osmotic pressure, and a good match for the stress components. This rather surprising

result was understood by physical arguments, and in consideration of the eigenvalue problem represented by the osmotic pressure. One important difference became evident in the comparison of the individual elements of the stress tensors. Here, the match between the parallel and perpendicular diagonal elements of the stress tensor in macrorheology contains no viscous stress: viscosity is strictly deviatoric in simply sheared suspensions. In contradistinction, viscous stress in microrheology is normal, and must appear on the diagonal of the stress tensor. When the viscous stress was removed, very good agreement between the first normal stress differences was found.

An additional important consideration in the comparison of micro- to macrorheology is the fact that microrheological flows are not viscometric: They do not produces statistically homogeneous flows and microstructures. The microstructure around a driven probe is statistically different than the structure away from the probe. The question then arises whether the suspension properties sampled by the probe reflect the bulk properties of the medium, as is the case in macrorheology. A similar concern arises in falling-ball rheometry. It has been proposed that the probe-phase stress is not the only contributor to overall particle-phase stress—that interactions between the bath particles themselves make a significant contribution (Squires, 2008). A simple scaling analysis shows that bath-bath particle interactions contribute only to $O(\phi_b^2)$, a negligible contribution for a dilute bath—and as shown in §4.7, the probe-bath measurement evidently matches dilute shear theory quite well. Nonetheless, one must carefully consider contributions to osmotic pressure due to collisions between the bath particles themselves. Brownian dynamics simulations for single-probe forcing, in a bath of interacting background particles were conducted in this investigation. The contribution to stress due to bath-bath particles was monitored, and found not to deviate from the equilibrium osmotic pressure. Thus we conclude that in suspensions of non-hydrodynamically interacting particles, forcing the probe through the suspension and computing the stress on the probe phase gives an accurate account of non-equilibrium stress.

Finally, we return to the idea that probe motion is a window through which we can view the connection between fluctuation and dissipation. Nonlinear microrheology provides far more than a microscale technique for interrogating complex fluids. We have asked the question: What can

non-equilibrium fluctuation and dissipation tell us more fundamentally about energy and motion? Avogadro's constant was the sought-after connection during the work of Einstein and Perrin. It establishes a relationship between the macroscopic gas constant $\mathcal{R}$ and Boltzmann's constant k, which connects energy at the atomic level to temperature at the macroscopic level. It allows the ideal gas equation of state to be stated in terms of the properties of molecules rather than the experimental constant $\mathcal{R}$. Here we have stated the equation of motion of an "ideal gas" of particles in terms of the properties of the individual particles and of the system. We related the energy density of the particles (the stress) to "effective temperature," at the macroscopic level. As we look toward the future, this leaves open an intriguing question: Can we formulate a more universal way to define temperature?

Appendix A

Perspectives on gradient-driven diffusion

In his theory on the diffusion of small particles (1906), Einstein asserted that the osmotic pressure is the driving force in the diffusive flux for non-interacting particles. The central assumption was the existence of thermodynamic and mechanical equilibrium. In his "Elementary Theory" for Brownian motion, he describes an osmotic force balance on suspended particles that causes the particles to undergo diffusive migration. Assuming a Fickian process, he deduced the diffusion coefficient for a spherical particle. In his paper on the subject, he exposes the idea with a somewhat different approach, supposing a suspension of particles of size a at number density n in a solvent of viscosity η, acted upon by a force derived from an external potential Φ. The suspension is in a finite container where for he sake of definiteness, its "bottom" surface is placed perpendicular to the line of the external force. He asserts that at equilibrium, the particles are arranged with a Boltzmann distribution

$$n(\boldsymbol{x}) = n_0 e^{-\Phi/kT}. \tag{A.1}$$

The external force $-\nabla\Phi$ drives advective flux $\boldsymbol{j}_{adv} = -n\boldsymbol{M}\cdot\nabla\Phi$, where the small particle size gives their Stokes velocity as the product of their hydrodynamic mobility $\boldsymbol{M}$ with the applied force. This advective flux gives rise to a concentration gradient near the opposing wall of the container, which drives a diffusive, down-gradient flux $\boldsymbol{j}_{diff} = -\boldsymbol{D}\cdot\nabla n$ in the opposite direction of the advective

flux. At equilibrium the net flux must be zero:

$$-n\boldsymbol{M}\cdot(\nabla\Phi)-\boldsymbol{D}\cdot\nabla n=0, \tag{A.2}$$

and $\nabla n=-(n/kT)\nabla\Phi$. Since the potential force is arbitrary, we have the result

$$\boldsymbol{D}=kT\boldsymbol{M}. \tag{A.3}$$

For spherical particles,

$$\boldsymbol{D}=\frac{kT}{6\pi\eta a}, \tag{A.4}$$

the familiar Stokes-Einstein relation giving the diffusivity of a spherical particle in a solvent. But how can this result be connected again to the osmotic pressure of the suspension of small particles?

Reconsidering Einstein's thought-experiment, Batchelor (1976) noted that the Boltzmann distribution (A.1) invoked by Einstein is equivalently given by the chemical potential:

$$\mu=kT\log(n/n_0)+\Phi, \tag{A.5}$$

Taking the gradient of the above expression recovers the flux balance (A.2) due to Einstein. But more importantly, Batchelor observed that since $-\nabla\Phi=kT\nabla\log(n/n_0)$, it is implied that the force $-\nabla\Phi$ on the particles is balanced by an equal and opposite force. That is, the effect of Brownian migration is the same as if an effective steady force acted on each particle:

$$\boldsymbol{F}^{th}\equiv-kT\nabla\log(n/n_0), \tag{A.6}$$

where the superscript th indicates that this is a "thermodynamic" force. The physical idea is that the effect of Brownian motion in a suspension of particles is to make their distribution statistically uniform—to restore the equilibrium distribution when the arrangement of particles is distorted by an external force. This tendency to make uniform the particle distribution is the driving force for

Brownian diffusion.

Rather than a Boltzmann distribution of particles, a more general condition to place on equilibrium particle behavior is the requirement for uniformity of chemical potential. A simple case in which to take such an approach is that of gradient diffusion in an inhomogeneous suspension. As a particle moves down gradient, the work required to move it from one region in space to another is the work required to add a new particle to a system, which is given by the chemical potential. The chemical potential is defined as the change in the Gibbs free energy G required in order to accommodate a new particle, holding pressure and temperature constant, $\mu(n, P, T) = (\partial G/\partial N)_{P,T}$. If an external field Φ acts on the particles, the chemical potential is modified accordingly:

$$\mu(n, P, T, \Phi) = \mu(n, P, T) + \Phi. \tag{A.7}$$

Because the Gibbs relation demands that the sum over species of the chemical potential is zero, the external force $\nabla\Phi$ is balanced exactly by the thermodynamic force $\boldsymbol{F}^{th} = -\nabla\mu(n, P, T)$. That is, the gradient in number density gives rise to a gradient in the chemical potential if the particles interact. Now in general, the presence of an external potential gradient gives rise not only to gradients in number density, but also in the pressure:

$$\nabla\mu = \left(\frac{\partial\mu}{\partial n}\right)_{P,T} \nabla n + \left(\frac{\partial\mu}{\partial P}\right)_{n,T} \nabla P. \tag{A.8}$$

For diffusion in the absence of an external force, the pressure gradient is zero. (However, below we shall see that the pressure gradient—and its diffusive character—plays an important role in the driving force away from equilibrium.) The advective flux $\boldsymbol{j}_{adv} = -n\boldsymbol{M}\nabla\mu$ due to the external potential is balanced by diffusive flux $\boldsymbol{j}_{diff} = -\boldsymbol{D} \cdot \nabla n$:

$$\boldsymbol{D}^c \cdot \nabla n = n\boldsymbol{M} \cdot \nabla\mu, \tag{A.9}$$

where the superscript c indicates that the coefficient of down-gradient diffusivity is the collective

diffusivity, $\boldsymbol{D}^c$. Now the chain rule gives $\nabla\mu = (\partial\mu/\partial n)\nabla n$; substituting this into the equation above gives for $\boldsymbol{D}^c$

$$\boldsymbol{D}^c = n\boldsymbol{M}\frac{\partial\mu}{\partial n}. \tag{A.10}$$

Equation (A.10) indicates that a number-density gradient in the chemical potential is the driving force for macroscopic *collective* diffusion. So far, we have established a connection between chemical potential gradients and Brownian diffusion. But the argument due to Einstein was able to show that equivalently, osmotic pressure gradients drive diffusion. Can the same connection be made here? Let us examine equation (A.10) more closely—in particular, the mobility $\boldsymbol{M}$—to see if it is so.

Because gradient diffusion is the same as sedimentation (Batchelor, 1972), the mobility in equation (A.10) is defined by the sedimentation coefficient $K(\phi)$: $\boldsymbol{M} = K(\phi)/6\pi\eta a\boldsymbol{I}$. When particles are close enough to interact hydrodynamically (*i.e.* the volume fraction of particles $\phi = 4\pi a^3 n/3$ is not small), down-gradient particle diffusion drives a backflow of fluid in order to conserve volume (Batchelor, 1972; Russel & Glendinning, 1981; Brady, 2011). In addition, one must properly account for the chemical potential gradient acting on the fluid. Moving this fluid force onto the particles so that the fluid is force-free gives

$$\boldsymbol{D}^c = \frac{K(\phi)}{6\pi\eta a}\frac{n}{1-\phi}\frac{\partial\mu}{\partial n}\boldsymbol{I}, \tag{A.11}$$

where $K(\phi) = 1 - 6.55\phi + O(\phi^2)$ is the sedimentation coefficient for a dilute dispersion of hydrodynamically interacting Brownian particles(Batchelor, 1972). The effect of particle interactions (in the dilute pair limit) on the chemical potential gradient is given by the second virial coefficient β; this is obtained from the partition function as $\beta = -8$, and the collective diffusivity becomes

$$\boldsymbol{D} = (1 + (\beta + 6.55\phi)\frac{kT}{6\pi\eta a}\boldsymbol{I} = (1 + 1.45\phi)\frac{kT}{6\pi\eta a}\boldsymbol{I}. \tag{A.12}$$

Now, this same approach can be generalized to the case of relative diffusion of particles amongst any number of other particle species. In the case of two species, A and B say, let us consider that $\phi_A \ll \phi_B$. This amounts to tagging species A as a tracer subset of B (cf chapter 3). The

labeling is done in such a way that there is a weak gradient in their concentration $\nabla\phi_A$, and hence a Fickian flux of species A. Because species A is dilute and their concentration much smaller than that of the species B, the A-particles interact only with the B-particles. The motion of species A is therefore unaffected by their gradient, in the sense that their mean drift is zero, and hence their mean-square displacement $\langle \boldsymbol{x}'\boldsymbol{x}' \rangle$ is unchanged from that of the monodisperse tagged particles above. Thus, the tracer situation is formally identical to the down-gradient diffusion of an infinitely dilute single species. Hence the self-diffusivity of species A can be described in the Fickian (macroscopic) sense but yet evaluated over short and long times. The tracer diffusivity is the self-diffusivity in the presence of a collection of background bath particles at concentration ϕ_B, but an additional hindrance to the motion of species A arises, that is, the presence of species B. Batchelor computed this contribution in a dilute suspension (1976) as $1.83\phi_B$ for same size A and B particles:

$$\boldsymbol{D} = (1 + 1.45\phi_A - 1.83\phi_B)\frac{kT}{6\pi\eta a}\boldsymbol{I}. \tag{A.13}$$

But due to their inconsequentially small number density, species A can migrate without driving backflow, and hence their migration lacks the character of sedimentation. Rather, the only hindrance to their motion is the passive hindrance of other particles, which as $\phi_A \to 0$ gives

$$\boldsymbol{D} = (1 - 1.83\phi_B)\frac{kT}{6\pi\eta a}\boldsymbol{I} = \boldsymbol{D}_A^S, \tag{A.14}$$

As discussed in chapter 2, the tracer diffusion of A through the species B suspension is formally equivalent to its self-diffusivity (Batchelor, 1976; Rallison & Hinch, 1986). In the case of no hydrodynamic interactions,

$$\boldsymbol{D}_A^S = (1 - 2.0\phi_B)\frac{kT}{6\pi\eta a}\boldsymbol{I}, \tag{A.15}$$

and the self-diffusivity of a particle in a suspension is recovered. In the limit of no species B, the Stokes-Einstein relation for the diffusivity of an isolated particle is recovered.

Now let us return to the Einstein's idea that osmotic pressure gradients drive diffusion. We know

that for a dilute dispersion of species A, $\Pi_A = n_A kT(1+4\phi_A)$, and so $\partial\Pi_A/\partial n_A = kT(1+8\phi_A) \approx kT$. The general expression above for the diffusivity is $\boldsymbol{D}_A = kT\boldsymbol{M}$. One might then propose that

$$\boldsymbol{D}_A = \boldsymbol{M}\frac{\partial \Pi_A}{\partial n_A}. \tag{A.16}$$

Recall that Π is the negative of one-third the trace of the suspension stress tensor, $\boldsymbol{\Sigma}$. This prompts us to propose a more general form of (A.16):

$$\frac{\partial \boldsymbol{\Sigma}}{\partial n} = -\boldsymbol{R}\cdot\boldsymbol{D}, \tag{A.17}$$

where the resistance tensor $\boldsymbol{R}$ is the inverse of the mobility tensor, $\boldsymbol{R} = \boldsymbol{M}^{-1}$. Evidently, gradients in the stress do indeed drive Brownian diffusion—whether the suspension is at equilibrium, or is linearly displaced from equilibrium.

Bibliography

Abbot, J. R., Graham, A. L., Mondy, L. A. & Brenner, H. 1997 Dispersion of a ball settling through a quiescent neutrally buoyant suspension. *J. Fluid Mech.* **361**, 309–331.

Asakura, S. & Oosawa, F. 1954 On interaction between two bodies immersed in a solution of macromolecules. *J. Chem. Phys.* **22(7)**, 1255–1256.

Avagadro, A. 1811 Essai d'une maniere de determiner les masses relatives des molecules elementaires des corps, et les proportions selon lesquelles elles entrent dans ces combinaisons. *J. Physique* **73**, 58–76.

Barnes, H. A., Hutton, F. F. & Walters, K. 1989 *An introduction to rheology*. Elsevier.

Batchelor, G. K. 1970 The stress in a suspension of force-free particles. *J. Fluid Mech.* **41(3)**, 545–570.

Batchelor, G. K. 1972 Sedimentation in a dilute dispersion of spheres. *J. Fluid Mech.* **52(2)**, 245–268.

Batchelor, G. K. 1976 Brownian diffusion of particles with hydrodynamic interaction. *J. Fluid Mech.* **74**, 1–29.

Batchelor, G. K. 1977 The effect of brownian motion on the bulk stress in a suspension of spherical particles. *J. Fluid Mech.* **83**, 97–117.

Batchelor, G. K. 1983 Diffusion in a dilute polydisperse system of interacting spheres. *J. Fluid Mech.* **131**, 155–175.

Batchelor, G. K. & Green, J. T. 1972 The hydrodynamic interaction of two small freely-moving spheres in a linear flow field. *J. Fluid Mech.* **56(2)**, 375–400.

Bergenholtz, J., Brady, J. F. & Vicic, M. 2002 The non-newtonian rheology of dilute colloidal suspensions. *J. Fluid Mech.* **456**, 239–275.

Bossis, G. & Brady, J. F. 1989 The rheology of brownian suspensions. *J. Chem Phys.* **91**, 1866–1874.

Brady, J. F. 1993*a* Brownian motion, hydrodynamics, and the osmotic pressure. *J. Chem Phys.* **98**, 3335–3341.

Brady, J. F. 1993*b* The rheological behavior of concentrated colloidal dispersions. *J. Chem Phys.* **99**, 567–581.

Brady, J. F. 1994 The long-time self-diffusivity in concentrated colloidal dispersions. *J. Fluid. Mech.* **272**, 109–133.

Brady, J. F. 2007 *Introduction to Suspension Dynamics*. Unpublished.

Brady, J. F. 2011 Particle motion driven by solute gradients with application to autonomous motion: continuum and colloidal perspectives. *J. Fluid. Mech.* **667**, 216–259.

Brady, J. F. & Morris, J. F. 1997 Microstructure of strongly sheared suspensions and its impact on rheology and diffusion. *J. Fluid. Mech.* **348**, 103–139.

Brady, J. F. & Vicic, M. 1995 Normal stresses in colloidal suspensions. *J. Rheol.* **39(3)**, 545–566.

Breedveld, J., den Ende, D. Van, Tripathi, A. & Acrivos, A. 1998 The measurement of the shear-induced particle and fluid tracer diffusivities in concentrated suspensions by a novel method. *J. Fluid Mech.* **375**, 297–318.

Brown, R. 1828 A brief account of microscopical observations made on the particles contained in the pollen of plants. *Phil. Mag.* **4**, 161–173.

Carnahan, N. F. & Starling, K. E. 1969 Equation of state for nonattracting rigid spheres. *J. Chem. Phys.* **51(2)**, 635–636.

Carpen, Ileana 2005 Studies of suspension behavior. PhD thesis, California Institute of Technology.

Carpen, I. C. & Brady, J. F. 2005 Microrheology of colloidal dispersions by brownian dynamics simulations. *J. Rheol.* **49**, 1483–1502.

Cordova-Figueroa, U. M. & Brady, J. F. 2008 Osmotic propulsion: The osmotic motor. *PRL* **100**, 158303–1–158303–4.

Davis, R. H. & Hill, N. A. 1992 Hydrodynamic diffusion of a sphere sedimenting through a dilute suspension of neutrally buoyant spheres. *J. Fluid Mech.* **236**, 513–533.

Einstein, A. 1906 On the theory of the brownian movement. *Ann. der Physik* **19**, 371–381.

Foss, D. R. & Brady, J. F. 2000*a* Brownian dynamics simulation of hard-sphere colloidal dispersions. *J. Rheol.* **44(3)**, 629–651.

Foss, D. R. & Brady, J. F. 2000*b* Structure, diffusion and rheology of brownian suspensions by stokesian dynamics simulation. *J. Fluid Mech.* **407**, 167–200.

G. A. Mansoori, N. F. Carnahan, K. E. Starling & T. W. Leland, Jr. 1971 Equilibrium thermodynamic properties of the mixture of hard spheres. *J. Chem. Phys.* **54(4)**, 1523–1525.

Green, M. S. 1954 Markoff random processes and the statistical mechanics of time-dependent phenomena ii. *J. Chem. Phys.* **22**, 398–413.

Habdas, P., Schaar, D., Levitt, A. C. & Weeks, E. R. 2004 Forced motion of a probe particle near the colloidal glass transition. *Europhys. Lett.* **67**, 477–483.

Haw, M. 2007 *Middle World - The Restless Heart of Matter and LIfe*. Macmillan.

Heath, J. R., Davis, M. E. & Hood, L. 2009 Nanomedicine–revolutionizing the fight against cancer. *Scientific American* **300**, 44.

Heyes, D. M. & Melrose, J. R. 1993 Brownian dynamics simulations of model hard-sphere suspensions. *J. Non-Newtonian Fluid Mech.* **46**, 1–28.

Hocquart, R. & Hinch, E. J. 1983 The long-time tail of the angular-velocity auto-correlation function for a rigid brownian particle of arbitrary centrally symmetric shape. *J. Fluid Mech.* **137**, 217–220.

Janke, C., Rogowski, K., Wloga, D., Regnard, C., Kajava, A. V., Strub, J. M., Temurak, N., van Dijk, J., Boucher, D., van Dorseelaer, A., Suryavanshi, S., Gaertig, J. & Edde, B. 2005 Tubulin polyglutamylase enzymes are members of the t.t.l. domain protein family. *Science* **308**, 1758–1762.

Kaffashi, B., O'Brien, V. T., Mackay, M. E. & Underwood, S. M. 1997 Elastic-like and viscous-like components of the shear viscosity for nearly hard sphere, brownian suspensions. *J. Colloid Interf. Sci.* **187**, 22–28.

Khair, A. S. & Brady, J. F. 2005 "Microviscoelasticity" of colloidal dispersions. *J. Rheol.* **49**, 1449–1481.

Khair, A. S. & Brady, J. F. 2006 Single particle motion in colloidal dispersions: a simple model for active and nonlinear microrheology. *J. Fluid Mech.* **557**, 73–117.

Khair, A. S. & Brady, J. F. 2008 Microrheology of colloidal dispersions: Shape matters. *J. Rheol.* **52**, 165–196.

Kubo, R. 1966 The fluctuation-dissipation theorem. *Rep. Prog. Phys.* **29**, 255–285.

Langevin, P. 1908 Sur la theorie du mouvement brownien (On the theory of Brownian motion). *C. R. Acad. Sci. (Paris)* **146**, 530–533.

Leighton, D. & Acrivos, A. 1987 Measurement of shear-induced self-diffusion in concentrated suspensions of spheres. *J. Fluid Mech.* **177**, 109–131.

Lionberger, R. A. & Russel, W. B. 1994 High frequency modulus of hard sphere colloids. *J. Rheol.* **38(6)**, 1885–1908.

Lucretius ca. 50 B.C. *De Rerum Natura* (On the nature of things) *trans. by J. S. Watson (1851)*. Henry G. Bohn.

Lukacs, G. L., Haggie, P., Seksek, O., Lechardeur, D., Freedman, N. & Verkman, A.S. 1999 Size-dependent DNA mobility in cytoplasm and nucleus. *J. Bio. Chem.*. **275(3)**, 1625–1629.

Mackay, M. E. & Kaffashi, B. 1995 Stress jumps of charged colloidal suspensions, measurement of the elastic-like and viscous-like stress components. *J. Colloid Interf. Sci.* **174**, 117–123.

MacKintosh, F. C. & Schmidt, C. F. 1999 Microrheology. *Curr. Op. Colloid Interf. Sci.* **4**, 300–307.

McQuarrie, D. A. 1976 *Statistical Mechanics*. Harper and Row.

Meyer, A., Marshall, A., Bush, B. G. & Furst, E. M. 2005 Laser tweezer microrheology of a colloidal suspension. *J. Rheol.* **50**, 77–92.

Morris, J. F. & Brady, J. F. 1996 Self diffusion in sheared suspensions. *J. Fluid. Mech.* **312**, 223–252.

Nägele, G. & Bergenholtz, J. 1998 Linear viscoelasticity of colloidal mixtures. *J. Chem. Phys.* **108**, 9893.

Perrin, J-. B. 1909 Mouvement brownien et réalité moléculaire (brownian movement and the molecular reality). *Ann. de Chimie et de Physique (VIII)* **18**, 5–114.

Perrin, J-. B. 1914 Les atomes) .

Rallison, J. M. & Hinch, E. J. 1986 The effect of particle interactions on dynamic light scattering from a dilute suspension. *J. Fluid Mech.* **167**, 131–168.

Russel, W. B. 1981 Brownian motion of small particles suspended in liquids. *Ann. Rev. Fluid Mech.* **13**, 425–455.

Russel, W. B. & Glendinning, A. B. 1981 The effective diffusion coefficient detected by dynamic light scattering. *J. Chem. Phys.* **74(2)**, 948–952.

Russel, W. B., Saville, D. A. & Schowalter, W. R. 1989 *Colloidal Dispersions*. Cambridge University Press.

Sami, Saud 1996 Stokesian dynamics simulation of brownian suspensions in extensional flow. PhD thesis, California Institute of Technology.

Shirai, Y., Osgood, A. J., Zhao, Y., Kelly, K. F. & Tour, J. M. 2005 Directional control in thermally driven single-molecule nanocars. *Nano Lett.* **5**, 2330–2334.

Squires, T. M. 2008 Nonlinear microrheology: Bulk stresses versus direct interactions. *Langmuir* **24**, 1147–1159.

Squires, T. M. & Brady, J. F. 2005 A simple paradigm for active and nonlinear microrheology. *Phys. Fluids* **17**, 073101–1–073101–2.

Suh, J., Wirtz, D. & Hanes, J. 2003 Efficient active transport of gene nanocarriers to the cell nucleus. *PNAS* **100(7)**, 3738–3882.

Valko, P. P. & Abate, J. 2002 Comparison of sequence accelerators for the gaver method of numerical Laplace transform inversion, computers and mathematics with applications. *CAM* **5307**, 1–10.

Verkman, A. S. 2002 Solute and macromolecule diffusion in cellular aqueous compartments. *Trends Biochem. Sci.* **27**, 27–33.

Watanabe, H., Sato, T. & Osaki, K. 1996*a* Relaxation of spherical micellar systems of styrene-isoprene diblock copolymers .2. nonlinear stress relaxation behavior. *Macromolecules* **29**, 3890–3897.

Watanabe, H., Yao, M-. L., Osaki, K., Shikata, T., Niwa, H. & Morishima, Y. 1996*b* Nonlinear rheological behavior of a concentrated spherical silica suspension. *Rheo. Acta* **35(5)**, 443–445.

Wilson, L. G., Harrison, A. W., Schofield, A. B., Arlt, J. & Poon, W. C. K. 2009 Passive and active microrheology of hard-sphere colloids. *J. Phys. Chem.* **113**, 3806–3812.

Zia, R. N. & Brady, J. F. 2010 Single particle motion in colloids: force-induced diffusion. *J. Fluid Mech.* **658**, 188–210.